Progress Towards Gas Mixture Selection and Heat Transfer Coefficient Measurements for the Shell-Side of a Joule-Thomson Cryocooler

By

Jennifer A. Detlor

A dissertation submitted in partial fulfillment of

the requirements for the degree of

Doctor of Philosophy

(Mechanical Engineering)

at the

UNIVERSITY OF WISCONSIN - MADISON

2022

Date of final oral examination: 12/21/2022

The dissertation is approved by the following members of the Final Oral Committee:

John Pfotenhauer, Professor, Mechanical Engineering
Gregory Nellis, Professor, Mechanical Engineering
Franklin Miller, Professor, Mechanical Engineering
Dakotah Thompson, Assistant Professor, Mechanical Engineering
Michael Corradini, Emeritus Professor, Engineering Physics

Abstract

Finned-tube heat exchangers are the most widely used heat exchanger for miniature Joule-Thomson (JT) cryocoolers. The basic configuration, known as a Giauque-Hampson (GH) or coiled tube heat exchanger, involves the high-pressure stream flowing through a finned-tube that is helically coiled upon a cylindrical core while the low-pressure stream flows over the fins in the annular space created by the core and the inner diameter of a shell. Recent advances in technology have increased interest in mixed-gas JT (MGJT) cryocoolers that can provide cooling potential in the temperature ranges of 125 to 150 K. While it has been suggested that the heat transfer coefficient (htc) of the return stream is a key parameter affecting the behavior of the entire heat exchanger of a MGJT cryocooler, the htc of the return stream is often neglected during the design due to the much larger surface area that is present on fin side of the heat exchanger. However, there is still no data or theory in open literature that characterizes the heat transfer and pressure drop characteristics of two-phase multi-component mixtures on the shell side in these heat exchangers.

Beyond the broad goal of investigating gas mixture selection for MGJT cryocoolers, the experimental work in this study aimed to gain insight into these thermal characteristics by developing a test facility capable of measuring the htc for this geometry at operating conditions of interest to MGJT cryocooling. The capabilities of the test facility were demonstrated with a semi-flammable mixture. The size of the GH heat exchanger prototype and operating parameters of the test facility were consistent with those of interest for MGJT cryocoolers. Measurements of the htc of the mixed gas on the shell-side of the GH heat exchanger prototype were collected, as well as select data for the friction factor. For the mixture examined, the two-phase htc was found to be between 12 to 19 W/m^2-K with uncertainties of approximately 12% for qualities in the range

of 0.31 to 0.62. This data reveals that the shell side of a MGJT cryocooler is the dominant resistance, even though it has a larger surface area. Therefore, the htc of the mixed gas on the shell-side of the GH heat exchanger is crucial for predicting the overall performance. While only a small amount of data was collected in this study, the data collected clearly demonstrates the need for and importance of developing accurate correlations for two-phase multi-component mixtures on the shell-side of the GH heat exchanger for operating conditions consistent with MGJT cryocoolers. A large data collection campaign is proposed and enabled by the test facility developed in this work. Only with these correlations can the effects of the mixture selection on the pressure drop and the effectiveness of the heat exchanger be considered in the design of a MGJT for optimal performance.

Table of Contents

Contents

List of Figures

List of Tables

Abbreviations, Nomenclature and Symbols

Abbreviations

BC	Boundary condition
CAD	Computer-aided design
CF	ConFlat
$CU( )$	Contribution to the uncertainty of
DAQ	Data acquisition
EES	Engineering Equation Solver
GC	Gas chromatograph
GH	Giauque-Hampson
H	Constant heat flux boundary condition
HC	Hydrocarbon
htc	Heat transfer coefficient
HP	High pressure
JT	Joule-Thomson
LP	Low pressure
MAD	Median absolute deviations
$MATLAB$	Matrix Laboratory
MG	Mixed gas
$MGJT$	Mixed gas Joule-Thomson
MLI	Multilayer insulation
MW	Molecular weight
PID	Proportional integral derivative
PRT	Platinum resistance thermometer
PVC	Polyvinyl chloride
$REFPROP$	Reference Fluid Thermodynamic and Transport Properties Database
RF	Response factor
RPM	Revolutions per minute
$RU( )$	Relative uncertainty
SF	Interaction with a secondary fluid
SF	Scaling factor
SR	Synthetic refrigerant
T	Constant temperature boundary condition
TCD	Thermal conductivity detector
$U( )$	Uncertainty of
VCR	Vacuum coupling radiation

Nomenclature

A	Peak area
A_c	Cross-sectional area for flow
$A_{c,hc}$	Cross-sectional area of flow for mixed gas using hypothetical cylinder concept
$A_{c,mg}$	Cross-sectional area of flow for mixed gas using projected area method
$A_{c,vc}$	Cross-sectional area of flow for mixed gas using free volume concept
A_s	Surface area for convection
c	Specific heat capacity
$\dot{C}$	Capacitance rate
c_P	Constant pressure specific heat capacity
C_R	Capacitance ratio
C_v	Flow Coefficient
COP	Coefficient of performance
$\widetilde{D}$	Inner diameter of 6.35 mm (1/8") VCR union
D_c	Mean diameter of coil
D_e	Effective mean diameter of shell
D_f	Outer diameter of fin
D_h	Hydraulic diameter
D_i	Inner diameter of tube
D_m	Outer diameter of mandrel
D_o	Outer diameter of tube (also the fin root diameter)
D_s	Inner diameter of shell
$\bar{f}$	Average friction factor
F	Number of internal properties required to fix the state of a substance
G	Mass flux
h	Enthalpy
h	Local heat transfer coefficient
$\bar{h}$	Average heat transfer coefficient
j	Colburn factor
k	Isentropic exponent
k	Thermal conductivity
k_{bp}	By-pass factor
K	K factor
L	Length
L_t	Length of tube
L_m	Length of mandrel
$\dot{m}$	Mass flow rate
n	Number of components in mixture
N_f	Number of fins per unit length
N_{tot}	Total number of fins
NTU	Number of transfer units
P	Pressure
p_c	Coil pitch

P_{dis}	Discharge pressure
p_f	Fin pitch
P_{sat}	Saturation pressure
P_{suc}	Suction pressure
per	Perimeter
$\dot{q}$	Heat transfer rate
$\dot{q}_{hx}$	Heat transfer rate in the heat exchanger
$\dot{q}_{load}$	Cooling capacity
$\dot{Q}/\dot{m}$	Refrigeration per mass flow
R_{cond}	Thermal resistance for conduction
R_{conv}	Thermal resistance for convection
Re	Reynolds number
R_f	Thermal resistance for the finned surface
R_{tot}	Total thermal resistance
R_{uf}	Thermal resistance for the unfinned surface
sp_f	Fin spacing
T	Temperature
T_c	Temperature at critical point
th	thickness
u_m	Mean velocity
u_b	Uncertainty from bias
u_c	Combined uncertainty
u_{DAQ}	Uncertainty from DAQ resolution
u_i	Uncertainty from resolution of instrument
u_p	Uncertainty due to precision
u_r	Uncertainty from repeatability
u_s	Uncertainty from sensitivity
u_V	Measured voltage uncertainty
UA	Conductance
$\dot{V}$	Volumetric flow rate
x	Quality
X	Molar fraction

Symbols

δ_t	Thermal boundary layer thickness
Δh_{hx}	Enthalpy difference of the heat exchanger
Δh_T	Isothermal enthalpy difference (ideal)
$\Delta h'$	Actual enthalpy difference
ΔP	Change in pressure

ΔT_{pp}	Pinch point temperature difference
Δx	Change in quality
ε	Effectiveness
λ_f	Flow channel aspect ratio
μ	Dynamic viscosity
η_{comb}	Combined efficiency
η_f	Fin efficiency
ρ	Density
Π	Number of phases

Other Common Subscripts and Superscripts

act	Actual
amb	Ambient
avg	Average
c	Corrected
f	Finned
G	Gas
He	Helium
HP	High pressure
HX	Heat exchanger
i	ith component
in	Inlet
j	jth component
L	Liquid
LP	Low pressure
m	Mass basis
max	Maximum
min	Minimum
MG	Mixed gas
N_2	Nitrogen
out	Outlet
ref	Reference
t	Tube
uc	Uncorrected
uf	Unfinned

1. Background and Motivation

The advantages of small closed-cycle Joule-Thomson (JT) cryocoolers that makes them attractive for many applications is their small size and the resulting fast cool-down time [1]. When compared specifically to Stirling-cycle coolers, they offer continuous flow for heat lift and heat rejection as well as low vibration [2]. Nonetheless, the use of small closed-cycle JT cryocoolers has been limited by the relatively low thermodynamic efficiency of the cycle at typical cryogenic device temperatures of 80 K. Recent advances in mid-wave infrared focal plane technology broaden the attractive temperature range of their operation up into the range of 125 to 150 K. Within this higher temperature range, JT cryocoolers can potentially achieve efficiencies comparable to Stirling-cycle coolers [3]. In order for the cycle to achieve relatively high efficiency and use a low-cost compressor, it is necessary that the JT cryocooler provide cooling at low pressure ratios and low values of operating pressures. To provide cooling under these conditions, a proper gas mixture must be selected as the working fluid. Proper selection of the gas mixture is the primary objective of the research outlined in this report. This selection process relies on understanding both the thermodynamic properties as well as the thermal-fluid behavior and therefore a substantial portion of this research is related to measuring the heat transfer coefficient for a mixed gas refrigerant flowing through a prototypic geometry. Let us begin with a detailed description of the cycle, the cooling potential and an explanation for choosing a gas mixture over a pure fluid.

1.1. The Joule-Thomson Cycle

The simplest mode of operation for a JT cryocooler is the Linde-Hampson cycle shown in Figure 1.1 [4]. In its simplest form, the cycle consists of a compressor, aftercooler, counter-flow

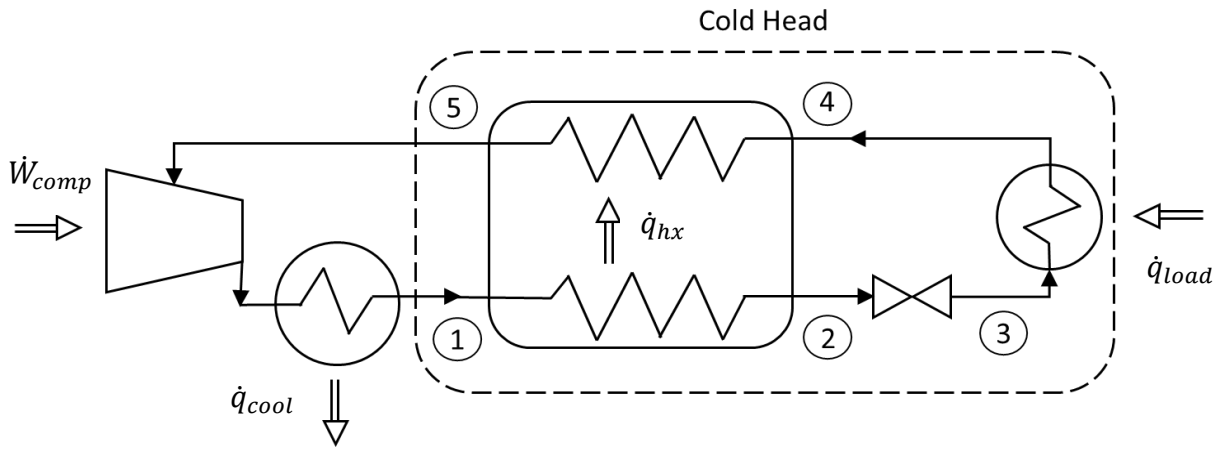

Figure 1.1. Diagram of simple Linde-Hampson cycle.

heat exchanger, expansion valve and load heat exchanger. There are five distinct state points within the cycle that are overlaid on a T-s diagram in Figure 1.2 to illustrate the cycle. At state 1 the gas exits the aftercooler at high-pressure (HP) and near room temperature. From states 1 to 2, the HP gas passes through the counter-flow heat exchanger rejecting heat to the low-pressure (LP) stream returning from the load. From states 2 to 3, the gas expands from HP to LP through the JT valve

at constant enthalpy. Below room temperature, this pressure drop at constant enthalpy is accompanied by a decrease in temperature for most gases. The fluid absorbs heat from the load between states 3 and 4. The LP fluid then passes back through the heat exchanger, precooling the incoming HP gas, and returns to the inlet of the compressor from states 4 to 5. The fluid is then compressed to HP with an increase of temperature and passes through the after cooler to begin the cycle again at state 1.

Enclosed by a dashed line in Figure 1.1, the cold head consists of the counter-flow heat exchanger, expansion valve and load heat exchanger. Applying the First Law of Thermodynamics to the cold head leads to an expression for the cooling capacity of the cryocooler:

$$\dot{q}_{load} = \dot{m}(h_1 - h_5) \tag{1.1}$$

where $\dot{q}_{load}$ is the cooling capacity, $\dot{m}$ is the mass flow rate, and h_1 and h_5 are the specific enthalpies at states 1 and 5, respectively. The enthalpy difference between states 1 and 5 is

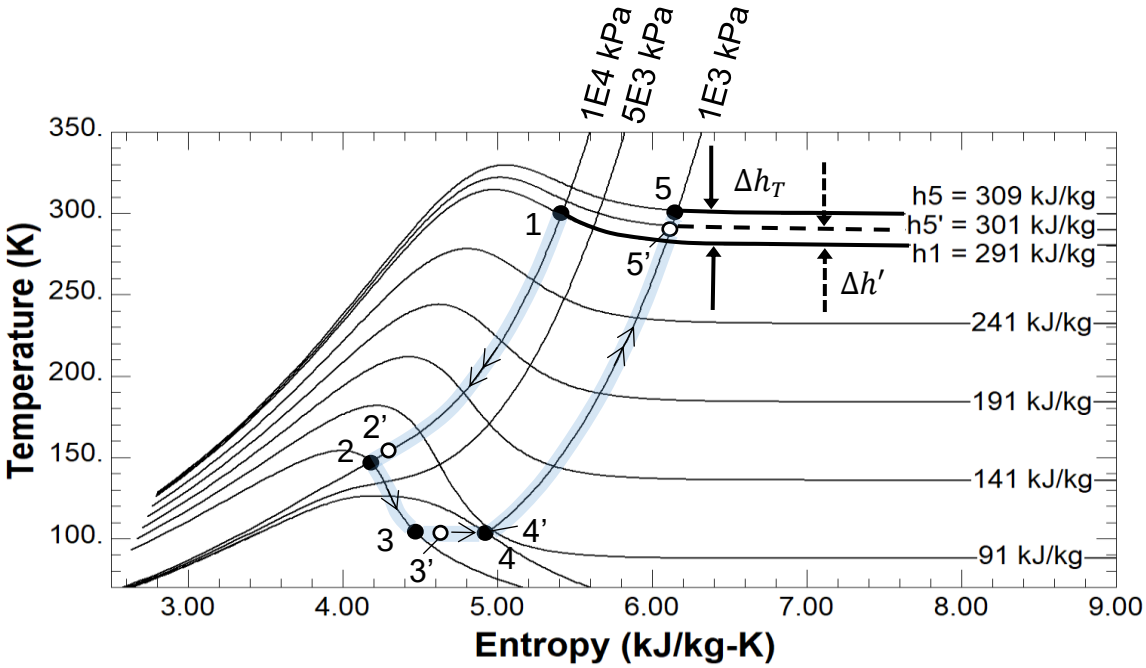

Figure 1.2. T-s diagram of Linde-Hampson cycle for nitrogen.

governed by the pinch point within the heat exchanger, as will be shown in the subsequent sections. Consequently, the pinch point limits the cooling capacity of the cycle.

1.2. The Pinch Point

The pinch point within a heat exchanger is defined as the location where the temperature difference between the fluid streams is a minimum. This can occur at any position along the heat exchanger. The temperature difference at this location is referred to as the pinch point temperature difference, ΔT_{pp} [5]. The temperature difference at the pinch point can approach zero and therefore the enthalpy difference at the pinchpoint can approach the isothermal enthalpy difference between the high- and low-pressure streams. This isothermal enthalpy difference therefore constrains the performance of the cryocooler. The enthalpy difference between the two streams must be equal at every location in the heat exchanger.

1.2.1. $\boldsymbol{\Delta h}$ of the Heat Exchanger

To illustrate, Figure 1.3 shows a counter-flow heat exchanger discretized into N sections. Control volumes encompass the high- and low-pressure stream within each section of the heat exchanger. Performing energy balances on the high- and low-pressure streams for the ith section leads to an expression for the heat transfer rate as given by Eq. (1.2):

$$\dot{q}_{hx_i} = \dot{m}\left(h_{x_{i-1},HP} - h_{x_i,HP}\right) = \dot{m}\left(h_{x_{i-1},LP} - h_{x_i,LP}\right) \tag{1.2}$$

Rearranging this expression shows that the enthalpy difference between the high- and low-pressure streams at the inlet and outlet of the *i*th section must be equal, as shown by Eq. (1.4):

$$h_{x_{i-1},HP} - h_{x_{i-1},LP} = h_{x_i,HP} - h_{x_i,LP} \quad (1.3)$$

$$\therefore \Delta h_{x_{i-1}} = \Delta h_{x_i} \quad (1.4)$$

Furthermore, since N can be increased such that the size of the control volume is infinitesimally small, this reveals that the enthalpy difference is the same between the high- and low-pressure streams throughout the heat exchanger. This enthalpy difference will be referred to as enthalpy difference of the heat exchanger, Δh_{hx}.

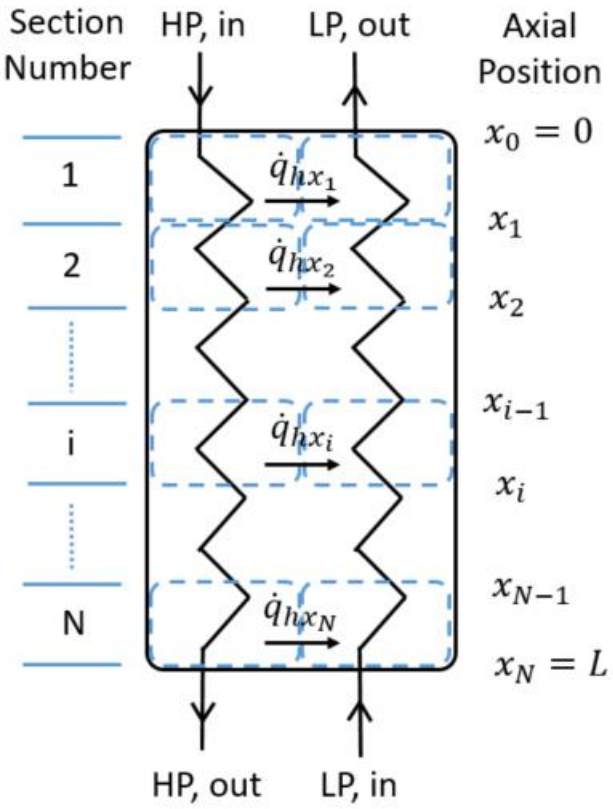

Figure 1.3. Counter-flow heat exchanger discretized into N sections.

Relating this to the expression for cooling capacity given by Eq. (1.1), it is now clear that the enthalpy difference between states 1 and 5 will be the same as the enthalpy difference between the high- and low-pressure streams anywhere along the heat exchanger, Δh_{hx}. Therefore, the cooling capacity will be governed by Δh_{hx}.

1.2.2. Minimum Δh_T

Now, the question at hand is how to determine Δh_{hx}. First let's consider the ideal case, where the heat exchanger is infinitely large with no pressure drop along the high- or low-pressure streams. Since the heat exchanger is infinitely large, the ΔT_{pp} will be zero. In this best-case scenario, there will be some axial location within the heat exchanger where the temperature of the two streams are equal; at this location, the enthalpy difference is equal to the *isothermal enthalpy difference* (i.e., the enthalpy of the low-pressure stream minus the enthalpy of the high-pressure stream, both evaluated at the same temperature). As an example, a plot of the isothermal enthalpy difference, Δh_T, as a function of temperature for 50% methane, 10% pentane and 40% propane on a molar basis with low and high pressures of 276 and 1103 kPa (40 and 160 psia), respectively, over the temperature range spanned by the heat exchanger is shown in Figure 1.4.

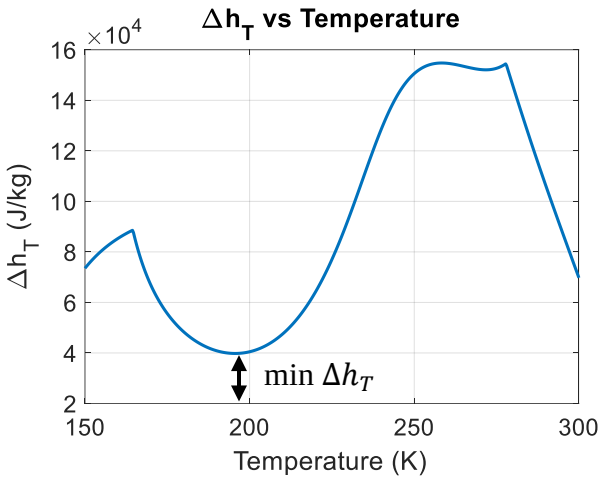

Figure 1.4. Isothermal enthalpy difference as a function of temperature.

The pinch point within the heat exchanger occurs at the location where the value of the Δh_T is at a minimum. For the example in Figure 1.4, the minimum value of Δh_T is 4x10^4 J/kg. It is not possible for the fluid streams under these conditions to transfer more energy per unit mass flow rate than the amount associated with the minimum value of Δh_T across this temperature range. The actual enthalpy difference between the two streams must be the same everywhere along the heat exchanger and as such the actual Δh_{hx} will be constrained to the minimum Δh_T. At locations other than the pinch point, the temperature difference between the high- and low-pressure streams

will increase until the actual value of the enthalpy difference at that location is equal to the value at the pinch point.

Furthermore, as it was said above that Δh_{hx} governs the cooling capacity of the cycle, then it follows that the minimum Δh_T limits the performance of the cycle. Thus, the maximum cooling capacity is governed by the pinch point and can be determined by the minimum value of Δh_T between the high- and low-pressure streams over the entire temperature span of the heat exchanger.

1.3. Effects of Departure from Ideal Behavior

The simple case discussed above was for an ideal cycle with an infinitely large heat exchanger with no pressure drop along the high- and low-pressure streams. This resulted in the maximum achievable cooling capacity as it did not take into account any non-ideal behaviors of the cycle. Departures from ideal behavior degrade the performance of the JT cycle by decreasing Δh_{hx} relative to the minimum value of Δh_T. Therefore, these non-ideal behaviors reduce the maximum achievable cooling of the cycle to the actual cooling.

1.3.1. Ineffectiveness of the Heat Exchanger

The effectiveness of the ideal, infinitely large heat exchanger considered in the previous section was 100%; this is consistent with a pinch point temperature difference of zero. One non-ideal behavior that degrades the performance of a real cycle is an effectiveness of the heat exchanger that is less than 100%. To understand this, consider Figure 1.2 which illustrates a situation in which the pinch point is at the hot end of the heat exchanger. The temperature of the LP gas exiting the heat exchanger at state 5 is the same temperature as the HP gas entering the heat exchanger at state 1, demonstrating that this is a perfectly effective heat exchanger with ΔT_{pp} equal to zero. The temperature of the LP gas exiting the heat exchanger at state $5'$ is colder than the temperature of the HP gas entering the heat exchanger at state 1, representing a non-zero ΔT_{pp}.

The decrease in effectiveness of the heat exchanger results in a decrease in the enthalpy difference between states 1 and 5 from the isothermal enthalpy difference, Δh_T, to the real enthalpy difference, $\Delta h'$.

Relating this to the conversation from above, the ineffectiveness of the heat exchanger reduces Δh_{hx} from Δh_T to $\Delta h'$. Figure 1.2 illustrates that this reduction degrades the cooling capacity of the cycle as the area of the polygon for states 1 to 5 (the ideal cycle) is larger than the area of the polygon for states 1 to 5' (cycle with decrease in effectiveness). Thus, the maximum cooling capacity associated with the minimum Δh_T has been degraded to the actual cooling capacity associated with $\Delta h'$. In addition, the less effective the heat exchanger, the larger the ΔT_{pp} and the lower the actual cooling capacity.

1.3.2. Pressure Drop in the Heat Exchanger

Another non-ideal effect that degrades cycle performance is pressure drop along the high- and low-pressure streams within the heat exchanger. The ideal cycle described above assumed all of the pressure drop occurred across the JT orifice, which resulted in the greatest temperature difference between states 2 and 3. However, in a real cycle there is pressure drop along both the high- and low-pressure streams within the heat exchanger. As the difference in pressure decreases along the high- and low-pressure streams, the Δh_{hx} will decrease, reducing the cooling capacity. In addition, these pressure drops degrade the pressure drop across the JT orifice and thereby reduce the cooling effect. Furthermore, any pressure drop along the low-pressure side will elevate the cold head temperature above the saturation value associated with the suction pressure at the compressor.

1.3.3. Parasitic Heat Loss

An additional non-ideal behavior that significantly impacts the performance of a small JT cryocooler is parasitic heat loss at the cold end. While design and construction of any micro-cooler places significant emphasis on the reduction of parasitic heat loss, there will still be some loss of performance due to axial conduction and radiation. The energy leaked to the cold end must be subtracted from the maximum cooling capacity and thus will increase the lowest attainable temperature of the cycle.

1.4. Advantages of a Gas Mixture over a Pure Fluid

Up until this point, the JT cycle and its maximum and actual cooling capacity have been discussed. An approach for selecting an optimal working fluid for the cycle has not been presented, though from the information presented above one might have an idea about where to start. The working fluid for the JT cycle must be selected to provide the greatest cooling capacity for the operating parameters with the non-ideal behaviors of the cycle discussed above taken into account as well as other, secondary considerations such as flammability and compatibility with the compressor. Therefore, to begin with, it is desirable to select a working fluid with the maximum value of the minimum Δh_T between the HP and LP streams over the entire temperature span of operation. Using an appropriate gas mixture as the working fluid can substantially increase the minimum Δh_T across a large temperature span as compared to its pure coolant counterparts. Thus, using an appropriate gas mixture as the working fluid can provide a greater cooling capacity.

Let us demonstrate this through an example. Figure 1.5 compares the Δh_T between the high- and low-pressure streams of the pure fluids R14 (blue) and R125 (yellow) and a 20/80 mixture of R14 and R125 on a molar basis (red). For the pure coolants, there is a distinctive range of temperatures for which the Δh_T peaks. This peak corresponds to the condition when the enthalpy

difference between the high- and low-pressure streams is large due to the difference in enthalpy between saturated vapor and saturated liquid across the vapor dome. However, compared to the pure coolants, the mixture has an increased temperature range for which the Δh_T is large. This increase in temperature range is related to the fact that the bubble and dew point for the mixture are much further apart than the saturation temperatures for the pure fluids at the two operating pressures.

Looking closely at the value of the Δh_T, if the temperature span of the JT cycle of interest is 160 to 300K, neither the pure coolants nor the mixture would provide refrigeration. The minimum Δh_T for the entire temperature span of the plot for both the pure coolants and the mixture is approximately zero and thus there would be no cooling capacity. However, if we were selecting an optimal fluid for a cycle operating between 190 and 300K, the minimum Δh_T for R14, R125 and the mixture are 2660 J/kg, 0 J/kg, and 6672 J/kg, respectively. Therefore, the 20/80 mixture of R14 and R125 has the maximum value of the minimum Δh_T for the fluids analyzed (by a factor of almost 3) and would produce a much larger cooling capacity than either of the pure fluids (assuming the mass flow rate for all of the fluids is approximately equal). It is important to note that the Δh_T for the pure coolants is not additive to determine the Δh_T for the mixture. The Δh_T for the mixture is governed by the properties of the mixture, which are a result of interaction parameters between the constituents.

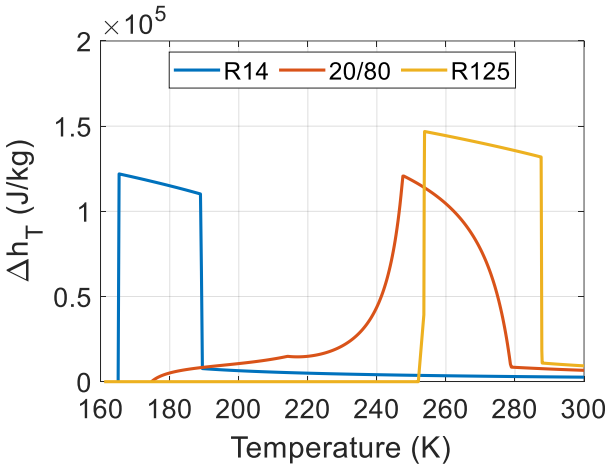

Figure 1.5. Δh_T as a function of temperature for selected pure coolants and mixture.

The capability of mixtures to provide an increased value of the minimum Δh_T when compared to pure fluids makes them an attractive option for maximizing Δh_{hx} and thus the cooling capacity of the JT cycle. However, for the advantages of using a gas mixture to be fully realized, the gas mixture must be properly matched to the real cycle, including the non-ideal behaviors of the heat exchanger discussed previously. These non-ideal behaviors are dependent upon the transport properties of the gas mixture selected, which adds another level of complexity to selecting an optimal working fluid.

1.5. Heat Exchanger Performance and Gas Mixture Selection

The mixture with the best real-world performance will take into account the effect of the mixture selection on the heat exchanger performance. The choice of working fluid significantly impacts the heat transfer coefficients as well as the phase of the fluid and pressure drop within the HP and LP streams. In turn, these impact the value of Δh_{hx} and therefore the actual achievable cooling capacity.

1.5.1. Heat Transfer Coefficients of HP and LP Streams

By maximizing the heat transfer coefficient of the high- and low-pressure streams, the resistance to heat transfer between the two streams will be minimized and the conductance, UA, of the heat exchanger will be maximized as shown in Eq. (1.5):

$$UA \approx \frac{1}{\frac{1}{\bar{h}_{LP} A_{s,LP}} + \frac{1}{\bar{h}_{HP} A_{s,HP}}} \tag{1.5}$$

where $\bar{h}_{LP}$ and $\bar{h}_{HP}$ are the heat transfer coefficients and $A_{s,LP}$ and $A_{s,HP}$ are the surface areas for convection for the LP and HP streams, respectively. In a heat exchanger where the capacitance

rates can be considered to be constant, the conductance and effectiveness, ε, are related as shown by Eq. (1.6) and Eq. (1.7):

$$NTU = \frac{UA}{\dot{C}_{min}} \tag{1.6}$$

$$\varepsilon = \begin{cases} \dfrac{1 - \exp[-NTU(1 - C_R)]}{1 - C_R \exp[-NTU(1 - C_R)]} & for\ C_R < 1 \\ \dfrac{NTU}{1 + NTU} & for\ C_R = 1 \end{cases} \tag{1.7}$$

where NTU is the number of transfer units, C_{min} is the heat capacity rate of the high- or low-pressure stream, whichever is lowest, and C_R is the capacity ratio [5]. While Eq. (1.6) and Eq. (1.7) are not applicable for a heat exchanger where capacitance rate is not constant, they nonetheless serve as an approximate representation that provides an intuitive expectation — maximizing the conductance of the heat exchanger will maximize the NTU and thus the effectiveness.

Therefore, it is desirable to choose a working fluid which maximizes the heat transfer coefficient of the high- and low-pressure streams as this will maximize the heat exchanger effectiveness. As shown previously in Section 1.3.1, the greater the effectiveness, the smaller the ΔT_{pp} and the greater the possible cooling capacity.

1.5.2. Phase of HP and LP Streams

The heat transfer coefficient of the high-pressure stream is related to the phase of the gas mixture within the heat exchanger. For internal flow through small diameter tubes, the heat transfer coefficients of gas mixtures can be substantially higher in the enhanced heat transfer region that occurs between 15% and 85% quality relative to the single-phase regions [6]. Therefore, it is ideal for the working fluid to be two-phase in the high-pressure stream in order to produce the greatest heat transfer coefficients and possible cooling capacity.

The heat transfer coefficient on the LP side is much less well-studied and therefore it is unknown if there is a strong relationship between the heat transfer coefficient of the low-pressure stream and the phase of the gas mixture within the heat exchanger. The low-pressure stream flows over coiled finned-tubes and there is no data or theory in open literature that relates the quality of a multi-component mixture to the heat transfer coefficient. Nonetheless, given the relationship shown for internal flow through small diameter tubes, it is not unreasonable to assume that it is also ideal for the working fluid to be two-phase in the low-pressure stream to produce the greatest heat transfer coefficients and possible cooling capacity. One of the key objectives of this thesis is to develop a test facility that can begin to examine this heat transfer coefficient experimentally.

It is also important note that that the fluid entering the compressor must be single phase gas to avoid issues with liquid in the compression space. This is obviously a difficult balance to achieve when both the high- and low-pressure streams are two-phase.

1.5.3. Pressure Drop in HP and LP Streams

To achieve the greatest cooling capacity, the pressure drops in the high- and low-pressure streams must be minimized in order to maximize Δh_{hx}. Mixture selection influences the pressure drop as the Reynolds number is dependent upon the dynamic viscosity, μ, and density, ρ, of the working fluid in each phase. The Reynolds number is used to determine the friction factor, which is directly related to single-phase pressure drop for internal flow by Eq. (1.8):

$$\Delta P = \bar{f} L \frac{\rho u_m^2}{2 D_h} \tag{1.8}$$

where $\bar{f}$ is the average friction factor, u_m is the mean velocity, D_h is the hydraulic diameter of the stream geometry and L is the length of the channel [5].

As mentioned above, it is ideal for the flow to be two-phase in the high- and low-pressure streams of the heat exchanger. For two-phase internal flow the pressure drop is related to mixture selection in the same manner as single-phase since the two-phase pressure drop can be approximated as a combination of the liquid and gas only pressure drops through the Müller-Steinhagen and Heck correlations as shown by Eq. (1.9):

$$\left(\frac{\Delta P}{L}\right) = \left\{\left(\frac{\Delta P}{L}\right)_L + 2\left[\left(\frac{\Delta P}{L}\right)_G - \left(\frac{\Delta P}{L}\right)_L\right] \cdot x\right\}(1-x)^3 + \left(\frac{\Delta P}{L}\right)_G \cdot x^3 \tag{1.9}$$

where $\left(\frac{\Delta P}{L}\right)_L$ and $\left(\frac{\Delta P}{L}\right)_G$ are the liquid and gas only pressure drop per unit length and x is the quality of the fluid [7].

The internal flow relations given by Eqs. (1.8) and (1.9) are approximately valid on the high-pressure side of a coiled finned-tube cryocooler as the high-pressure fluid flows through a helically coiled tube. Thus, Eqs. (1.8) and (1.9) will aid in the selection of a mixture that minimizes the pressure drop of the high-pressure stream. However, the low-pressure stream flows over a coiled finned-tube. This flow is complex and there is not a general correlation available in current literature that can be used to predict the pressure drop of a multi-component fluid over a coiled finned-tube. The scarcity of available experimental data and theory to predict the heat transfer coefficient and pressure drop of the low-pressure stream makes it challenging to select an optimal gas mixture that accounts for the impact of mixture selection on performance of the low-pressure stream.

1.6. The JT Orifice and Optimal Flow Rate

The above arguments focused on selecting an optimal gas mixture by balancing the thermodynamic cooling capacity with good heat transfer and low pressure drop in the heat

exchanger. However, to produce the best real-world performance there is yet one more factor beyond mixture selection that must be considered and that is the flow rate. The flow rate is determined from fluid properties, characteristics of the compressor and the hydraulic resistance of the system which is primarily related to the size of the JT orifice. The size of the JT orifice can be changed to alter the flow rate within the cycle. Maximizing the real-world performance is a balance of optimizing the flow rate for effectiveness of the heat exchanger and pressure drop across the JT orifice. Decreasing the flow rate has the potential to increase the effectiveness of the heat exchanger, which increases the Δh_{hx}. However, increasing the flow rate increases the cooling capacity for a fixed enthalpy difference as shown by Eq. (1.1). Therefore, there is an optimal flow rate produced by an optimal JT orifice that will provide the best real-world performance.

1.7. Thermodynamic Efficiency

To quantify improvements from proper gas mixture selection, the coefficient of performance, COP, must be examined. The COP for a JT cycle is determined from the ratio of the cooling capacity of the cycle to the power needed for the compressor. The power input for the compressor can be estimated based on a compressor model as shown in Eq. (1.10), which assumes ideal gas behavior in the compression space:

$$Power = \frac{1}{\eta_{comb}} \dot{V} P_{suc} \left(\frac{k}{k-1}\right) \left[\left(\frac{P_{dis}}{P_{suc}}\right)^{\frac{k-1}{k}} - 1\right] \tag{1.10}$$

where η_{comb} is a combined motor and compressor efficiency, $\dot{V}$ is the volumetric flow rate at the inlet of the compressor, k is the isentropic exponent, P_{suc} and P_{dis} are the suction and discharge pressures, respectively [8]. From this expression, it follows that gas mixture selection will impact the power input of the compressor through the volumetric flow rate and the isentropic exponent.

It also demonstrates that for an equivalent production of cooling (i.e. maintaining an equivalent value of $\dot{m}\Delta h_T$), lowering the operating pressures and pressures ratio will decrease the power input and therefore a higher thermodynamic efficiency can be achieved.

Selecting a gas mixture with the best real-world performance is a challenging task. A method of balancing the thermodynamic cooling capacity with good heat transfer and low pressure drop in the heat exchanger must be identified and experimentally validated. This task is made arduous by the interwoven complexities introduced above and the scarcity of experimental data and theory for two-phase multi-component gas mixtures. However, carrying out this task will allow for the selection of a gas mixture with the best real-world performance for a JT cycle with low operating pressures and pressure ratios. The literature review to follow examines previous research conducted to optimize gas mixture selection, including measurements of heat transfer coefficients and frictional pressure drop of two-phase multi-component gas mixtures.

2. Literature Review

2.1. Common Mixture Components for JT Cryocoolers

A range of mixtures have been examined either experimentally or analytically for JT cryocoolers. A table highlighting the evolution of mixtures for JT cryocoolers is detailed in Maytal and Pfotenhauer [2]. Maytal and Pfotenhauer note the following:

1. Argon is the primary component used to reach cold-end temperatures of 90 to 120K
2. For higher temperatures, such as 120 to 185K, the primary component may be methane, krypton or R14.
3. The most commonly used components are nitrogen, methane, ethane, and propane, followed by argon, butane, and R14 [2].

While the mixtures listed in this table were analyzed for a wide range of operating pressures, pressure ratios and cold-end temperatures, the common components listed above are a starting point for selection of components for mixture optimization.

2.2. Effects of Mixture Components on Thermodynamic Cooling Capacity

2.2.1. Components to Suppress a Mixture's Liquefaction

Mixtures composed solely of components with critical temperatures, T_C, above 300K tend to liquefy at temperatures above 160K [2]. This is not ideal for JT cycles that must operate below 160K as the fluid within some section of the heat exchanger is likely to be single-phase, the heat transfer coefficient and therefore the heat exchanger effectiveness will decrease in the single-phase region and thus the cooling capacity will decrease. For the mixture to remain two-phase at lower temperatures, components with low boiling point temperatures, such as argon or nitrogen, must be added. For example, Grezin and Zacharov demonstrate that an addition of only 0.6% nitrogen to

an equimolar mixture of propene and propane (with boiling point temperatures of 226.2 K and 231.2 K, respectively) suppresses the mixture's point of liquefaction such that it becomes a liquid at 77.4.K [9] at the pressures of interest. It is important to note that the linear combination of the component's boiling temperatures will not provide a good estimate of the bubble point of the mixture. As with enthalpy, the bubble point is a result of interaction parameters of the components.

2.2.2. Components to Increase the Spread of the Δh_T Profile

Fluids with values of T_C greater than 300 K can increase the spread of the Δh_T peaks over a larger temperature interval. Figure 2.1 demonstrates that, for a binary mixture of nitrogen and propane, increasing the molar fraction of propane from 20% to 40% moves the peak on the right to higher temperatures such that the temperature at which the minimum value of the Δh_T occurs is changed from 300 K to approximately 155 K. This increases the minimum value of the Δh_T by 17% [2].

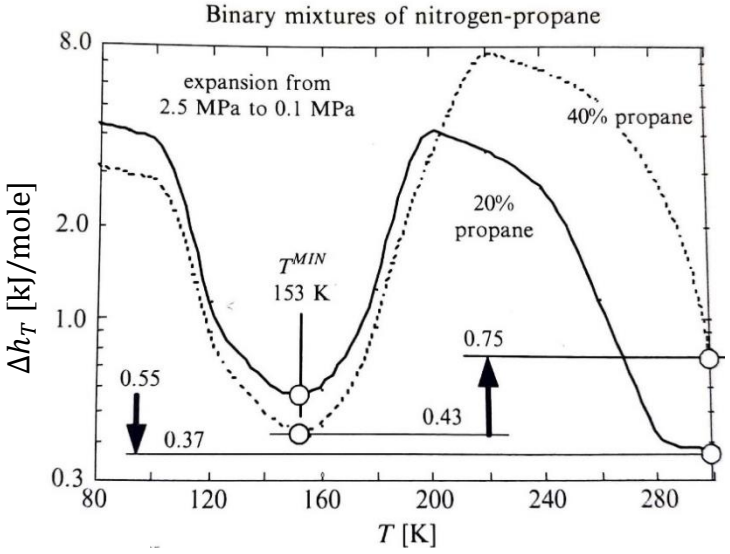

Figure 2.1.Binary mixtures of nitrogen and propane [2].

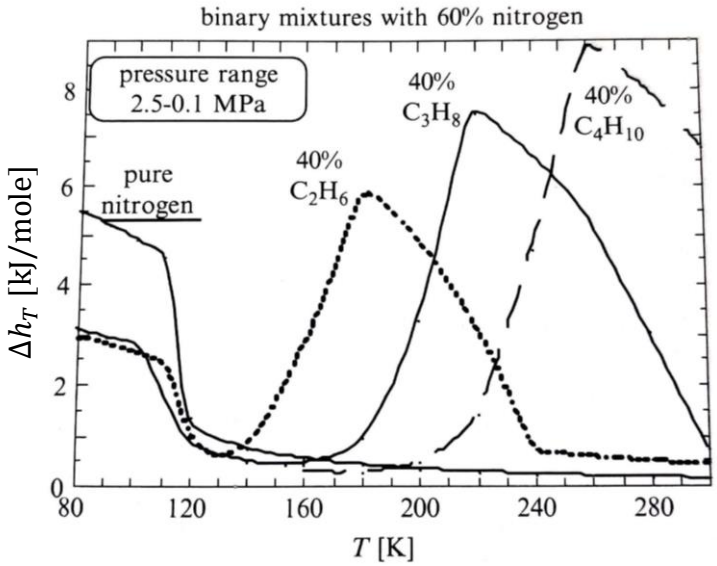

Figure 2.2. Binary mixtures with 60% nitrogen and 40% ethane, propane or butane [2].

However, it is not always the case that shifting the peak results in an increased value of the minimum Δh_T.

From Figure 2.1, it can be seen that the increase in propane concentration actually reduces the value of Δh_T at 155 K and this reduction can lead to a lower value of the minimum Δh_T depending on the profile of the Δh_T. Furthermore, Figure 2.2 shows that in a binary mixture with nitrogen, replacing ethane with fluids that have higher T_C such propane or butane increases the spread of the peaks of the mixture over a larger temperature interval but the minimum value of the Δh_T either remains the same or is decreased in the process. Therefore, while adding or increasing the amount of fluid with a higher T_C can increase the spread of the Δh_T peaks over a larger temperature interval, it may increase or decrease the maximum achievable cooling capacity depending upon the profile of the Δh_T.

2.2.2. Bridging Components to Increase the Minimum Δh_T

As was observed in Figure 2.1 and Figure 2.2, it is common for mixtures to exhibit a temperature interval such that two separate peaks of Δh_T create a "valley" in-between. This valley defines a local value of the minimum Δh_T that acts to constrain the cooling capacity of the mixture. However, by including fluids with T_C below 300 K, a bridging effect can occur which elevates the value of the minimum Δh_T [2]. Mostitski et al. suggest using R14 as an additive to hydrocarbon mixtures to improve the efficiency of the cycle. Wickemann and Oellrich also suggest using R14 as a bridging component [10, 11]. Luo et al. recommends including both methane and R14 as bridging components in mixtures and ethylene was suggested as a bridging component by Maytal and Pfotenhauer [12, 2]. The bridging effect creates a more uniform distribution for the profile of Δh_T and therefore increase the cooling capacity of the mixture.

2.3. Previous Work to Optimize Mixtures for JT Cryocoolers

The optimization of mixtures for mixed-gas Joule-Thomson (MGJT) cycles has been an area of substantial research. At the University of Wisconsin – Madison, optimal mixture selection

for cryosurgical probes has been an area of particular interest. Skye used a computational model to select an optimal mixture and manufactured an experimental test facility to investigate the behavior of various mixtures for a cryosurgical probe [13]. Modeling, experimentation and optimization of MGJT cycles also been investigated by Fredrickson, Keppler, Passow, Pettit, and Rule at UW-Madison [14, 15, 16, 17, 18]. Elsewhere, modeling and experimentation to optimize mixture selection based upon thermodynamic properties has been pursued by Tzbar [19, 20, 21] and Luo et al. [12] among various others and mixture selection for infra-red detectors has been investigated by Arkhipov [22]. These mixture optimization efforts selected mixtures with the greatest thermodynamic cooling capacity through selection of mixture components and compositions that generate the maximum value of the minimum Δh_T over the temperature range of operation. However, most optimizations do not consider in sufficient detail the effects of mixture selection on the performance of the heat exchanger that lies at the heart of the JT system. If the heat exchanger is considered at all, researchers use a conductance model where the heat exchanger performance is matched to a conductance that is assigned by the user to the cycle. Using this method, the conductance and therefore the heat transfer coefficient area product is set to a constant that can be assigned based on previous experience or tuned to match data rather than a value that is calculated from first principles. As discussed previously, when in the enhanced heat transfer region, between 15 and 85 percent quality, the heat transfer coefficients can be up to three times higher than in the single-phase regions [6], at least on the tube side. Thus, the heat transfer coefficients can be a strong function of quality and should not be assumed constant.

Work by Hinze et al. optimized the performance of a MGJT cycle by selecting gas mixtures with the greatest cooling capacity while constraining the heat exchanger to remain in the enhanced heat transfer region [23, 24]. The model optimized mixture composition and discharge pressure

simultaneously. These mixtures were optimized for temperature intervals spanning 150-240 K or 170-300 K with suction pressures of 100 or 150 kPa (16 to 22 psia) and discharge pressures up to 3300 kPa (479 psia). The model generally assumed a ΔT_{pp} of zero (due to computational expense) and pressure drop entirely across the JT valve. The results were not validated by experiments.

The model of Hinze et al. was a step closer to selecting a gas mixture with the best real-world performance. It selected optimal mixtures based not only upon thermodynamic cooling capacity but also with some consideration of how the mixture selection would impact the heat exchanger performance. To include in detail the effects of mixture selection on the performance of the heat exchanger, one must determine the impact of the gas mixture on the heat transfer coefficient and pressure drop in both the high- and low-pressure streams of the MGJT cycle. However, as the literature review of the proceeding sections will show, this deceptively straightforward task is muddled by the fact that the behavior of two-phase multi-component fluids within the low-pressure stream of MGJT heat exchangers is not yet well characterized.

2.4. Measurements of heat transfer and pressure drop characteristics for MGJT systems

Finned-tube heat exchangers are the most widely used heat exchanger for miniature Joule-Thomson cryocooling [2]. The basic configuration, known as a Giauque-Hampson (GH) or coiled tube heat exchanger, is shown in Figure 2.3.The high-pressure stream flows through finned tube

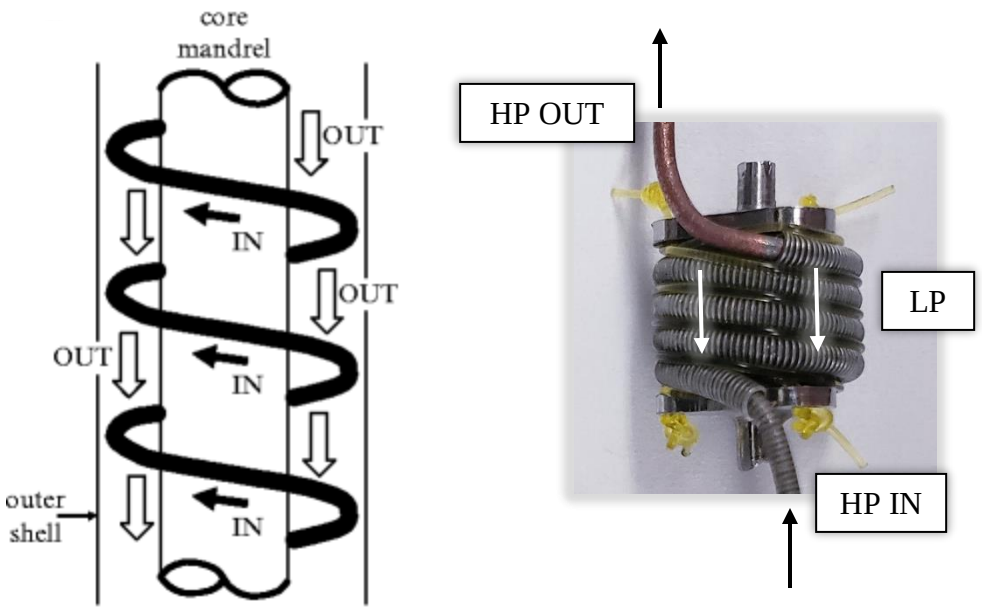

(a) (b)

Figure 2.3. Illustration of a Giauque-Hampson (coiled tube) heat exchanger (a) [2] and photo of high-pressure finned-tube helically coiled upon a cylindrical coil (without shell) (b).

that is helically coiled upon a cylindrical core (or mandrel) while the low-pressure stream flows over the fins in the annular space created by the core and the inner diameter of a shell. While the flow exhibits both counter-flow and cross-flow characteristics, within this text the heat exchanger will be referred to as having a counter-flow configuration. A growing demand for two-phase compact heat exchangers operating with multi-component mixtures has given rise to an increase in publications characterizing flow of multi-component mixtures flowing inside tubes. However, there is still no data or theory in open literature that characterizes the heat transfer and pressure drop characteristics of two-phase multi-component mixtures on the shell side in these heat exchangers. This is surprising as the heat transfer coefficient of the return stream has been suggested to be a key parameter affecting the behavior of the entire heat exchanger of a MGJT cryocooler operating with mixed coolants [25]. Additionally, there is some, but only a limited amount of experimental data available that characterizes the heat transfer and pressure drop for *single-phase pure* fluids on the shell side in these heat exchangers. The sections that follow will

detail correlations and insights available for single-phase pure fluids on the shell side in GH heat exchangers and, more broadly, two-phase multi-component mixtures in various geometries. However, while these studies can provide invaluable insight, the findings and correlations available cannot be directly applied for two-phase multi-component mixtures on the shell side of GH heat exchangers without experimental validation.

2.4.1. Heat transfer and pressure drop characteristics of pure fluids over helically coiled finned-tubes for Giauque-Hampson heat exchangers

Heat transfer measurements for internal flow can be categorized based on the thermal boundary condition that is imposed at the wall – constant heat flux, constant wall temperature or interaction with a secondary heat transfer fluid. A constant heat flux boundary condition can be generated using an electrical heater wound around a nonconductive wall or an electrical current passed directly through the channel. A constant temperature boundary condition can be generated using an electrical heater wound around a highly conductive wall or via phase change of a single component fluid over the external channel wall. When the heat load is applied via interaction with a secondary heat transfer fluid, the applied heating load must be determined indirectly using an energy balance on the heat exchanger. Measurement of frictional pressure drop for internal flow is found from the pressure drop measured at the inlet and the exit of the tube and fluid properties. Table 2.2 provides an overview of available literature for measurements of heat transfer and pressure drop characteristics of pure fluids over helically coiled finned-tubes relevant for MGJT systems. Each source is categorized as experimental or numerical and a glance at the column for boundary condition (BC) will give the reader an idea of the experimental or numerical set-up for the data collected. Note that H and T represent a constant heat flux and temperature boundary condition, respectively, and SF represents a secondary heat transfer fluid.

Geist and Lashmet evaluated several compact GH heat exchangers with small diameter tubes using nitrogen and hydrogen to characterize the heat transfer and pressure drop characteristics [26]. They reported results for Reynolds numbers ranging from 30-4000. However, their heat transfer results were reported in terms of the overall average Colburn factor, J, and an approximated Colburn factor, j, for the shell-side of the heat exchanger. The approximation for the film Colburn factor assumed the resistance to heat transfer on the inside of tubes and on the shell-side was approximately equal. However, more recent research has shown that the resistance of the shell-side is greater than the tube-side and can be the most dominant resistance in estimations of the overall heat transfer [27].

Croft and Tebby proposed a correlation for the heat transfer coefficient of the shell-side that was validated against the performance of a heat exchanger manufactured for helium liquefaction at the Clarendon Laboratory [28, 29]. The diameter of the fins was approximately double the outside diameter of the tubes, resulting in correlations for high finned-tubes (tubes with fin height, $h_f > 1.5$ mm (0.06 inch)). However, their publication made no mention of the operating regime for which the correlation is suited.

Almost 40 years later, Gupta et al used helium to study both the heat transfer and pressure drop characteristics for the shell-side of a Giauque-Hampson heat exchanger [27, 30]. The overall heat transfer coefficient was measured experimentally and the heat transfer coefficient inside the helically coiled tubes was estimated with the Dittus-Boelter equation to deduce the heat transfer coefficient of the shell-side [31]. The study investigated the applicability of correlations available for plain tubes, high finned-tubes and low finned-tube bundles for estimating the heat transfer coefficient of the shell-side. Gupta et al found that these correlations could be used with a fair degree of accuracy if the appropriate method for calculating the free-flow area of the return stream

was applied, but the accuracy of the correlation was highly sensitive to clearance provided between the fins and the shell for manufacturing the heat exchangers. The study suggested appropriate pre-existing correlations to use based upon clearance and estimation of the free-flow area and additionally purposed a more accurate correlation from the experimental data. For the study of pressure drop characteristics, measurements were carried out at low values of effective Reynolds number from 25-155 on the shell-side of the heat exchanger and a new correlation for predicting the shell-side friction factor for the low Reynolds number flow regime was proposed [30].

Most recently, Howard et al developed a numerical model to predict the heat transfer and pressure drop characteristics of the shell-side of GH heat exchangers operating at cryogenic temperatures [32]. Howard et al experimentally validated the numerical model for Reynolds numbers of 100-500 and used this data to baseline the numerical simulations. Correlations considering geometric parameters of the flow channel are proposed for the Colburn factor, j, and friction factor. A transition similar to the laminar-turbulent transition is observed at $Re \geq 2000$ and $Re \geq 3000$ for the friction factor and Colburn factor, respectively. The correlations proposed are separated based upon this transition. The proposed correlation was compared to the experimental results of Gupta et al and Croft and Tebby [27, 30, 28]. For $Re < 500$, the thermal correlation underestimates the results of Gupta et al and, for $Re > 5000$, it overestimates the results of Croft and Tebby.

Other papers, such as Alimoradi et al and Sepehr et al provide correlations from numerical simulations for either or both the heat transfer and pressure drop characteristics of helically coiled finned-tubes in shells [33, 34]. However, the finned tubes analyzed were not closely coiled on a mandrel and fit snuggly into a shell. Many other authors, such as Timmerhuas and Flynn, Genić et al, Jian et al, and Ghorbani et al, collected experimental data on the heat transfer characteristics

on the shell-side of helically wound coiled tubes or tube bundles [35, 36, 37, 38]. However, these studies, focused on plain tubes and are not applicable for characterizing coiled finned-tube heat exchangers. Furthermore, many researchers have investigated the heat transfer and pressure drop characteristics for condensation and boiling on the tube-side of helically coiled tubes and a comprehensive literature review is provided by Onal et al [39]. While useful for GH heat exchangers, these works do not characterize the shell-side flow. As far as this author knows, this is all the literature available that characterizes heat transfer and pressure drop characteristics of flow over helically coiled finned-tubes for GH heat exchangers.

Table 2.2 provides an overview of the literature discussed. From the table, it can be observed that a standard method of calculating and reporting non-dimensional quantities for the geometry of the shell-side of the GH heat exchanger should be developed in order to ease comparison between data sets and correlations. The dimensions for the heat exchanger are reported with the nomenclature listed in Table 2.1. While dimensions such as fin height to tube size could be listed as a non-dimensional parameter, a high finned tube is currently defined as a tube with $h_f > 1.5$ mm (0.06 inch). This makes it difficult to determine if a correlation such as that of Croft and Tebby is applicable when tube size varies.

Other parameters such as clearance to mean coil diameter that have been proposed to impact heat transfer and pressure drop characteristics should also be reported in terms of non-dimensional quantities for ease of comparison. Howard et al proposes an aspect ratio of the flow channel based upon fin height, pitch and thickness and utilizes this in both his heat transfer and pressure drop correlations [32]. However, he does not appear to vary clearance in his simulations, making his correlations most appropriate for a clearance of zero. Gupta et al discusses clearance in his work and incorporates this parameter (along with fin height, thickness, spacing, etc.) into

his correlation through the use of an effective Reynolds number [27]. The effective Reynolds number is based upon the cross-sectional free flow area of the shell-side estimated by the free volume concept and a by-pass factor that estimates the actual flow rate over the fins (with some flow moving through the clearance). However, the discussion of Gupta et al is still based upon set clearance values of 0 to 1.2 mm (0.05”), making it challenging to determine which correlations are most suited for coils of varying mean diameter.

D_i	Inner diameter of tube	h_f	Height of fins
D_o	Outer diameter of tube	N_f	Number of fins per unit length
D_f	Diameter of fins	th	Thickness of fins
D_c	Mean diameter of coil	p_f	Fin pitch
D_s	Inner diameter of shell	p_c	Coil pitch
c	Clearance between fins and inner diameter of shell		

Table 2.1. Nomenclature for dimensions of helically coiled finned-tube for GH heat exchangers.

Source	E/N	BC	Fluid	Dimensions	Operating Conditions	Reynolds number	Reported
Geist and Lashmet (1960) [26]	E	SF	N_2 and H_2	D_o = 0.38-3.18 mm (0.015-0.125”) $h_f = D_o/2$ N_f = 1102-1890 m^{-1} (28-48 in^{-1}) D_c = 12.7-25.4 mm (0.5-1”)	HP = 10,342 kPa (1500 psia) LP = 103 kPa (15 psi) T_{warm} = Ambient T_{cold} = 76-88K	30-4000 (D_h)	J = 0.007-0.021 j = 0.015-0.041 f = 0.1-1.1
Cosier and Croft (1970) [29]	E	SF	He	D_i = 6.35 – 9.5 mm (0.25-0.375”) D_o = 8.13-11.3 mm (0.32-0.445”) D_f = 18.0-28.9 mm (0.71-1.1”) N_f = 354 m^{-1} (9 in^{-1}) $D_f \sim 2D_o$	T_{warm} = 288 K T_{cold} = 20K ΔP_{HP} = NA ΔP_{LP} = 8.1 kPa (1.2 psi) $\dot{m}$ = NA	NA	$\dot{Q}_{cool}$ Correlation for h in another paper [28]
Gupta et al (2009) [27]	E	SF	He	D_i = 8.2 mm (0.32”) h_f = 1.4 mm (0.055”) D_f = 13.5 mm (0.53”) th = 0.3 mm (0.012”) N_f = 1024 m^{-1} (16 in^{-1}) D_c = 145 mm (5.7”) c = 0-1.2 mm (0.05”)	T_{in} (shell) = 82-295.5 K T_{out} (shell) = 282-295K P (shell) = 100 kPa (14.5 psi) $\dot{m}$ = 1.6-5.5 g/s	500-1900 (effective)	U = 200-600 Evaluated pre-existing correlations and proposed new correlation for h
Gupta et al (2010) [30]	E	SF	He	D_c = 70-333 mm (2.8-13.1”) Other parameters same as above.	$T\ (shell)$ = Ambient P_{out} (shell)= 100 kPa (14.5 psi) $\dot{m}$ = 0.3-4.0 g/s	25-155 (effective)	f = 2-5.5 Correlation for f
Howard et al (2021) [32]	N	H	N_2	D_o = 9.5-15.9 mm (0.38-0.63”) h_f = 6.4-9.5 mm (0.25-0.38”) th = 0.5-0.8 mm (0.02-0.03”) p_f = 2.1 mm (0.08”) D_c = 143 mm (5.63”) p_c = 28.5 mm (1.13”)	T_{in} (shell) = 100-300 K P_{out}(shell) = 100 kPa (14.5 psi)	100-10000 (D_h)	j = 0.003-0.02 f = 0.02-0.12 Correlations for j and f

Table 2.2. Overview of literature for heat transfer and pressure drop characteristics of flow over helically coiled finned-tubes wrapped tightly around a mandrel in a shell.

2.4.2. Heat transfer characteristics of two-phase multi-component gas mixtures for MGJT systems

Experimental measurements of heat transfer and pressure drop characteristics for two-phase multi-component mixtures in the shell-side of a GH type heat exchanger have not been reported in open literature. However, discussion of the theory of two-phase heat transfer and literature presenting experimental measurements of heat transfer characteristics of two-phase multi-component mixtures in other geometries will provide invaluable insight into their behavior.

The physical process involved in evaporation of a two-phase fluid flowing through a duct is more complicated than with a single-phase fluid undergoing internal forced convection. The process, referred to as flow boiling, involves both nucleate and convective boiling and is pictorially represented in Figure 2.4. When a sub-cooled fluid enters a horizontal tube heated above the saturation temperature of the fluid, the fluid adjacent to the wall is heated and undergoes nucleate boiling. Eventually, the bubbles force the liquid towards the wall and the flow enters an annular flow regime where the wall is coated with liquid and there is a vapor core. The liquid film in contact with the walls continues to experience nucleate boiling and vapor is produced by evaporation of the liquid at the liquid-vapor interface through convective boiling. The presence of both these boiling processes contributes to the high heat transfer coefficients associated with flow boiling. As boiling continues, the liquid film at the wall is thinned until it is not sufficient to wet the entire perimeter and dry out occurs. The liquid-wall interface has a much higher heat transfer

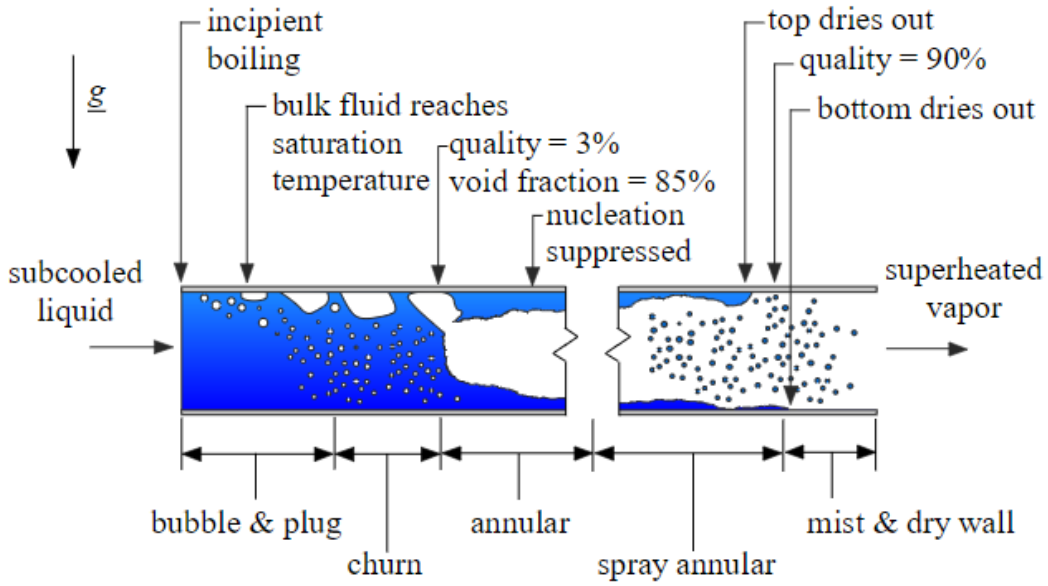

Figure 2.4. Flow regimes for flow boiling [40].

coefficient than the vapor-wall interface and thus the heat transfer coefficient tends to drop substantially at dry out [40].

The simplistic description of flow boiling presented characterizes heat transfer of two-phase pure fluids. However, several studies have shown that mixtures behave differently than pure fluids when they undergo phase change. A significant amount of research has been conducted to characterize two-phase flow boiling of binary mixtures in channels and extensive literature reviews have been provided by authors such as Cheng and Mewes and Celata et al [41, 42]. As has been shown by numerous experiments, the heat transfer coefficients of mixtures are degraded when compared to the heat transfer coefficients of the pure components at the same flow conditions [43, 44, 45, 46, 47]. Jung et al reported that the measured heat transfer coefficients for mixtures were as much as 36% lower than values calculated using an ideal mixing rule (i.e. linear mole fraction weighting) for the pure fluids at the same flow conditions [43]. The deterioration of the heat transfer coefficient is explained as an increased heat transfer resistance due to mass diffusion as the concentration difference between the liquid and the vapor increases [41] and the nonlinear and

strong variation in physical properties associated with mixtures with change in composition and temperature. An increased mass transfer resistance suggests that suppression of nucleate boiling would be easier to achieve with mixtures than pure fluids and Ross et al observed such a trend [45]. The deterioration has been shown to be less substantial in the convection-dominated regime where nucleate boiling has been fully suppressed, but the deterioration is still present [43, 45].

Now, at this point one may question the selection of a two-phase multi-component gas mixture as the working fluid in a MGJT system. However, remember the diagrams of Δh_T vs temperature discussed in the previous chapter. While the flow boiling heat transfer coefficients of the mixture in the heat exchanger will be reduced when compared to the pure components, the mixture can produce cooling over a wider range of temperatures than any pure component can. Therefore, these two competing effects must be balanced when selecting an operating fluid.

While much research has been pursued to characterize two-phase flow boiling of binary (and some ternary) mixtures in channels, this research has not been conducted on gas mixtures and in operating regimes that are of particular interest for MGJT systems. Gas mixtures can be divided into two main groups – azeotropic and non-azeotropic mixtures. Azeotropic mixtures behave as pure substances at phase change (i.e., the temperature remains constant during the phase change) while non-azeotropic mixtures boil or condense over a range of temperature between the bubble and dew point as they change phase. The temperature difference between the bubble and dew point is known as the temperature glide. In general, existing data are focused on measurements of flow boiling heat transfer coefficients of binary mixtures operating near room temperature with small temperature glides. The mixtures of interest for MGJT systems are non-azeotropic with large temperature glides (100-200K) operating at cryogenic temperatures. The large temperature glide increases the probability that the gas mixture will be two-phase in both the high- and low-pressure

streams and tends to increase the value of Δh_T over a large temperature range. The remainder of this literature review focuses on experimental research to characterize the heat transfer characteristics of non-azeotropic two-phase multi-component mixtures with large temperature glides in small channels. An overview of the literature is provided in .

Ardhapurkar et al, Boiarski et al. and Gong et al. analyzed multi-component gas mixtures at cryogenic temperatures for tube-in-tube and paired-tube heat exchangers in operating ranges of interest for MGJT research [19, 20, 21]. However, their results were reported in terms of the overall average heat transfer coefficient, *U*. The overall average heat transfer coefficient is a measure of the area-specific total resistance between the fluid streams of a heat exchanger. The average heat transfer coefficients for each stream cannot be isolated. Consequently, the overall heat transfer coefficient data cannot be extrapolated to other systems with system geometries and operating parameters differing from those reported. Furthermore, knowledge of the local heat transfer coefficients is essential to better understand the specific mechanisms that drive two-phase multi-component heat transfer.

Chen and Shi, Nellis et al and Barraza et al measured local flow boiling heat transfer coefficients for multi-component mixtures at cryogenic temperatures [48, 49, 50]. Chen and Shi measured the local flow boiling heat transfer coefficient of two-phase liquid natural gas (LNG) in a horizontal tube of diameter 8 mm (0.32”). LNG is a multi-component nitrogen-hydrocarbon mixture consisting mainly of methane (at 80% mol fraction or above). Nellis et al. and Barraza et al. measured local flow boiling heat transfer coefficients for gas mixtures at cryogenic temperatures in small diameter horizontal tubes ranging in size from 0.5 to 3 mm (0.02” to 0.12”) [49, 6, 50]. Nellis et al. provides data for nitrogen-hydrocarbon gas mixtures for a select range of composition, temperatures, mass flow rates and pressures. Barraza et al provides data for

hydrocarbon and fluorocarbon gas mixtures for a larger range of composition, temperatures, mass flow rates and pressures.

According to the results of Nellis et al, the heat transfer coefficients for mixtures under single-phase conditions are well predicted by standard correlations for single phase flow such as Dittus-Boelter. Both Nellis et al and Barraza et al found that the two-phase flow boiling heat transfer coefficient is significantly higher than the single-phase heat transfer coefficient for multi-component mixtures in small diameter horizontal tubes. Barraza et al reports the enhanced heat transfer region to be in the range of quality between 0.15 and 0.85 [50]. Nellis et al and Barraza saw a dramatic decrease in the local heat transfer coefficient above qualities of 0.85 while Chen and Shi noted a decline in the heat transfer coefficient above a quality of 0.5 for their data [48]. For both Barraza et al and Chen and Shi, typical values of the heat transfer coefficients for the nitrogen-hydrocarbon mixtures ranged between 2000-8000 W/m^2-K for the specified mixtures and operating ranges. Barraza et al found typical values of the local heat transfer coefficients for fluorocarbon mixtures to be in the range of 1000-4000 W/m^2-K for the specified mixtures and operating ranges. Barraza et al also reports that dilution of both mixtures increases the temperature glide but degrades the heat transfer coefficient.

Barraza et al. performed an exhaustive comparison of the currently available correlations for predicting heat transfer coefficients of two-phase multi-component mixtures in small diameter tubes. The Granryd correlation was reported to provide the best agreement with the measured heat transfer coefficients for all the experimental data collected while the correlation by Little et al showed the best agreement for high Reynolds number, high thermodynamic quality or both [51, 52, 50]. These suggested correlations can be used to estimate the heat transfer coefficients for two-

phase multi-component gas mixtures in small diameter horizontal tubes for similar gas mixtures and operating parameters.

Researchers such as Ardhapurkar et al and Gomse et al have analyzed the experimental data of Nellis et al, Barraza et al and Chen and Shi to propose modified correlations for flow boiling of multi-component gas mixtures. Ardhapurkar et al analyzed the data of Nellis et al to propose a modified Granryd correlation to better fit mixtures boiling with higher mass velocity [53]. Gomse et al analyzed the data of Nellis et al, Barraza et al and Chen and Shi to propose a modified correlation that captures the dramatic decrease in the flow boiling heat transfer coefficient at dry-out [54]. These modified correlations are used to predict the flow boiling heat transfer coefficients in further studies of tube-in-tube heat exchangers. Ardhapurkar et al used the modified Granryd correlation and experimental data for U to assess correlations for flow condensation in tube-in-tube heat exchangers. They recommended the use of the Cavallini and Zecchin correlation for flow condensation for similar scenarios. However, Ardhapurkar et al noted that the use of the modified Granryd correlation in conjunction with the Cavallini and Zecchin correlation better predicted experimental values for mixtures with low temperature glides (~130K) [55, 56]. Damle et al and Kruthiventi et al have used these correlations to develop computational models for further study of multi-component gas mixtures in tube-in-tube heat exchangers.

The data collected by Chen and Shi, Nellis et al and Barraza et al provides an extensive library of local flow boiling heat transfer coefficients for two-phase multi-component mixtures in small diameter tubes operating in flow regimes ranging in Reynolds number from 150 to 75,000. However, it is only the beginning of the data collection and analysis necessary to be able to predict heat transfer characteristics for gas mixtures with varied or alternative components and for compact heat exchangers of alternative geometries. Nonetheless, the trends observed from the

experimental data and the magnitudes of the values for these parameters give invaluable insight into the thermal behavior of two-phase multi-component gas mixtures.

Source	BC	Geometry	Dimensions	Operating Conditions	Mixtures	Non-dimensional parameters	Reported
Ardhapurkar et al [57]	SF	Tube-in-tube (helically coiled)	D_i = 4.83 mm (0.19”) D_o = 6.35 mm (0.25”) D_s = 7.89 mm (0.31”) D_c = 200 mm (7.9”) L = 15 m (49.2 ft)	T_{hot} = Ambient T_{cold} = 98-147K $P_{h,in}$ = 1117-1508 kPa (162-219 psi) $P_{c,in}$= 532-611 kPa (77-89 psi) $\dot{m}$ = 2.6-3.8 g/s	N_2-hydrocarbon (CH_4, C_2H_6, C_3H_8 and i-C_4H_{10})	NA	U = 871-1169 W/m^2-K
Boiarski et al [58]	SF	Paired-tube & tube-in-tube (tube bundle)	NA	T_{hot} = Ambient T_{cold} = 80-240K HP = 1520-2533 kPa (221-367 psi) LP = 152 – 608 kPa (22-88 psi)	Ar, CH_4, C_2H_6, C_3H_8, He, N_2, R14, R13, R218, R22	NA	Refrigeration capacity and heat exchanger efficiency
Gong et al [59]	SF	Tube-in-tube (tube bundle)	D_i = 2 mm (0.08”) D_o = 3mm (0.12”) D_s = 10.5-14.5 mm (0.41-0.57”) 7-10 tubes	T_{hot} = Ambient T_{cold} = 80-180K HP = 108-1390 kPa (157-202 psi) LP = 295-330 kPa (42.8-48 psi)	C_2H_6, C_3H_8, i-C_4H_{10}, i-C_5H_{12}, N_2, Ne and R14	NA	U = 332-673 W/m^2-K
Chen & Shi [48]	H	Horizontal tube	D_i = 8 mm (0.32”)	T = 148-156K P_{in} = 0.3-0.7 MPa G = 49-202 kg/m^2-s	LNG (CH_4, C_2H_6, C_3H_8, C_4H_{10}, N_2)	NA	Local flow boiling h = 2000-8000 W/m^2-K
Nellis et al [49]	T	Horizontal tube	D_i = 0.813 mm (0.032”)	T_{in} = 111-296K P_{in} = 394-1439 kPa (57-209 psi) $\dot{m}$ = 0.14-0.65 g/s	N_2-hydrocarbon (CH_4, C_2H_6, C_3H_8, and i-C_4H_{10})	Re = 1,000-75,000 Nu = 10-325	Local flow boiling h = 2000-16000 W/m^2-K
Barraza et al [50]	T	Horizontal tube	D_i = 0.5-3 mm (0.02-0.12”)	T_{in} = 103-275K P_{in} = 265-791 kPa (38 – 115 psi) G = 200-900 kg/m^2-s	N_2-hydrocarbon (CH_4, C_2H_6, and C_3H_8) Ar-refrigerant (R14, R23, R32, and R134a)	Re = 150-50,000 Nu = 4-1,000	Local flow boiling h = 2000-8000 W/m^2-K (hydro) h = 1000-4000 W/m^2-K (refs)

Table 2.3. Literature available for measurements of heat transfer coefficients for two-phase multi-component gas mixtures.

3. Primary Objective of Research

Many researchers have proposed methodologies to optimize gas mixtures for MGJT cryocoolers. However, the bulk of this research focuses on the thermodynamic optimization of the mixture composition and the associated performance of the cryocooler without adequately accounting for the effect that mixture selection has on the heat exchanger performance. Specifically, for GH heat exchangers, the literature review shows a lack of experimental data and understanding of the heat transfer and pressure drop characteristics associated with the flow of a gas mixture through the shell-side of the heat exchanger. With such a scarcity of experimental data and theory, the effect of heat transfer and pressure drop cannot be adequately accounted for in mixture selection. Beyond the broad goal of investigating gas mixture selection for a MGJT cryocooler, this research aims to design and build a test facility that can be used to acquire data to gain insight into heat transfer characteristics of the shell-side flow of GH heat exchangers.

Temperature Span:	110 K to 300 K
Operating Low Pressure:	345 to 1034 kPa (50 to 150 psia)
Output Pressure Ratios:	2:1 to as high as 7:1
Flow Rate:	0.05 – 0.15 g/s

Table 3.1. Target operating and design parameters for gas mixture selection and thermal-fluid measurements.

The specific operating parameters of interest for gas mixture selection and thermal-fluid measurements are outlined in Table 3.1. The operating pressures and pressure ratios of interest are lower than those investigated in previous works because these lower operating pressures, pressure ratios correspond to higher compressor efficiency [60].

The components and composition of the mixtures analyzed in the present study have been chosen for their applicability to MGJT systems with cooling power in the range from 110-180K. Components analyzed for gas mixtures selection included argon, butane, ethane, krypton, methane, R14, R116, R134a, R218, R23, R32 and N_2. The selected mixtures will have a temperature glide between room temperature and the temperature at which cooling power is needed. The anticipated outcome is that two-phase flow should exist on both sides of the heat exchanger in order to increase the heat exchanger effectiveness and the efficiency of the cycle. Although hydrocarbon refrigerants have been shown to have a higher thermodynamic cooling capacity than synthetic refrigerant mixtures, concerns due to flammability have limited their use. Thus, flammable, semi-flammable and non-flammable mixtures are all considered in this study.

4. Thermodynamic Mixture Optimization

4.1. Model Description

A MATLAB program was developed to investigate optimal three-component mixture selection for a MGJT cryocooler with target operating parameters given in Table 3.1. The thermodynamic analysis is based upon the maximum value of the minimum Δh_T that occurs for each mixture over the operating temperature range given a list of fluids, load and supply temperatures, and suction and discharge pressures [61]. This process is accomplished using three nested functions that are referred to as the outer, intermediate, and inner functions.

4.1.1. Outer Function

The outer function returns tables of optimal compositions and maximum values of the minimum Δh_T that occur for all of the three-component mixtures that are analyzed by applying the process described below:

1. Generates an array of all possible three-component mixture combinations from the list of fluids
2. Selects the three-component mixture from the first row of the array
3. Passes the three-component mixture to the intermediate function along with the specified supply and load temperatures and suction and discharge pressures
4. Stores the optimal composition and the associated maximum value of the minimum Δh_T that is associated with the three-component mixture; these parameters are returned as outputs from the intermediate function in a table
5. Repeats steps 2-4 for the next three-component mixture in the array and so on until all the possible three-component mixtures have been analyzed

6. Sorts the table of results in ascending order according to the maximum value of the minimum Δh_T and prints the results
7. Repeats steps 2-6 for the next load temperature in a user-specified set of load temperatures until all load temperatures have been analyzed

4.1.2. Intermediate Function

The intermediate function uses nested loops to run through a range of possible molar compositions for the three-component mixture that is passed from the outer function. Two concentration parameters are passed to the inner function along with the specified three-component mixture and the values of supply and load temperatures and suction and discharge pressures. The inner function is discussed subsequently; this function returns the value of the minimum Δh_T associated with the three-component mixture and the specified concentration parameters. The intermediate function assigns these values to a results array. After the nested loop has completed, the intermediate function searches the results array for the maximum value of the minimum Δh_T that is obtained over all compositions and returns this value along with the associated optimal mixture composition.

The scatter plot in Figure 4.1(a) shows the minimum Δh_T obtained for each molar composition of a three-component mixture consisting of R134a, argon, and isobutane at a load temperature of 140 K and suction and discharge pressures of 345 and 1034 kPa (50 and 150 psi), respectively. (Note that the molar fractions of R134a and argon are shown on the axes of the plot. The molar fraction of isobutane is one minus the sum of the molar fractions of R134a and argon). Examination of the plot shows the maximum value of the minimum Δh_T that can be obtained using this mixture and operating parameters. By interpolating these values to a contour plot that is shown

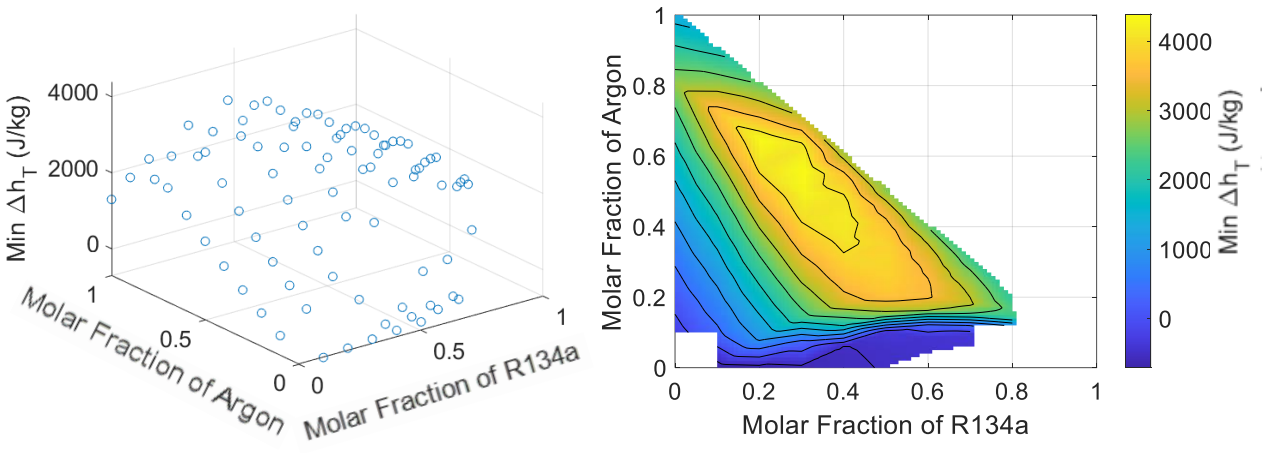

(a) (b)

Figure 4.1. Visualization of the unconstrained results of the intermediate function – scatter plot (a) and contour plot (b) of the minimum Δh_T.

in Figure 4.1(b), the optimal mixture composition is evident. In this example, the intermediate function will return 4392 J/kg as the maximum value of the minimum Δh_T that occurs and an associated optimal mixture composition of 20% R134a, 64% argon, and 16% isobutane on a molar basis.

Note that the gaps in the contour plot in Figure 4.1(b) result from molar compositions that do not return a value of minimum Δh_T. For these mixtures, the property routine REFPROP does not return enthalpy data that spans the entire specified temperature range and thus a minimum Δh_T cannot be estimated at these points [62].

Additionally, the intermediate function limits the molar fraction of a component based upon the experimental charge pressure and the saturated vapor pressure, P_{sat}, of the component at room temperature to ensure that a single-phase gas is used to charge the cryocooler. The experimental charge pressure is set to half of the sum of the suction and discharge pressures. For the example gas mixture and operating parameters shown in Figure 4.1, the intermediate function sets the charge pressure to 100 psi. The molar fractions of R134a and argon are not limited under

these conditions. However, the P_{sat} of isobutane at room temperature is 54 psi. Thus, the molar fraction of isobutane is limited to 54% to ensure the cryocooler can be charged with isobutane as a gas. This limitation constrains the molar compositions sent to the inner function and will alter the results of the intermediate function as shown in Figure 4.2. For R134a, argon and isobutane with the example operating parameters, the optimal mixture composition is not altered as it falls within the constrained molar compositions.

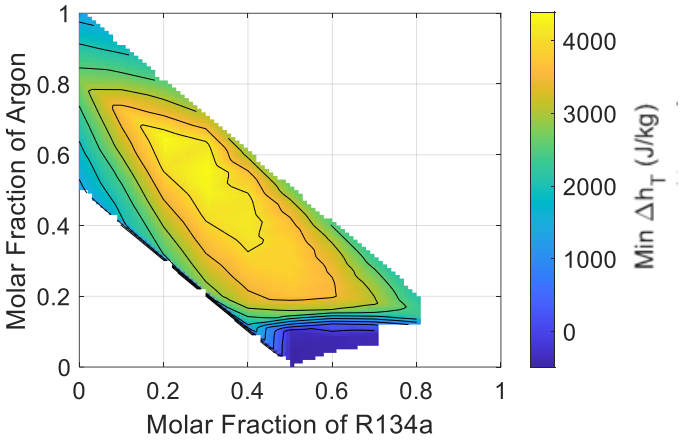

Figure 4.2. Results of the intermediate function with constrained molar fractions.

4.3.3. Inner Function

The inner function returns the minimum Δh_T that occurs for a specified composition of the three-component mixture analyzed by the process described below:

1. Convert the concentration parameters passed from the intermediate function to mass fractions
2. For a temperature range that is slightly larger than the load temperature to supply temperature range, call REFPROP for raw enthalpy data and assigns all enthalpy and temperature data returned to temporary vectors
3. Remove enthalpy values from temporary vectors that are determined to be outliers
4. Remove enthalpy values from temporary vectors that are not thermodynamically consistent (e.g., ones that decrease as temperature rises)

5. Generate enthalpy data for high- and low-pressure streams by linearly interpolating temporary vectors for specified temperature range
6. Calculates the minimum Δh_t that occurs for specified temperature range

Figure 4.3 shows a visualization of the process used by the inner function. The specific example shown is for the optimal mixture selected by the intermediate function described above with the load temperature decreased to 110 K. Figure 4.3(a) displays the enthalpy data obtained from REFPROP corresponding to the high- and low-pressure streams for the specified composition of the three-component mixture. For the temperature range of 125 to 300 K, there is a clear trend line demonstrating that an increase in temperature corresponds to an increase in enthalpy. However, below 125 K there are enthalpy data obtained from REFPROP that do not fit this trend. This is highlighted in Figure 4.3(b) by focusing on the temperature range of 100 to 130 K.

The low-pressure stream in Figure 4.3(b) displays enthalpy data obtained from REFPROP that clearly falls below the trend line. These unexpected values in the enthalpy data are due to issues of convergence within the property routine REFPROP. These values of enthalpy, along with their corresponding temperatures, are considered to be outliers and removed from the temporary vectors that store the low-pressure stream data. Details regarding the outlier detection of the mixture optimization model can be found in Appendix 8.1. The enthalpy data obtained from REFPROP with the potential outliers removed is displayed in Figure 4.3(c).

In Figure 4.3(c), there are values of enthalpy that decreases as the temperature rises for the high-pressure stream. These values of enthalpy were not marked as outliers as the trend line for enthalpy is increasing significantly near these points. However, this behavior is not thermodynamically consistent and therefore these value of enthalpy along with their corresponding temperatures are removed from the temporary vectors that store the high-pressure stream data.

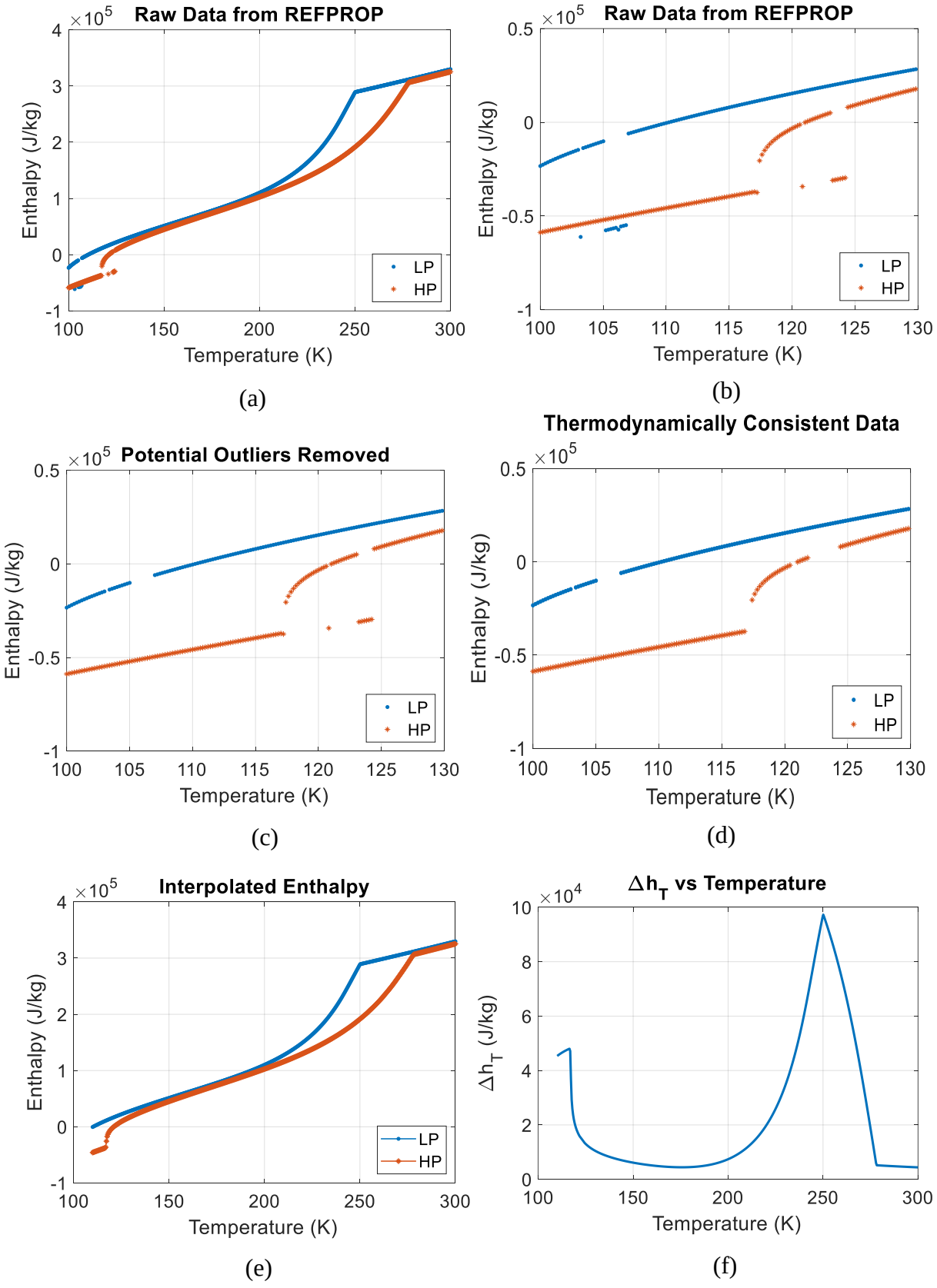

Figure 4.3. Visualization of the process used by the inner function.

Details regarding the process of checking for thermodynamically consistent enthalpy data can be found in Appendix 8.2. The thermodynamically consistent enthalpy data is then displayed in Figure 4.3(d).

After the enthalpy data obtained from REFPROP has been checked and modified based on the existence outliers and the need for thermodynamic consistency, the inner function linearly interpolates the temperature and enthalpy vectors for the desired temperature range. The linearly interpolated data is shown in Figure 4.3(e). Finally, the inner function calculates the Δh_T between the high- and low-pressure streams for the desired temperature range and displays the results in Figure 4.3(f). The minimum Δh_T that occurs can be seen for the specified composition of the three-component mixture.

4.2. Model Results

Mixture optimization was carried out for flammable and non-flammable mixtures. The fluids analyzed for the flammable mixture optimization included argon, butane, isobutane, ethane, methane, pentane, propane, and nitrogen. The fluids analyzed for the non-flammable mixture optimization included argon, R14, R23, R116, R134a, R218, krypton and nitrogen.

The flammable and non-flammable mixture optimizations were performed for three sets of suction and discharge pressures: 345 and 1034 kPa (50 and 150 psia), 276 and 1103 kPa (40 and 160 psia), and 517 and 1551 kPa (75 and 225 psia). This allows for a comparison between a set of suction and discharge pressure that have the same pressure ratio but different operating pressures and those with the same approximate operating pressure but a different pressure ratio. All mixtures were analyzed for load temperatures ranging from 110-180 K in increments of 10 K while the supply temperature remained constant at 300 K.

The following details the effects of flammability, operating pressures and pressure ratios on refrigeration per mass flow, $\dot{Q}/\dot{m}$, for the optimal gas mixtures at each load temperature. Additionally, the fraction of the temperature range that is in the two-phase region for the optimal gas mixtures is analyzed as this metric will tend to provide better recuperator performance due to heat transfer coefficient within the heat exchanger. Finally, the overall confidence in the results is discussed as it relates to the amount of information that must be removed from the REFPROP output based on outliers and thermodynamic inconsistency.

4.2.1. Operating Pressure and Pressure Ratio Comparison

Figure 4.4 illustrates the refrigeration per mass flow, $\dot{Q}/\dot{m}$, as a function of load temperature for the three sets of suction and discharge pressures. Each marker represents the maximum value of the minimum $\dot{Q}/\dot{m}$ that occurs for the optimal combination of three fluids and is related to composition that is selected specifically for that load temperature (i.e., these curves should not be interpreted as load curves for a specific mixture but rather as the absolute maximum potential of all combinations of three fluids considered). The optimal three-component mixture at each load temperature and its associated maximum value of the minimum $\dot{Q}/\dot{m}$ can found in Appendices 8.3, 8.4, and 8.5 for suction and discharge pressures of 345 and 1034 kPa (50 and 150 psi), 276 and 1103 kPa (40 and 160 psi), and 517 and 1551 kPa (75 and 225 psi), respectively. The refrigeration per mass flow for the non-flammable mixtures shown in the upper right of Figure 4.4 is scaled for easy comparison with the flammable mixtures while the same plot is shown again on the bottom with another scale to allow for better viewing of the trend lines.

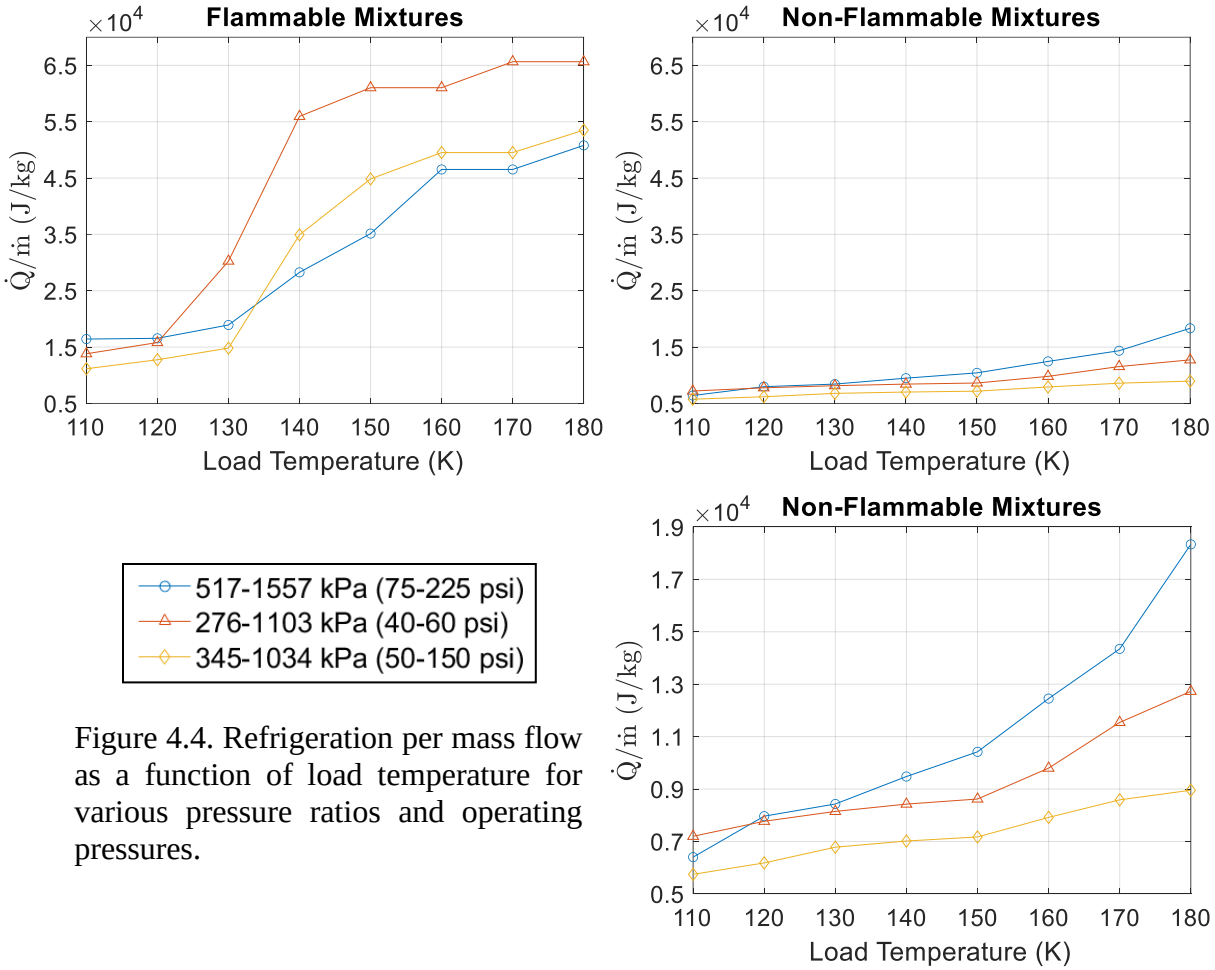

Figure 4.4. Refrigeration per mass flow as a function of load temperature for various pressure ratios and operating pressures.

For the non-flammable optimal mixtures, suction and discharge pressure of 345-1034 kPa (75-225 psi) produce the greatest values of $\dot{Q}/\dot{m}$ for load temperatures of 120 K and above while pressures of 345-1034 kPa (50-150 psi) produces the lowest values. Thus, within the target operating parameters, it is important to increase the operating pressures and pressure ratio to select a non-flammable mixture with the greatest value of $\dot{Q}/\dot{m}$.

This trend is not observed for the flammable mixtures. Suction and discharge pressures of 517-1157 kPa (75-225 psi) produce the lowest values of $\dot{Q}/\dot{m}$ for load temperatures of 140 K and above while suction and discharge pressures of 276-1103 kPa (40-160 psi) produce the greatest values of $\dot{Q}/\dot{m}$ for load temperatures of 120 K and above. Therefore, within the target operating parameters, it is more beneficial to increase the pressure ratio rather than the operating pressures

to select a flammable mixture with the greatest value of $\dot{Q}/\dot{m}$. As a result, it is expected that for optimal semi-flammable mixtures there will be a flammability limit for which increasing the pressure ratio is more beneficial than increasing the operating pressures.

It is also significant to note the magnitudes of $\dot{Q}/\dot{m}$ in Figure 4.4. For the flammable mixtures, the value of $\dot{Q}/\dot{m}$ is reduced by over half for the optimal mixture at a load temperature of 140 K to the optimal mixture at a load temperature of 120 K for suction and discharge pressures of 345-1034 kPa (50-150 psi). For suction and discharge pressure of 276-1103 kPa (40-160 psi), the value of $\dot{Q}/\dot{m}$ is reduced by over 70% for the same load temperatures. This illustrates the difficulty of finding a mixture that will produce cooling at load temperatures below 140 K. Furthermore, the values of $\dot{Q}/\dot{m}$ for the optimal non-flammable mixtures are significantly lower than the values for the optimal flammable mixtures. This is shown more clearly in Figure 4.5. $\dot{Q}/\dot{m}$ only approaches similar values for load temperatures of 130 K and below and even for these load temperatures the values of $\dot{Q}/\dot{m}$ for the optimal flammable mixtures are approximately double the values of $\dot{Q}/\dot{m}$ for the optimal non-flammable mixtures. A similar trend was observed for suction and discharge pressures of 217-1557 kPa (75-225 psi).

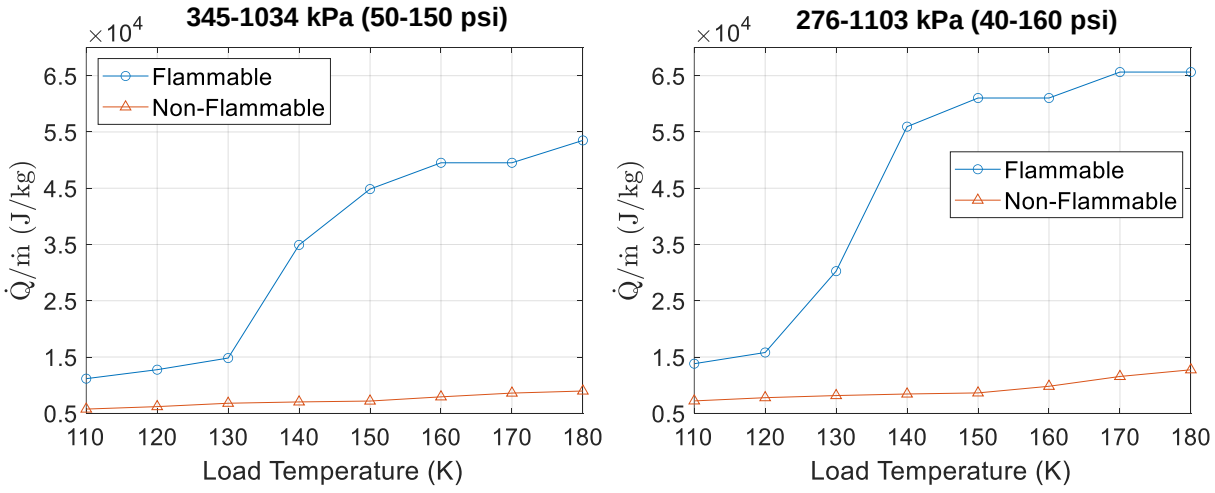

Figure 4.5. Refrigeration per mass flow rate as a function of load temperature.

4.2.2. Percent Two-Phase

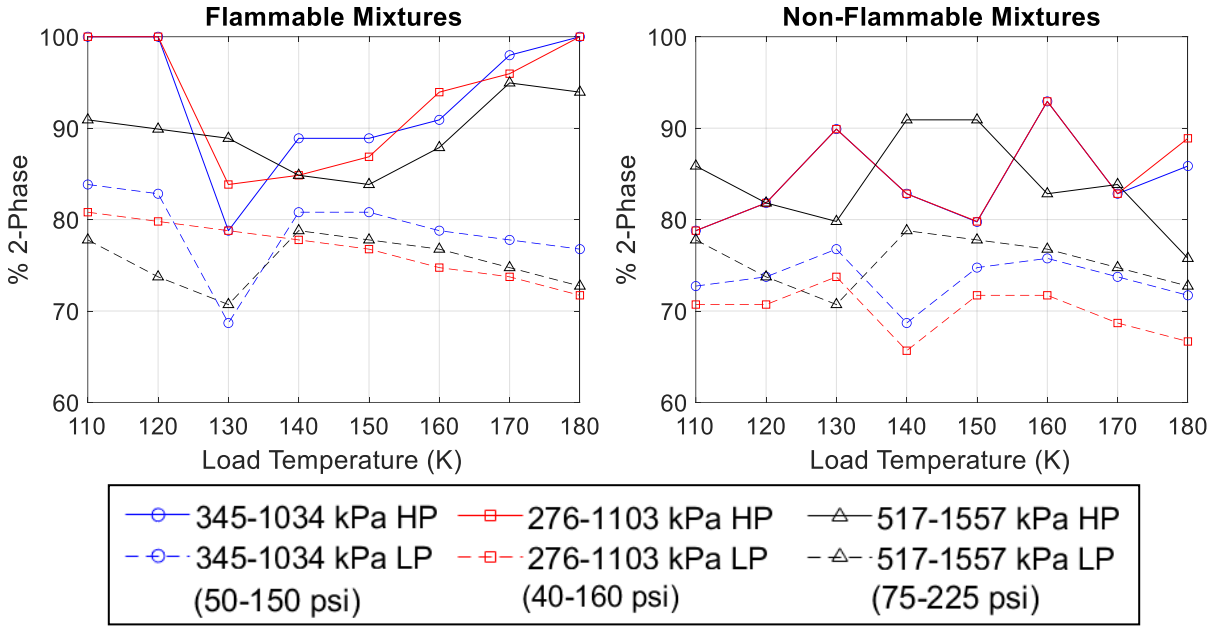

Figure 4.6. % 2-Phase as a function of load temperature for various pressures and pressure ratios.

The percent of the temperature range of the recuperator where the mixtures is in the two-phase region is one metric that can be used to further distinguish between candidate mixtures. As discussed earlier, the heat transfer coefficient associated with a two-phase state is much larger than a single-phase state [6]. Therefore, given the same thermodynamic performance, represented by $\dot{Q}/\dot{m}$, a mixture that is two-phase over a larger fraction of the temperature range will be practically superior as a smaller recuperator can be employed (or better performance can be obtained from the same recuperator size). The percent of the temperature range of the recuperator in a two-phase state was calculated using the bubble and dew points for the optimal mixtures and comparing them to the load and supply temperatures.

Figure 4.6 illustrates that the optimal flammable mixtures are in the two-phase region for a greater percentage of the temperature span than the optimal non-flammable mixtures for load temperatures greater than 160 K and below 130 K. For the load temperatures in-between, the

optimal flammable and non-flammable mixtures are in the two-phase region for a similar percentage of the temperatures span.

For the optimal flammable and non-flammable mixtures, the percent of the recuperator that is two-phase for load temperatures below 130 K may be overestimated. Data for the bubble point was not always returned from REFPROP, especially at load temperatures below 130 K, which currently results in an overestimation of the percent of the recuperator that is two-phase. These issues will be discussed in more detail in the next section.

4.3.4. Maximum Temperature Gap

In the inner function of the mixture optimization model, REFPROP is called to obtain values of enthalpy for the high and low pressures streams. The enthalpy values are placed into temporary vectors where outliers are removed and thermodynamic consistency is checked before the values of enthalpy are interpolated and used to analyze the mixture. However, values of enthalpy are not always available from REFPROP for the desired temperature range and mixture.

The temperature gap is the largest range of temperature where values of enthalpy are missing in the temporary vectors storing enthalpy data. The maximum temperature gap is found by analyzing the top ten optimal mixtures for each set of suction and discharge pressures and load temperature. These missing values of enthalpy may not be available from REFPROP for the desired mixture or may have been removed through outlier detection and/or the thermodynamic consistency check. The larger temperature gaps shown in Figure 4.7 are generally the result of unavailable values of enthalpy from REFPROP. The outlier detection and thermodynamic consistency check will then add to the gap by removing additional values of enthalpy. The smaller temperature gaps are generally the product of an outlier removal.

Figure 4.7 illustrates that below a load temperature of 130 K, larger gaps of values of enthalpy may exist for both the optimal flammable and non-flammable mixtures. The optimal flammable and non-flammable mixtures with a higher pressure ratio tend to have a slightly larger maximum temperature gap. At 130 K and above, the high- and low-pressure streams generally have a maximum temperature gap that is consistent with the temperature segmentation that is used to call REFPROP, indicating that values of enthalpy are consistently returned from REFPROP and are kept for interpolation. (Note that the dashed line with triangles for the flammable mixtures in Figure 4.7 represents the low-pressure of all suction and discharge pressures analyzed). As a result, the consistency in values of enthalpy returned from REFPROP for mixtures at or above 130K allows for greater confidence in the accuracy of these results.

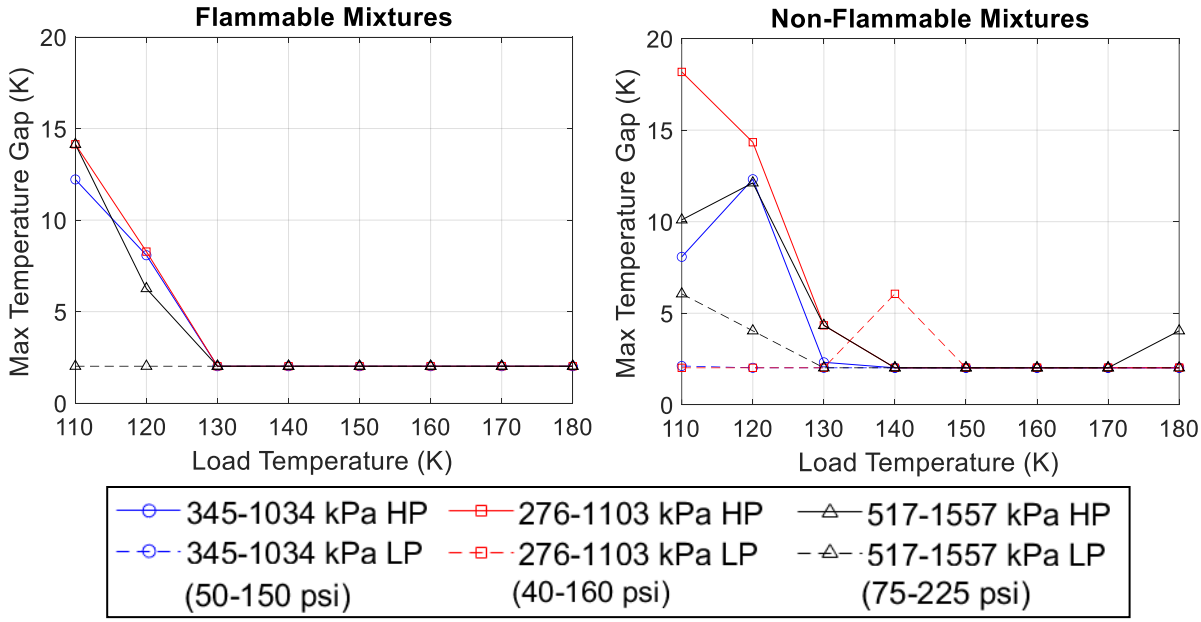

Figure 4.7. Maximum temperature gap as a function of load temperature for various pressures and pressure ratios.

5. Giauque-Hampson Heat Exchanger Test Section for HTC Measurements

5.1. Design Considerations for Test Section

The purpose of the GH heat exchanger test section is to measure the shell-side local two-phase heat transfer coefficient and pressure drop of a multi-component mixture within a reasonable degree of uncertainty for the targeted operating parameters listed in Table 5.1. For the heat transfer measurement, a heat load is applied to the gas mixture via interaction with a secondary heat transfer fluid and the applied heating load is determined indirectly using an energy balance on the heat exchanger. For the proposed test section, helium is used as the secondary fluid and it travels inside the finned high-pressure tube. From the measurements of flow rates and the inlet and outlet temperatures and pressures of the helium and mixed gas, the htc of the mixed gas can be determined provided that the heat transfer coefficient associated with the helium flow is known. To design the test section, one must select an appropriate finned high-pressure tube applicable for MGJT cryocoolers, consider the placement of the temperature and pressure measurements, and determine an appropriate length of the test section which will allow measurements of the htc within reasonable uncertainty.

Operating Parameter	Value
Inlet temperature of MG ($T_{in,mg}$)	110-300 K
Mass flow rate of MG ($\dot{m}_{mg}$)	0.05-0.15 g/s
Inlet pressure of MG ($P_{in,mg}$)	345-862 kPa (50-125 psi)
Inlet pressure of He ($P_{in,he}$)	862 kPa (125 psia)
Operating fluid	Range of gas mixtures composed of Ar, butane, ethane, methane, R14, R23, R32 and N_2

Table 5.1. Target operating parameters for test section.

5.1.1. Selection of Finned High-Pressure Tube

When selecting a finned-tube for the high-pressure stream of a GH heat exchanger, the parameters of interest are the material and size of the high-pressure tube and fins, the fin density, and the method of attaching the fin to the tube. According to Maytal and Pfotenhauer, typical ratios of the external finned surface area to the internal surface area are about 8-12 and, in general, the ranges of inside and outside diameters are 0.25-0.8 mm (0.01-0.03 inch) and 0.4-1.2 mm (0.02-0.05 inch) for JT systems [2]. The preferred material for the high-pressure tube is copper or a copper-nickel alloy because of its high thermal conductivity, and the most widely used material for the fins is copper. Typical density of the fins ranges from 1.5-4 windings per millimeter (38-102 windings per inch) along the axis of the high-pressure tube [2]. Beyond the properties, size and density of fins, a crucial factor for an efficient finned tube is the thermal contact between the fins and tube. A thin layer of tin solder is often used for this purpose due to ease of manufacturing, even though alternative methods of improving thermal contact have been proposed. In like manner, Table 2.3 of the literature review demonstrates that small diameter tubes are of significant interest for MGJT systems. Previous heat transfer coefficient measurements by Nellis et al. and Barraza et al. focused on minichannels [49, 50]. In the literature, minichannels are classified as tubes with inner diameter between 0.2 - 3.0 mm (0.008 - 0.12 inch) [63]. Thus, the finned high-pressure tube of the test section was selected to be a 70/30 CuNi finned-tube with inner and outer diameter of 0.493 and 1.001 mm (0.019-0.039 inch), respectively, and fin density of 3.94 fins per millimeter (100 fins per inch) available from Energy Transfer.

5.1.3. Placement of Temperature and Pressure Measurements

To determine the applied heating load to the mixed gas indirectly using an energy balance on the heat exchanger, the inlet and outlet temperatures and pressures of the helium and mixed gas

must be known with the smallest possible uncertainty. For the mixed gas, which is two-phase in the test section, it is important that the temperature and pressure are directly measured at the inlet and outlet of the heat exchanger such that no calculations need to be performed to determine these parameters.

For the helium flowing through the helically coiled finned-tube with inner diameter of 0.493 mm (0.019 inch), it was not possible to measure the pressure and temperature directly at the inlet and outlet of the heat exchanger without disrupting the flow stream of the mixed gas. Therefore, the temperature and pressure measurements are located within 1/8" vacuum coupling radiation (VCR) fittings at the inlet and outlet of the shell as shown in the rendering of the test section in Figure 5.1. The change in temperature and pressure from the location of measurement inside the 1/8" fitting (at the inlet of the shell) to the small diameter of the finned high-pressure tube (at the

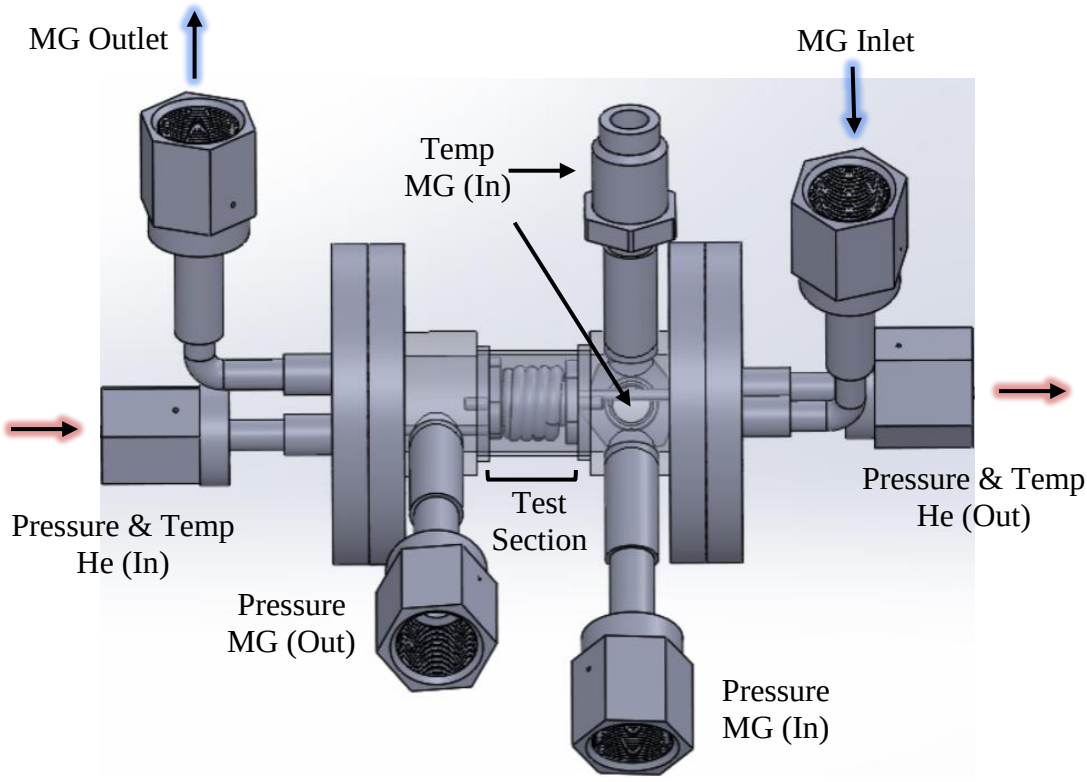

Figure 5.1. SolidWorks rendering of heat exchanger for test section.

inlet of the heat exchanger) is determined by Bernoulli's equation for incompressible flow. Likewise for the change in temperature and pressure from the measurement at the outlet of shell to the outlet of the heat exchanger.

5.1.2. Scaling Factor to Predict HTC of Mixed Gas

To define the necessary length of the finned high-pressure tube in the test section, the value of the htc of the mixed gas in the test section must be estimated. As the literature review discussed, for GH heat exchangers there is a lack of experimental data and understanding of heat transfer characteristics of the flow on the shell-side of the heat exchanger for two-phase multi-component mixtures. This means not only is there no correlation available to predict the htc for two-phase multi-component mixtures but the *magnitude* of the htc is unknown. While this provides an opportunity to do meaningful research, this poses quite a challenge when trying to determine the length of fabrication for the test section.

To gain insight into the magnitude of the htc, a scaling factor, SF, is estimated using the correlation from Gupta et al. to predict the htc of a pure fluid on the shell-side of a GH heat exchanger and compare it to the htc of the same fluid flowing through a horizontal tube of dimensions and operating conditions used in experimental measurements of Barraza et al [27, 6]. Assuming that mixed gases and pure fluids scale the same between two different geometries, the scaling factor is applied to experimental data from Barraza et al for the htc of mixed gases, h_{mg}, in a horizontal tube to make a loose approximation of the h_{mg} on the shell-side of a GH heat exchanger. For clarity, the process is outlined in Figure 5.2.

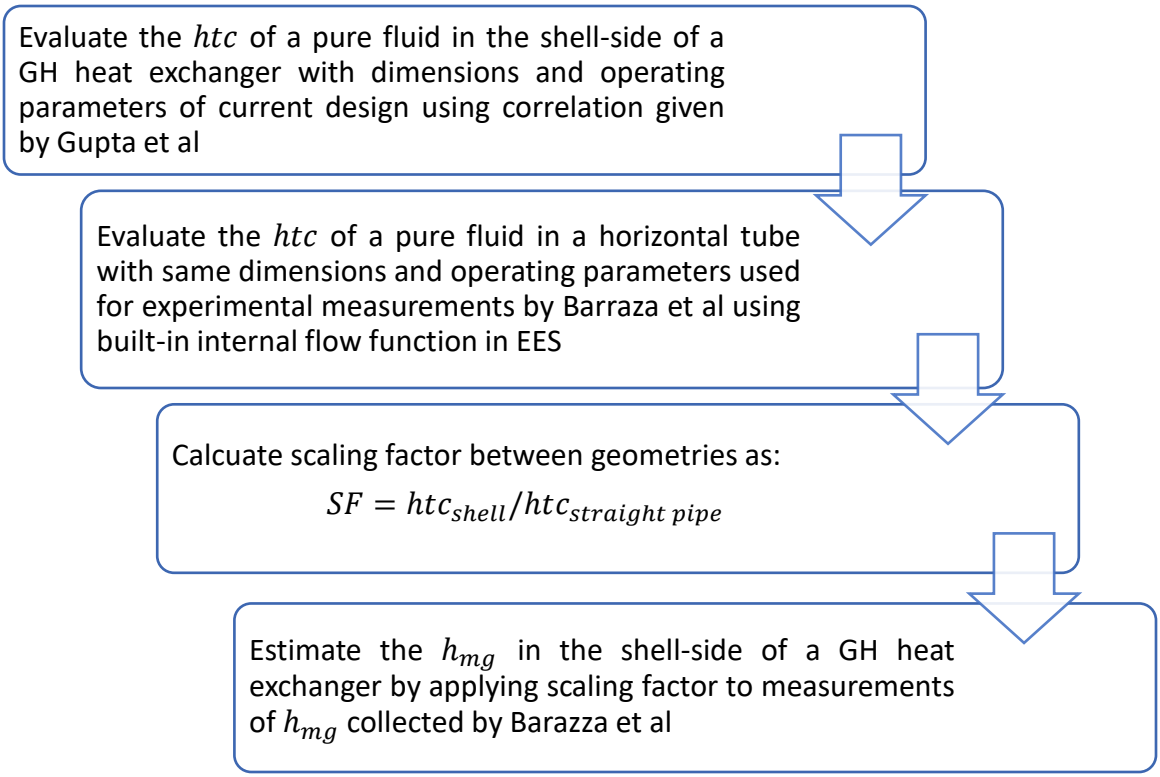

Figure 5.2. Flow diagram for prediction of htc_{mg}.

The SF is calculated for operating parameters within the range of interest and pure fluids including butane, ethane, methane, R32, R23 and R14. Figure 5.4(a) shows that varying the operating pressure of ethane in the shell-side of the GH heat exchanger from $P1$ = 345 kPa (50 psi) to $P2$ = 862 kPa (125 psi) does not significantly impact the SF. However, varying the mass flow rate from 0.05 to 0.15 g/s does have a significant impact on the SF as it is approximately doubled for the higher flow rate. This aligns with expectation as the heat transfer coefficient of the ethane is more significantly impacted by a change in flow rate at these operating conditions. Figure 5.4(b) shows the change in SF dependent upon the operating fluid at the upper limit of the targeted mass flow rate of 0.015 g/s and a pressure of 862 kPa (125 psi). The greatest SF estimated is given by butane at 0.62. These calculations were also run for the lower limit of the targeted mass flow

rate at 0.05 g/s and similar trends were observed. The lowest SF estimated was associated with R32 at 0.04.

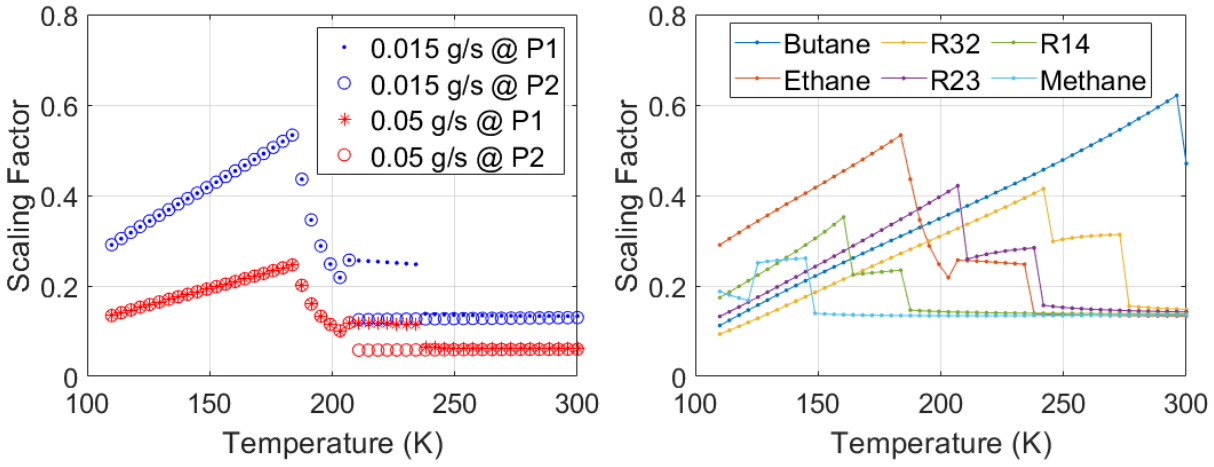

(a) (b)

Figure 5.4. Scaling factor as a function of pressure and mass flow rate for ethane (left) and varying pure fluids at constant pressure and mass flow rate (right).

The values of the measured h_{mg} by Barraza et al were multiplied by the upper and lower estimations for the SF of 0.62 and 0.04, respectively, to loosely predict the upper and lower limits for the heat transfer coefficients of a hydrocarbon and synthetic refrigerant mixture. Figure 5.3 shows the prediction of the h_{mg} as a function of quality for a hydrocarbon mixture of 50% methane, 35% ethane and 15% butane and synthetic refrigerant mixture of 80% R32 and 20% R14 on a molar basis. From this rough estimation, the heat transfer coefficient is predicted to fall between the very large range of 20 to 3000 W/m^2-K.

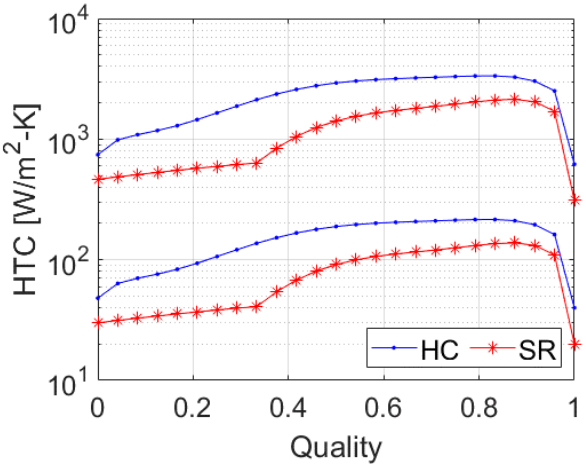

Figure 5.3. Predicted htc for a hydrocarbon mixture (HC) and synthetic refrigerant mixture (SR) for varying quality.

5.1.3. Length of Finned High-Pressure Tube

To define the length of the finned high-pressure tube, an analysis is carried out in order to understand the tradeoff between the uncertainty of the h_{mg}, $U(h_{mg})$, and the change in quality of the mixed gas, Δx_{mg}, that occurs between the inlet and the outlet of the heat exchanger. As discussed above, the h_{mg} is predicted to fall in the range between 20 and 3000 W/m^2-K. For higher values of h_{mg}, the mixed gas stream will experience an increased change in temperature and thus Δx_{mg} will be increased. An increased Δx_{mg} means a larger change in the properties of the mixed gas between the inlet and outlet of the heat exchanger. Large variation in the fluid properties is undesirable as the heat exchanger performance calculations using the $\varepsilon - NTU$ method assuming that the capacitance rates of the fluid streams are constant throughout the heat exchanger. Additionally, the target objective of the test section is to measure the *local* h_{mg}. To measure the local h_{mg}, the change in fluid properties must be minimized. Therefore, analyzing $U(h_{mg})$ using the greatest predicted h_{mg} will ensure the test section is fabricated to a length such that Δx_{mg} is minimized while h_{mg} can still be measured within reasonable uncertainty.

The relative uncertainty, RU, as a function of flow rate of the helium for the most challenging condition (the hydrocarbon mixture with a heat transfer coefficient of 3000 W/m^2-K) is shown in Figure 5.5 for various lengths of the finned high-pressure tube including 0.08 m (3 in), 0.11 m (4 in), and 0.15 m (6 in). The RU of a parameter (for example h_{mg}) is given by Eq. (5.1):

$$RU(h_{mg}) = \frac{U(h_{mg})}{h_{mg}} \tag{5.1}$$

Figure 5.5 shows that for all lengths considered, the $RU(h_{mg})$ is increased for both low and high values of average helium velocity, $\bar{u}_{he}$, in the test section. The Δx_{mg} for a length of 0.11 m (4

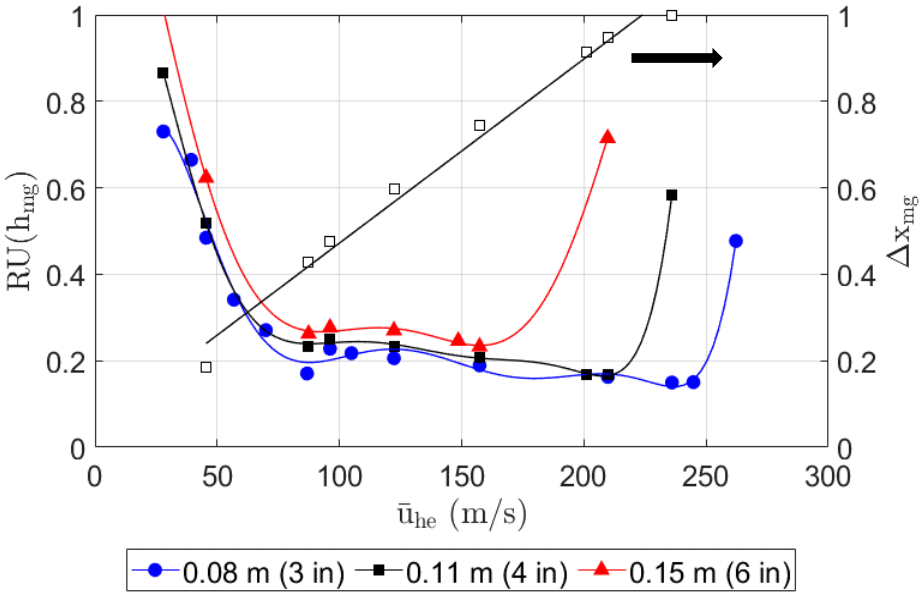

Figure 5.5. $RU(h_{mg})$ and Δx_{mg} for a gas mixture of 50% methane, 35% ethane and 15% butane on a molar basis versus $\bar{u}_{he}$ for three different lengths of finned tube.

inch) is shown on the right axis of Figure 5.5. As the helium flow rate increases, the heat transfer from the helium to the mixed gas increases and thus so does Δx_{mg}. As discussed previously, the heat exchanger analysis breaks down when the Δx_{mg} is large. Thus, from Figure 5.5, the $\bar{u}_{he}$ must be minimized to minimize Δx_{mg}. However, as $\bar{u}_{he}$ is decreased below values of approximately 75 m/s, the $RU(h_{mg})$ increases. Therefore, a helium flow rate must be selected that balances the increase in $RU(h_{mg})$ and the increase in change of quality of the mixed gas that is observed at higher helium flow conditions.

Let us investigate the increase in $RU(h_{mg})$ at low values of $\bar{u}_{he}$ by taking a closer look at the case where the length of the finned tube is 0.11 m (4 in) in Figure 5.5. At first glance, one might suspect that $RU(h_{mg})$ is dominated by the uncertainty of the temperature sensor measurements. At low values of $\bar{u}_{he}$, the heat exchanger is unbalanced and consequently, the pinch point temperature difference, ΔT_{pp}, is reduced. While this is true, Figure 5.6 demonstrates that at

the lower limit for the $\bar{u}_{he}$, the ΔT_{pp} is still significantly larger than the uncertainty in the temperature sensor measurements. At the lowest values of $\bar{u}_{he}$ analyzed, the ΔT_{pp} is 5. 8 K. The uncertainty in the temperature sensors measurements is an order of magnitude lower than this, at 0.25 K [64]. Thus, the uncertainty in the temperature sensors measurements is not contributing significantly to the increase in the $RU(h_{mg})$ at low values of $\bar{u}_{he}$.

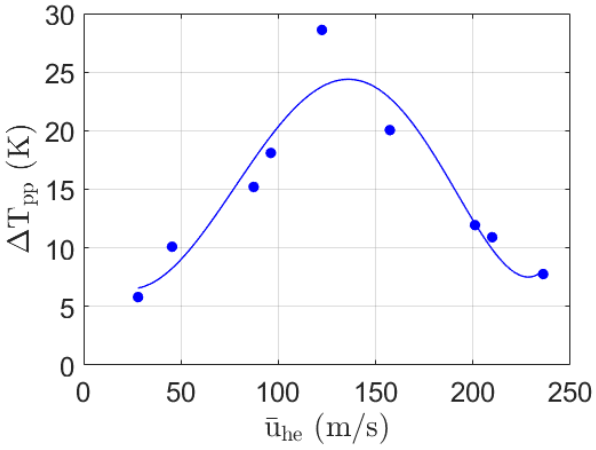

Figure 5.6. Pinch point temperature difference, ΔT_{pp}, versus $\bar{u}_{he}$.

Figure 5.7(a) shows the contribution of $U(\bar{h}_{he})$, $U(\dot{m}_{mg})$ and $U(\dot{V}_{he})$ to the $U(h_{mg})$ as a function of $\bar{u}_{he}$. The contributions to the uncertainty are labeled $CU(h_{mg})$. At low values of $\bar{u}_{he}$, $U(\bar{h}_{he})$ and $U(\dot{V}_{he})$ contribute approximately 48% and 32%, respectively, to the $U(h_{mg})$. As $\bar{u}_{he}$

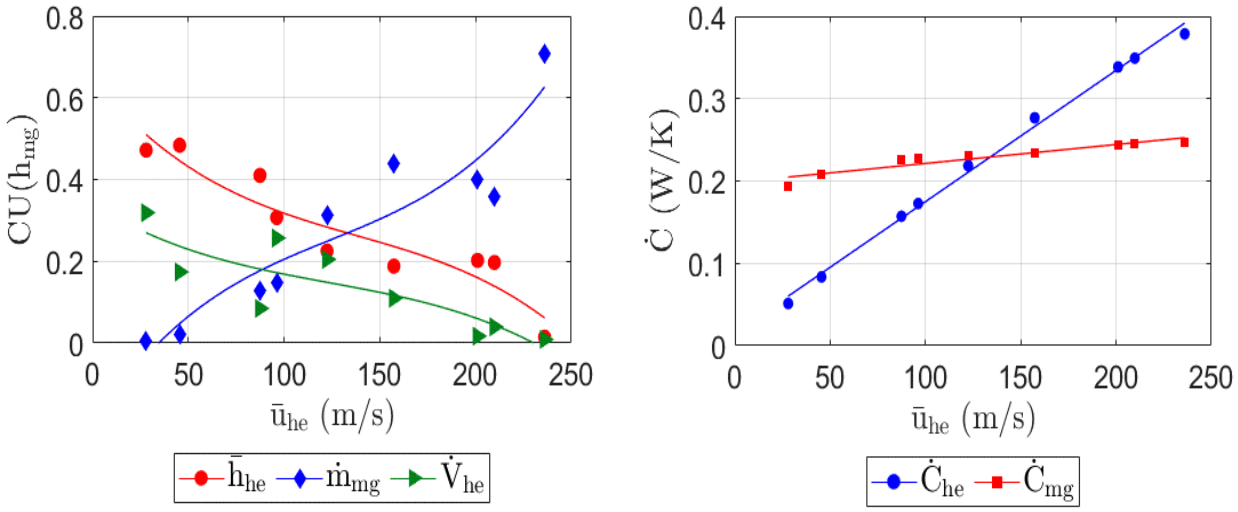

(a) (b)

Figure 5.7. Contribution of $U(\bar{h}_{he})$, $U(\dot{m}_{mg})$ and $U(\dot{V}_{he})$ to the $U(h_{mg})$ as a function of $\bar{u}_{he}$ (left) and $\dot{C}_{he}$ and $\dot{C}_{mg}$ as a function of $\bar{u}_{he}$ (right).

increases, the contribution of $U(\bar{h}_{he})$ and $U(\dot{V}_{he})$ to $U(h_{mg})$ decrease and the contribution of $U(\dot{m}_{mg})$ increases. The contribution of $U(\dot{V}_{he})$ and $U(\dot{m}_{mg})$ to the $U(h_{mg})$ aligns with expectation. Figure 5.7(b) shows that the stream of minimum capacitance, $\dot{C}_{min}$, changes from the helium to the mixed gas as $\bar{u}_{he}$ is increased and thus the sensitivity of $U(h_{mg})$ changes from being dominated by $U(\dot{V}_{he})$ to $U(\dot{m}_{mg})$. However, the largest contributor to the $U(h_{mg})$ at low values of $\bar{u}_{he}$ is $U(\bar{h}_{he})$. This is due to the influence of $U(\bar{h}_{he})$ on the resistances of the test section.

The conductance, UA, of the test section is given by Eq. (5.2):

$$UA = \frac{1}{R_{tot}} = \frac{1}{R_{he} + R_{cond,t} + R_{mg}} \tag{5.2}$$

where R_{tot} is the total resistance from the helium to the mixed gas, R_{he} is the helium convective resistance, $R_{cond,t}$ is the resistance to radial conduction through the finned tube and R_{mg} is the mixed gas convective resistance. R_{mg} accounts for the convective resistance to the mixed gas from both the finned and unfinned surface of the finned tube. Figure 5.8 shows the values of R_{he} and R_{mg} (based upon the heat transfer coefficient of 3000 W/m^2-K from the SF) as a function of $\bar{u}_{he}$. At low values of $\bar{u}_{he}$, R_{he} is an order of magnitude larger than R_{mg} with values of 4.5 and 0.4 W/K, respectively. Since the R_{he} is so much larger than R_{mg}, even a low $U(\bar{h}_{he})$ will have a significant impact on the $U(h_{mg})$. As $\bar{u}_{he}$ increases, $\bar{h}_{he}$ increases and R_{he} decreases. As the value of R_{he} approaches the value of R_{mg}, the contribution of $U(\bar{h}_{he})$ to the $U(h_{mg})$ also decreases. Therefore, at low

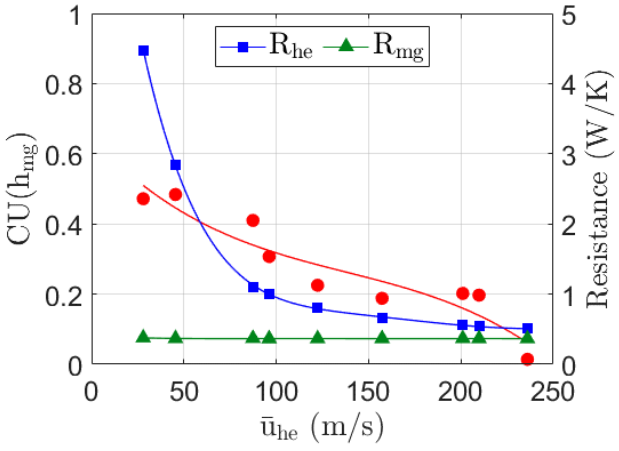

Figure 5.8. R_{he} and R_{mg} as a function of $\bar{u}_{he}$.

values of $\bar{u}_{he}$, the $U(h_{mg})$ is most sensitive to $U(\bar{h}_{he})$ due to the importance of R_{he} in the calculation for UA.

From Figure 5.5 and the analysis described above, a finned high-pressure tube length of 0.11 m (4 inch) is selected for the test section and a helium flow rate of approximately 85 m/s (0.03 g/s, 1 L/min) is selected as the targeted helium flow rate. A length of 0.11 m (4 inch) allows for the heat exchanger to be composed of 4 coiled turns. Howard et al. demonstrated that four coiled turns are sufficient to properly resolve the hydraulic entrance and exit effects of the flow for a wide range of Reynolds numbers [32]. With a helium flow rate of 85 m/s (0.03 g/s, 1 L/min), a Δx_{MG} of approximately 25% is expected. To measure the *local* h_{mg}, a Δx_{MG} less than 5-10% is ideal. This was not possible with the constraints of the analysis above. However, this analysis was performed for the largest htc predicted as this also yielded the largest Δx_{MG}. If the h_{mg} is lower, the Δx_{MG} will be decreased.

5.2. Fabrication of the Test Section

A SolidWorks CAD rendering of the test section was shown above in Figure 5.1. The test section is a counter-flow heat exchanger with high pressure helium flowing through a small diameter helically coiled tube and the low-pressure mixed gas flowing over the finned-tube in the annulus of a stainless-steel shell. An overview of the dimensions of the test section are given in .

	Parameter	SI (mm)	English (inch)	Source
Finned-tube	Inner diameter (D_i)	0.487±0.009	0.0192±0.0004	Microscope
	Outer diameter (D_o)	0.974±0.003	0.0384±0.0001	Microscope
	Diameter of fins (D_f)	1.458±0.009	0.0574±0.0004	Microscope
	Length (L_t)	98.12±0.20	3.863±0.008	Calculated
	Thickness of fin (th)	0.144±0.001	0.00567±0.00004	Microscope
	Fin spacing (sp_f)	0.134 ± 0.001	0.00528±0.00004	Microscope
Mandrel	Inner diameter	4.750±0.013	0.1870±0.0005	Calipers
	Outer diameter (D_m)	6.375±0.013	0.2510±0.0005	Calipers
	Length (L_m)	6.820±0.013	0.2685±0.0005	Calipers
Shell	Inner diameter (D_s)	10.033±0.013	0.3950±0.0005	Calipers
	Outer diameter	11.027±0.013	0.4340±0.0005	Calipers

Table 5.2. Dimensions of test section.

5.2.1. G10 Mandrel and Winding of the Heat Exchanger

The helium stream flows through the test section in a 70/30 CuNi finned-tube custom manufactured by Energy Transfer Durafin Tube [65]. The sales drawing can be found in Appendix 8.6Sales Drawing of Finned-tubing for GH Prototype. The finned-tube is helically coiled around a hollow G10 mandrel filled with polystyrene foam. The G10 mandrel is closed at both ends by

(a) (b) (c)

Figure 5.9. Mandrel plugs shown from top view (a) and side view (b). Assembled G10 mandrel (c).

stainless steel mandrel plugs. The mandrel plugs provide structure for the assembly of the heat exchanger while eliminating the flow path through the G10 mandrel. Further details regarding the design and manufacturing of the mandrel plug can be found in Appendix 8.7. Figure 5.9 shows the mandrel plugs and assembled G10 mandrel.

The finned-tube is helically wound around the G10 mandrel. During winding, a monofilament wire is wound on the inside and outside of the finned-tube as illustrated in Figure 5.10(a). The monofilament wire ensures the mixed gas flows over the fins rather than through gaps between the finned-tube in the annulus. A picture of the wound finned-tube on the mandrel is shown in Figure 5.10(b).

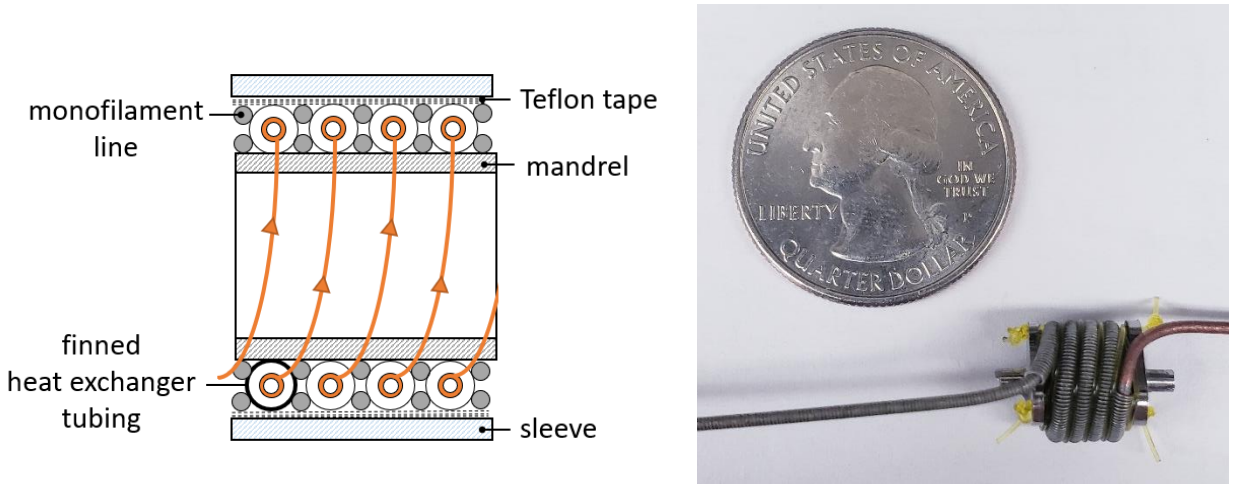

(a) (b)

Figure 5.10. Diagram (a) and picture (b) of coiled finned-tube heat exchanger.

5.2.2. Stainless-Steel Sleeve of Test Section

The heat exchanger is placed inside a stainless-steel sleeve composed of two 33.8 mm (1.33 inch) ConFlat (CF) weld necks with rotatable flanges adapted for the test section with a thin stainless-steel tube welded in-between as shown in Figure 5.11(a). Teflon tape was wound around the heat exchanger to ensure a snug a fit in the sleeve and shrink wrap covered the length of

unfinned-tube within the sleeve to reduce heat transfer between the mixed gas and CuNi tube before the start of the test section.

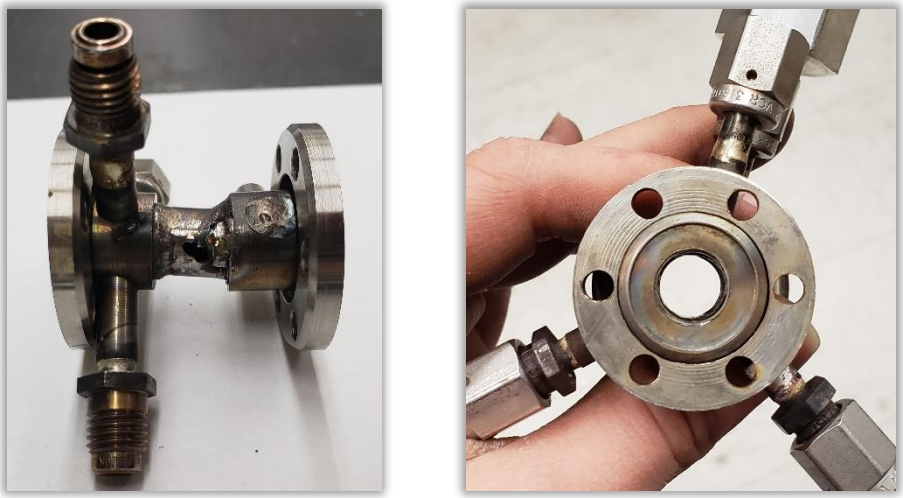

(a) (b)

Figure 5.11. Stainless-steel sleeve of test section (a) and inside of the sleeve (b).

The two 33.8 mm (1.33 inch) CF blank weld necks were adapted with 3.2 mm (1/8 inch) VCR socket welds to allow temperature and pressure measurements of the mixed gas directly at the inlet and outlet of the heat exchanger. The cross-sectional area remained constant throughout the test section (in both the stainless-steel tube and weld necks) as show in Figure 5.11(b) to reduce minor losses and the JT effect. Further details regarding the design and manufacturing of the CF weld necks can be found in the Appendix.

5.2.3. Helium Entrance and Exit

The helium and mixed gas enter and exit the test section through 3.2 mm (1/8 inch) VCR socket welds brazed to 33.8 mm (1.33 inch) CF flanges. To create the leak tight entrance and exit for the helium, a 3.2 mm (1/8 inch) VCR blank socket weld was adapted such that the tubing could run through the socket weld and be sealed by solder at the entrance (ensuring the helium flowed through the tube). To accomplish this, the blanket socket weld was drilled open for all but 1.27

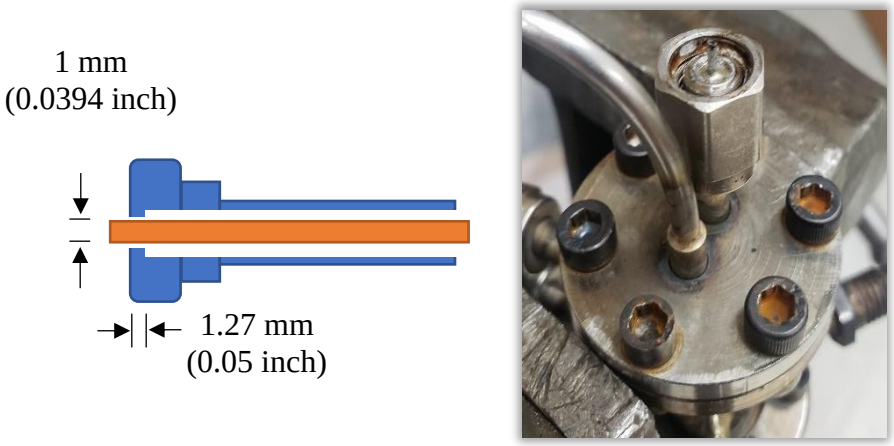

(a) (b)

Figure 5.12. Illustration (a) and picture (b) of adapted socket weld for helium entrance/exit.

mm (0.05”) of length at the entrance. A #60 drill bit was used to punch a small hole through the remaining length. A length of only 1.27 mm (0.05”) reduced the possibility of the drill bit breaking during this process.

The tube and entrance of the socket weld were then coated with Stay Clean soldering flux, tinned with Stay Brite #8 and slowly heated until the Stay Brite #8 solder liquefied to create the seal. This slow heating was accomplished by wrapping the socket weld with a large piece of copper material and applying the heat directly to the copper. An illustration of the adapted socket weld for the helium entrance and exit is shown in Figure 5.12 along with an actual picture of the connection. Finally, Figure 5.13 shows the fully assembled test section.

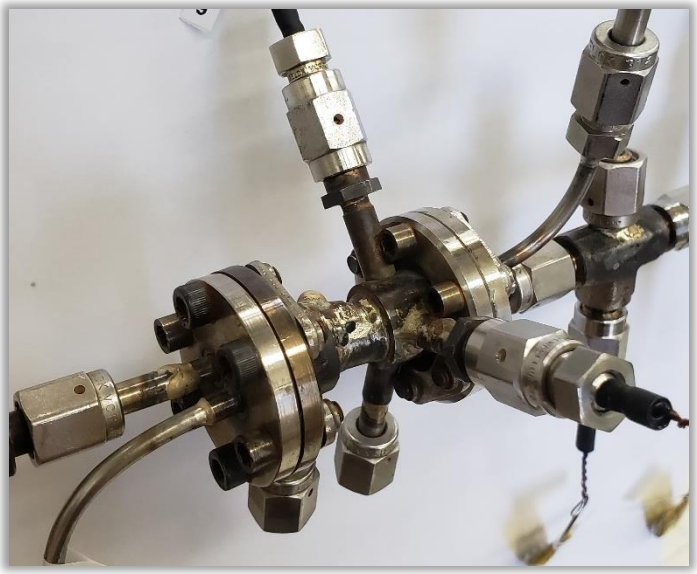

Figure 5.13. Fully assembled test section.

5.3. Experimental Test Facility

The test section is currently installed in a test facility capable of providing a range of gas compositions, flow rates and pressures. The test facility consists of a compressor station for the mixed gas, helium loop, vacuum chamber, and data acquisition. A picture of the facility is shown in Figure 5.14 (the compressor for the cold head, roughing pump for the vacuum chamber, and gas chromatograph (GC) are out of view). A schematic of the experimental facility is shown in Figure 5.15.

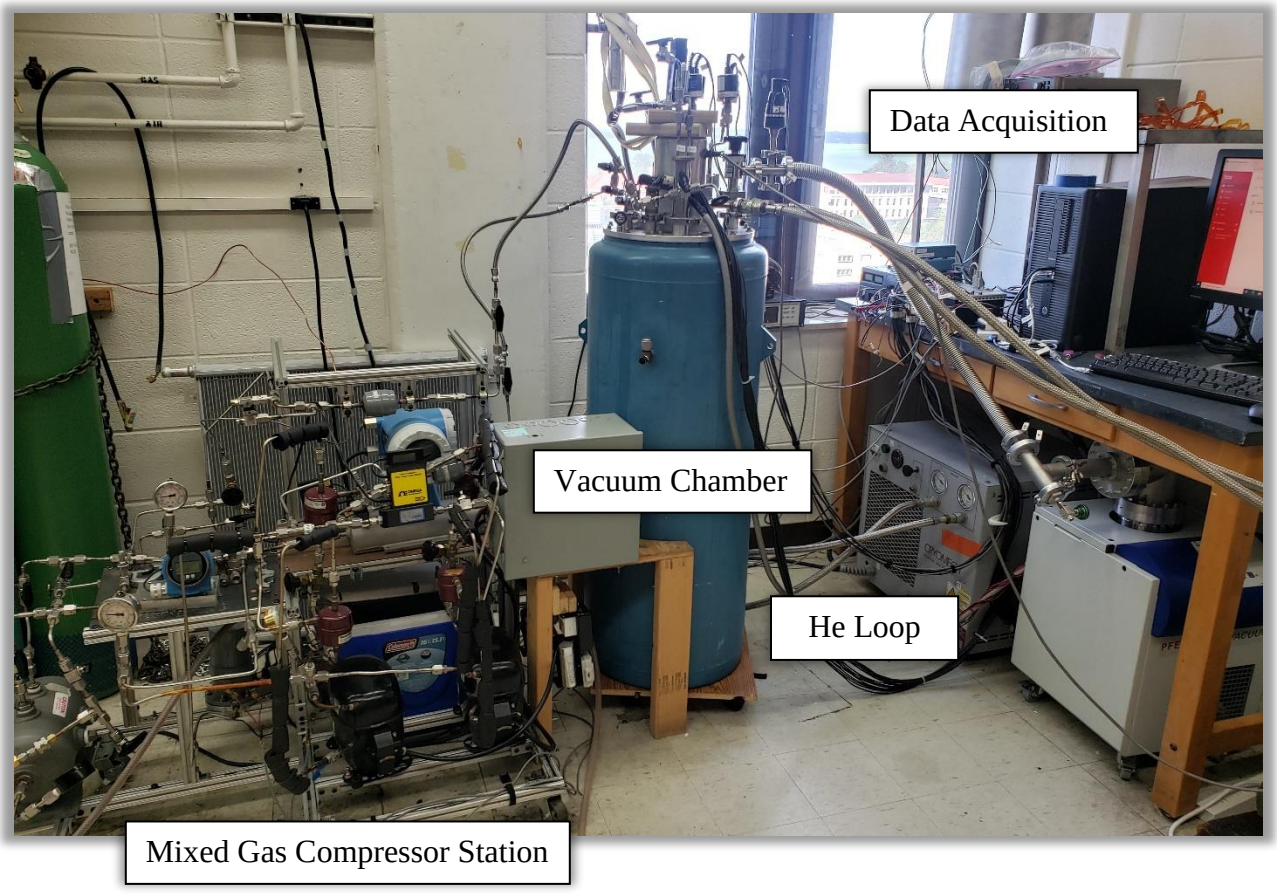

Figure 5.14. Photo of experimental test facility.

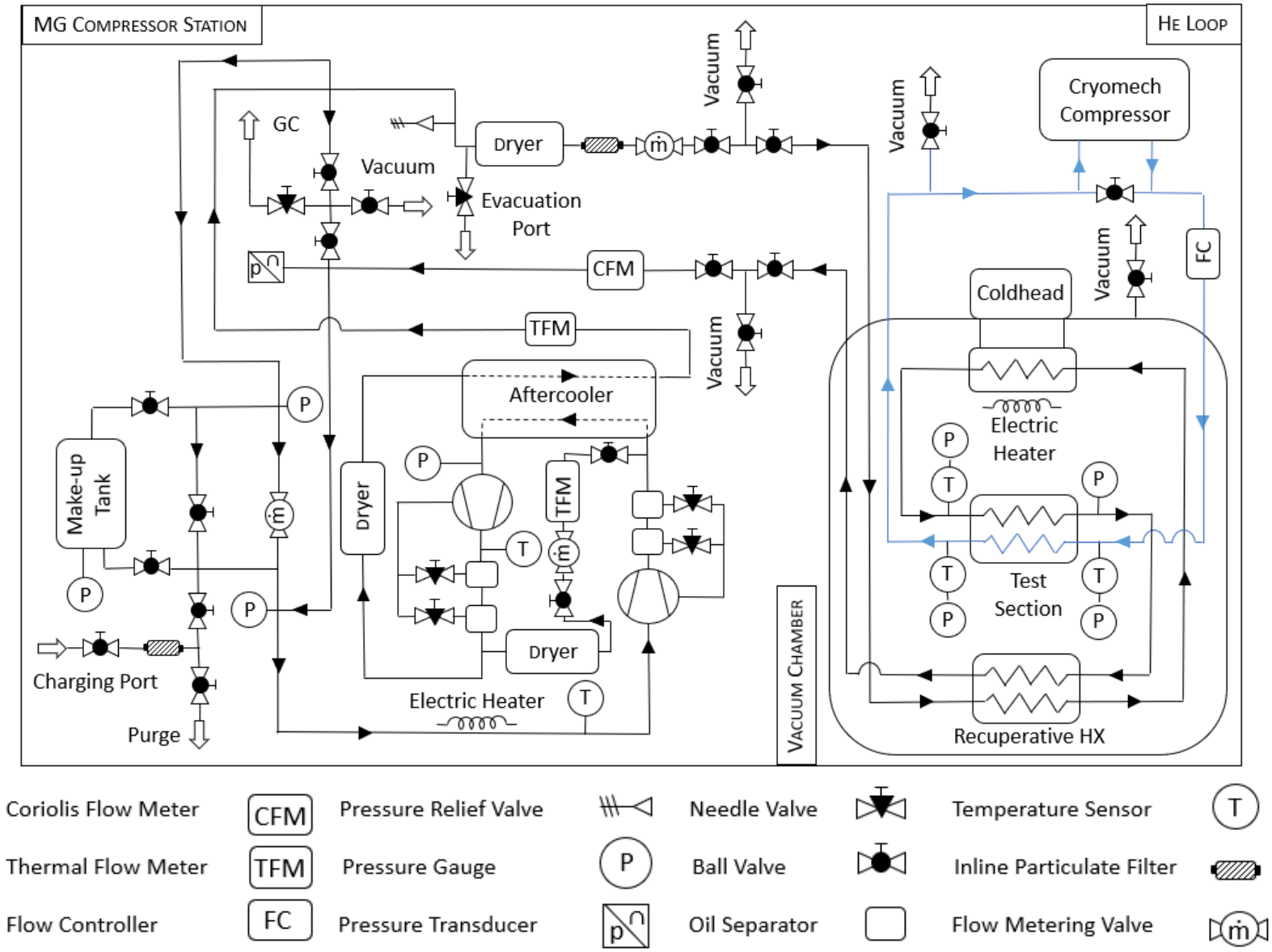

Figure 5.15. Schematic of experimental test facility.

5.3.1. Mixed Gas Compressor Station

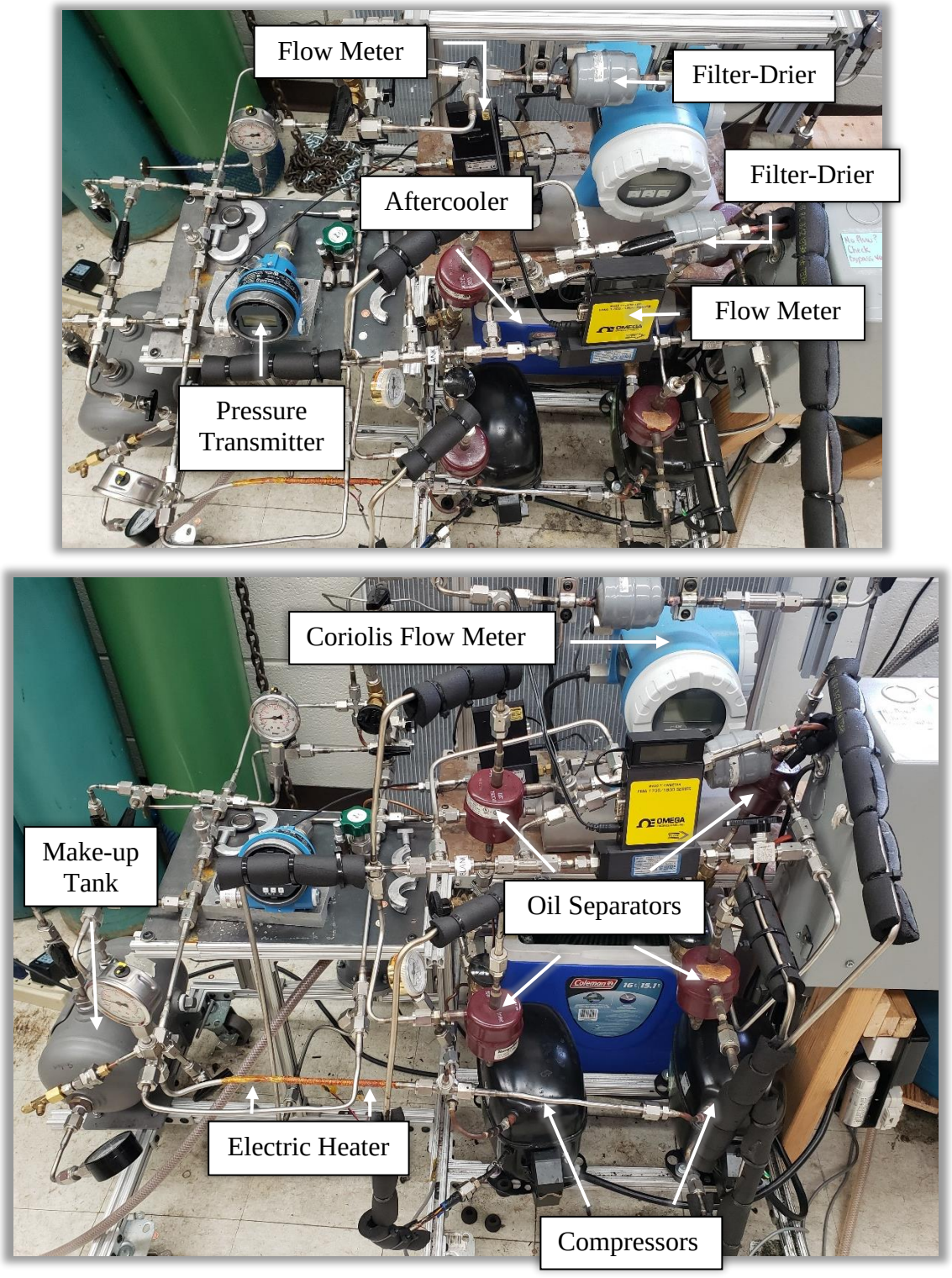

Figure 5.16. Photo of the mixed gas compressor station from the top (top) and front (bottom).

Component	Make and Model (Quantity)	Operating Range	Limitations of Operation
Aftercooler	In house (1)	NA	NA
Amp clamp	Sperry DSA600TRMS (1)	0-600A	NA
Box fan	Lasko (1)	NA	NA
Compressor [66]	Danfoss SC18CLX.2 (2)	13:1 with N_2	See Appendix 8.11.
Coriolis flow meter [67]	Endress & Hauser Promass 83A DN2 (1)	0.05 – 1.011 g/s [N_2]	P_{max} = 2496 kPa (362 psi) $253\ K \leq T \leq 333\ K$
Current source	Lake Shore Cryotronics Model 120 CS (1)	1 μA – 100 mA	NA
Filter-drier [68]	Catch-All C-R420 (1) C-052-S-HH (2)	NA	P_{max} = 4482 kPa (650 psi)
In-line particulate filter [69]	Swagelok SS-4F-VCR-7 (1)	7 Micron	P_{max} = 11307 – 20684 kPa (1640 – 3000 psi)
	Swagelok SS-4FW-15 (1)	15 Micron	P_{max} = 22615 – 41368 kPa (3280 – 6000 psi)
Make-up tank [70]	Manchester-Tank #304978 (1)	NA	$P_{\text{max.}}$ = 1379 kPa (200 psi) at 616 K
Mass flow meter [71]	Omega FMA 1828 (2)	0-50 L/min	$P_{\text{max.}}$ = 6998 kPa (1015 psi) $273\ K \leq T \leq 323\ K$
Mass flow metering valve [72]	Swagelok SS-SVR4 (1)	0-0.004 C_v	P_{max} = 13790 kPa (2000 psig) $250\ K \leq T \leq 477\ K$
	Swagelok SS-MGVR4 (2)	0-0.03 C_v	P_{max} = 6895 kPa (1000 psig) $250\ K \leq T \leq 477\ K$
Oil separator [73]	Temprite Model 320 (4)	NA	$P_{\text{max.}}$ = 4482 kPa (650 psi)
Power Supply	BK Precision 1685B (1)	1-60 VDC 0-5A	NA
	Hewlett Packard 6236B (1)	0-6V/0-20V 0-2.5A/0-0.5A	NA
Pressure relief valve [74]	Circle Valve Tech. 532B-2M (1)	3.5 - 1138 kPa (0.5 - 150 psig)	P_{max} = 2861 kPa (400 psig)
Pressure transmitter	Endress & Hauser Cerabar PMP51 (1)	0-1034 kPa (0-150 psia)	$P_{\text{max.}}$ = 2761 kPa (400.5 psi)
Roughing pump	Trivac D8A (1)	1E-4 -101 kPa (1E-3 – 760 Torr)	NA
Temperature sensor [75]	Lake Shore Cryotronics PT-100 (2)	14-873 K	NA

Table 5.3. List of equipment for mixed gas compressor station with operating range and limitations.

Figure 5.16 shows an overview of the equipment that comprises the mixed gas compressor station and Table 5.3 lists each component with its manufacturer, model, operating range, and limitations. The mixed gas compressor station was modified from the previous work done by Barraza [6] and Schwartz [76]. Modifications made to the system allowed for higher operating pressures and pressure ratios as well reduced the possibility of contamination of the mixed gas. With the increase in operating pressures and pressure ratios, additional updates were necessary to monitor the operation of the compressors to prevent burn-out. Modifications to the station included the following:

1. Removal of the suction and discharge tanks as well as the in-line pressure regulator and air-cooled aftercooler.
2. Installation of a water-cooled aftercooler to allow for higher operating pressures.
3. Replacement of the 4-gallon make-up tank with a smaller 1.1-gallon tank to conserve gas.
4. Installation of an in-line particulate filter at the charging port and a dryer and in-line particulate filter at the inlet of the test section to reduce possibility of contamination.
5. Reorientation of filter/dryer after compressors from horizontal to vertical to reduce possibility of contamination.
6. Installation of mass flow metering valve at the inlet to test section to increase control of mass flow rate of mixed gas to the test section.
7. Reconfiguration of the compressors from parallel flow to series.
8. Installation of a return line between the compressors including a dryer, mass flow metering valve and mass flow meter on the return line.

9. Installation of temperature sensors at the inlet of the first compressor and outlet of the second compressor, pressure gauge at intermediate pressure between the compressors, mass flow meter and amp clamp to monitor temperatures and pressures of the compressors as well as flow rate and current to the compressors.
10. Installation of a temperature sensor and an electronically controlled electric heater before the first compressor to ensure the mixed gas enters the compressor as a single-phase gas.

Let us trace the flow path through the compressor station. After leaving the test section, the mixed gas returns to the compressor station and passes through the Coriolis flow meter, which records the mass flow rate of the mixed gas in the test section. It mixes with the mixed gas running through the test section by-pass line and passes through the electric heater and in-stream PRT before entering the compressor. The electric heater and in-stream PRT are shown in Figure 5.17. The electric heater is composed of two Lake Shore Cryotronics nichrome wires wrapped around a 6.35 mm (0.25 inch) diameter stainless-steel. The nichrome wire has a diameter of 0.20 mm (0.008”) and fuse current of 2.5 A in air [77]. The wires are installed in parallel and have resistances

Figure 5.17. Photo of the electric heater and in-stream PRT before first compressor.

of 20 ohm. If operated at maximum power, the electric heater can provide 250 W to the gas mixture. A LabView program actively monitors the inlet temperature to the compressor and low-pressure of the mixed gas. The program calls REFPROP to estimate the dew point temperature of the mixture at the measured pressure and checks if the mixed gas is at least 15 K above the dew point. If the temperature of the mixed gas is within 15 K of the dew point, a Proportional-Integral-Derivative (PID) controller adjusts the power supplied to the heater until it is maintained 15 K above the dew point. As the pressure and temperature of the mixed gas entering the compressor is continuously changing until the gas mixture reaches a quasi-steady-state in the test section, the LabView program is continuously checking these values. Further details of the LabView program can be found in Appendix 8.9.

After leaving the first compressor, the mixed gas travels through two oil separators as shown in Figure 5.16. The oil separators filter oil out of the fluid stream and return it back to the compressor through needle valves. The needle valves are currently open ¼ turn each as recommended by Barraza [6] and Schwartz [76]. The mixed gas then travels through the aftercooler.

The aftercooler is composed of helically coiled copper tubes submerged in a water bath with lengths of approximately 7.8 m (308 inches) after both the first and second compressor. The inner and outer diameter of the tube is 3.05 mm (0.12 inch) and 4.76 mm (0.19 inch), respectively. The aftercooler is contained inside the blue Coleman cooler as shown in Figure 5.18. The water bath is chilled by cold water from the faucet running through another helically coiled copper pipe. This aftercooler allows the compressor station to achieve increased high-pressure values as previously this component limited the pressure that could be achieved during measurements by

Barraza [6]. The temperature of the mixed gas entering the test section has never been more than room temperature for a variety of gas mixtures and high pressures up to 1379 kPa (225 psia).

Figure 5.18. Photo of water-cooled aftercooler.

After leaving the aftercooler, the mixed gas stream continues through the second compressor and another set of oil separators. A PRT is externally mounted at the exit of the second compressor. The temperature at this point should not rise above 375 K for normal operation or 410 K for max operation. Further details of this are discussed in Appendix 8.11. At this point, the mixed gas either travels forward through a filter-drier and the aftercooler or it returns back to the second compressor through the compressor return line. The compressor return line is equipped with a filter-drier, medium mass flow metering valve and flow meter as shown in Figure 5.19. The mass flow metering value allows for the reduction of flow through the return line, which in turn drives a larger pressure differential in the compressor station. If the mass flow metering value is fully open, more than 50 L/min of fluid runs through the return line. The position of the valve is set in order to achieve the pressure desired from the compressor station and the flow rate desired for the test section. Changing the position of this valve will change both the high and low pressure of the system as well as the flow rate to the test section. This valve should not be closed so far as to drop the flow through the return line to less than 15 L/min. Flow from the return line and first

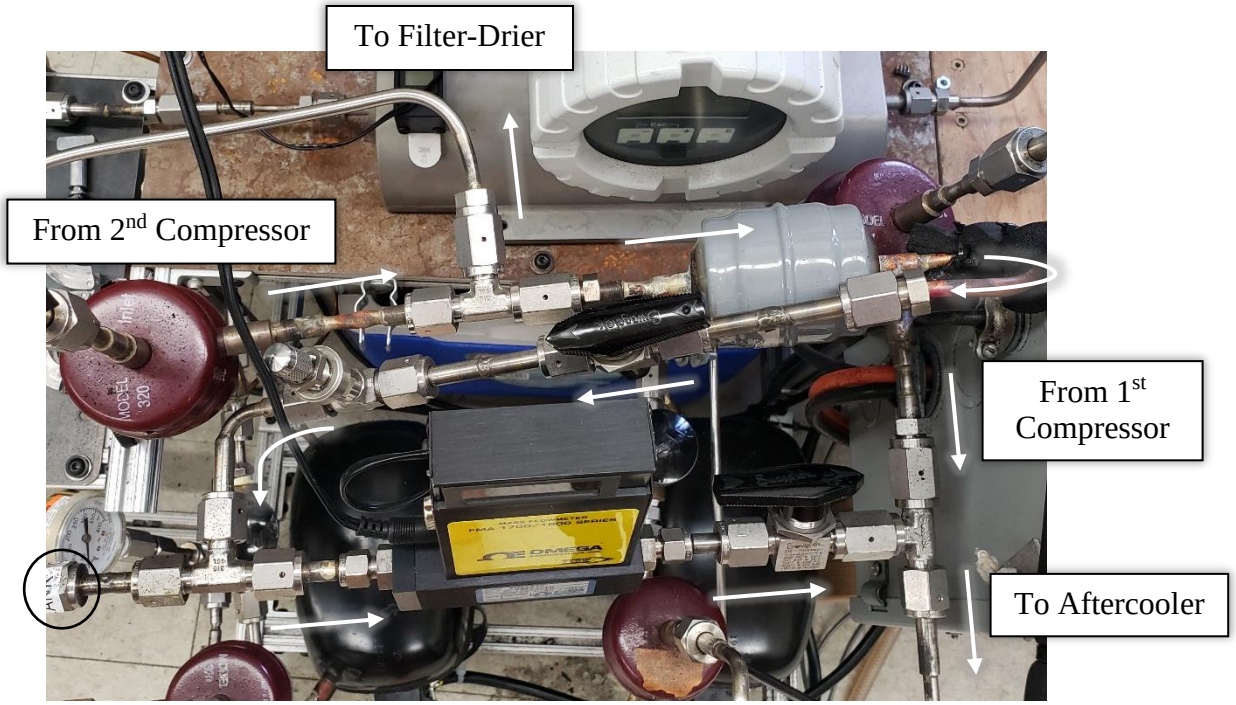

Figure 5.19. Photo of the compressor return line.

compressor come together to flow through the second compressor. If the flow rate through the second compressor is too low, it could burn-out. While this value is somewhat arbitrary, with at least 15 L/min of flow through the return line the second compressor has not experienced burn-out during testing thus far.

In Figure 5.19, two ball valves are also visible on the return line. This allows for removal of the flow meter for flushing with only minimal loses of mixed gas from the compressor station. If the flow meter malfunctions due to oil contamination, flush the flow meter with isopropyl alcohol using an air stream on the lab bench. Proper replacement of the in-line filter-dryer should prevent this from occurring. One further note - between the compressor return line and the line forward to the filter-drier and aftercooler there is a 6.35 mm (1/4 inch) VCR blank installed to prevent flow through a T-union. The blank is circled in Figure 5.19 and shown in Figure 5.20. This connection provides structural support for the compressor return line but does not allow flow.

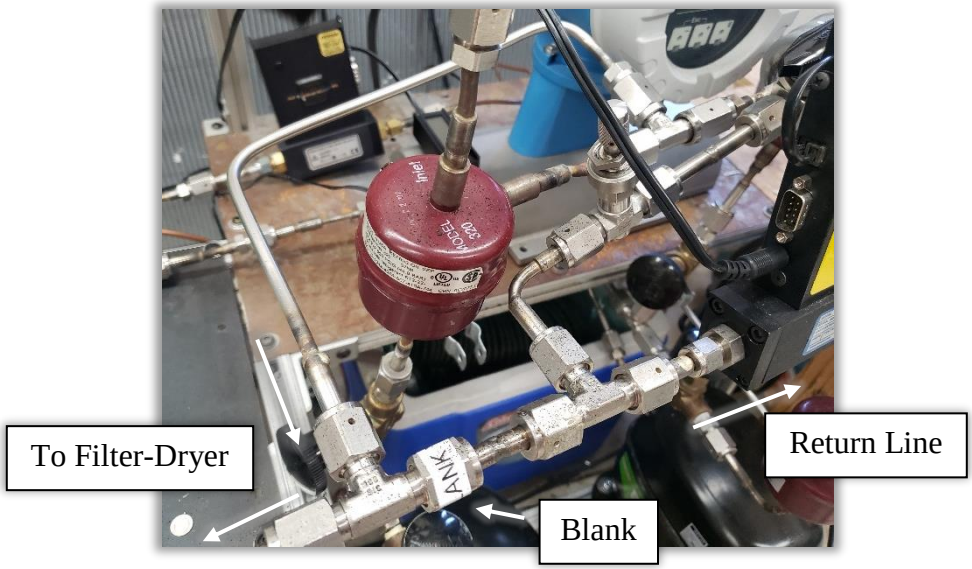

Figure 5.20. Photo of blank located within compressor station.

The mixed gas next goes through a filter-drier and then the aftercooler. Upon exiting the aftercooler, it passes through a flow meter. This thermal flow meter records the total rate of flow through the compressor station. When starting the station, more than 50 L/min of total flow travels through the compressor station. As the mixed gas cools in the test-section, some of the components begin to condense out of the mixture and the total flow rate in the compressor station decreases. The total flow rate should not drop below 15 L/min. Again, this is a somewhat arbitrary value but with 15 L/min of total flow the compressors have not experienced burn-out.

At this point, the mixed gas either travels to the test section or through the test section by-pass. The test section by-pass is shown in Figure 5.21. It contains a medium mass flow metering valve and multiple ball valves. The ball valves above the make-up tank are used to add or remove mass from the compressor station to keep the pressure in the test-section constant or reduce the temperature of the compressors. The other ball valve and medium mass flow metering valve shown in Figure 5.21 are installed in parallel to restrict flow through the test section by-pass. The ball valve is closed first and the metering valve is then slowly closed to further restrict the flow.

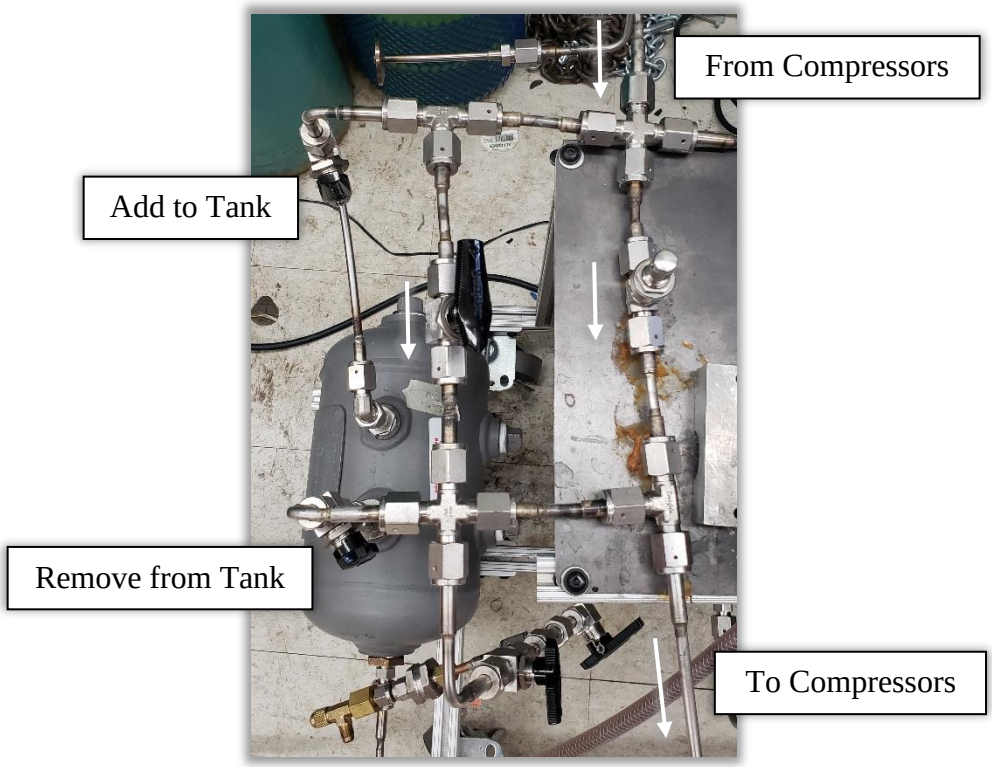

Figure 5.21. Photo of test section by-pass.

Opening and closing of these valves provide some control of high and low pressures of the system and the flow rate to the test section. The position to set for operation is dependent upon the desired operating conditions. These valves should not be closed so many turns as to prevent the required 15 L/min of flow passing through the compressor station.

If the mixed gas from the compressors does not travel through the test section by-pass, the mixed gas travels to the test section. On the way it passes through a filter-drier, in-line particulate filter and small mass flow metering valve as shown in Figure 5.22. The mass flow metering valve can be used to fine tune the mass flow rate to the test section.

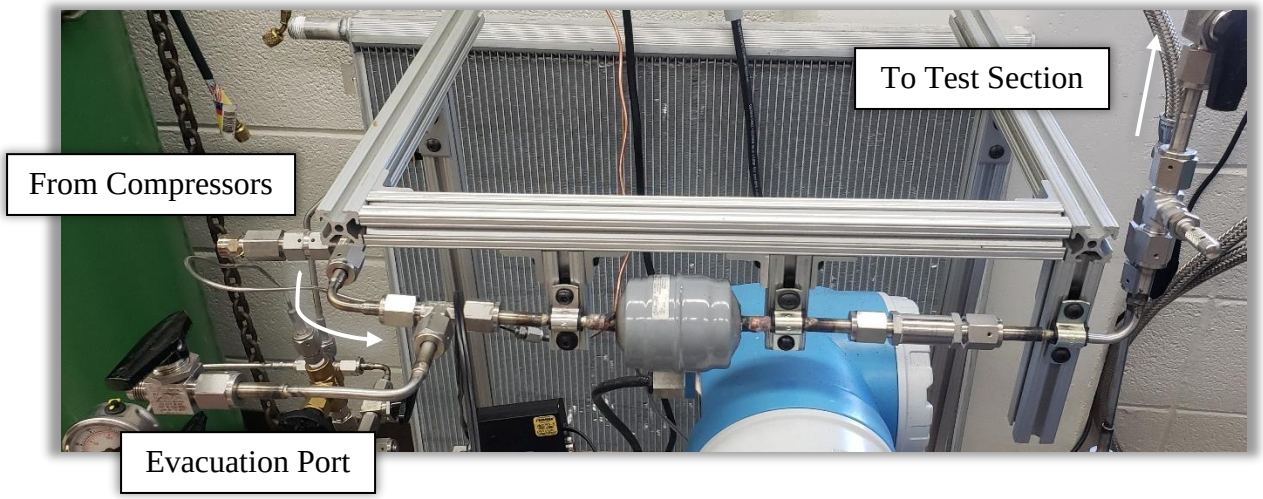

Figure 5.22. Photo of equipment directly on path to the test section.

There are a few additional components on the mixed gas compressor station that have yet to be mentioned – the evacuation port, charging port and union for the GC and roughing pump. The evacuation port is shown in Figure 5.22 and is used to easily attach a plastic hose and evacuate the mixed gas to the fume hood. The charging port is shown in Figure 5.23 and is used to fill the compressor station with mixed gas. Once the desired composition of the mixed gas is known, the compressor station is filled to the appropriate pressure for each component (i.e. the partial pressure

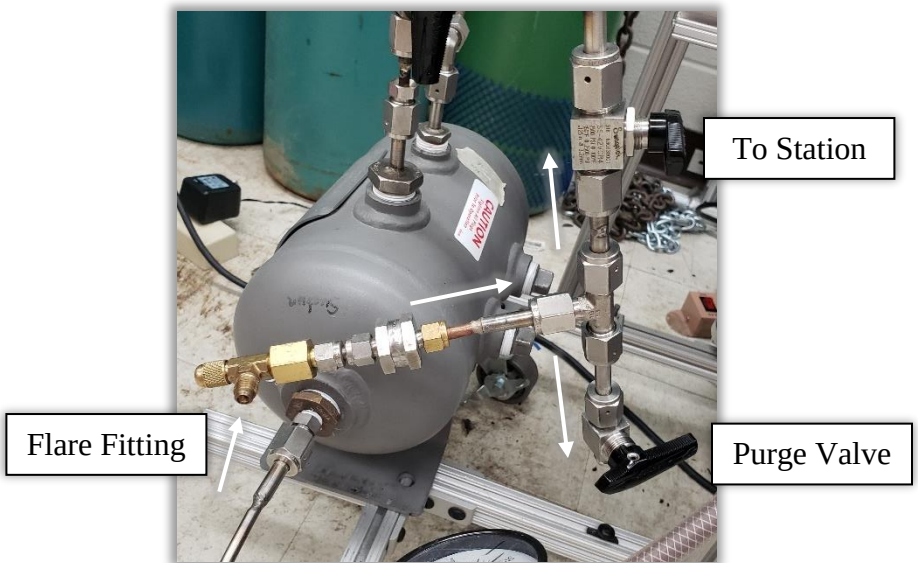

Figure 5.23. Photo of charging port.

that corresponds to the molar fraction for each component) using the electronic pressure transmitter. This can be done by connecting the yellow jacket hose to the flare fitting. All the pressure regulators on the tanks in the lab are also equipped with flare fittings for easy exchange of gases. The charging port is equipped with an in-line particulate filter and purge valve. Before releasing the gas into the station, air from the yellow jacket line and charging port should be purged from the connections using the purge valve. Gases should be removed and added to the station at a controlled rate of approximately 69 kPa/min (10 psi/min) to prevent displacement of oil from the compressors to undesired locations in the test facility [76].

The union for the GC and roughing pump is a five-way 6.35 mm (1/4 inch) VCR union (with only 4 of the connections currently being utilized). It is shown in Figure 5.24. This union allows for sampling of the mixed gas to the GC from the high- or low-pressure side of the compressor station through opening of one of the two ball valves shown. Only one of these ball

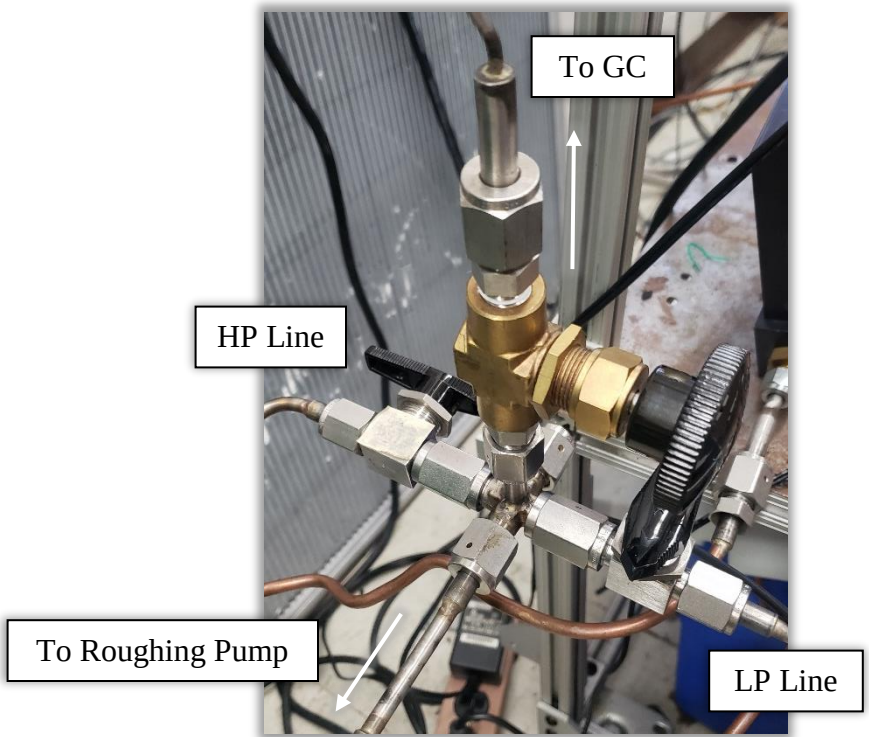

Figure 5.24. Photo of union for GC and vacuum.

valves should be open during operation. This union also serves as a connection to the roughing pump. Before filling the station with mixed gas, the station should be flushed at least three times with helium and then pumped to remove any residual gas remaining in the system.

5.3.2. Helium Loop

(a) (b) (c)

Figure 5.25. Photo of equipment for the helium loop – compressor package (a), cryogenic hose (b) and mass flow controller (c).

Component	Make and Model (Quantity)	Operating Range	Limitations
Compressor package	Cryomech Inc. CP820 (1)	NA	NA
Cryogenic hose	P5400-S5-8 (2)	NA	NA
DAQ device [101]	National Instruments USB-6008 (1)	0-5 V	NA
Mass flow controller [100]	Omega FMA-5516A (1)	0-2 L/min [N_2]	P_{max} = 6998 kPa (1015 psi) ΔP_{max} = 345 kPa (50 psi) ΔP_{min} = 7.31 kPa (1.06 psi)
Power Supply	BK Precision 1685B	1-60 VDC 0-5A	NA

Table 5.4. List of equipment for the helium loop with operating range and limitations.

Figure 5.25 consists of three photos that make up the equipment for the helium loop – the compressor package (a), cryogenic hoses (b) and mass flow controller (c). Table 5.4 lists each component with its manufacturer, model, operating range, and limitations. The Cryomech

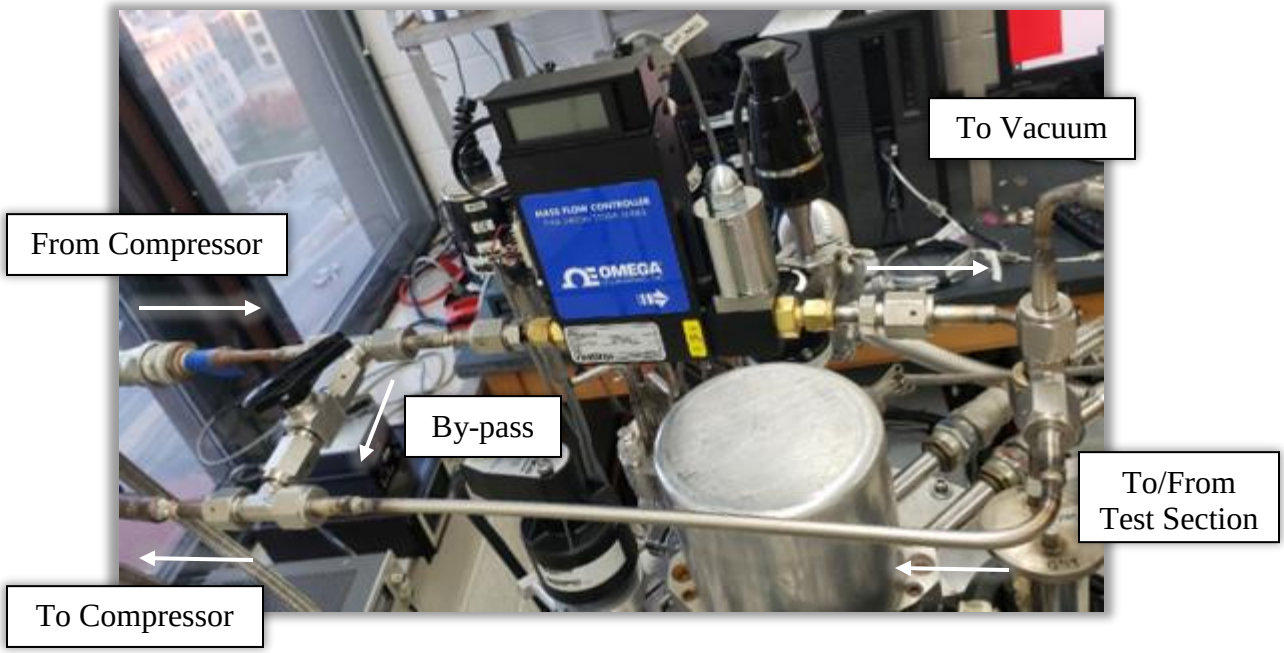

Figure 5.26. By-pass on helium loop.

compressor package provides the flow rate for the helium to the test section and can provide a much larger flow rate than the targeted operating flow rate of 85 m/s (0.03 g/s, 1 L/min). Therefore, a bypass line is installed in the helium loop to direct most of the flow back to the compressors without going through the test section. The ball valve shown in Figure 5.26 is used to restrict the flow in the bypass line enough to promote a low amount of flow to the test section. Upon start-up, the ball valve is closed until a pressure differential of approximately 345 kPa (50 psi) is achieved. The compressor package automatic shut-off limits operation for larger pressure differentials. For current testing conditions, the Cryomech compressor package is charged with helium to 689 kPa (100 psi), resulting in high and low pressures for the helium loop of approximately 862 kPa (125 psi) and 517 kPa (75 psi).

The mass flow controller is powered by a BK Precision power supply and electronically opens and closes a valve inside the device to maintain a constant flow rate. The setpoint between

0-2 L/min is controlled remotely by a 0-5 V signal excitation from a National Instruments DAQ device.

5.3.3. Vacuum Chamber

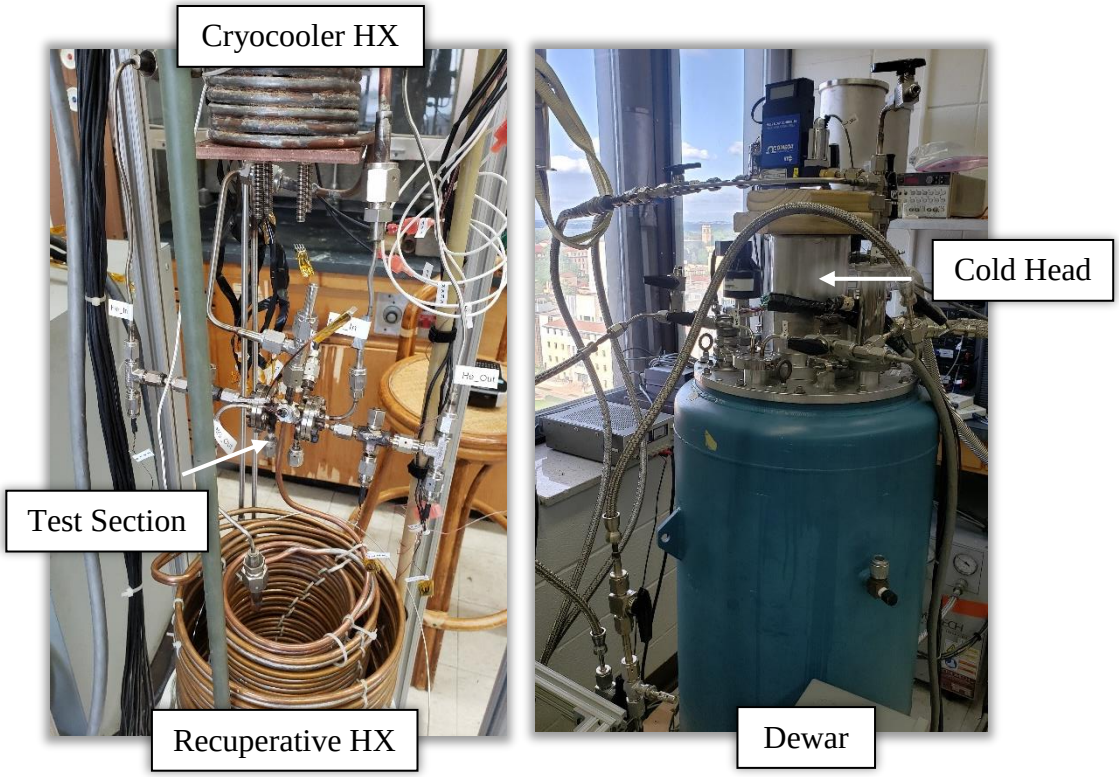

(a) (b)

Figure 5.27. Photos of vacuum chamber – internal (a) and external (b).

Figure 5.27 shows an overview of the vacuum chamber – internal (a) and external (b). Table 5.5 lists the components of the vacuum chamber and supporting equipment with manufacturer, model, operating ranges and limitations. The vacuum chamber was adapted from previous work done by Barraza [6] and Schwartz [76]. Modifications allowed for the second fluid stream to enter and exit the chamber as well as temperature and pressure measurements for the second stream.

	Component	Make and Model (Quantity)	Operating Range	Limitations
Internal	Cartridge heater [78]	Lake Shore HTR-25-100 (2)	0-100 W	NA
	Cryocooler HX	In-house [6] (1)	NA	NA
	Indium Gasket	In-house [6] (1)	NA	NA
	Isothermal shield	In-house [6] (1)	NA	NA
	MLI	NA	NA	NA
	Recuperative HX	In-house [6] (1)	NA	NA
	Temperature sensor [75]	Lake Shore Cryotronics PT-103/111 (6)	14-873 K	NA
External	Cold cathode gauge and controller [79]	MKS HPS Products Series 423 I-MAG (1)	1E-12 – 1E-3 kPa (1E-11 – 1E-2 Torr)	NA
		MKS HPS Products Series 943 (1)	1E-11 – 1E-3 kPa (1E-10 – 1E-2 Torr)	NA
	Cold head [6]	Cryomech Inc. Gifford McMahon AL-125 (1)	0-160W for 27-160K	NA
	Compressor package	Cryomech Inc. CP640 (1)	NA	NA
	Current source	Lake Shore Cryotronics Model 120CS (2)	1 μA – 100 mA	NA
	Power Supply	BK Precision 1685B (1)	1-60 VDC 0-5A	NA
		Extech Instruments 382213 (1)	0-30 VDC 0-3 A	NA
	Pressure transducer [80]	Setra Model 206 (2)	0-793 kPa (115 psi)	P_{max} = 2172 kPa (315 psi)
		Setra Model 206 (2)	0-3661 kPa (515 psi)	P_{max} = 6998 kPa (1015 psi)
	Roughing pump	Varian SD-90 (1)	1E-4 -101 kPa (1E-3 – 760 Torr)	NA
	Turbo pump	Pfeiffer Vacuum TSU-281 (1)	1E-7 – 1E-4 kPa (7.5E-7 – 1E-3 Torr)	NA
	Vacuum gauge and controller	Leybold TR 901 (1)	1E-4 -101 kPa (1E-3 - 760 Torr)	NA
		Inficon IG3 (1)	1E-4 -101 kPa (1E-3 - 760 Torr)	NA
	Water filter	Aqua-Pure AP101T (1)	NA	NA
	Vacuum Dewar	Precision Cryogenic Systems Inc. NA (1)	NA	NA

Table 5.5. Internal and external components of vacuum chamber and supporting equipment.

The mixed gas and helium enter and exit the vacuum chamber through the connections shown in Figure 5.28. One may notice in this photo that there are many ball valves on the entrance and exit of the mixed gas line. The entire network from the mixed gas station to the vacuum chamber is shown in Figure 5.27(b). These ball valves allow the mixed gas compressor station and vacuum chamber to be completely detached from each other and the vacuum chamber can be opened (for updates or repairs) with minimal loss of gas. Additional ball valves provide locations for a vacuum pump attachment to remove air from the lines before the mixed gas is reintroduced. The helium line can also be detached from the helium compressor package through removal of the Aeroquip fittings on the cryogenic hoses. Again, this allows the vacuum chamber to be opened with minimal loss of the helium. There is also a ball valve located on the helium loop to provide a location for a vacuum pump attachment to remove air and water vapor when needed.

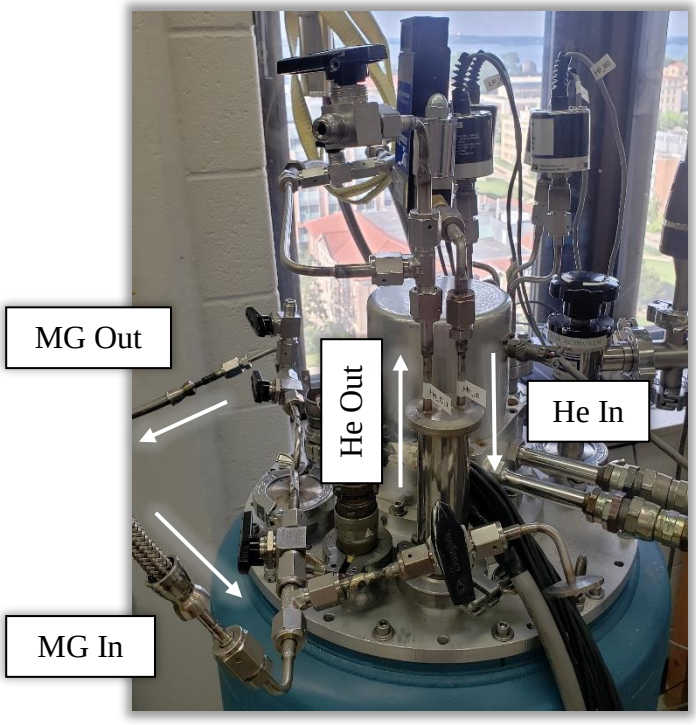

Figure 5.28. Photo of inlet and exit for helium and mixed gas into the vacuum chamber.

The mixed gas enters the vacuum chamber at room temperature and is cooled to the targeted test condition (between 110-300 K) in two stages. First, the gas mixture is precooled using a recuperative heat exchanger shown in Figure 5.27(a) where the gas mixture exiting the vacuum chamber removes thermal energy from the gas mixture entering the chamber. Then, the gas mixture flows through the cryocooler heat exchanger were the Cryomech cold head removes the necessary thermal energy to cool the gas mixture to its target temperature.

The cold head and its attachment to the cryocooler heat exchanger is shown Figure 5.29. An indium gasket crushed between the cold head and cryocooler heat exchanger increases the thermal contact and thus the cooling power of the cryocooler heat exchanger. The cold head of the cryocooler is equipped with two Lake Shore cartridge heaters powered by a BK Precision power supply to control the temperature of the gas mixture entering the test section. Further details of the design and build of the recuperative and cryocooler heat exchanger can be found in Barraza [6] and Schwartz [76].

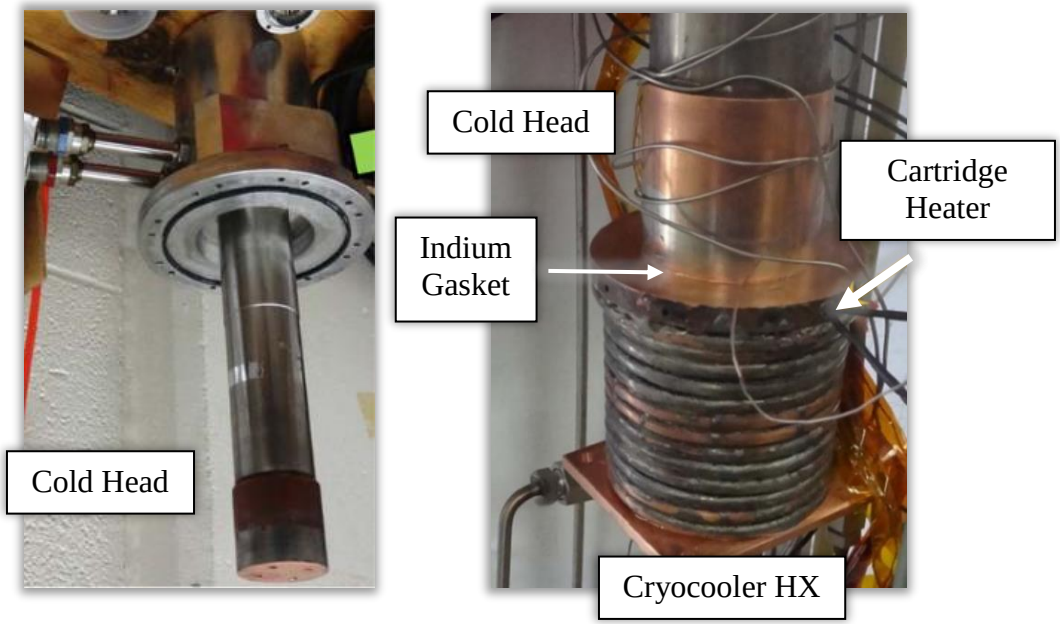

(a) (b)

Figure 5.29. Photo of Cryomech cold head (a) and connection of cold head to cryocooler heat exchanger (b) [6].

As shown in the experimental test facility schematic in Figure 5.15, the mixed gas travels through the recuperative heat exchanger, cryocooler heat exchanger, test section and back through the recuperative heat exchanger before exiting the vacuum chamber. The helium gas enters the vacuum chamber at room temperature, is cooled as it exchanges energy with the mixed gas stream in the test section and then exits the vacuum chamber. An image of the test section where the fluid streams exchange energy is shown in Figure 5.30.

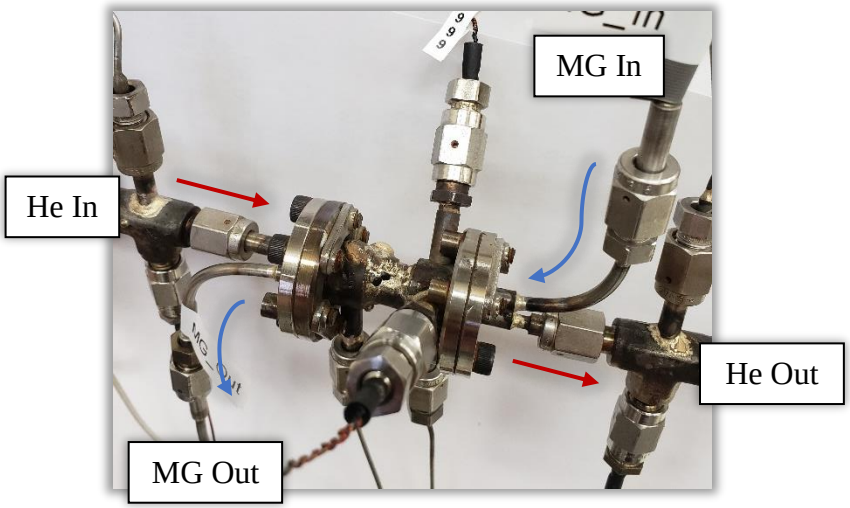

Figure 5.30. Photo of test section.

Pressure taps for the helium are connected to the 6.35 mm (1/4 inch) VCR union crosses before and after the helium passes through the test section. The pressure tap for the inlet of the helium stream is shown in Figure 5.31(a). The pressure tap for the outlet is fashioned in the same manner on the other side of the test section. Pressure taps for the mixed gas stream are located within the shell of the test section both before and after the heat exchanger as shown in Figure 5.31(b). The pressure taps for both the helium and mixed gas are connected to Setra pressure transducers on the outside of the vacuum chamber. The Setra pressure transducers are powered by an Extech Instruments power supply.

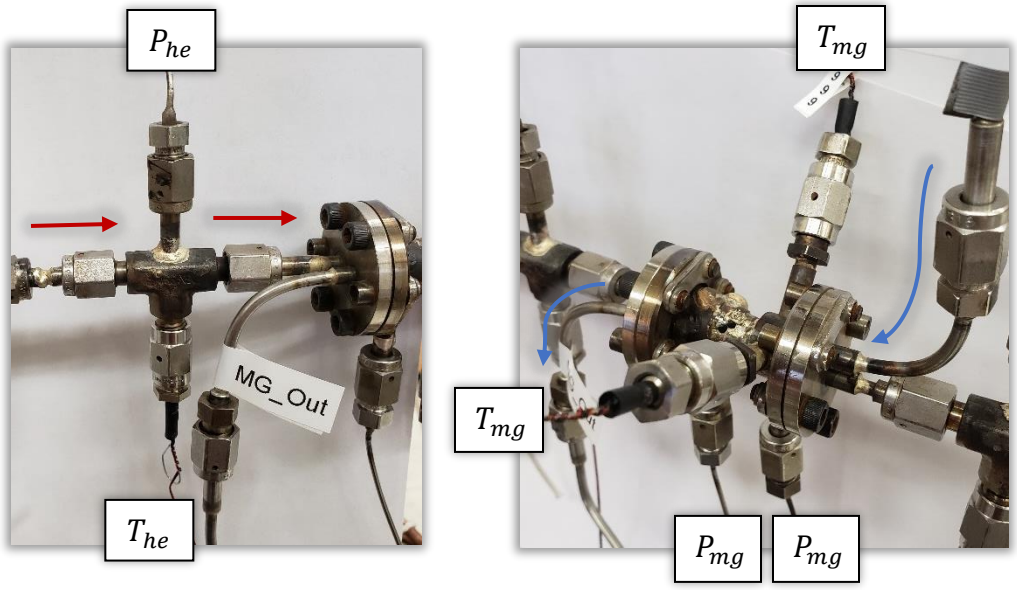

Figure 5.31. Photo of temperature and pressure measurements for the test section – helium inlet (a) and mixed gas (b).

Temperature sensors for the helium are located in-stream inside 6.35 mm (1/4 inch) VCR union tees and crosses before and after the helium passes through the test section. The temperature sensors for the inlet are shown in Figure 5.31(a). The temperature sensors for the outlet are positioned in like manner on the other side of the test section. Temperature sensors for the mixed gas are located in-stream within the shell before the heat exchanger as shown in Figure 5.31(b). The temperature sensors are Lake Shore Cryotronics PT-111 and PT-103 platinum resistance thermometers (PRTs) in a 4-wire configuration. The PRTs are supplied with a continuous excitation of 1 mA by a Lake Shore Cryotronics current source. The details associated with constructing the in-stream temperature sensors are presented in Appendix 8.10.

During operation, the test section is surrounded by multilayer insulation (MLI) and an isothermal shield as shown in Figure 5.32. The isothermal copper shield is connected to the cryocooler heat exchanger and is assumed to achieve the cryocooler temperature. It is coated with an MLI layer at its inner and outer surface to minimize its emissivity. In between the test section and isothermal shield are 4 layers of MLI with Dacron netting in-between to reduce the heat transfer by conduction through contact of the MLI.

Figure 5.32. Photo of MLI and isothermal shield.

The vacuum chamber is maintained at a vacuum pressure of $1x10^{-5}$ Torr to minimize convective losses by a Varian roughing pump and Pfeiffer turbo pump shown in Figure 5.33. The chamber pressure is monitored by an Inficon vacuum controller and Leybold vacuum gauge while it is in a low vacuum environment and an MKS HPS Products cold cathode gauge and controller when a high vacuum environment has been achieved. The monitoring equipment are shown in Figure 5.34.

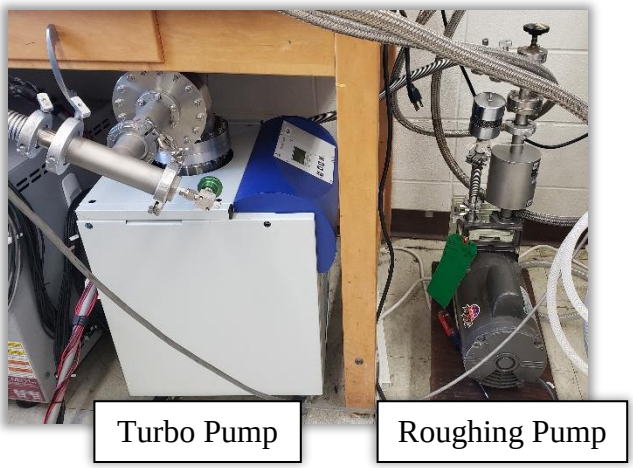

Figure 5.34. Photo of turbo and roughing pumps.

(a) (b) (c)

Figure 5.33. Photos of vacuum and cold cathode controllers (a), cold cathode gauge (b), and Pirani vacuum gauge (c).

As discussed previously, a Cryomech cold head is used to reduce the temperature of the mixed gas to the target operating temperature. The Cryomech compressor package shown in Figure 5.35(b) supplies the helium flow for the operation of the cold head. The compressor package is capable of providing more cooling power than is necessary for the target operating conditions. For current operating conditions, it is only charged to 862 kPa (125 psi). This provides enough cooling for the mixed gas to reach the target operating temperature. The compressor package is water-cooled. The water-cooling system from the lab faucet is shown in Figure 5.35(c). It includes an

(a) (b) (c)

Figure 5.35. Photos of the cold head (a), compressor package (b) and water-cooling system for compressor package (c).

Aqua-pure filtration system to reduce fouling of the compressor package. Further details of the water-cooling system can be found in Schwartz [76].

5.3.4. Data Acquisition

Figure 5.36 shows the components of the data acquisition system including (a) the data logger and (b) the gas chromatograph (GC). Table 5.6 lists the components of the system and supporting equipment with manufacturer, model, operating ranges and other limitations. The data

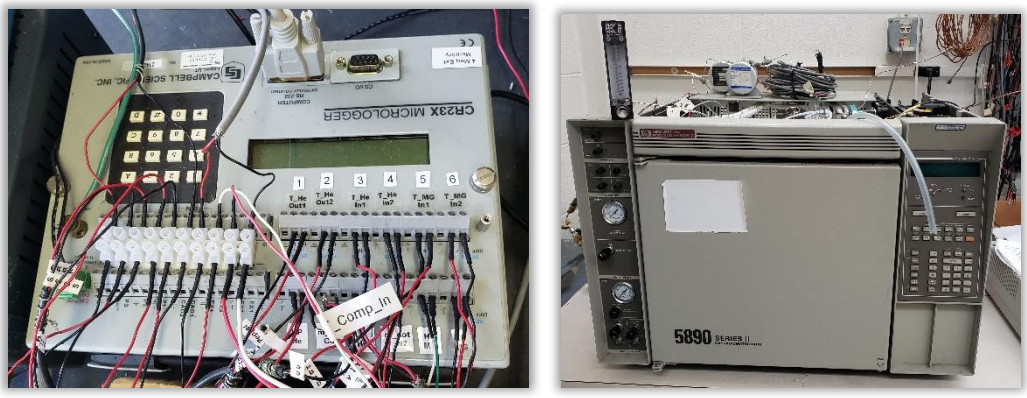

(a) (b)

Figure 5.36. Photos of components for the data acquisition system - the data logger (a) and GC (b).

Component	Make and Model (Quantity)	Operating Range	Limitations
Data Logger	Campbell Scientific Micrologger CR23X (1)	NA	NA
Filter-drier	Parker LLD – 083S (1)	NA	P_{max} = 4482 kPa (650 psi)
GC	Hewlett Packard 5890 Series II (1)	NA	NA
GC column	Alltech HayeSep D 20ft	NA	T_{max} = 563 K (290 ^{o}C)
Hydrocarbon trap	Alltech Associates Inc. Hydrocarbon Trap (1)	NA	P_{max} = 1827 kPa (265 psi)
In-line particulate filter	NURPO NA (1)	NA	NA
Moisture trap	Alltech Associates Inc. Hydro-Purge II (1)	< 1 ppm	P_{max} = 793 kPa (115 psi)
Oxygen trap	Alltech Associates Inc. Oxy-Purge N (1)	< 30 ppb	P_{max} = 1827 kPa (265 psi)
Pressure regulator	Spectra Gases 44-2862-241-131 (1)	NA	$P_{max,out}$ = 793 kPa (115 psi)

Table 5.6. Equipment for data acquisition system.

acquisition system was adapted from previous work done by Barraza [6] and Schwartz [76]. Modifications were made which reduced the possibility of contamination to the GC and allowed for measurements of the temperatures, pressures, and mass flow rate of the secondary fluid stream. A Campbell Scientific Micrologger shown in Figure 5.36(a) is used as the data acquisition system in this test facility. The DAQ measures the voltage across the temperature sensors, pressure transducers, Coriolis mass flow meter and mass flow controller. The data logger measures the voltage three times every second and records the average of these values.

The composition of the circulating mixture composition is monitored using a gas chromatograph equipped with a thermal conductivity detector (TCD) shown in Figure 5.36(b). When the mixture is two-phase in the test section, some of the components of the mixture will

preferentially condense and this results in a change in the composition of the circulating mixture as the experiment progresses.

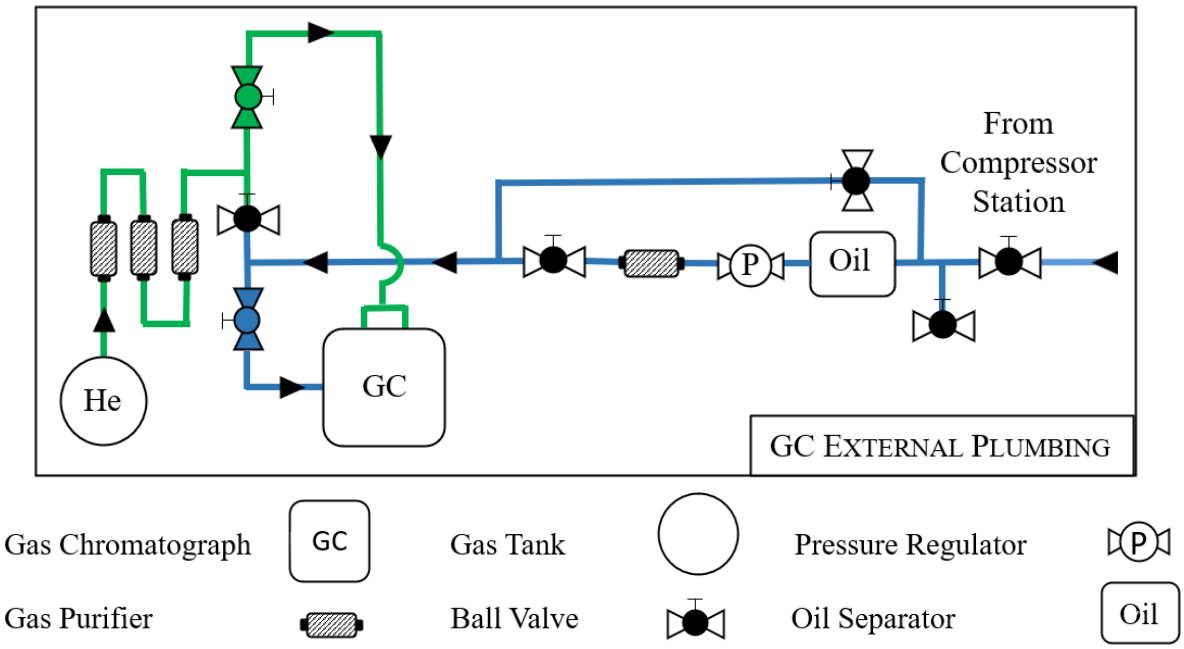

Figure 5.37. Schematic of external plumbing for GC.

A schematic of the external plumbing to the GC is shown in Figure 5.37. The gas mixture is sampled at room temperature from either the low- or high-pressure side of the system and passes through a filter-drier, pressure regulator and in-line particulate filter on its way to the GC as shown in Figure 5.38. The filter-drier and in-line particulate filter remove moisture and contamination from the mixed gas before entering the GC. The pressure regulator is used to set the sample gas flow rate into the GC.

Figure 5.39. Photo of mixed gas sampling line to the GC.

Figure 5.38. Photos of moisture, hydrocarbon and oxygen traps.

The carrier and reference gas for the GC is high-purity helium. Before the helium enters the GC, it passes through moisture, hydrocarbon and oxygen traps as shown in Figure 5.39. Moisture, hydrocarbons and oxygen from the carrier gas stream and line can cause noisy baselines and extraneous peaks in the GC data. The traps reduce contamination of the carrier gas stream and provide a steady baseline for data collection.

The mixed gas and helium both flow into the GC for the gas mixture analysis, as shown in the schematic in Figure 5.37. The helium is split into two streams – a reference stream and carrier stream (that mixes with the gas mixture sample). When the gas mixture is injected into the GC, the carrier gas (helium) pushes the gas mixture through a long internal column within the oven as

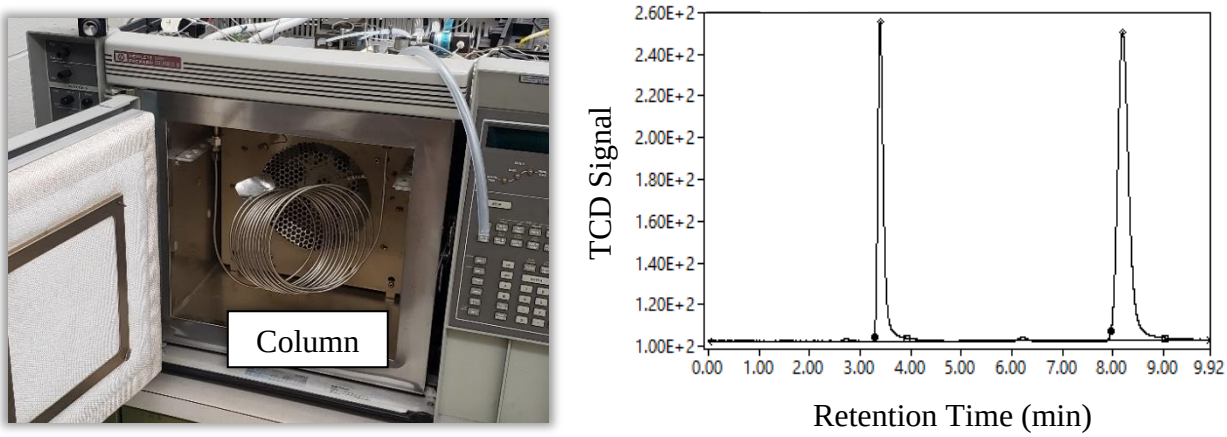

(a) (b)

Figure 5.40. Photo of the GC oven and column (a) and sample gas chromatogram (b).

shown in Figure 5.40(a). The column currently installed is a packed column, meaning it is packed with finely divided inert material coated with a stationary phase (chemical substance). The amount each component of the gas mixture is attracted to the stationary phase differs and thus the components will separate in time as they move through the column. After exiting the column, the carrier stream (helium and separated gas mixture) passes through the TCD. The TCD measures the difference in thermal conductivity between the reference stream (helium) and carrier stream. The detector response is plotted as a function of time to generate a peak area for each component on a gas chromatogram. An example gas chromatogram is shown in Figure 5.40(b) for a two-component mixture.

5.3.5. Operating Range for Experimental Testing

Parameter	Operating Range
Inlet pressure of mixed gas, $P_{mg,in}$	0-793 kPa (115 psi)
Inlet pressure of helium, $P_{he,in}$	0-1034 kPa (150 psi)
Inlet temperature of mixed gas, $T_{mg,in}$	110-300 K
Inlet temperature of helium, $T_{he,in}$	Uncontrolled
Flow rate of mixed gas, $\dot{m}_{mg}$	0.05 g/s – $\dot{m}_{max}$
Flow rate of helium, $\dot{m}_{he}$	0-0.07 g/s (2.85 L/min)
Gas mixture composition, X_i	P_{sat}

Table 5.7. Current operating range for experimental testing.

The experimental test facility was designed to provide a range of operating pressures, temperatures, and flow rates for a variety of gas mixtures. The relevant pressure and temperature limitations of each device were listed in Table 5.3, Table 5.4, Table 5.5, and Table 5.6 in the preceding sections. It is important to note that, in general, the operating conditions for testing are currently limited by the test section and not the experimental test facility. If the test section is updated, a larger span of operating conditions can be achieved with this facility.

The inlet pressure of the mixed gas in the test section is currently limited by the Setra pressure transducers, in-stream temperature sensors and maximum operating conditions of the compressors. The Setra pressure transducers for the mixed gas only have an operating range of 0-793 kPa (115 psi). These pressure transducers can easily be replaced with pressure transducers of a larger operating range if testing with higher pressures is desired. However, the pressure of the mixed gas in the test section is limited by the in-stream temperature sensors. The epoxy to stainless-steel bond of the in-stream temperature sensors fails at pressures of approximately 1034 kPa (150 psi) and thus both streams of the test section cannot currently be pressurized above this. This failure was seen on multiple occasions with the current in-stream temperature sensors designed as described in Appendix 8.10. For higher operating pressures, an in-stream temperature sensor utilizing an electrical feedthrough is required.

Another limiting factor for the inlet pressure for the mixed gas is the maximum operating conditions for the compressors. The maximum operating conditions (and therefore maximum inlet pressure) are dependent upon the working fluid. In-house testing of the compressors was performed for a sample of pure gases and gas mixtures by monitoring the running current and compressor outlet temperatures to determine allowable operating conditions. For the gases tested, the maximum allowable charge pressure and high pressure of the mixed gas compressor station are 689 kPa (100 psi) and 1034 kPa (150 psi), respectively. The maximum allowable pressure ratio and running current for each compressor are 2.5 and 10.5 Amps, respectively. These results are used to guide maximum operating conditions during operation of the test section. Details of the compressor testing and results can be found in Appendix 8.11.

The inlet temperature range of the mixed gas in the test section is 110-300 K. As mentioned previously, the Cryomech cold head is capable of providing enough cooling power to reach the desired temperatures for the targeted operating conditions. The inlet temperature of the helium in the test section is uncontrolled and thus, due to axial conduction, the inlet temperature is dependent upon the steady-state temperature of the test section.

The flow rate of the helium is currently limited by the Omega mass flow controller. The mass flow controller has a range of 0-0.32 g/s (2 L/min) for nitrogen. This corresponds to an approximate flow range of 0-0.07 g/s (2.85 L/min) for the helium. The flow rate of the mixed gas is monitored by a Coriolis flow meter. The minimum flow rate that the Coriolis flow meter is capable of measuring is 0.05 g/s. The maximum measurable flow rate is dependent upon the density of the gas, as given by:

$$\dot{m}_{max} = \frac{100\ \left(\frac{kg}{hr}\right) \cdot \rho_{mg}}{32\ \left(\frac{kg}{m^3}\right)} \tag{5.3}$$

where the values are chosen based on the make and model of the Coriolis flow meter [67]. Additionally, the maximum flow rate is dependent on the maximum achievable flow rate of the compressors. At low qualities of the gas mixture, the mass flow rate becomes limited by the volume of mixed gas in the compressor station. As the high boiling components of the mixture begin to condense out, mass accumulates in the cryocooler heat exchanger, recuperative heat exchanger and test section. This means less mass is circulating in the mixed gas compressor station. This reduces the achievable inlet pressure of the mixed gas and limits the mass flow rate to the test section.

Gas mixture compositions are currently limited by gas availability and saturation pressure of pure components at room temperature. In the lab, the following are available as pure gases – argon, ethane, helium, n-butane, nitrogen, R14, R23, R32, and R134a. Isobutane and R218 are available in very low quantity. R410a is also available. R410a is a mixture of 70% R32 and 30% R125 on a molar basis and thus provides low mole fractions of R125 in gas mixtures. Gas mixtures are currently composed by adding the appropriate partial pressure of each pure single-phase gas to the compressor station as described in Schwartz [76]. From the list of gases above, this limits the mole fraction of isobutane and n-butane in the gas mixture compositions as the saturation pressure at room temperature of isobutane and n-butane are 372 kPa (54 psi) and 255 kPa (37 psi), respectively.

5.4. Data Reduction

The experimental measurements for the mixed gas and helium streams that are collected during operation of the test facility are listed in Table 5.8. In addition, the atmospheric pressure, P_{atm}, and ambient temperature, T_{amb}, are recorded. Measurements of the geometry required for the data reduction are listed in Table 5.9. An outline of the data reduction for determining the heat transfer coefficient, h_{mg}, and friction factor, f_{mg}, of the mixed gas from experimental measurements is shown in Figure 5.41, along with other results and assumptions made during the process. A detailed description of the calculations follows.

Mixed Gas		Helium	
Inlet pressure	$P_{mg,in}$	Inlet pressure in VCR union	$\tilde{P}_{he,in}$
Outlet pressure	$P_{mg,out}$	Outlet pressure in VCR union	$\tilde{P}_{he,out}$
Inlet temperature	$T_{mg,in}$	Inlet temperature in VCR union	$\tilde{T}_{he,in}$
Mass flow rate	$\dot{m}_{mg}$	Outlet temperature in VCR union	$\tilde{T}_{he,out}$
Uncorrected peak areas for each component from the GC	$A_{uc,i}$	Reference volumetric flow rate of helium	$\dot{V}_{ref}$

Table 5.8. Experimental measurements for helium and the mixed gas collected during test facility operation.

Finned-tube	Inner diameter	D_i
	Outer diameter	D_o
	Diameter of fins	D_f
	Length	L_t
	Thickness of fin	th
	Number of fins per unit length	N_f
Mandrel	Outer diameter	D_m
	Length	L_m
Shell of test section	Inner diameter	D_s
VCR union	Inner diameter	$\tilde{D}$

Table 5.9. Measurements of geometry required for data reduction.

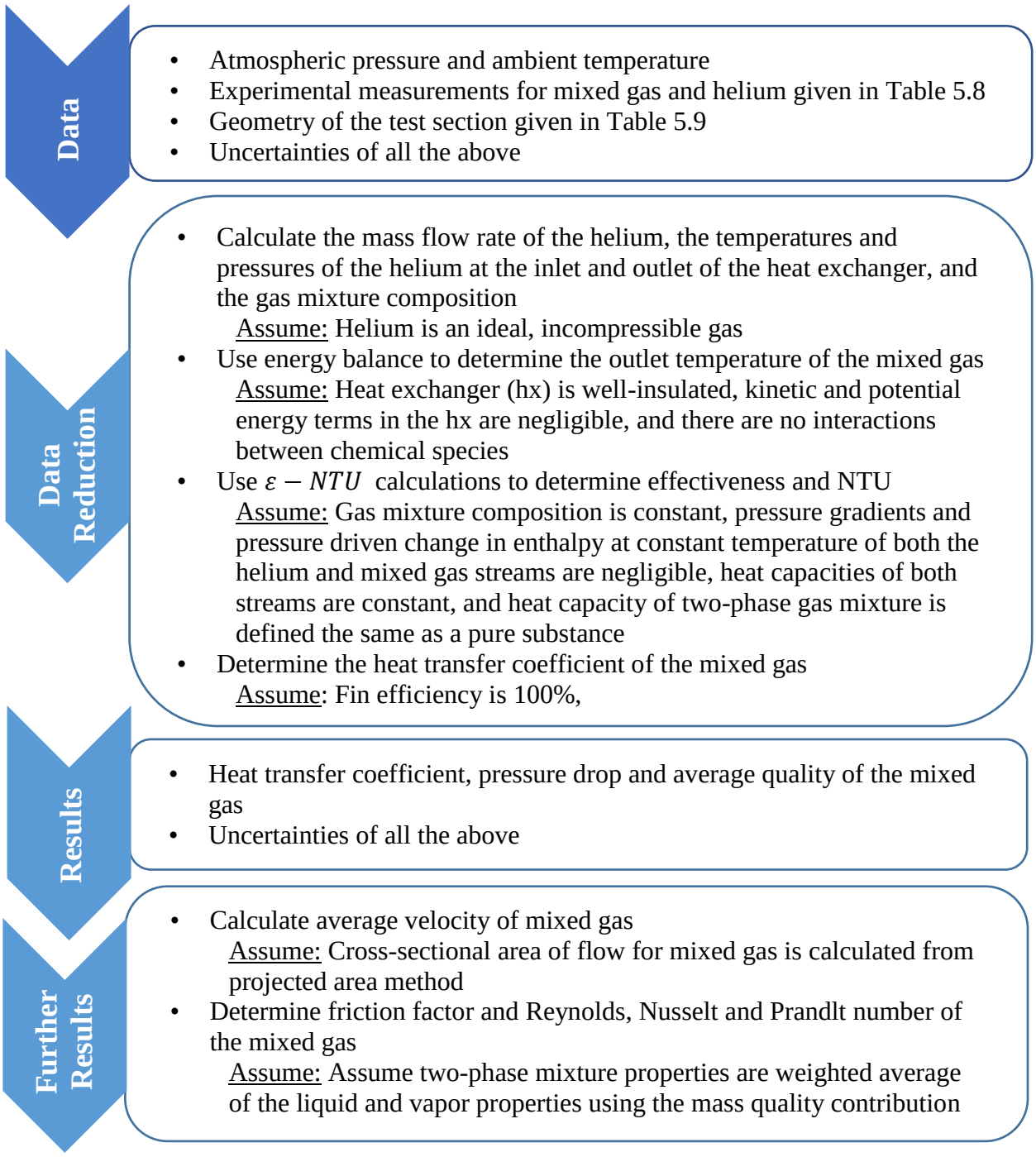

Figure 5.41. Outline of data reduction and assumptions for calculating heat transfer coefficient of mixed gas and further results from experimental measurements.

5.4.1. Preliminary Calculations

To determine the heat transfer coefficient of the mixed gas, an energy balance is performed on the heat exchanger. However, the experimental measurements listed in Table 5.8 cannot be directly used in this analysis. Preliminary calculations are performed to convert these experimental measurements into those parameters needed for the energy balance and the $\varepsilon - NTU$ calculation that ultimately leads to the heat transfer coefficient. Preliminary calculations include the following:

- the mass flow rate of the helium, $\dot{m}_{he}$, is calculated from the reference volumetric flow rate of the helium, $\dot{V}_{ref}$
- the pressures and temperatures of the helium at the inlet and outlet of the test section, P_{he} and T_{he}, are calculated from the pressures and temperatures of the helium measured in the 6.35 mm (1/8 inch) VCR unions, $\tilde{P}_{he}$ and $\tilde{T}_{he}$
- the gas mixture composition on a molar basis is calculated from the uncorrected peak areas from the GC, $A_{uc,i}$

The measurement of the volumetric flow rate for helium, $\dot{V}_{ref}$, was taken by an Omega mass flow controller. The mass flow controller was calibrated using nitrogen as the reference gas. A relative K factor is used to relate the calibration of the actual gas (He) to the reference gas (N_2) according to:

$$K = \frac{K_{act}}{K_{ref}} \tag{5.4}$$

The K factor for the actual and reference gas are given by:

$$K = \frac{1}{\rho c_p} \tag{5.5}$$

where ρ and c_p are determined at ambient temperature and inlet pressure of the mass flow controller [81]. The K factor is related to the actual volumetric flow rate of the helium, $\dot{V}_{he}$, by:

$$K = \frac{\dot{V}_{he}}{\dot{V}_{ref}} \tag{5.6}$$

Once the actual volumetric flow rate of the helium at the mass flow controller is known, the mass flow rate is calculated by:

$$\dot{m} = \rho \dot{V} \tag{5.7}$$

where, again, ρ is determined at ambient temperature and the inlet pressure of the mass flow controller.

The temperatures and pressures of the helium are measured in VCR unions with a larger diameter than the helically coiled finned-tube. Due to minor losses and the JT effect, the pressures and temperatures within the VCR unions will not be same as the temperatures and pressures at the inlet and outlet of the heat exchanger. The change in state is calculated from Bernoulli's equation. For the current operating conditions, the change in density of helium is small and thus will be assumed incompressible. Additionally, there is no vertical displacement between the VCR unions and the inlet and outlet of the heat exchanger and thus this will be neglected in Bernoulli's equation.

Bernoulli's equation for incompressible flow with no vertical displacement is given by Eq. (5.8):

$$\tilde{P} + \frac{1}{2}\tilde{\rho}\tilde{u}_m^2 = P + \frac{1}{2}\rho u_m^2 \tag{5.8}$$

where a tilde (~) above a parameter represents the state inside the VCR union and no tilde represents the state at the actual inlet or outlet of the heat exchanger. The velocity of helium in the VCR unions and at the inlet and outlet of the heat exchanger is calculated by Eq. (5.9):

$$u_m = \frac{\dot{m}}{\rho A_c} \tag{5.9}$$

where ρ and A_c is determined by the states and geometry at the location of interest. Eq. (5.8) holds at both the inlet and outlet of the test section and, when coupled with Eq. (5.9), provides the pressures and temperatures of the helium at the inlet and outlet of the heat exchanger, P_{he} and T_{he}.

Once the mass flow rate and inlet and outlet conditions for the helium and the mixed gas are known, the last unknown in the energy balance and $\varepsilon - NTU$ calculations is the gas mixture composition. As discussed previously, the GC generates peak areas for each component in the gas mixture, which will be referred to as the uncorrected peak areas, $A_{uc,i}$. While these peak areas are related to the concentration of each component in the gas mixture, they are not necessarily proportional to concentration. If one constituent has a higher thermal conductivity than another then the peak areas for these constituents will not be related to concentration in the same way. Increased accuracy of the gas mixture composition can be achieved if the GCs response is calibrated based on its sensitivity to different components and the peak areas are then normalized by this sensitivity.

A response factor (RF) is calculated to calibrate the GCs response for each component. The RF is determined by sampling each pure gas multiple times with constant conditions and obtaining an average peak area, A_{avg}, for each gas type. As the detector's sensitivity changes some

from day to day, all runs are performed on the same day. The RF is found by dividing the known amount of the component by the average peak area as given by:

$$RF = \frac{X}{A_{avg}} \tag{5.10}$$

where X is the molar fraction of component in the pure sample [82]. For the purposes of this research, all pure gas samples were taken from bottles with purity of greater than 99.9% and thus X is assumed to be 100%. However, if sampling from a lower grade bottle then the purity of the gas should be considered. The RF is sensitive to the operating conditions of the GC. Therefore, the RF should be collected for the operating conditions (such as sample flow rate and injector temperature) that will be used during collection of the gas mixture from the mixed gas compressor station. Example RFs for various GC operating conditions are given in Appendix 8.12.

During operation of the test section, the gas mixture is sampled from the mixed gas compressor station three times at constant conditions. An average of the peak area for each component is obtained, known as the uncorrected peak area, A_{uc}. The corrected (i.e., calibrated) peak area, A_c, for each constituent is determined by [82]:

$$A_c = A_{uc}RF \tag{5.11}$$

The corrected areas for each component are then normalized to determine the composition of the gas mixture. The mole fraction of each constituent, X, is given by [82]:

$$X = \frac{A_c}{\sum_{i=1}^{n} A_{c,i}} \tag{5.12}$$

where n is the total number of components in the gas mixture and i represents each component.

5.4.2. Heat Exchanger Calculations

Mixed Gas		Helium	
Inlet pressure	$P_{mg,in}$	Inlet pressure	$P_{he,in}$
Outlet pressure	$P_{mg,out}$	Outlet pressure	$P_{he,out}$
Inlet temperature	$T_{mg,in}$	Inlet temperature	$T_{he,in}$
Mass flow rate	$\dot{m}_{mg}$	Outlet temperature	$T_{he,out}$
Gas mixture composition	X_i	Mass flow rate of helium	$\dot{m}_{he}$

Table 5.10. Parameters for helium and the mixed gas after preliminary calculations have been performed.

Table 5.10 lists the known parameters for the helium and the mixed gas after the preliminary calculations have been performed. Assuming the heat exchanger is well-insulated, the kinetic and potential energy of the fluid streams are negligible and there are no interactions between the species of the gas mixture, an overall energy balance on the heat exchanger at steady-state leads to:

$$\dot{q} = \dot{m}_{he}\left(h_{he,in} - h_{he,out}\right) = \dot{m}_{mg}\left(h_{mg,out} - h_{mg,in}\right) \tag{5.13}$$

where h is the specific enthalpy of the fluid and $\dot{q}$ is the heat transfer rate between the fluid streams. The number of internal properties that are required to fix the state of a substance, F, in equilibrium is given by the phase rule:

$$F = n - \Pi + 2 \tag{5.14}$$

where Π is the number of phases present. Thus, the specific enthalpy of a pure, single-phase substance is fixed by the specification of two intensive properties, such as temperature and pressure:

$$h = (T, P) \tag{5.15}$$

The specific enthalpy of a two-phase mixture is fixed by the specification of the composition of the mixture and two intensive properties, such as temperature and pressure:

$$h = (X[1..n], T, P) \tag{5.16}$$

$h_{he,in}$, $h_{he,out}$, and $h_{mg,in}$ are determined from the known parameters above and the relationships given in Eqs. (5.15) and (5.16). Eq. (5.16) is coupled with Eq. (5.13) to determine $\dot{q}$ and $T_{mg,out}$.

Assuming that the composition of the gas mixture remains constant, the change in enthalpies in Eq. (5.13) can be expanded to the following:

$$\Delta h = \left(\frac{\Delta h}{\Delta T}\right)_P \Delta T + \left(\frac{\Delta h}{\Delta P}\right)_T \Delta P \tag{5.17}$$

Assuming the pressure gradients and pressure driven change in enthalpy at constant temperature of both the helium and mixed gas streams are negligible and the temperature driven change in enthalpy at constant pressure of both streams is constant, the overall energy balance in Eq. (5.13) reduces to:

$$q = \dot{m}_{he} c_{he}\left(T_{he,in} - T_{he,out}\right) = \dot{m}_{mg} c_{mg}\left(T_{mg,out} - T_{mg,in}\right) \tag{5.18}$$

where c is the constant pressure heat capacity defined as:

$$c_P = \left(\frac{\partial h}{\partial T}\right)_P \tag{5.19}$$

As the current testing conditions have been selected to minimize the change in thermophysical properties of the mixed gas stream, assuming the pressure driven change in enthalpy is negligible and using a constant heat capacity throughout the test section for the mixed gas is reasonable. On the other hand, the largest possible change in properties for the helium in the test section is a change in temperature from 300 to 110 K and a pressure change of 862 kPa (125 psi) to 517 kPa (75 psi). The enthalpy of the helium at 300 and 110 K changes only 0.07% and 0.15%, respectively, from 862 kPa (125 psi) to 517 kPa (75 psi). The c_{he} at a constant pressure of 862 kPa (125 psi)

and 517 kPa (75 psi) changes only 0.23% and 0.14%, respectively, from 300 to 110 K. Thus, it is also reasonable to assume for helium that the pressure driven change in enthalpy is negligible and the heat capacity is constant throughout the test section.

The specific heat capacity of helium, c_{he}, is obtained from the thermophysical properties database in the Engineering Equation Solver (EES) software [83] at the average temperature and pressure of the helium in the heat exchanger. The specific heat capacity of the two-phase mixed gas, c_{mg}, is not available in the Reference Fluid Thermodynamic and Transport Properties (REFPROP) database [62] as the specific heat capacity given in Eq. (5.19) is only defined for pure, single-phase substances. Nevertheless, the constant pressure heat capacity of the mixed gas is estimated as:

$$c_{p,mg} = \left(\frac{\partial h}{\partial T}\right)_P = \left(\frac{h_{out,mg} - h_{in,mg}}{T\left(h_{out,mg}, P_{in,mg}\right) - T_{in,mg}}\right) \tag{5.20}$$

where the outlet temperature of the mixed gas is determined for the ideal situation where there is no pressure drop in the test section.

The product of the mass flow rate and the specific heat capacity that appears in the Eq. (5.18) is referred to as the capacitance rate of the fluid:

$$\dot{C}_{he} = \dot{m}_{he} c_{he} \tag{5.21}$$

$$\dot{C}_{mg} = \dot{m}_{mg} c_{mg} \tag{5.22}$$

Substituting Eq. (5.21) and (5.22) into Eq. (5.18) leads to:

$$q = \dot{C}_{he}\left(T_{he,in} - T_{he,out}\right) = \dot{C}_{mg}\left(T_{mg,out} - T_{mg,in}\right) \tag{5.23}$$

To quantify the performance of the heat exchanger, the effectiveness of the heat exchanger, ε, is calculated as:

$$\varepsilon = \frac{\dot{q}}{\dot{q}_{max}} \tag{5.24}$$

where $\dot{q}_{max}$ is the maximum possible heat transfer rate given by:

$$\dot{q}_{max} = \dot{C}_{min}\left(T_{he,in} - T_{mg,in}\right) \tag{5.25}$$

and $\dot{C}_{min}$ is the minimum of the fluid capacitance rates given in Eq. (5.21) and (5.22). The capacitance ratio of the heat exchanger is given by:

$$C_R = \frac{\dot{C}_{min}}{\dot{C}_{max}} \tag{5.26}$$

where $\dot{C}_{max}$ is the maximum of the fluid capacitance rates given in Eq. (5.21) and (5.22).

The ε-NTU solution provides a relationship between the ε, C_R, and number of transfer units (NTU). The ε-NTU solution is the analytical solution to the governing differential equations that account for the local heat transfer rate between the streams and the associated temperature change. The solution to the governing differential equations for a counter-flow heat exchanger is given by:

$$NTU = \begin{cases} \dfrac{\ln\left(\dfrac{1-\varepsilon C_R}{1-\varepsilon}\right)}{1-C_R} & for\ C_R < 1 \\ \dfrac{\varepsilon}{1-\varepsilon} & for\ C_R = 1 \end{cases} \tag{5.27}$$

The NTU is related to the conductance of the heat exchanger, UA, by:

$$NTU = \frac{UA}{\dot{C}_{min}} \tag{5.28}$$

where UA is given by:

$$UA = \frac{1}{R_{tot}} \tag{5.29}$$

R_{tot} is the total thermal resistance that separates the two fluid streams. R_{tot} for the test section is given by:

$$R_{tot} = R_{conv,he} + R_{cond} + \left(\frac{1}{R_{f,mg}} + \frac{1}{R_{uf,mg}}\right)^{-1} \tag{5.30}$$

where $R_{conv,he}$ is the convection resistance for the helium, R_{cond} is the cylindrical resistance of the 70/30 CuNi tubes, $R_{f,mg}$ is the convection resistance of the mixed gas from the fins and $R_{uf,mg}$ is the convection resistance of the mixed gas from the un-finned area. The resistances are defined as follows:

$$R_{conv,he} = \frac{1}{\bar{h}_{he}\pi D_i L_t} \tag{5.31}$$

$$R_{cond} = \frac{\ln\left(\frac{D_o}{D_i}\right)}{2\pi k_t L_t} \tag{5.32}$$

$$R_{f,mg} = \frac{1}{\eta_f h_{mg} A_{s,f} N_{tot}} \tag{5.33}$$

$$R_{uf,mg} = \frac{1}{h_{mg} A_{s,uf}} \tag{5.34}$$

where D_i, D_o, and L_t are assigned in Table 5.9 and $A_{s,f}$ is the surface area of one fin, N_{tot} is the total number of fins, and $A_{s,uf}$ is the unfinned surface area the tube. The fin efficiency, η_f, is assumed to be 100%. $A_{s,f}$ and $A_{s,uf}$ are given by:

$$A_{s,f} = 2\pi\left(\left(\frac{D_f}{2}\right)^2 - \left(\frac{D_o}{2}\right)^2\right) + \pi D_f th \tag{5.35}$$

$$A_{s,uf} = \pi D_o (L_t - N_{tot} \cdot th) \tag{5.36}$$

where D_f and th are assigned in Table 5.9.

The resistance R_{cond} is calculated from the known geometric parameters and thermophysical properties of the coiled finned-tube. To calculate $R_{conv,he}$, the average heat transfer coefficient for helium must be estimated. With the mass flow rate and inlet and outlet conditions of helium known for the test section, the average thermodynamic properties within the heat exchanger are calculated and used to determine the Nusselt number of the helium in the helically coiled tube. The Nusselt number is estimated using the helical pipe flow procedure in the Engineering Equation Solver (EES) software [83]. For the current testing conditions, the Reynolds number of the helium is less than 2300, indicating laminar flow. Thus, this procedure uses the correlation provided by Bennett [84] to estimate the Nusselt number for laminar flow in a straight tube and then modifies the straight tube results to account for the curvature of the coil using correlations in *The Heat Exchanger Design Handbook* [85] and Barron (1999) [86]. Since the flow is laminar, the Nusselt number is dependent upon the boundary condition. The Nusselt number for a constant temperature boundary condition is used to calculate the average *htc* of the helium, $\bar{h}_{he}$, as the current testing conditions have been selected to minimize the change in thermophysical properties of the mixed gas stream. $\bar{h}_{he}$ is calculated from the Nusselt number by:

$$\bar{h}_{he} = \frac{\overline{Nu} \cdot k}{D_i} \tag{5.37}$$

where k is the average thermal conductivity of the helium in the test section. $R_{conv,he}$ is then calculated from Eq. (5.31).

Finally, Eq. (5.30) is coupled with Eqs. (5.33) and (5.34) to calculate h_{mg}. The measured h_{mg} depends on the average conditions between the inlet and the outlet of the test section. The test section and operating conditions were chosen to minimize the change in the thermophysical properties of the mixed gas at the inlet and the outlet. However, even though the inlet and outlet conditions may be thermodynamically close to one another, they are indeed different. In this way, a pseudo-local heat transfer coefficient of the mixed gas is captured.

5.4.3. Calculations for Further Results

Further assumptions and calculations are made to determine the velocity, friction factor and Reynolds, Nusselt, and Prandlt number of the mixed gas. The projected area method is employed to estimate the cross-sectional area of flow for the mixed gas, $A_{c,mg}$. This approach assumes that the shell of the heat exchanger is made into a flat surface of an equivalent length πD_e, where D_e is the effective mean diameter of the shell. The heat exchanger in the test section is wrapped with Teflon tape for a tight fit. Thus, the outer diameter of the cross-sectional area of flow is reduced from the inner diameter of the shell, D_s, to the outer diameter of the coiled finned-tube wrapped around the mandrel. Therefore, the effective mean diameter of the shell is given by:

$$D_e = D_m + D_f \tag{5.38}$$

The finned-tube is projected in the space of the shell as shown in Figure 5.42. The clearance between the heat exchanger and the shell, denoted c in Figure 5.42, is 0 for the test section. $A_{c,mg}$ is obtained by deducting the projected area of the finned-tube from total cross-sectional area available in the space of the shell of length πD_e [27]. This is given as

$$Ac_{mg} = \pi D_e \left(\left(D_f - D_o \right) \left(1 - N_f \cdot th \right) \right) \tag{5.39}$$

The average velocity of the mixed gas, $\bar{u}_{mg}$, is then calculated from Eq. (5.9) using Eq. (5.39) and the average density of the mixed gas in the test section.

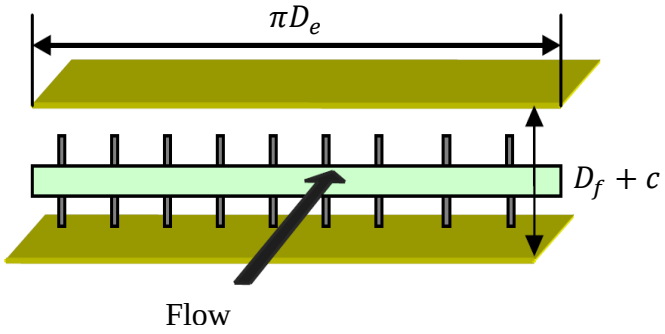

Figure 5.42. Projected area of equivalent length πD_e [5].

The average viscosity of the mixed gas, $\bar{\mu}_{mg}$, average thermal conductivity, $\bar{k}_{mg}$, and average Prandtl number, $\overline{Pr}$, are estimated as a weighted average of the liquid and vapor properties using the mass quality contribution, given by Eqs. (5.40) through (5.42) [6]:

$$\bar{\mu}_{mg} = \bar{x}_m \cdot \bar{\mu}_G + (1 - \bar{x}_m) \cdot \bar{\mu}_L \tag{5.40}$$

$$\bar{k}_{mg} = \bar{x}_m \cdot \bar{k}_G + (1 - \bar{x}_m) \cdot \bar{k}_L \tag{5.41}$$

$$\overline{Pr}_{mg} = \bar{x}_m \cdot \overline{Pr}_G + (1 - \bar{x}_m) \cdot \overline{Pr}_L \tag{5.42}$$

where the subscripts G and L represent the vapor and liquid transport properties of the mixture and $\bar{x}_m$ is the average quality of the mixture in the test section on a mass basis. $\bar{\mu}_G$, $\bar{\mu}_L$, $\bar{k}_G$, $\bar{k}_L$, $\overline{Pr}_G$, $\overline{Pr}_L$, and $\bar{x}_m$ are calculated in REFPROP at the average pressure and temperature of the mixed gas in the test section.

The Reynolds number of the mixed gas is then given by Eq. (5.43):

$$Re_{mg} = \frac{\bar{\rho}_{mg} \bar{u}_{mg} D_{h,mg}}{\bar{\mu}_{mg}} \tag{5.43}$$

where the hydraulic diameter of the mixed gas, $D_{h,mg}$, is calculated as:

$$D_{h,mg} = \frac{4A_{c,mg}}{per_{mg}} \tag{5.44}$$

The wetted perimeter of the mixed gas, per_{mg}, includes the finned and unfinned surface of the coiled finned-tube and is determined by:

$$per_{mg} = \frac{\pi D_e}{D_f}\left(A_{s,f}N_f + \pi D_o\left(1 - N_f th\right)\right) \tag{5.45}$$

The Nusselt number of the mixed gas is given by Eq. (5.46):

$$Nu = \frac{h_{mg}D_h}{\bar{k}_{mg}} \tag{5.46}$$

Additionally, the friction factor of the mixed gas, f_{mg}, is estimated according to Eq. (5.47):

$$f_{mg} = \frac{\Delta P_{mg}}{L_m}\frac{2D_{h,mg}}{\bar{\rho}_{mg}\bar{u}_{mg}^2} \tag{5.47}$$

5.5. Uncertainty Analysis

The uncertainty of an experimental measurement, U, is calculated as the combination of systematic and random errors, given by Eq. (5.48):

$$U = \sqrt{u_i^2 + u_{DAQ}^2 + u_p^2 + u_b^2} \tag{5.48}$$

where u_i is the uncertainty from resolution of the instrument, u_{DAQ} is the uncertainty from resolution of the DAQ system, u_p is the uncertainty due to precision, and u_b is the uncertainty related to bias. The uncertainty related to bias, u_b, is neglected in the following analysis. Details of the instrumental, DAQ, and precision uncertainties are provided in the following sections.

5.5.1. Instrumental Uncertainties

Experimental Measurement	Measuring Instrument	Instrument Uncertainty (u_i)
Ambient pressure, P_{amb}	Barometer	$\pm$0.007 kPa ($1x10^{-3}$ psi)
Ambient temperature, T_{amb}	Mercury thermometer	$\pm$0.6 K
Inlet pressure of He, $\tilde{P}_{he,in}$	Setra 206 Pressure transducer	$\pm$4.5 kPa (0.65 psi)
Outlet pressure of He, $\tilde{P}_{he,out}$		
Inlet pressure of MG, $P_{mg,in}$	Setra 206 Pressure transducer	$\pm$0.90 kPa (0.13 psi)
Outlet pressure of MG, $P_{mg,out}$		
Inlet temperature of He, $\tilde{T}_{he,in}$	Lake Shore Cryotronics PT-103/111 PRT	$\pm$0.25 K
Outlet temperature of He, $\tilde{T}_{he,out}$		
Inlet temperature of MG, $T_{mg,in}$		
Volumetric flow rate of reference gas, $\dot{V}_{ref}$	Omega FMA 5516A Mass flow controller	$\pm$0.02 L/min
Mass flow rate, $\dot{m}_{mg}$	Endress Hauser 83A Coriolis flow meter	See below
Response factors, RF	Hewlett Packard 5890 II GC	See below

Table 5.11. Instrumental uncertainty for experimental measurements.

Table 5.11 provides an overview of the instrument uncertainty. The pressure at the inlet and outlet of the test section for both the helium and mixed gas streams are measured using Setra Model 206 pressure transducers. The range of the pressure transducers used on the mixed gas side is 0 – 689 kPa (100 psi) and on the helium side is 0 – 3447 kPa (500 psi). The pressure transducers measure pressure with an accuracy of 0.13% of the full range [80]. This gives an accuracy of $\pm$ 896 Pa (0.13 psi) and $\pm$ 4482 Pa (0.65 psi) for the pressure transducers of the mixed gas and helium, respectively. The pressure transducers were calibrated with an Endress & Hauser Cerabar PMP51 pressure transmitter.

The temperature measurements at the inlet and outlet of the test section for the helium and the inlet of the test section for the mixed gas are carried out with in-stream temperature sensors using Lake Shore Cryotronics PT-103 and PT-111 PRTs in a 4-wire configuration. The in-stream PRTs and their construction are shown in Appendix 8.10. The PRTs have an accuracy of $\pm$0.25 K when each sensor is calibrated using two temperature points to create a linear relationship between the measured voltage and the temperature of the PRT [75]. As shown in Figure 5.43, the PRTs were field calibrated using a two-point calibration at the saturation temperature of liquid nitrogen

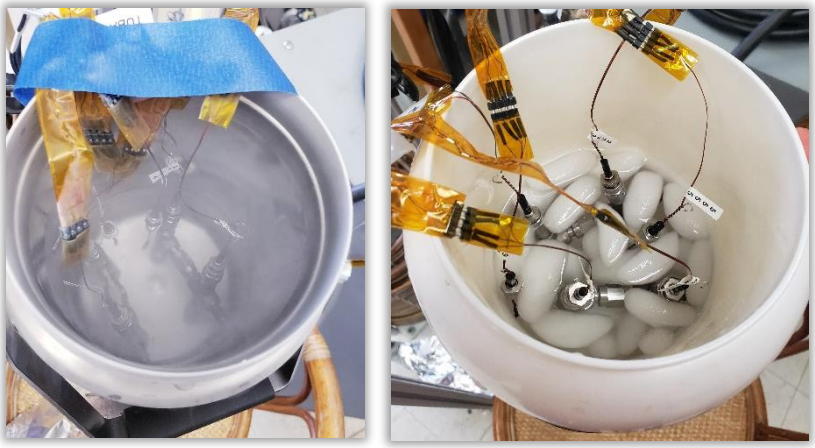

(a) (b)

Figure 5.43. Calibration of PRTs in liquid nitrogen (a) and an ice water bath (b).

(77.2K @ 98.8 kPa) and the freezing point of water (273.15K). The freezing point of water was obtained with an ice water bath.

The volumetric flow rate of the helium is measured with an Omega FMA 5516A mass flow controller, as previously shown in Figure 5.26. The mass flow controller has a range of 0 – 2 L/min for nitrogen. The flow controller has an accuracy of 1% of the full range [81]. This gives an accuracy of $\pm$0.02 L/min for nitrogen.

The mass flow rate of the mixed gas is measured with an Endress & Hauser Promass 83A02 Coriolis mass flow meter as previously shown in Figure 5.16. The mass flow control has a range of 0.05 g/s to $\dot{m}_{max}$, where $\dot{m}_{max}$ is defined in Eq. (5.3). Figure 5.44 shows the relative uncertainty of flow meter as a function of the mass flow rate. The largest relative uncertainty of 2.5% is observed when the mass flow rate is 0.05 g/s. As the flow rate increases from 0.05 to approximately 0.3 g/s, the relative uncertainty decreases to 0.5% and remains at 0.5% for flow rates greater than 0.3 g/s. Target flow rates for the mixed gas range from 0.05 to 0.15 g/s. Thus, the relative uncertainty of the Coriolis flow meter will range from 2.5% to approximately 1.25%.

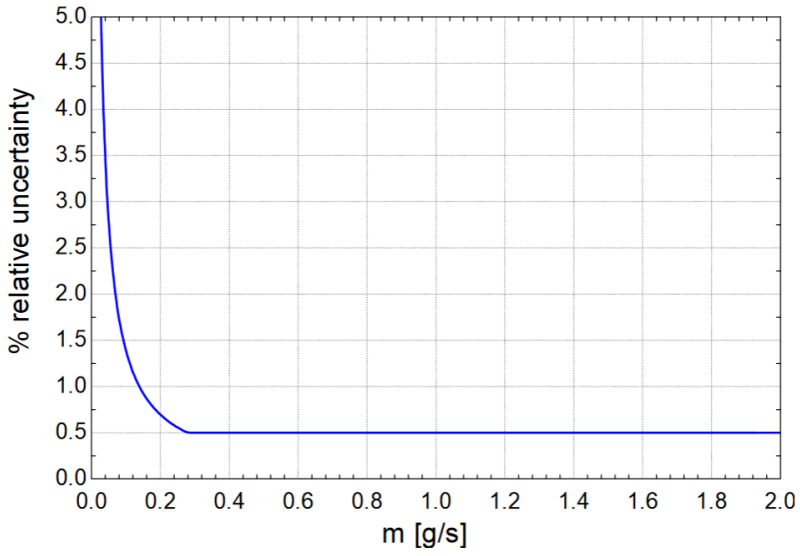

Figure 5.44. Relative uncertainty of Coriolis flow meter as a function of mass flow rate [6].

The uncorrected peak areas and responses factors used to measure the composition are measured with a Hewlett Packard 5890 II GC equipped with a TCD as shown previously in Figure 5.36(b). As described previously, the RFs are determined by sampling each pure gas multiple times with constant conditions and obtaining an average peak area, A_{avg}, for each gas type. The detector's sensitivity changes slightly from day to day. Thus, it is best practice to obtain a RF for each pure component of the gas mixture on the same day the gas mixture is sampled. However, due to limitations on helium availability, the RFs for each pure gas were not collected each day that a gas mixture was sampled. A repeatability and sensitivity analysis was performed for the RFs of pure gases to quantify the uncertainty of the RFs. The RFs and absolute and relative uncertainties are given in Table 5.12. Details of the repeatability and sensitivity analysis can be found in Appendix 8.12.

Gas	Argon	R23	R14	Nitrogen	Ethane	R32
RF	0.02184 ±0.00123	0.01641 ±0.00087	0.01528 ±0.00016	0.02379 ±0.00333	0.01782 ±0.00095	0.01738 ±0.00056
%RU	5.62%	5.32%	1.01%	13.97%	5.31%	3.14%

Table 5.12. Response factors and uncertainties for select pure gases.

5.5.2. DAQ Uncertainties

Table 5.13 provides an overview of the DAQ uncertainty for experimental measurements. A Campbell Scientific CR23X micrologger, as shown previously in Figure 5.36(a), measures the voltage across the pressure transducers, temperature sensors, and flow meters. The micrologger has an accuracy of 0.025% of the full-scale range [87]. The full-scale range can be set to 10, 50, 200, 1000, or 5000 mV. The full-scale value is set to 5000 mV for the pressure and flow measurements and 200 mV for the temperature measurements. This gives an uncertainty in the measured voltage, u_V, of ± 1.25 and ± 0.05 mV, respectively. The DAQ uncertainty, u_{DAQ}, is then

Experimental Measurement	Measured Voltage Uncertainty (u_V)	DAQ Uncertainty (u_{DAQ})
Inlet pressure of He, $\tilde{P}_{he,in}$	$\pm$1.25 mV	$\pm$0.86 kPa (0.13 psi)
Outlet pressure of He, $\tilde{P}_{he,out}$		
Inlet pressure of MG, $P_{mg,in}$	$\pm$1.25 mV	$\pm$0.17 kPa (0.025 psi)
Outlet pressure of MG, $P_{mg,out}$		
Inlet temperature of He, $\tilde{T}_{he,in}$	$\pm$0.05 mV	$\pm$0.12 K
Outlet temperature of He, $\tilde{T}_{he,out}$		
Inlet temperature of MG, $T_{mg,in}$		
Volumetric flow rate of reference gas, $\dot{V}_{ref}$	$\pm$1.25 mV	$\pm$0.0005 L/min
Mass flow rate, $\dot{m}_{mg}$	$\pm$1.25 mV	$\pm$0.0031 g/s

Table 5.13. DAQ uncertainty for experimental measurements.

determined by the relationship between the measured voltage, V, and the desired experimental measurement. The relationship is programmed into the micrologger in the form:

$$Experimental\ Measurement = a\,V + b \tag{5.49}$$

where a and b are constants dependent upon the experimental measurement. For the pressure and temperature measurements, a and b are determined from the calibrations described above. For the flow measurements, a and b are determined from the linear relationship between the voltage and flow rate as given in the users' manuals [67, 81]. u_{DAQ} is then given by Eq. (5.50):

$$u_{DAQ} = a u_V \tag{5.50}$$

Values of the u_{DAQ} for the experimental measurements are listed in Table 5.13.

5.5.3. Precision Uncertainty

To quantify the uncertainty due to precision, the random error of the pressure, temperature and flow rate measurements is analyzed by taking the standard deviation of 180 data points (3 recorded per second) at steady-state conditions. The uncertainty due to precision is listed in Table 5.14 for a sample data point detailed in Table 5.15.

Experimental Measurement	Precision Uncertainty (u_p)
Ambient pressure, P_{amb}	NA
Ambient temperature, T_{amb}	NA
Inlet pressure of He, $\tilde{P}_{he,in}$	$\pm$0.13 kPa (0.020 psi)
Outlet pressure of He, $\tilde{P}_{he,out}$	$\pm$0.13 kPa (0.019 psi)
Inlet pressure of MG, $P_{mg,in}$	$\pm$0.32 kPa (0.047 psi)
Outlet pressure of MG, $P_{mg,out}$	$\pm$0.31 kPa (0.045 psi)
Inlet temperature of He, $\tilde{T}_{he,in}$	$\pm$0.016 K
Outlet temperature of He, $\tilde{T}_{he,out}$	$\pm$0.038 K
Inlet temperature of MG, $T_{mg,in}$	$\pm$0.094 K
Volumetric flow rate of reference gas, $\dot{V}_{ref}$	$\pm$0.002 L/min
Mass flow rate, $\dot{m}_{mg}$	$\pm$0.0025 g/s
Response factor for R32, RF_{R32}	NA
Response factor for R14, RF_{R14}	NA

Table 5.15. Precision uncertainty of experimental measurements for a sample data point.

5.5.4. Example Results for Uncertainty Analysis

Experimental Measurement	Measured Value	Combined Uncertainty (U)
Ambient pressure, P_{amb}	98.25 kPa (14.25 psi)	±0.007 kPa (1E-3 psi)
Ambient temperature, T_{amb}	299.8 K	±0.6 K
Inlet pressure of He, $\tilde{P}_{he,in}$	509.9 kPa (73.96 psig)	$\pm$4.6 kPa (0.66 psi)
Outlet pressure of He, $\tilde{P}_{he,out}$	491.0 kPa (71.22 psig)	$\pm$4.6 kPa (0.66 psi)
Inlet pressure of MG, $P_{mg,in}$	177.6 kPa (25.75 psig)	$\pm$0.97 kPa (0.14 psi)
Outlet pressure of MG, $P_{mg,out}$	177.2 kPa (25.70 psig)	$\pm$0.96 kPa (0.14 psi)
Inlet temperature of He, $\tilde{T}_{he,in}$	225.90 K	$\pm$0.28 K
Outlet temperature of He, $\tilde{T}_{he,out}$	196.78 K	$\pm$0.28 K
Inlet temperature of MG, $T_{mg,in}$	173.82 K	$\pm$0.29 K
Volumetric flow rate of reference gas, $\dot{V}_{ref}$	0.20	$\pm$0.02 L/min
Mass flow rate, $\dot{m}_{mg}$	0.1524 g/s	$\pm$0.0043 g/s
Response factor for R32, RF_{R32}	0.01683	±0.00036
Response factor for R14, RF_{R14}	0.01515	±0.00003

Table 5.14. Combined uncertainty of experimental measurements for a sample data point.

Once u_i, u_{DAQ}, and u_p are known, the combined uncertainty, U, is calculated from Eq. (5.48). The combined uncertainty for a sample data point is listed in Table 5.15. The measured values and uncertainties of the geometric measurements were given in Table 5.2.

Heat transfer coefficient of mixed gas

The heat transfer coefficient of the mixed gas, h_{mg}, is a function of inlet and outlet temperatures and pressures of the helium and mixed gas, flow rates of the helium and mixed gas, gas mixture composition and test section geometry as given by Eq. (5.51):

$$h_{mg} = f(T_{he,in}, T_{he,out}, P_{he,in}, P_{he,out}, T_{mg,in}, T_{mg,out}, P_{mg,in}, P_{mg,out}, \dot{m}_{he}, \dot{m}_{mg}, X[1..n], \text{and geometry}) \quad (5.51)$$

Given the experimental measurements required to determine these parameters, Eq. (5.51) expands to:

$$h_{mg} = f(\tilde{T}_{he,in}, \tilde{T}_{he,out}, \tilde{P}_{he,in}, \tilde{P}_{he,out}, \tilde{D}, T_{mg,in}, P_{mg,in}, P_{mg,out}, \dot{V}_{ref}, P_{amb}, T_{amb}, \dot{m}_{mg}, RF[1..n], A_{uc}[1..n], D_i, D_o, D_f, N_f, th, \text{and } D_m) \quad (5.52)$$

Consequently, the uncertainty in the heat transfer coefficient of the mixed gas, $U(h_{mg})$ is given by:

$$U(h_{mg}) = \sqrt{\left(\frac{\partial h_{mg}}{\partial \tilde{T}_{he,in}} U(\tilde{T}_{he,in})\right)^2 + \left(\frac{\partial h_{mg}}{\partial \tilde{T}_{he,out}} U(\tilde{T}_{he,out})\right)^2 + \ldots + \left(\frac{\partial h_{mg}}{\partial D_m} U(D_m)\right)^2} \quad (5.53)$$

Once the combined uncertainty for each experimental measurement is known, the uncertainty propagation feature provided by EES [83] is used to determine $U(h_{mg})$. Table 5.16 shows the results of the uncertainty analysis for the same example data point as above. Note that

experimental measurements are only shown if the contribution to heat transfer coefficient of the mixed gas, $CU(h_{mg})$, was 0.1% or greater; measurements that do not contribute significantly are omitted. The uncertainty in the measurement of the volumetric flow rate of the reference gas, $\dot{V}_{ref}$, has the greatest contribution to the uncertainty of the measured htc.

$\boldsymbol{h_{mg} = 21.3 \pm 2.5 \frac{W}{m^2K}}$	$\boldsymbol{RU(h_{mg})}$ **= 12%**
Parameter	$CU(h_{mg})$
Diameter of fins, D_f	2.0%
Inlet pressure of He, $\tilde{P}_{he,in}$	0.5%
Inlet temperature of He, $\tilde{T}_{he,in}$	0.4%
Inlet temperature of MG, $T_{mg,in}$	0.7%
Outlet temperature of He, $\tilde{T}_{he,out}$	2.0%
Volumetric flow rate of reference gas, $\dot{V}_{ref}$	94.3%

Table 5.16. Results of the uncertainty analysis for one data point for the h_{mg}.

Friction factor of mixed gas

The friction factor of the mixed gas, f_{mg}, is a function of the inlet and outlet temperatures and pressures of the mixed gas, flow rate of the mixed gas, and geometry of the test section as given by Eq. (5.54):

$$f_{mg} = f\left(T_{mg,in}, T_{mg,out}, P_{mg,in}, P_{mg,out}, \dot{m}_{mg}, X[1..n], and\ geometry\right) \tag{5.54}$$

Given the experimental measurements required to determine these parameters, Eq. (5.54) expands to:

$$\begin{aligned} f_{mg} = f\big(&\tilde{T}_{he,in}, \tilde{T}_{he,out}, \tilde{P}_{he,in}, \tilde{P}_{he,out}, \tilde{D}, T_{mg,in}, P_{mg,in}, P_{mg,out}, \dot{m}_{mg}, \dot{V}_{ref}, \\ &P_{amb}, T_{amb}, RF[1..n], A_{uc}[1..n], D_o, D_f, N_f, th, D_m, L_m, and\ D_s\big) \end{aligned} \tag{5.55}$$

Consequently, the uncertainty in the friction factor of the mixed gas, $U(f_{mg})$ is given by:

$$U(f_{mg}) = \sqrt{\left(\frac{\partial f_{mg}}{\partial \tilde{T}_{he,in}} U(\tilde{T}_{he,in})\right)^2 + \left(\frac{\partial f_{mg}}{\partial \tilde{T}_{he,out}} U(\tilde{T}_{he,out})\right)^2 + \ldots + \left(\frac{\partial f_{mg}}{\partial D_s} U(D_s)\right)^2} \quad (5.56)$$

Table 5.17 shows the results of the uncertainty propagation of the friction factor in EES for the same example data point as above. Again, experimental measurements are only shown if the contribution to the friction factor of the mixed gas, $CU(f_{mg})$, was 0.1% or greater. The uncertainty in the measurements of the inlet and outlet pressures of the mixed gas have the greatest contribution to the uncertainty of the measured friction factor of the mixed gas.

$\boldsymbol{f_{mg} = 0.74\ (+2.86/-0.74)}$	
Parameter	$CU(f_{mg})$
Inlet pressure of mixed gas, $P_{mg,in}$	50.3%
Outlet pressure of mixed gas, $P_{mg,out}$	49.7%

Table 5.17. Results of the uncertainty analysis for one data point for the f_{mg}.

Average quality of mixed gas

The average quality of the mixed gas, $\bar{x}_{mg}$, is a function of the inlet and outlet temperatures and pressures of the mixed gas and the gas mixture composition as given by Eq. (5.57):

$$\bar{x}_{mg} = f(T_{mg,in}, T_{mg,out}, P_{mg,in}, P_{mg,out}, and\ X[1..n]) \quad (5.57)$$

Given the experimental measurements required to determine these parameters, Eq. (5.57) expands to:

$$\bar{x}_{mg} = f(\tilde{T}_{he,in}, \tilde{T}_{he,out}, \tilde{P}_{he,in}, \tilde{P}_{he,out}, \tilde{D}, T_{mg,in}, P_{mg,in}, P_{mg,out}, \dot{m}_{mg}, \dot{V}_{ref}, P_{amb}, T_{amb}, RF[1..n], A_{uc}[1..n]) \quad (5.58)$$

Consequently, the uncertainty in the average quality of the mixed gas, $U(\bar{x}_{mg})$ is given by:

$$U(\bar{x}_{mg})$$

$$= \sqrt{\left(\frac{\partial \bar{x}_{mg}}{\partial \tilde{T}_{he,in}} U(\tilde{T}_{he,in})\right)^2 + \left(\frac{\partial \bar{x}_{mg}}{\partial \tilde{T}_{he,out}} U(\tilde{T}_{he,out})\right)^2 + \cdots + \left(\frac{\partial \bar{x}_{mg}}{\partial A_{uc,n}} U(A_{uc,n})\right)^2} \quad (5.59)$$

Table 5.18 shows the results of the uncertainty propagation of the average quality in EES for the same example data point as above. Again, experimental measurements are only shown if the contribution to the average quality of the mixed gas, $CU(\bar{x}_{mg})$, was 0.1% or greater. The uncertainty in the measurements of the response factor of R32 has the greatest contribution to the uncertainty of the measured average quality of the mixed gas.

$\bar{x}_{mg} = 0.324 \pm 0.008$	$RU(\bar{x}_{mg}) = 3.5\%$
Parameter	$CU(\bar{x}_{mg})$
Inlet temperature of mixed gas, $T_{mg,in}$	0.1%
Response factor for R14, RF_{R14}	9.5%
Response factor for $R32$, RF_{R32}	90.3%

Table 5.18. Results of the uncertainty analysis for one data point for the $\bar{x}_{mg}$.

5.5. Experimental Measurements and Discussion

Beyond the broad goal of investigating gas mixture selection for a MGJT cryocooler, this research aimed to design and build a test facility capable of measuring the heat transfer coefficient associated with these mixtures on the shell-side of a GH heat exchanger. To demonstrate the capability of the test facility to accomplish this, the compressor station was charged with a gas mixture of 80% R32 and 20% R14 on a molar basis. This mixture is attractive for MGJT cryocoolers as thermodynamically it is capable of providing a cooling capacity from 300 to 150 K for the operating conditions of interest (i.e., a high-pressure of 827 kPa (120 psi) and low-pressure of 276 kPa (40 psi)). As shown in Figure 5.45, the minimum isothermal enthalpy change, Δh_T, is 7027 J/kg for these conditions and thus the mixture can theoretically provide a cooling power of 1 W with a mass flow rate of 0.15 g/s. Additionally, at the high pressure of 827 kPa (120 psi), the bubble and dewpoint temperatures of this mixture are 179 and 265K, respectively. At the low pressure of 276 kPa (40 psi) 40 psi, the bubble and dewpoint temperatures of this mixture are 151 and 237K, respectively. Therefore, the mixture will be two-phase in both the high- and low-pressure streams for a significant portion of the temperature range of interest.

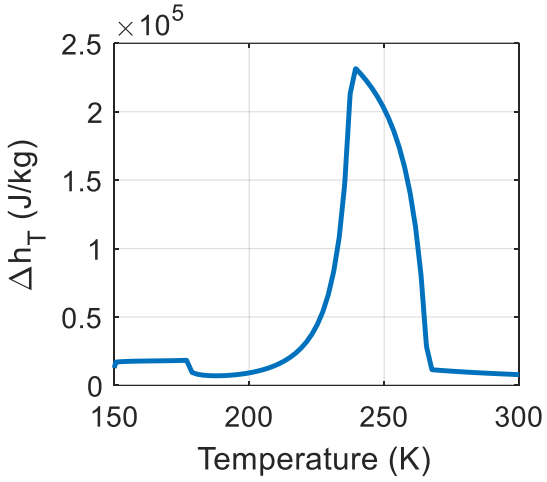

Figure 5.45. Δh_T as a function of temperature for 80% R32 and 20% R14 for high and low pressures of 827 kPa (120 psi) and 276 kPa (40 psi), respectively.

5.5.1. Operating Conditions for Measurements

	Parameter	Operating Range
Mixed Gas	Inlet Temperature, $T_{mg,in}$	174-267 K
	Inlet Pressure, $P_{mg,in}$	268-311 kPa (39-45 psi)
	Mass flow rate, $\dot{m}_{mg}$	0.15-0.16 g/s
Helium	Inlet Temperature, $T_{he,in}$	226-275 K
	Inlet Pressure, $P_{he,in}$	608-721 kPa (88-105 psi)
	Volumetric flow rate, $\dot{V}_{ref}$	0.19 L/min

Table 5.19. Operating conditions for heat transfer coefficient measurements.

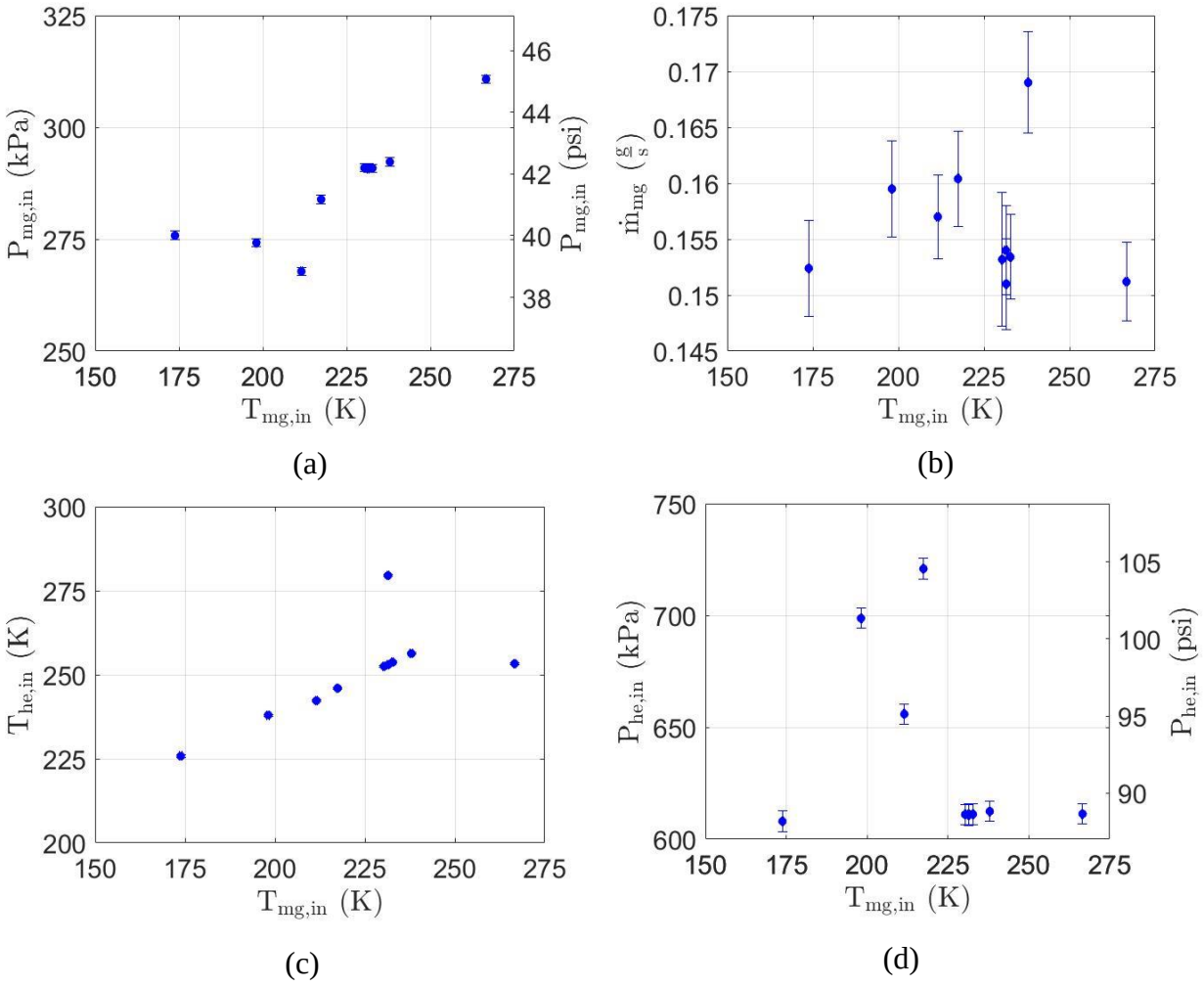

Figure 5.46. Operating conditions during data collection as a function of the inlet temperature of the mixed gas – inlet pressure of mixed gas (a), mass flow rate of mixed gas (b), and inlet temperature and pressure of the helium (c) and (d).

Table 5.19 shows the operating range for the measurements that were collected. The inlet temperature of the mixed gas was varied to capture a range of quality for the htc measurements. The inlet temperature was varied by altering the power supplied to the cold head by the two cartridge heaters shown in Figure 5.29(b). The volumetric flow rate of the helium was electronically controlled by the Omega mass flow controller. The inlet pressure and mass flow rate of the mixed gas was manually adjusted using the ball valves and mass flow metering valves on the mixed gas compressor station, in addition to using the make-up tank to add and remove mass from the station. The inlet pressure and temperature of the helium was not controlled and varied during data collection. Figure 5.46 illustrates the variation in the operating conditions during data

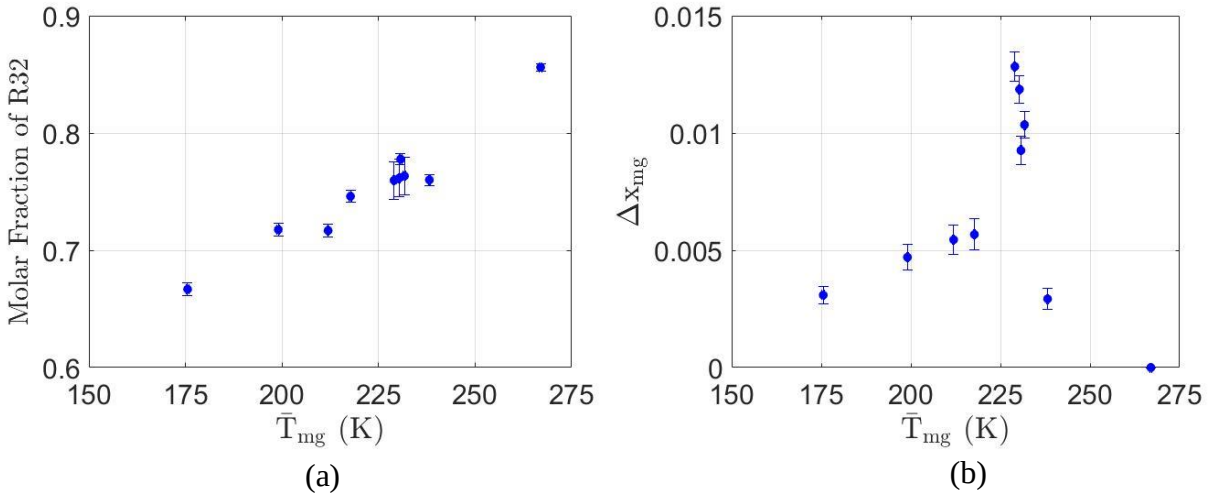

Figure 5.47. Molar fraction of R32 (a) and the change in quality of the mixed gas in the test section (b) as a function of average temperature of the mixed gas.

collection.

Figure 5.47(a) shows the variation in the gas mixture composition as a function of the average temperature of the mixed gas in the test section. As expected, the molar fraction of R32 in the mixture decreases as the average temperature decreases in the test section. R32 is the higher boiling component in the gas mixture and begins to condense out of the mixture at higher

temperatures than R14. Figure 5.47(b) illustrates the change in quality of the mixed gas between the inlet and outlet of the test section. The maximum change in quality of the mixed gas in the test section for the measurements collected is approximately 1.3%.

Figure 5.48 illustrates the average quality as a function of the average temperature of the mixed gas in the test section. The gas mixture experiences a change in quality of approximately 50% between 231 and 238 K, making it challenging to reach steady-state conditions for this quality range. Within this range, small variations in the operating conditions of the mixed gas or helium stream drive the steady-state temperature to the upper or lower bound of this region. GC measurements were not collected for three data points in this region to maintain a constant inlet pressure for the mixed gas. The increased uncertainty in the gas mixture composition of these points can be seen in Figure 5.47(a) and Figure 5.48. Further details of estimating the gas mixture composition for these points can be found in Appendix 8.13.

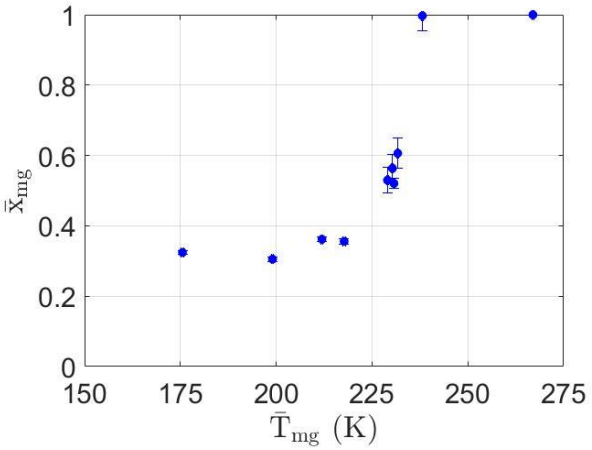

Figure 5.48. Average quality as a function of average temperature of the gas mixture.

5.5.2. Reynolds Number for Mixed Gas

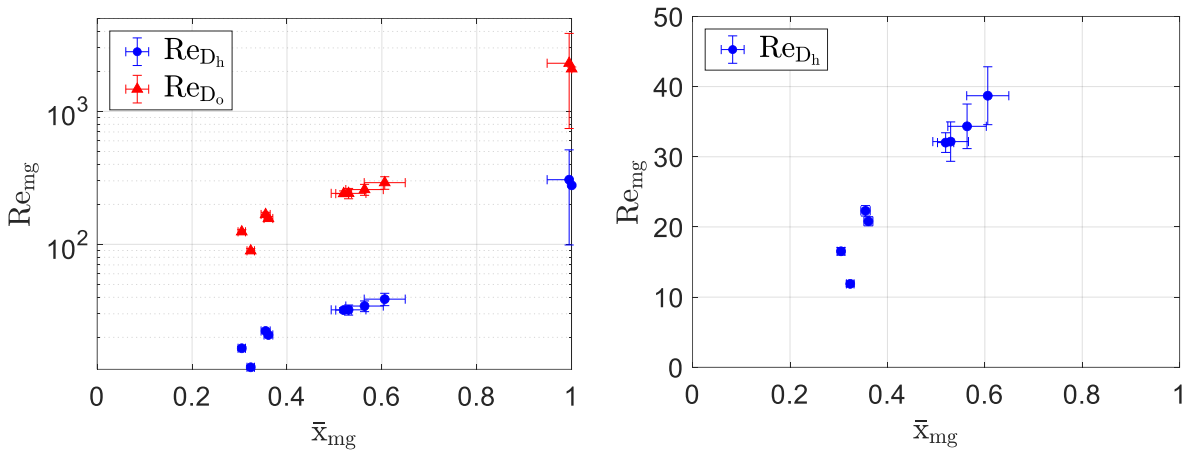

Figure 5.49. Reynolds number as a function of average quality of the mixed gas.

Figure 5.49(a) illustrates the Reynolds number of the mixed gas as a function of average quality of the gas mixture. Figure 5.49(b) presents a selection of the data for a smaller range of Re_{mg}. The Re_{mg} increases with average quality of the gas mixture as the average. Re_{D_h} uses the hydraulic diameter to calculate Re_{mg} as given in Eqs. (5.43) and (5.44) while Re_{D_o} uses the outer diameter of the finned-tube, D_o. It is common in the literature to calculate the Reynolds number for shell and tube bundles using this parameter and so both definitions are examined [27]. As seen, Re_{D_h} and Re_{D_o} give significantly different values for Re_{mg}. The Re_{mg} in the two-phase region (for average qualities of 0.32 to 0.61 for the data collected) ranges from 12 to 39 when using D_h as the characteristic diameter and ranges from 90 to 291 when using D_o. The relative uncertainty of Re_{mg} ranges from 3% to 11% for qualities in the two-phase region. Using either D_h or D_o as the characteristic diameter for Re_{mg} reflects that the Reynolds number in the two-phase region is low.

5.5.3. Measured Heat Transfer Coefficients

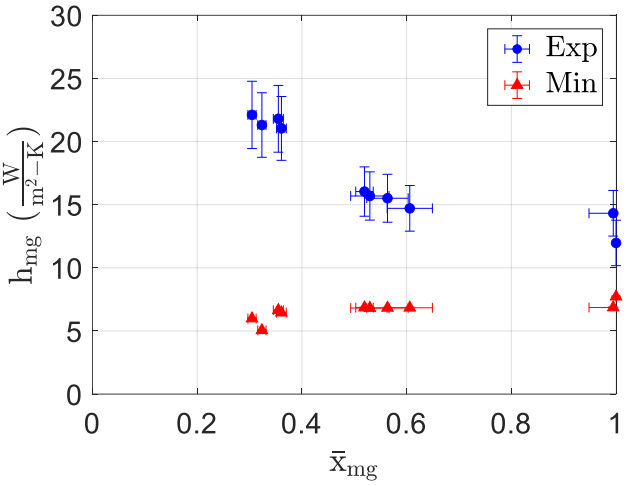

Figure 5.50. Measured and minimum h_{mg} as a function of average quality of the mixed gas.

Figure 5.50 illustrates the experimental heat transfer coefficient of the mixed gas as a function of the average quality of the gas mixture. The most significant characteristic of this plot is the magnitude of h_{mg}. The measured h_{mg} ranges from 12 to 22 W/m^2-K with uncertainties of 12-15%. The h_{mg} at a quality of 1 was measured to be 12 W/m^2-K while the h_{mg} within the two-phase region increased to the 15 to 22 W/m^2-K range. These very low values of the h_{mg} reveal that the shell-side of the GH heat exchanger may be the dominant thermal resistance in the heat exchanger for these flow conditions.

Figure 5.50 also shows a comparison of the measured h_{mg} to one estimate of the theoretical minimum heat transfer coefficient that might exist for the mixed gas, h_{min}. For laminar flow, the thermal boundary layer can be approximated as a conduction resistance to heat transfer. Therefore, the heat transfer coefficient can be written approximately as:

$$h \approx \frac{k}{\delta_t} \tag{5.60}$$

where k is the thermal conductivity of the fluid and δ_t is the thermal boundary layer thickness. The minimum k is the gas only thermal conductivity, k_g, and the maximum height of δ_t is the height between the outer diameter of the mandrel and the inner diameter of the shell. Therefore, the minimum theoretical htc of the mixed gas is given by Eq. (5.61):

$$h_{min} = \frac{k_g}{(D_s - D_m)/2} \tag{5.61}$$

As seen in Figure 5.50, the measured h_{mg} is above h_{min}. At high qualities, the measured h_{mg} is 33% larger than the theoretical minimum. As quality decreases, the k_{mg} increases from k_g to the liquid only thermal conductivity k_l. This results in a htc further increased from the theoretical minimum. The measured h_{mg} is 280% larger than the theoretical minimum at the lowest measured quality of 0.32.

5.5.4. Measured Friction Factor

The pressure drop of the mixed gas as a function of quality is shown in Figure 5.51(a). The friction factor of the mixed gas as a function of quality and Reynolds number is shown in Figure 5.51(b) and Figure 5.51(c), respectively. As previously noted, the uncertainties in the inlet and outlet pressures are the largest contributors to the uncertainty in the friction factor at low qualities of 0.32 to 0.36. At these low qualities, the pressure measurements at the inlet and outlet are within the uncertainty of the pressure transducers and thus the values of the pressure drop and friction factor are not meaningful. This data has been omitted from the plots.

Nonetheless, a selection of data collected captured meaningful results for the friction factor of the mixed gas. At qualities of 0.52 to 0.61, the friction factors ranged from 20 to 35 with uncertainties of 10 to 12% and at a quality of 1, the friction factor is 3.1 with an uncertainty of

20%. As shown in Figure 5.51(b), the friction factor behaves as expected with an increase in the friction factor as the Reynolds number decreases.

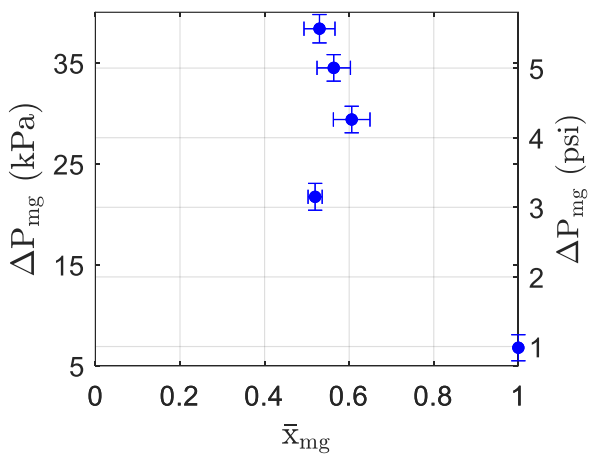

(a)

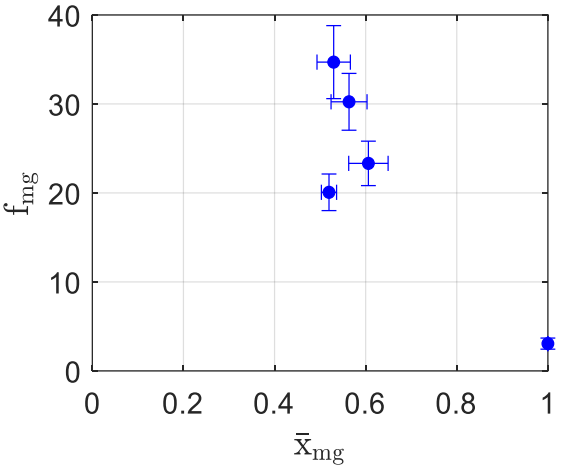

(b)

Figure 5.51. The pressure drop of the mixed gas (a) and friction factor (b) as a function of average quality. The friction factor of the mixed gas as a function of Reynolds number (c).

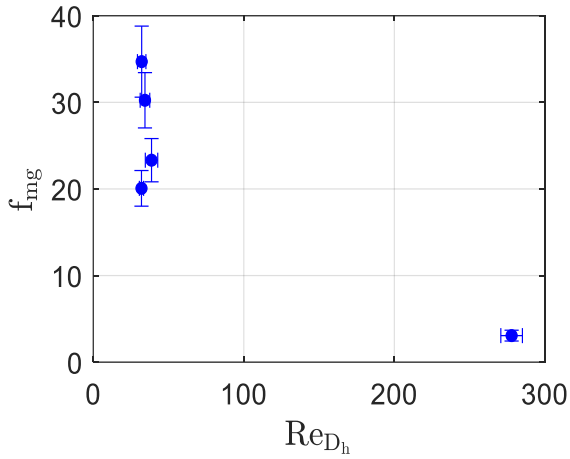

(c)

5.5.5. Bias in Measurements

For the experimental set-up, there are three phenomena that can produce bias error – self heating of PRTs, heat leak due to axial conduction through the PRT wires, and heat loss due to convection along the unfinned portion of the finned-tube in the test section for the helium stream. Self-heating of the PRTs is the generation of heat due to the excitation provided by the current source. The self-heating of the PRTs was tested by providing 0.3, 1.0, and 3.0 Amps as excitation.

A measurably different reading was not observed for any of these conditions. The heat leak due to conduction is controlled by wrapping the PRT wires around the support structure submerged in flow for the in-stream PRTs.

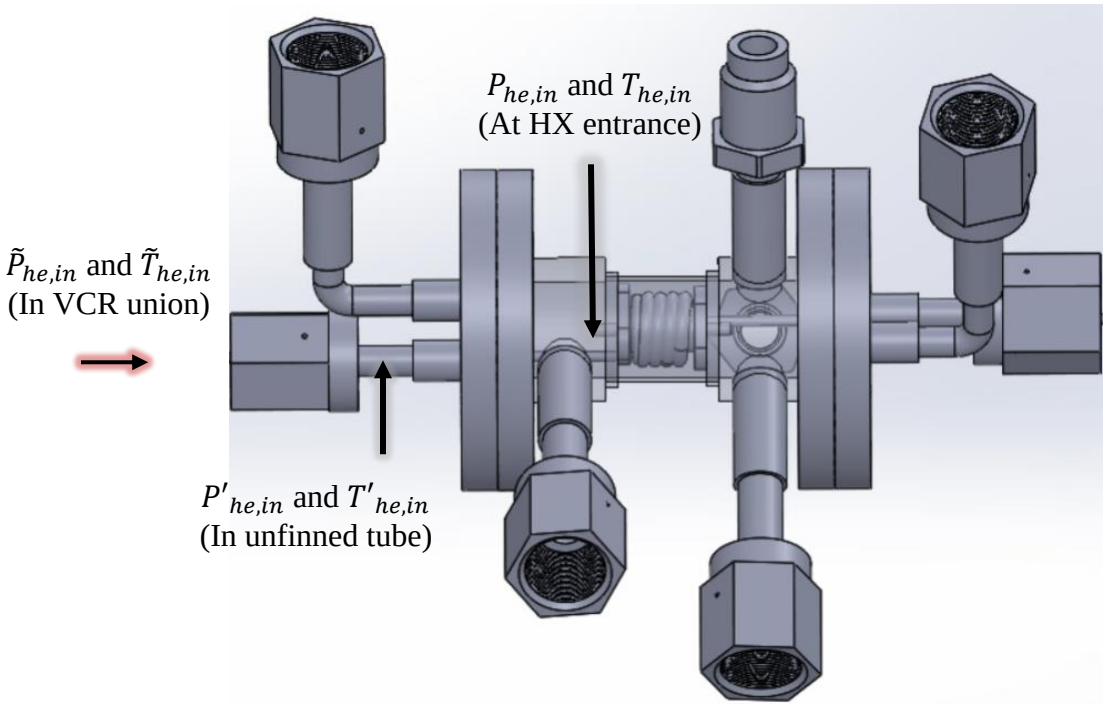

Figure 5.52. Illustration of bias in temperature and pressure measurements of the helium stream at the inlet to the test section.

Figure 5.52 illustrates the sources of bias in temperature and pressure measurements of the helium stream at the inlet to the test section. The pressure and temperature measurements of the helium, $\tilde{P}_{he}$ and $\tilde{T}_{he}$, are located in the 3.18 mm (1/8 inch) VCR union-crosses before the shell of the test section. Eq. (5.8) accounts for the change in pressure and temperature of the helium that occurs between the 6.35 mm (1/8 inch) VCR union and the small inner diameter of the tube for the helium stream. In the above calculations, this was considered to be the pressure and temperature of the helium at the inlet of the heat exchanger. However, there is approximately 25 mm (1 inch) of un-finned tube between the 3.18 mm (1/8 inch) VCR union and the inlet of the heat exchanger. The un-finned tubing is surrounding by heat shrink to reduce the heat loss due to

convection with the mixed gas, as shown in Figure 5.53. Nonetheless, pressure drop along this tube and heat loss due to convection with the mixed gas will reduce the inlet pressure and temperature to the heat exchanger. Likewise, at the exit of the heat exchanger, there is a 25 mm (1 inch) section of un-finned tube before the helium exits the tube and expands into the 6.35 mm (1/8 inch) VCR union. This will also impact the outlet pressure and temperature of the heat exchanger.

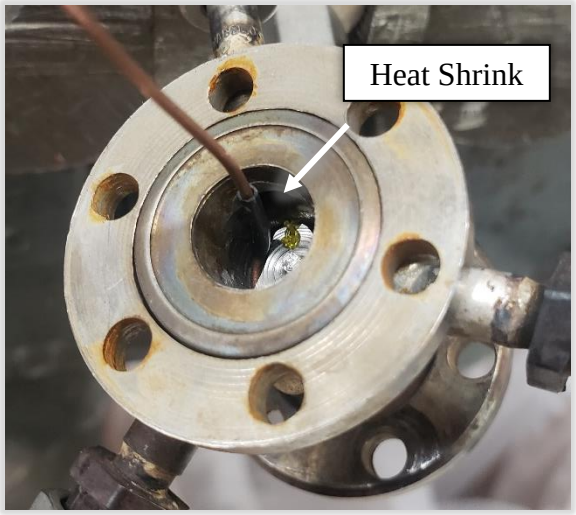

Figure 5.53. Photo of heat shrink around unfinned portion of finned-tube.

Calculations to account for the changes in pressure and temperature are incorporated in the data reduction. The pressure drop along these sections of tube are calculated using the internal flow correlations in EES [83]. As the mixed gas changes temperature by 3 K or less within the shell, the convection losses are modeled as internal flow to a constant ambient temperature (the average temperature of the mixed gas). For the inlet, an energy balance on the pipe is given as Eq. (5.62):

$$T_{he,in} = \bar{T}_{mg} - \left(\bar{T}_{mg} - T'_{he,in}\right) \exp\left(-\frac{UA}{\dot{m}_{he} cp_{he}}\right) \tag{5.62}$$

For the outlet, an energy balance is given as Eq. (5.63):

$$T'_{he,out} = \bar{T}_{mg} - \left(\bar{T}_{mg} - T_{he,out}\right) \exp\left(-\frac{UA}{\dot{m}_{he} cp_{he}}\right) \tag{5.63}$$

$T'_{he,in}$ and $T'_{he,out}$ are the temperatures calculated from Bernoulli's equation given in Eq. (5.8) and UA is the inverse of the total resistance. The total resistance is given as the sum of the resistances

due to convection from the helium to the inner surface of the tube, radial conduction through the 70/30 CuNi tube, radial conduction through the heat shrink, and convection with the mixed gas on the outside of the tube. The heat shrink is modeled as polyvinyl chloride (PVC) with a thickness of 0.165 mm (0.0065 inch). The htc and friction factor of the mixed gas with the bias accounted for is referred to as the corrected heat transfer coefficient, $h_{c,mg}$, and friction factor, $f_{c,mg}$, of the mixed gas.

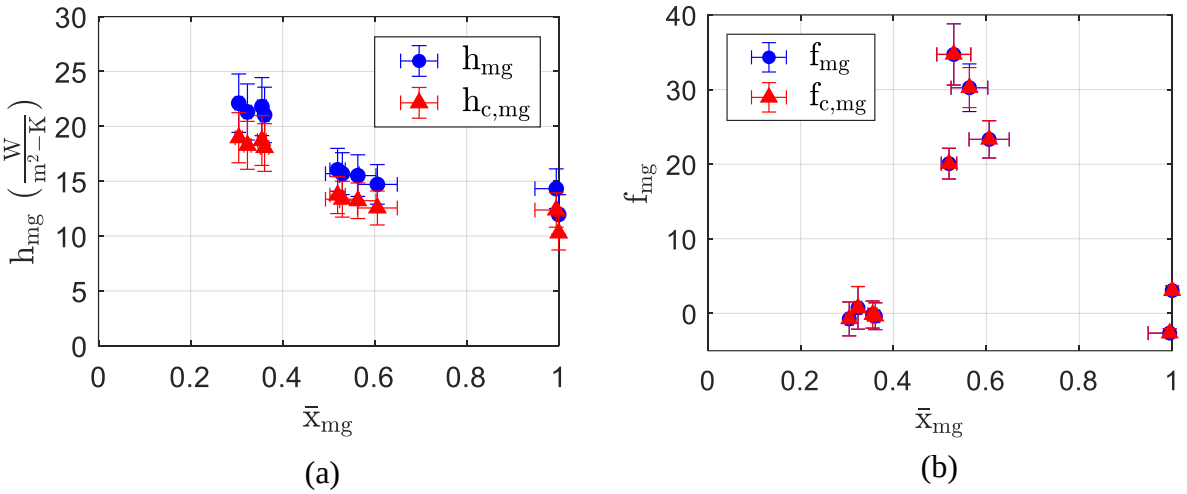

(a) (b)

Figure 5.54. Comparison of the mixed gas heat transfer coefficient (a) and friction factor (b) with and without consideration of bias in measurements.

Figure 5.54 illustrates the heat transfer coefficient and friction factor with and without the consideration of the bias in measurements considered. Figure 5.54(b) demonstrates that there is no significant difference in f_{mg} and $f_{c,mg}$. Without the bias in measurements considered, there is a 0.2% or less error in the f_{mg}. In contrast, Figure 5.54(a) demonstrates that there is a significant bias error of 16-17% in the h_{mg}. The corrected heat transfer coefficient, $h_{c,mg}$, is decreased and ranges from 10 to 19 W/m^2-K with uncertainties of 12 to 15%. Nonetheless, these values of the $h_{c,mg}$ are still very low.

5.5.6. Nusselt Number of the Mixed Gas

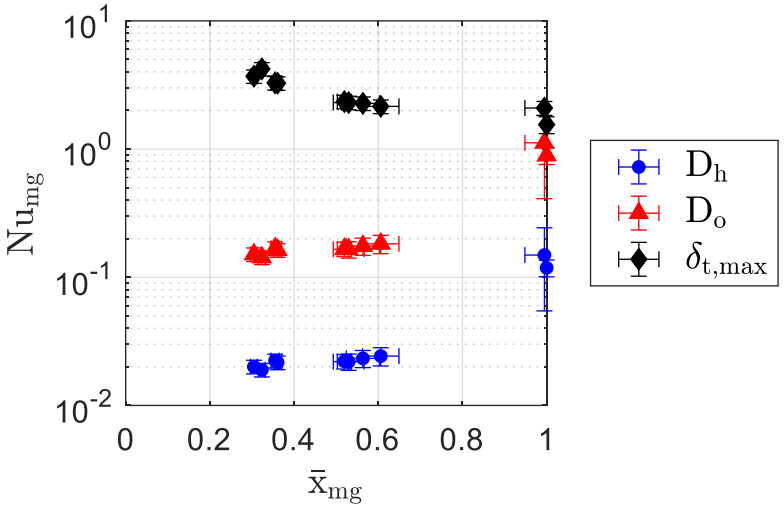

(a)

Figure 5.55. Nusselt number as a function of average quality of the two-phase mixed gas.

Figure 5.55(a) illustrates the Nusselt number as a function of the average quality of the gas mixture defined with $h_{c,mg}$. The Nusselt number is shown using the characteristic lengths of D_h and D_o previously mentioned. For an average quality of the mixed gas ranging from 0.31 to 0.62, the Nusselt number varies from 0.019 to 0.024 using D_h and from 0.14 to 0.18 using D_o. However, the most relevant values of characteristic length and thermal conductivity to use in defining the Nusselt number are $\delta_{t,max}$ and k_g. $\delta_{t,max}$ is the maximum height of the boundary layer thickness given by the height between the outer diameter of the mandrel and the inner diameter of the shell and k_g is the gas-only thermal conductivity. This definition of the characteristic length and thermal conductivity make the most physical sense for the Nusselt number. For laminar flow, the Nusselt number is a length ratio - a ratio of the maximum thermal boundary layer thickness to the actual thermal boundary layer thickness. The Nu_{mg} using $\delta_{t,max}$ and k_g is also shown on Figure 5.55 as a function of quality. For qualities of 0.31 to 0.62, the Nusselt number varies from 2.2 to 4.2.

5.5.7. Comparison of Corrected HTC to Existing Correlations

Croft and Tebby [28], Gupta et al [27], and Howard et al [32] provide correlations for the heat transfer coefficient of a single-phase pure gas on the shell side of a GH heat exchanger. The correlation by Timmerhaus and Flynn [35] is also recommended by Gupta et al for this geometry even though the correlation was developed for an edge-wound copper helix wrapped in an annular space of tube-in-tube heat exchanger.

The correlation by Croft and Tebby was developed for GH heat exchangers with high-finned tubes (i.e. h_f > 1.5 mm (0.06 inch)) and is given as:

$$h_{CT} = 0.021 c \dot{m}^{0.8} \mu^{0.2} A_{c,hc}^{-1} (\pi D_o)^{0.2} \tag{5.64}$$

A range of Reynold numbers for which the correlation is suited was not mentioned. Gupta et al recommends the use of this correlation for heat exchangers with no clearance when the shell side free flow area is defined using the hypothetical cylinder concept [27]. The shell side free flow area using the hypothetical cylinder concept, $A_{c,hc}$, is given as:

$$A_{c,hc} = \frac{\pi^2 D_e}{4 D_f} (D_f^2 - D_o^2)(1 - N_f th) \tag{5.65}$$

Calculated as such, the heat transfer coefficient has an error band of $\pm 10\%$.

The correlation by Gupta et al. is suited for Re_f of 500 to 1900 for GH heat exchangers with clearances of 0.7 to 1.2 mm (0.03 to 0.05 inch). The error bands are $\pm 10\%$ or $\pm 20\%$ for clearances of 1.2 mm (0.05 inch) and 0.7 to 1 mm (0.03 to 0.04 inch), respectively. The correlation is given as:

$$h_G = 0.19 \left(\frac{k}{D_o}\right) Re_{f,vc}^{0.703} Pr^{1/3} \tag{5.66}$$

The effective Reynolds number, $Re_{f,}$, estimates the actual flow rate over the fins (with some flow moving through the clearance). Re_f is given as follows:

$$Re_f = \frac{Re_{D_h}}{k_{bp} + 1} \tag{5.67}$$

where the bypass factor, k_{bp}, is the ratio of the clearance cross-sectional area to the free-flow area of the fins. Gupta et al. recommends the use of his correlation with the free flow area based upon the free volume concept. The shell side free flow area using the free volume concept, $A_{c,vc}$, is given as:

$$A_{c,vc} = \pi D_e \left(D_f - \frac{\pi}{4D_f} \left(D_o^2 \left(1 - N_f th \right) + D_f^2 N_f th \right) \right) \tag{5.68}$$

Teflon tape was wrapped around the heat exchanger of the test section to provide a snug fit and as such there is no clearance between the fins and the inner diameter of the shell. Thus, k_{bp} is zero and Re_f is equal to Re_{D_h} in the above equations. As there is no clearance, the correlation by Gupta has larger uncertainty than is reported. Nonetheless, error bands of $\pm$20% are shown in Figure 5.56.

The correlation by Timmerhuas and Flynn is given as:

$$h_{TF} = 0.118 \frac{\dot{m}c}{A_{c,vc}} {Re_{D_h}}^{-0.3} Pr^{-\frac{2}{3}} \tag{5.69}$$

It is suited for Re_{D_h} of 400 to 10,0000. Gupta et al. recommends the use of this correlation for heat exchangers with no clearance when the shell side free flow area is defined using the free volume concept, as given in Eq. (5.68) [27]. Calculated as such, the heat transfer coefficient has an error band of $\pm$20%.

The correlation by Howard et al. was developed numerically and experimentally validated for Re_{D_h} of 100 to 500. Additionally, it was compared to the experimental data of Gupta et al and Croft and Tebby. The correlation is designated for both the laminar and turbulent flow regimes and is given as:

$$h_H = \begin{cases} 0.4019\, Re_{D_h}{}^{-0.5393} \lambda_f^{0.057} \left(\dfrac{\dot{m}c}{A_{c,mg}}\right) Pr^{-2/3} & 100 < Re_{D_h} < 3000 \\ 0.0584\, Re_{D_h}{}^{-0.3044} \lambda_f^{0.057} \left(\dfrac{\dot{m}c}{A_{c,mg}}\right) Pr^{-2/3} & 3000 \leq Re_{D_h} < 10{,}000 \end{cases} \tag{5.70}$$

where λ_f is the flow channel aspect ratio defined as:

$$\lambda_f = \frac{(D_f - D_o)/2}{p_f - th} \tag{5.71}$$

The author reports an error band of $\pm 3\%$. These correlations from the literature are summarized in Table 5.20.

Source	Correlation	Reynolds Number $\pm$ Error Band
Croft and Tebby [32, 5]	$h_{CT} = 0.021 c \dot{m}^{0.8} \mu^{0.2} A_{c,hc}^{-1} (\pi D_o)^{0.2}$	Range for Re not available $\pm 10\%$
Gupta et al [5]	$h_G = 0.19 \left(\dfrac{k}{D_o}\right) Re_f{}^{0.703} Pr^{1/3}$	$500 < Re_f < 1900$ $> 20\%^*$
Timmerhaus and Flynn [33, 5]	$h_{TF} = 0.118 \dfrac{\dot{m}c}{A_{vc}} Re_{D_h}{}^{-0.3} Pr^{-\frac{2}{3}}$	$400 < Re_{D_h} < 10{,}000$ $\pm 20\%$
Howard et al [7]	$h_H = \begin{cases} 0.4019\, Re_{D_h}{}^{-0.5393} \lambda_f^{0.057} \left(\dfrac{\dot{m}c}{A_{c,mg}}\right) Pr^{-2/3} \\ 0.0584\, Re_{D_h}{}^{-0.3044} \lambda_f^{0.057} \left(\dfrac{\dot{m}c}{A_{c,mg}}\right) Pr^{-2/3} \end{cases}$	$100 < Re_{D_h} < 3000$ $3000 \leq Re_{D_h} < 10{,}000$ $\pm 3\%$

Table 5.20. Correlations for single-phase pure gases in similar geometries to the shell side of the GH heat exchanger.

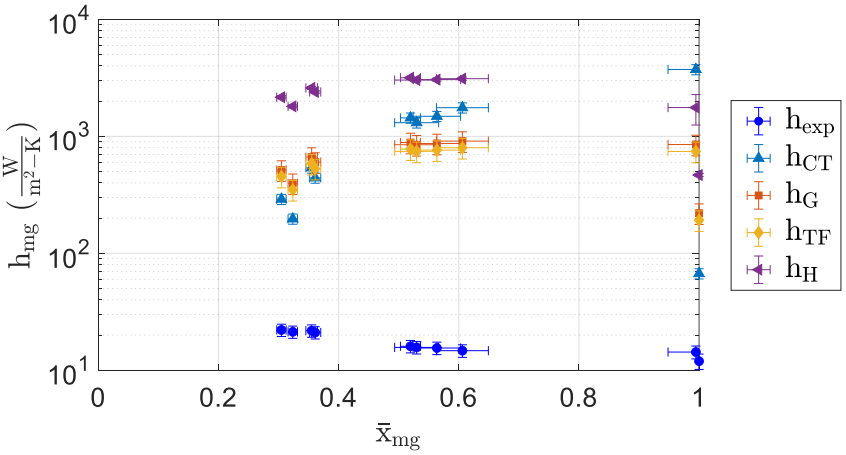

Figure 5.56. Measured h_{mg} compared to select correlations for pure gases as a function of average quality of the mixed gas.

Figure 5.56 illustrates the $h_{c,mg}$ and the predicted h_{mg} from the correlations of Croft and Tebby, h_{CT}, Gupta et al, h_G, Timmerhaus and Flynn, h_{TF}, and Howard et al, h_H. As seen, the measured h_{mg} is significantly (1-2 orders of magnitude) lower than the estimated heat transfer coefficients from the pre-existing correlations. While the correlations listed in Table 5.20 are applicable for the shell side of a GH heat exchanger, these correlations were developed for *single-phase pure* fluids at relatively high Reynolds number. These correlations cannot be directly applied for two-phase multi-component mixtures such as the one tested without experimental validation and adjustment. Additionally, the Reynolds numbers for the experimental measurements are an order of magnitude lower than the recommended ranges for the correlations of Gupta et al, Timmerhaus and Flynn, and Howard et al. Therefore, these correlations are not suited to accurately predict the htc of a two-phase multi-component mixture on the shell side of a GH heat exchanger for the operating conditions investigated.

5.5.8. Comparison of Measured Friction Factor to Existing Correlations

Gupta et al [88] and Howard et al [32] provide correlations for the pressure drop of a single-phase pure gas on the shell side of a GH heat exchanger. The correlation by Gupta et al is given as:

$$f_G = 24.7 \cdot Re_f^{-0.489} \tag{5.72}$$

where the effective Reynolds number is defined using the projected area method for the shell side free flow area as given in Eq. (5.39). (Note Re_f is different $Re_{f,vc}$ in the corrleation for the h_{mg} by Gupta et al [27]. $Re_{f,vc}$ is defined using the free volume concept for the shell side free flow area as previously discussed.) The correlation is suited for Re_f of 25 to 155 with an error band of $\pm 5\%$. The correlation by Howard et al is given as:

$$f_H = \begin{cases} 0.6094 \cdot Re_{D_h}^{-0.6017} \lambda_f^{0.758} & 100 < Re_{D_h} < 2000 \\ 0.0139 \cdot {Re_{D_h}}^{-0.1009} \lambda_f^{0.758} & 2000 \leq Re_{D_h} < 10{,}000 \end{cases} \tag{5.73}$$

The correlation is suited for Re_{D_h} of 100 to 10,0000 with an error band of ± 3 %.

Figure 5.57 illustrates the measured f_{mg} and estimated friction factor of the mixed gas from the correlation by Gupta et al, f_G, and Howard et al, f_H. The Reynolds number for the measurement at a quality of 1 is larger than the recommend range Gupta et al but within the recommended range for Howard et al. The measured f_{mg} is most similar to the estimated values at this quality. The measured f_{mg} at a quality of 1 is 3.1, approximately double the predicted value from Gupta et al. of 1.6 and a magnitude larger than the prediction from Howard et al of 0.032. As the quality of the mixed gas decreases to the range of 0.52 to 0.61, the Reynolds number decreases into the range recommended for the correlation by Gupta et al and out of the range recommended for Howard et al. However, the measured and predicted f_{mg} become more dissimilar with measured values 5 to

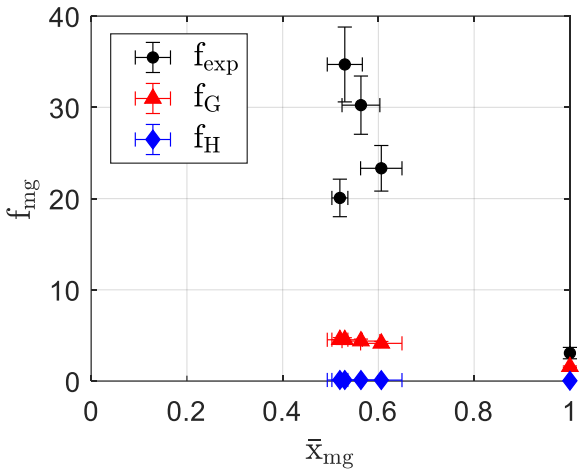

Figure 5.57. Measured f_{mg} compared to correlation for single-phase pure gases as a function of average quality of the mixed gas.

8 times greater than the predicted values of Gupta et al. Overall, the measured f_{mg} is increased compared to the existing correlations for single-phase pure fluids and again it is concluded that pre-existing correlations are not suited to accurately predict the friction factor of a two-phase multi-component mixture on the shell side of a GH heat exchanger for the operating conditions investigated.

5.5.9. Significance for MGJT Cryocooler Design

While the heat transfer coefficient of the return stream in a GH heat exchanger had been purposed as the key parameter to determining the behavior of the entire heat exchanger for a JT cryocooler operating with mixed coolants, there was no data or theory in open literature that allowed for an estimate of the *magnitude* of the h_{mg}. As seen above, the existing correlations for single-phase pure fluids do not accurately predict the h_{mg} and thus using these in cryocooler design leads to significant error. With the data collected in the above study, it is possible to investigate the importance of the heat transfer of the mixed gas on the shell side of a GH heat exchanger in the overall performance of a MGJT cryocooler by estimating the conductance and comparing the

relative resistances of the convection inside the coiled high-pressure finned-tube with the convection of the mixed gas on the shell-side.

The conductance and corresponding resistances for a GH heat exchanger were given in Eqs. (5.29) through (5.34). To analyze the performance of a MGJT cryocooler, the resistance due to convection of the helium on the inside of the coiled finned-tube is replaced with a resistance due to convection of the mixed gas flowing internally through the coiled finned-tube, $R_{in,mg}$, given by:

$$R_{mg,t} = \frac{1}{h_{mg,t}\pi D_i L_t} \tag{5.74}$$

where $h_{mg,t}$ is the heat transfer coefficient of the mixed gas flowing internally through the coiled finned-tube.

Barraza et al [50] measured the local flow boiling heat transfer coefficients for mutli-component mixtures at cryogenic temperatures in horizontal, small diameter tubes. A scaling factor, SF, is estimated using the built-in function for helical pipe flow in EES to determine the htc of a pure fluid in a helically coiled tube of dimensions and operating conditions of the test section and comparing it to the htc of the same fluid flowing through a horizontal tube of dimensions and operating conditions used in experimental measurements of Barraza et al. Assuming the heat transfer coefficient of mixed gases and pure fluids scale the same between two different geometries, the scaling factor is applied to experimental data from Barraza et al for the htc of mixed gases in a horizontal tube to make a loose approximation of the $h_{mg,t}$. For clarity, the process is outlined in Figure 5.58.

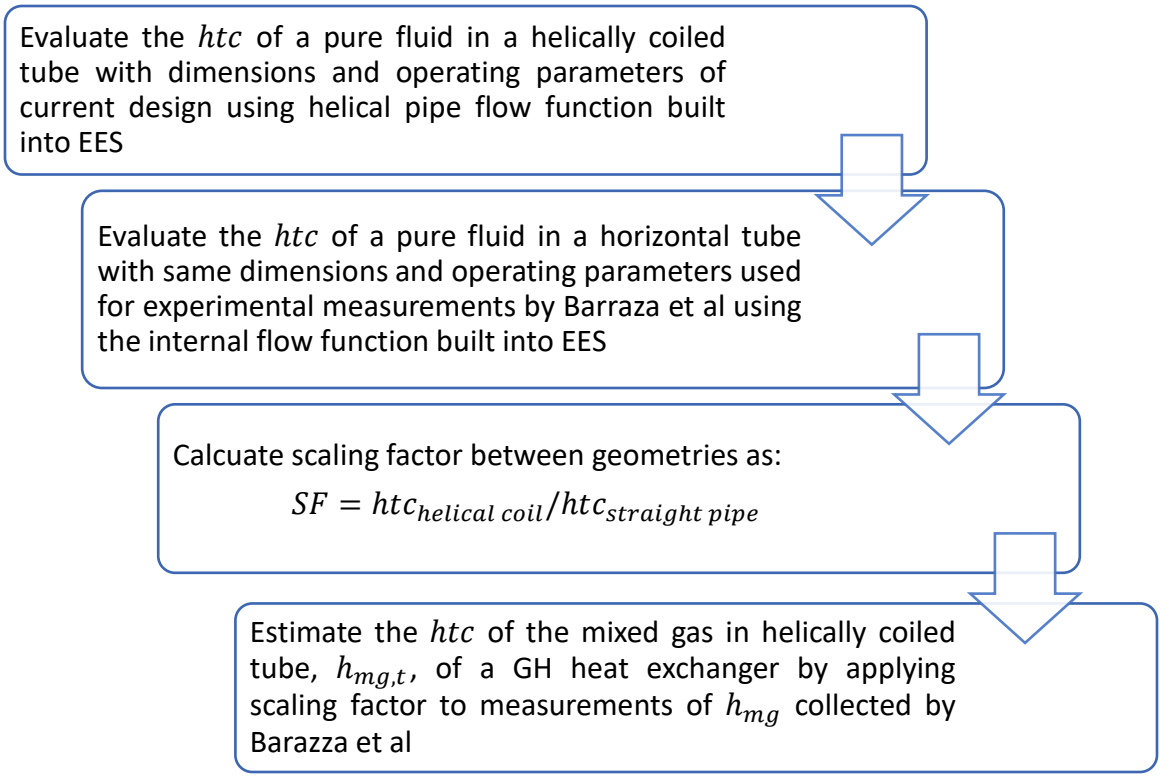

Figure 5.58. Flow diagram for prediction of $h_{mg,t}$.

The SF is calculated for a mass flow rate of 0.15 g/s and an operating pressure of 827 kPa (120 psi) to give a 3:1 pressure ratio between the high- and low-pressure streams of the GH heat exchanger. R32 and R14 are investigated as pure operating fluids. Figure 5.59(a) illustrates the dependency of the SF upon the operating fluid. The SF remains consistently at a value of 4 for both R14 and R32 unless the stream in the straight pipe has changed phases before a phase change is experienced in the helical coil geometry. After both geometries have experienced a phase change, the SF again approaches a value of 4.

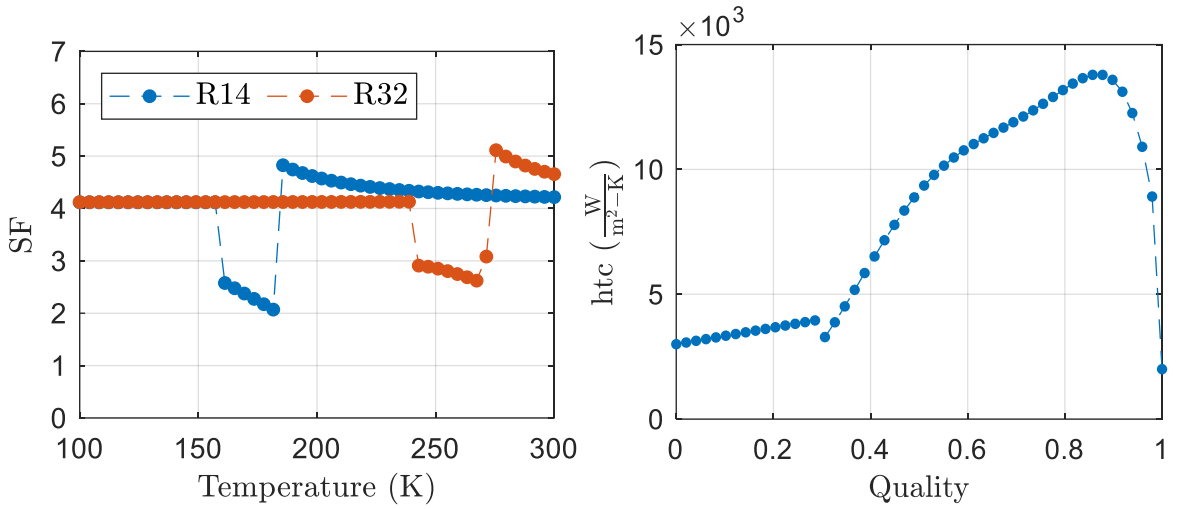

(a) (b)

Figure 5.59. Scaling factor as a function of temperature (a) and predicted $h_{mg,t}$ as a function of quality for a synthetic refrigerant mixture (b).

The values of the measured h_{mg} by Barazza et al for a synthetic refrigerant mixture of R14, R23, R32, R134a and Argon were multiplied by the SF of 4 to loosely predict the $h_{mg,t}$. Figure 5.59 (b) shows the prediction of $h_{mg,t}$ as a function of quality of the mixed gas. From this rough estimation, $h_{mg,t}$ is predicted to fall between 2,000 to 14,000 W/m^2-K. This prediction is used to estimate the resistance to convection of the mixed gas inside the helically coiled tube of the test section, $R_{mg,t}$ with a mass flow rate of 0.15 g/s and an operating pressure of 827 kPa (120 psi).

While the range of h_{mg} measured by Barraza et al provide insight into the thermal characteristics of two-phase multi-component synthetic refrigerant mixtures, the mixture measured by Barraza et al does not have the same make or composition as the mixture tested in the shell side of the GH test section. Thus, the h_{mg} measured by Barraza et al may not reflect the actual values of the R32 and R14 mixture in the same straight tube. To make a conservative estimate of $h_{t,mg}$, the htc of each pure component is investigated over the operating range of interest. Figure 5.60 illustrates the lower limit of the htc of each pure component at a mass flow rate of 0.15 g/s,

operating pressure of 827 kPa (120 psi) and flowing through a helically coiled tube of the same geometry as the test section. The lowest htcs occurs when both R14 and R32 are single phase. Using an ideal mixing rule for the two pure components (i.e. a linear mole fraction weighting) and assuming a gas mixture composition of 80% R32 and 20% R14, the lowest single-phase htc estimated for the mixture in the operating regime of interest is approximately 2000 W/m^2-K. Heat transfer coefficients of mixtures are degraded compared to estimates using the ideal mixing rules. To make a very conservative estimate, let us degrade the htc of the ideal mixture by 75% to give a lower bound on the estimated $h_{mg,t}$ of 500 W/m^2-K.

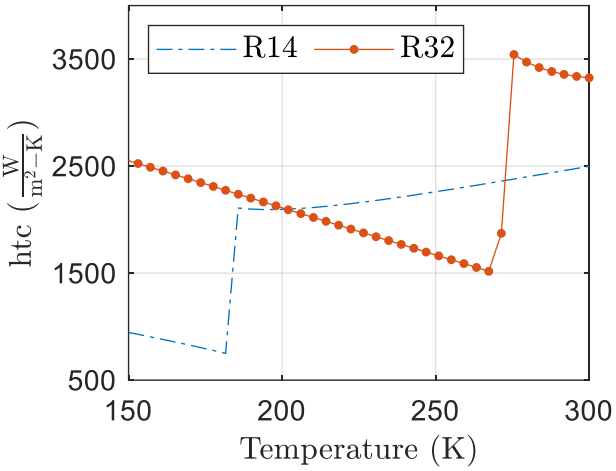

Figure 5.60. Heat transfer coefficients as a function of temperature for pure components for estimate of $h_{mg,t}$.

The total resistance to convection from the mixed gas in the shell side of the GH test section, $R_{mg,s}$, is the sum of the resistance of convection from the finned and unfinned surfaces. Figure 5.61 compares $R_{mg,s}$ using the measured and corrected $h_{c,mg}$ to $R_{mg,t}$ estimated using data collected by Barraza et al (Tube (B) in the figure) and the conservative estimate made by degrading the lower bound of the htc of the ideal mixture (Tube (IM) in the figure). The $R_{mg,s}$ is a over a magnitude lower than $R_{mg,t}$ even using the conservative estimate that $h_{mg,t}$ is 500 W/m^2-K. Using the data collected by Barraza et al, $R_{mg,s}$ is two magnitudes larger than $R_{mg,t}$ at low qualities of 0.32 to 0.36 and three magnitudes larger at qualities of 0.52 to 0.61. With either estimate, the resistance due to convection of the mixed gas on the shell side of the GH heat exchanger is

significantly larger than the resistance due to convection of the mixed gas in the helically coiled tube.

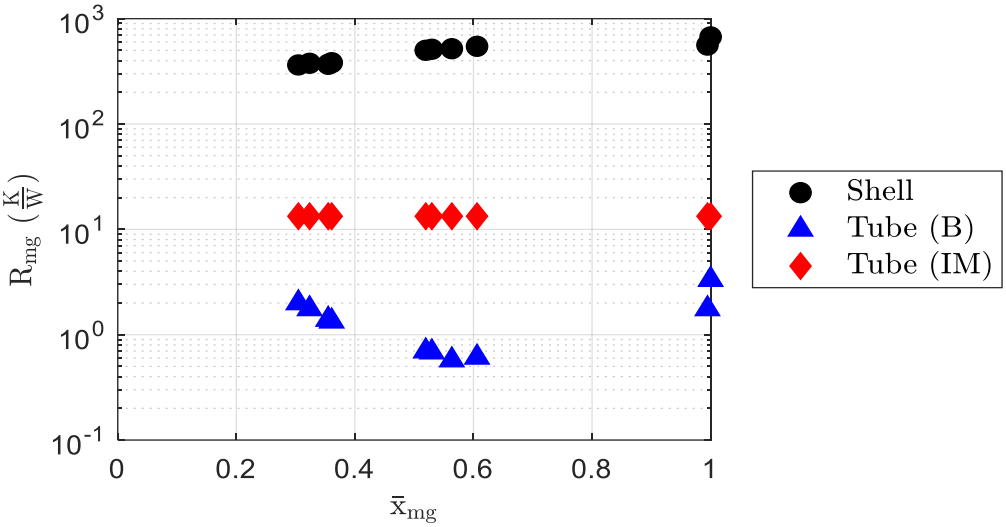

Figure 5.61. Comparison of convective resistances of the mixed gas in the helically coiled tube and shell-side of the GH heat exchanger.

As the dominant resistance in determining the conductance of the heat exchanger, the h_{mg} on the shell side is controlling the thermal performance of the heat exchanger. In cryocooler design, much time and attention should be paid to selecting a gas mixture with an increased h_{mg} on the shell side or adapting the design for better thermal performance. In addition, the experimental data collected in this study also indicates that the friction factor on the shell side of the GH heat exchanger is significant and must be taken into consideration during cryocooler design. All in all, to increase the performance of MGJT cryocoolers using a GH heat exchanger, further investigation of the thermal and pressure drop characteristics of mixed gases on the shell side of the heat exchanger must be pursued.

6. MGJT Cryocooler

A prototype MGJT cryocooler was designed and fabricated for future work of verifying and improving optimal mixture selection for a mixed gas Joule-Thompson (MGJT) cryocooler. A SolidWorks rendering of the cryocooler is shown in Figure 6.1 and dimensions are given in Table 6.1. Not shown for rendering simplicity in the software is the winding technique performed to construct the heat exchanger.

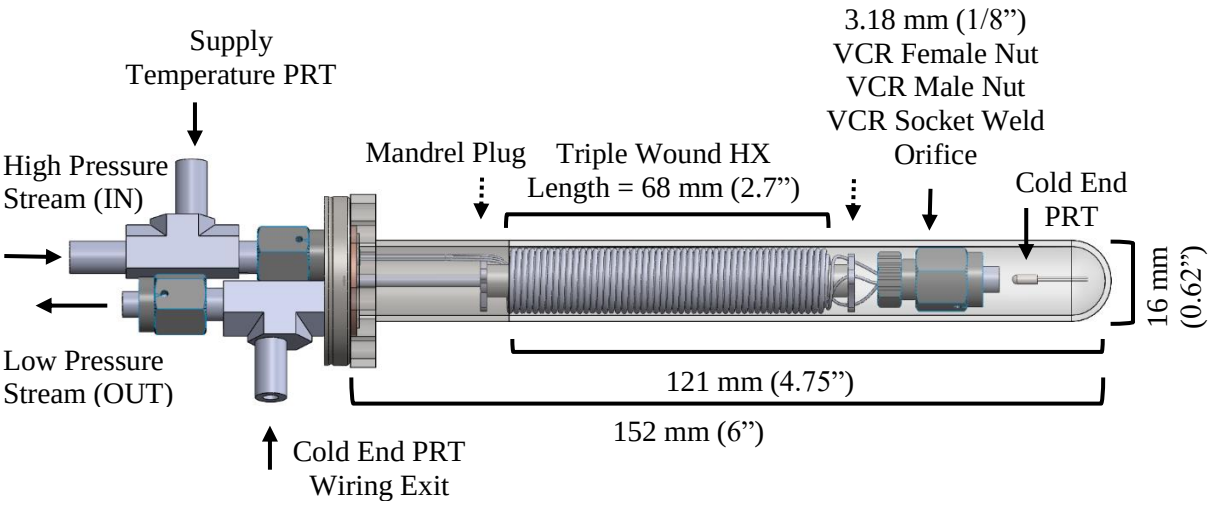

Figure 6.1. SolidWorks rendering of MGJT cryocooler.

	Parameter	SI (mm)	English (inch)	Source
Finned-tube	Inner diameter	0.305±0.025	0.012±0.001	Mfr. specs* [1]
	Outer diameter	0.508±0.025	0.020±0.001	Mfr. specs
	Diameter of fins	1.016±0.051	0.040±0.002	Mfr. specs
	Length	1524±3	60.000±0.125	Mfr. specs
	Thickness of fins	0.076±0.025	0.003±0.001	Mfr. specs
	Number of fins per unit length	3.74±0.20	95±5	Mfr. Specs
Mandrel	Inner diameter	4.750±0.013	0.1870±0.0005	Calipers
	Outer diameter	5.563±0.076	0.219±0.003	Calipers
	Length	67.882±0.013	2.6725±0.0005	Calipers
Shell	Inner diameter	12.954±0.013	0.510±0.0005	Micrometer
	Outer diameter	15.62±0.013	0.6150±0.0005	Calipers

Table 6.1. Dimensions of MGJT cryocooler.

Mfr. specs* = Manufacturer's specifications

6.1. Design and Fabrication

6.1.1. G10 Mandrel

Figure 6.2. Mandrel plugs.

The high-pressure stream enters the cryocooler and splits into three tubes with fins that are helically coiled around a hollow G10 mandrel filled with polystyrene foam. The three 70/30 CuNi finned-tubes are custom manufactured by Energy Transfer Durafin Tube and the sales drawing can be found in Appendix 8.14. [65]. The G10 mandrel is closed at both ends by stainless steel mandrel plugs shown in Figure 6.2. The mandrel plugs provide structure for the assembly of the heat exchanger while eliminating the flow path through the G10 mandrel. Manufacturing instructions for the mandrel plugs can be found in Appendix 8.7. The wiring for the cold end platinum resistance thermometers (PRTs) run through the mandrel plugs and G10 mandrel to the outlet of the ConFlat. Figure 6.3 shows the PRT wiring inside the mandrel as well as the assembled G10 mandrel.

Figure 6.3. PRT wiring inside mandrel and assembled G10 mandrel.

6.1.2. JT Orifice

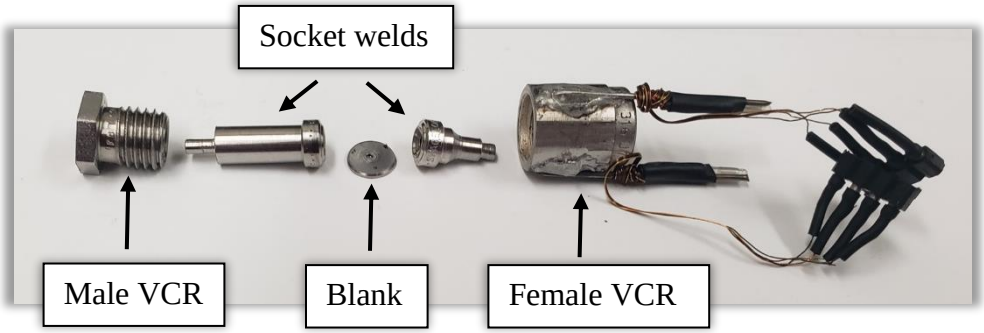

Figure 6.4. JT orifice assembly.

The three finned heat exchanger tubes merge back into one flow path at the JT valve. The JT orifice consists of a 3.18 mm (1/8 inch) blank with either a small diameter hole in its center or a ruby jewel orifice epoxied into a ledge on the blank. The orifice is held in position by 3.18 mm (1/8 inch) VCR male nut and female nut turned down to fit inside the glass dome. The JT orifice assembly is shown in Figure 6.4 and details of manufacturing the JT orifice can be found in Appendix 8.15. The low-pressure stream then returns to the outlet of the ConFlat by flowing over the fins on the outside of the high-pressure stream coiled finned-tubing. The heat exchanger and JT valve are enclosed by a 15.88 mm (5/8 inch) Kovar-to-7052 glass domed adapter manufactured by Larson Electronic Glass.

6.1.3. Winding of the Heat Exchanger

The design of the three finned heat exchanger tubes wound around the G10 mandrel was given much consideration. To reduce the possibility of flow maldistribution of the high-pressure stream and the resultant performance deterioration, the length of flow passage for each finned heat exchanger tube is the same. If the length of flow passage was not equal, shorter tubes would offer lower resistance and thus carry a higher rate of flow [89]. To maintain uniform flow of the low-pressure stream, the radial spacing of the finned heat exchanger tubes and monofilament line is uniform. Otherwise, the flow would not be uniform over the cross-section of the heat exchanger

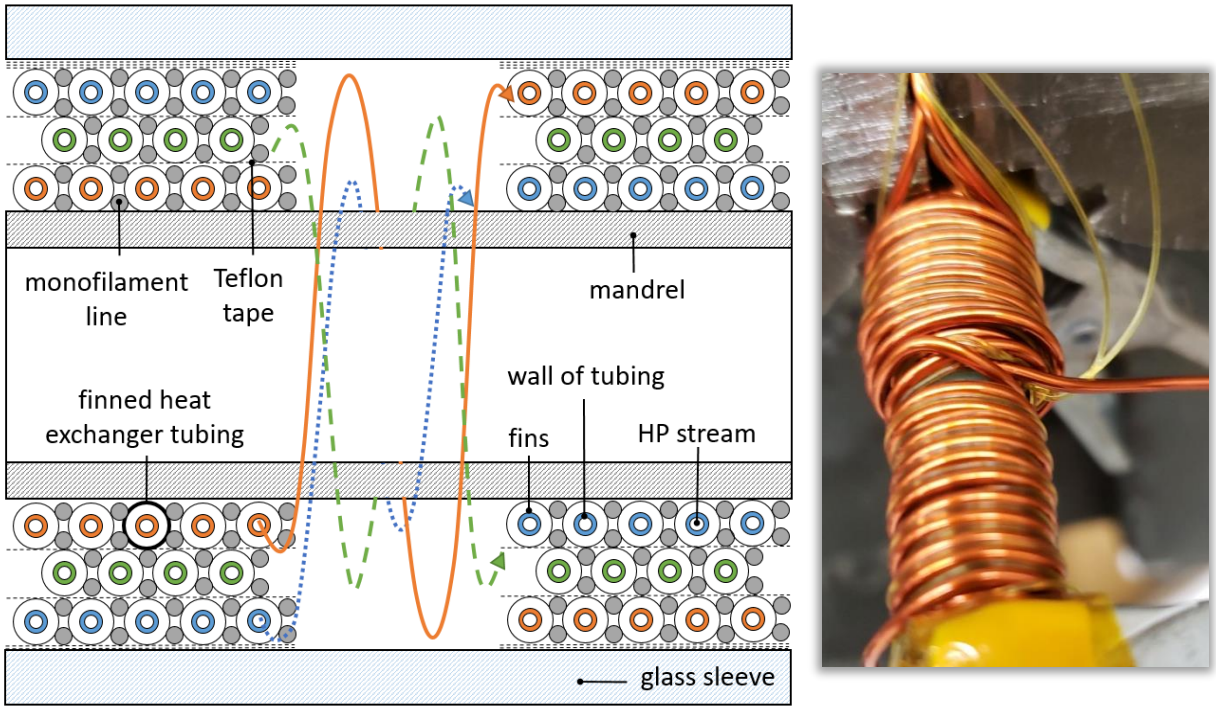

(a) (b)

Figure 6.5. Visualization of the winding technique used to construct the helically coiled heat exchanger (a) and a picture of the cross-over during a practice trial (b).

as the flow would follow the path of widest spacing [89]. The length of each finned heat exchanger tube when wound is the same to avoid flow maldistribution due to unequal temperature distributions within the wound finned tubes.

To maintain equal flow passage length, wound length and radial spacing, the inner and outer layers of the finned heat exchanger tubing are swapped three times on the G10 mandrel during construction. The middle layer of tubing remains in the middle throughout. An illustration of the cross-over technique is shown in Figure 6.5(a) (the length of the cross-over has been greatly exaggerated for illustrative purposes) and a picture of the cross-over technique from a practice winding is shown in Figure 6.5(b). Pictures of the prototype heat exchanger winding are shown in Figure 6.6. Each layer of finned heat exchanger tubing is wound in opposite directions with a layer of Teflon tape in between to assist with monofilament line placement on each layer. The heat

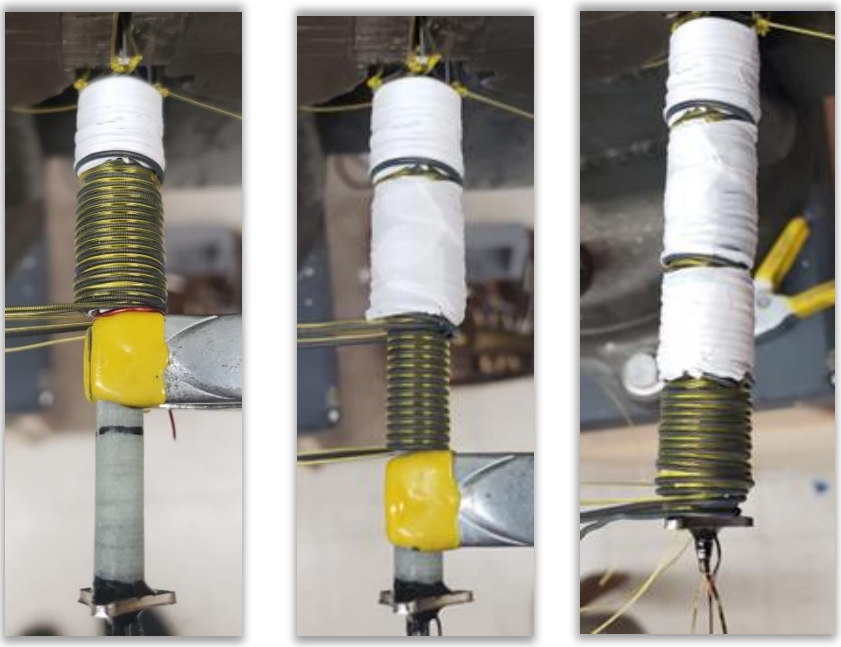

Figure 6.6. Cryocooler heat exchanger winding.

exchanger has an average outer diameter of 12.7 mm (0.50 inch). Additional Teflon tape is wrapped around the outside of the heat exchanger to create a snug fit with the glass dome.

6.1.4. Leak Tight Connections

Figure 6.7 highlights three joints within the cryocooler that require leak tight connections to maintain stream pressure and velocity. After the heat exchanger is wound and screwed into the ConFlat, the connection between the three finned heat exchanger tubes and the sleeve is soldered, as shown in Figure 6.8. This connection is accomplished by tinning the three heat exchanger tubes and carefully tinning around three 0.53 mm (0.021 inch) holes in the sleeve with Stay Brite 8. The

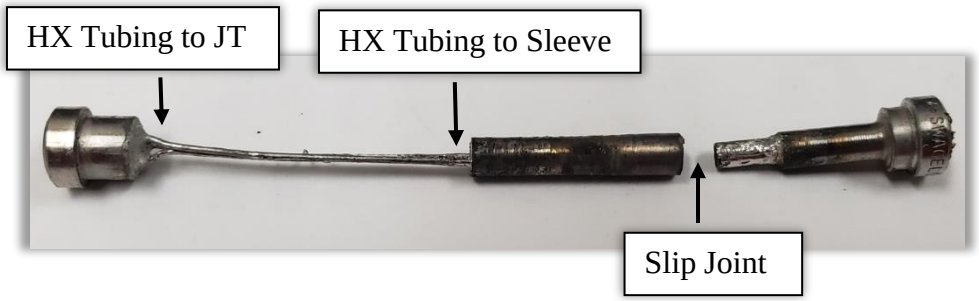

Figure 6.7. Leak tight connections within cryocooler.

joint is then heated through a copper block that is itself being heated by an acetylene torch. After sufficient heating, a drop of Stay-Clean flux is added to help the Stay Brite 8 run.

Figure 6.8. Soldering of heat exchanger tubing to sleeve.

The socket weld of the slip joint in Figure 6.7 is welded into the ConFlat and provides the connection between the inlet of the HP stream and the sleeve to the finned heat exchanger tubing. This joint allows for complete removal of the heat exchanger assembly from the ConFlat if desired or necessary. The slip joint is soldered together by tinning the lip of the socket weld and inside rim of the sleeve and then heating the joint through a copper block as was done for the previous connection. The set-up for soldering the slip joint is shown in Figure 6.9(a) and (b). In a similar manner, the connection between the three finned heat exchanger

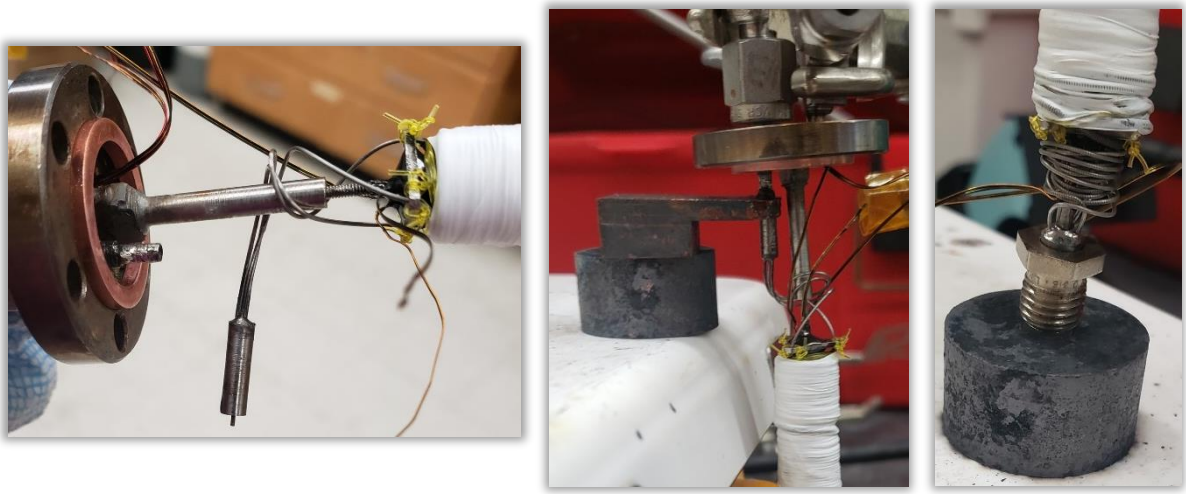

(a) (b) (c)

Figure 6.9. Soldering of the slip joint to the ConFlat (a and b) and solder of the heat exchanger tubing to JT orifice (c).

tubes and the socket weld leading into the JT orifice is soldered. The set-up for soldering this joint is shown in Figure 6.9(c).

6.1.5. Fully Assembled Cryocooler

Figure 6.10 shows the fully assembled MGJT cryocooler prototype without the glass dome including close-up images of the hot-end, cold-end and support structure for the two cold-end PRTs. To support the PRTs, a 3.18 mm (1/8 inch) VCR female nut was machined with two small groves and two small diameter steel rods are soldered to the sides. Pin-pin connectors located at the cold-end make it possible to remove the cold-end PRT support structure (i.e. the 3.18 mm (1/8 inch) VCR female nut) to access the JT valve. Pin-pin connectors located at the hot-end make it possible to remove the entire heat exchanger for another prototype.

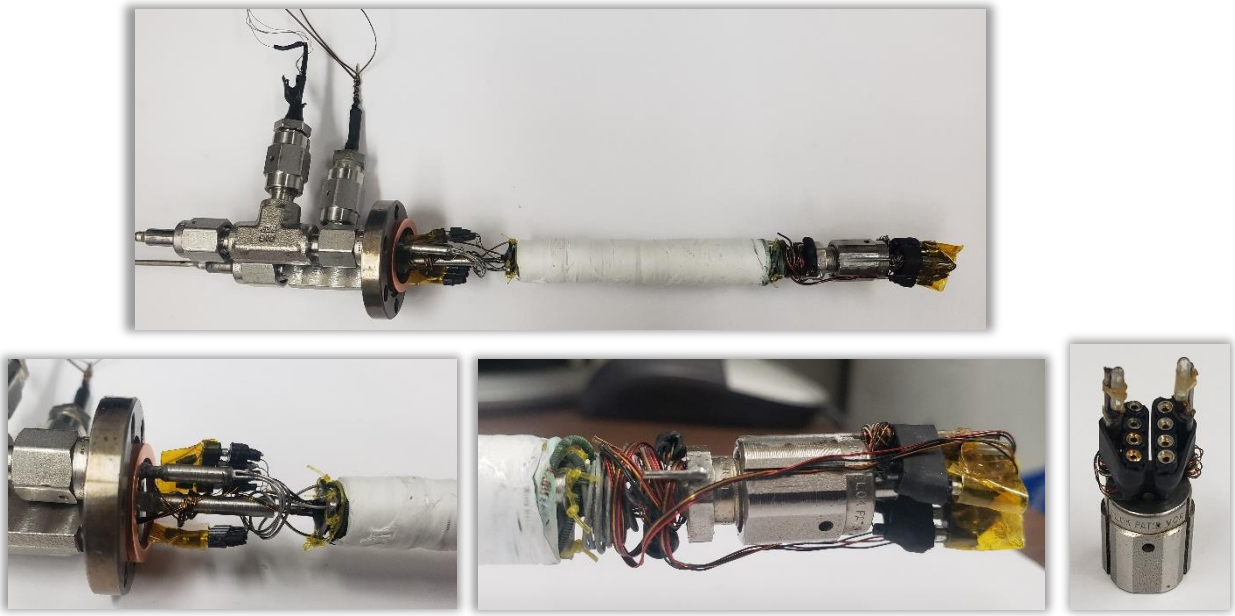

Figure 6.10. Assembled MGJT cryocooler without glass dome.

6.2. Experimental Test Facility

The cryocooler can be operated with same mixed gas compressor station previously described by disconnecting and removing the vacuum dewar and helium loop. A schematic of the experimental test facility for the cryocooler is shown in Figure 6.11.

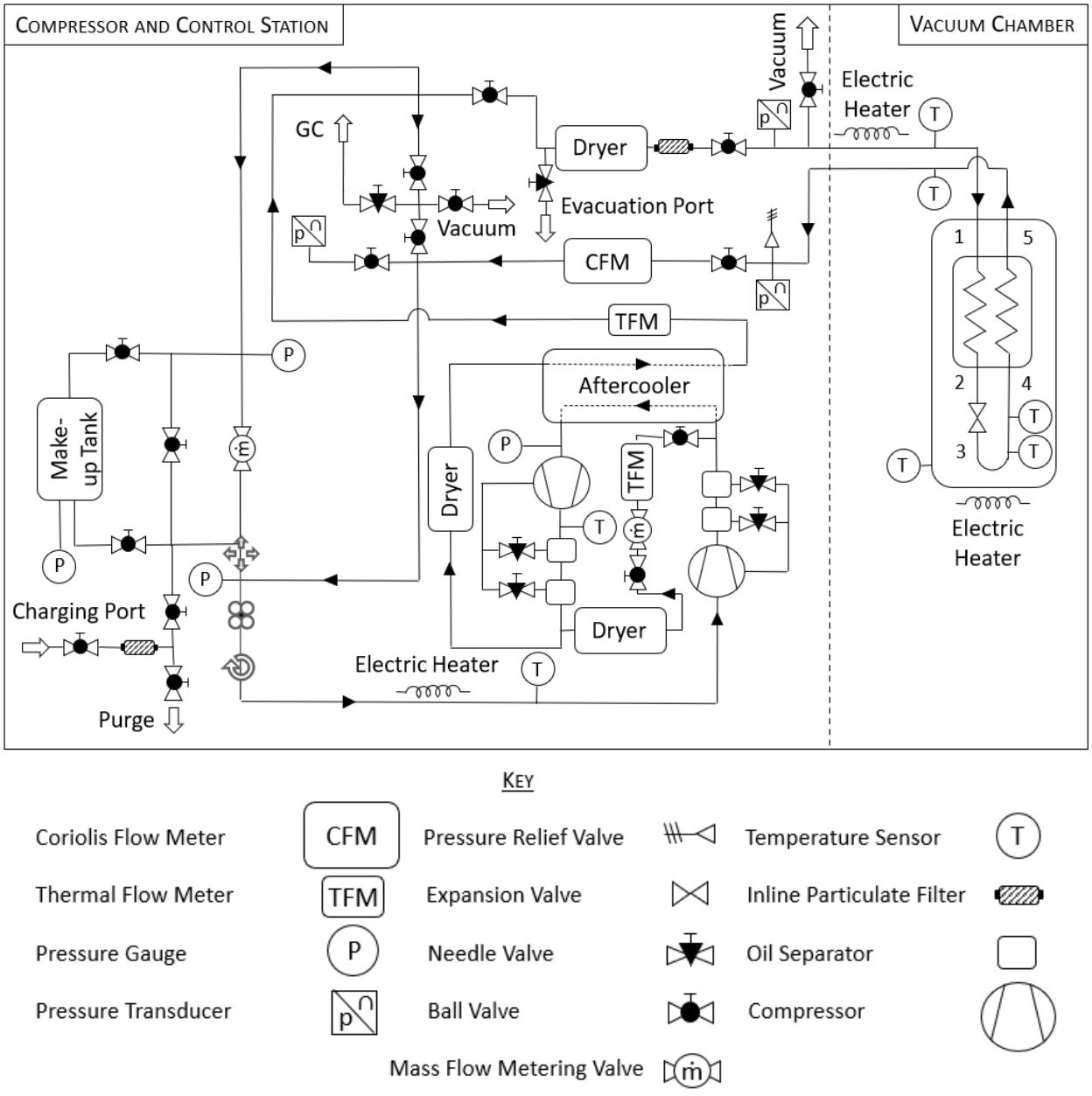

Figure 6.11. Schematic of experimental facility for cryocooler.

(a) (b)

Figure 6.13. View of vacuum chamber (a) and cryocooler mounted on chamber stand (b).

(a) (b)

Figure 6.12. Cryocooler wrapped in MLI (a) and three layers of the seven layers of radiation shielding (b).

The cryocooler assembly is mounted inside a vacuum chamber as shown in Figure 6.13. As previously, a roughing pump and turbo vacuum pump are used to create the high vacuum environment to minimize convection losses. Seven layers of multi-layer insulation (MLI) and dacron netting spacer are installed around the cryocooler to minimize radiation losses. The layers of MLI have varied lengths to reduce conduction from the hot-end of the MLI to the cold-end of

the cryocooler. The cryocooler wrapped in MLI is shown in Figure 6.12(a) and three layers of the seven layers of radiation shielding are shown in Figure 6.12(b).

The cryocooler is equipped with five PT-111 Lake Shore Cryotronics platinum resistance thermometers (PRTs) to measure the temperatures at the inlet and exit of the cryocooler, exit of the JT orifice, and the outside of glass dome at the cold-end. The wiring for the PRT mounted on the glass dome is wrapped around the cryocooler to prevent parasitic heat leak through axial conduction of the PRT wires. The dome PRT is picture in Figure 6.14(a). There are two PRTs installed in-stream at the exit of the JT orifice as shown in Figure 6.14(b) to characterize the variability of the cold-end temperature. The wires for these PRTs run through the G10 mandrel (sealed with epoxy at both ends), through the outlet of the ConFlat and into the vacuum chamber through the outlet PRT structure and epoxy as capture in Figure 6.14(e). The outlet PRT is positioned in-stream and shown in Figure 6.14(e). Details of constructing the in-stream PRT can be found in Appendix 8.10.

The inlet PRT is again positioned in-stream. However, its construction is different than those previously mentioned. As noted before, the in-stream PRTs built as described in Appendix 8.10. does not remain leak tight above 1034 kPa (150 psi). As higher inlet pressures are desirable, the inlet PRT is constructed with an electrical feedthrough rather than epoxy closure as shown in Figure 6.14(d). The electrical feedthrough is mounted in a 12.7 mm (1/2 inch) VCR male plug. Due to space constraints, the inlet PRT structure and the electrical feedthrough are joined together by a 3.18 mm (1/8 inch) VCR union tee as shown in Figure 6.14(c). The PRT structure is epoxied into a 3.18 mm (1/8 inch) VCR blank socketweld and is extended into the 3.18 mm (1/8) VCR union tee at the cryocooler. In this way, the inlet PRT is still positioned in-stream at the cryocooler entrance. The PRT wires from the electrical feedthrough were feed through a small diameter pipe

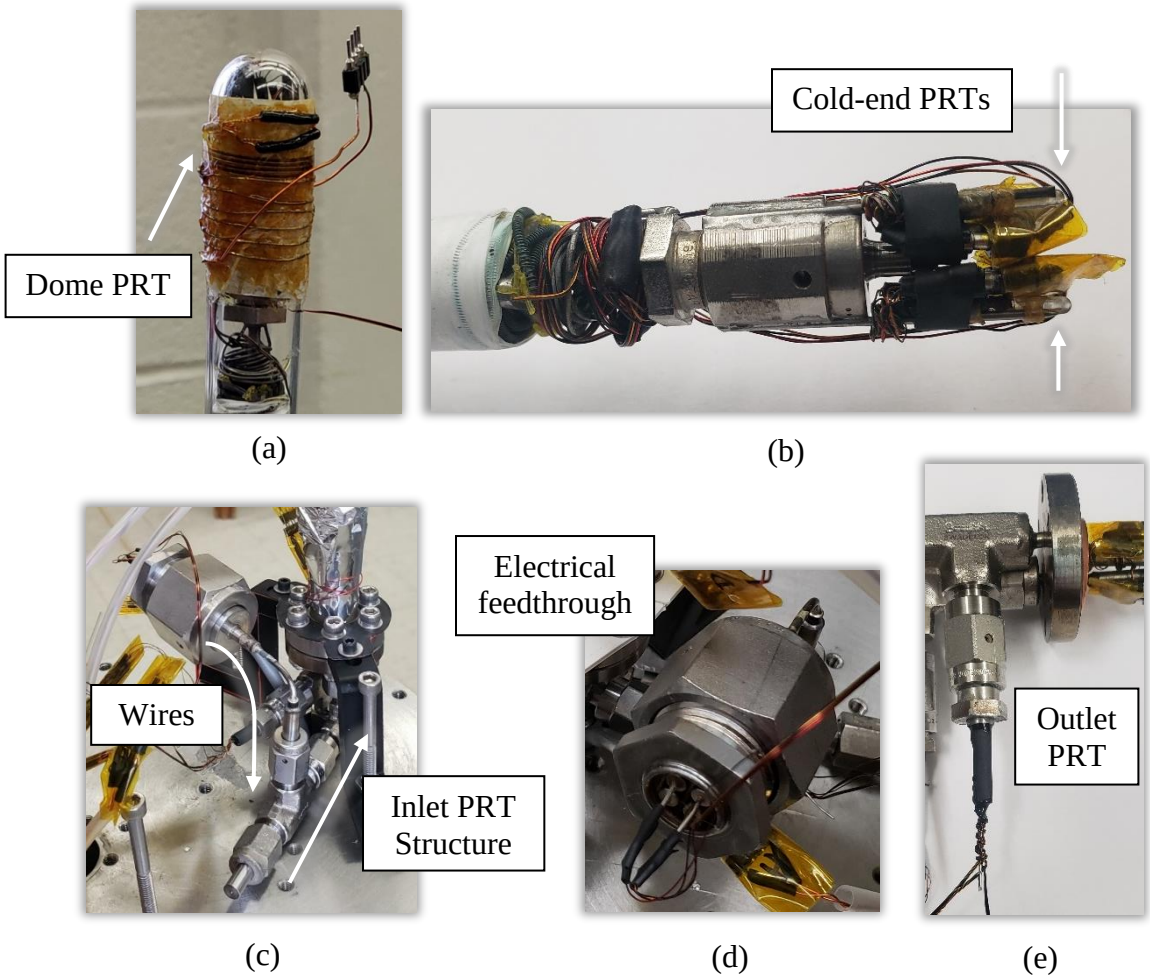

Figure 6.14. PRTs installed on the cryocooler – dome PRT (a), cold-end PRTs (b), inlet PRT (c and d), and outlet PRT (e).

that connects these pieces together. If removal of this PRT is desired or necessary, it should be removed directly at the cryocooler with the other remaining VCR connections intact.

The cryocooler is equipped with an electric heater at the cold-end to provide a heating load and an electric heater on the tubing to the inlet of the cryocooler to allow investigation of above ambient inlet temperatures. As with the previous experimental set-up, the suction and discharge pressures are measured by Setra Model 206 pressure transducers. The mass flow rate is measured by an Endress and Hauser Coriolis mass flow meter. Data is collected through a Campbell Scientific CR23X-TD Datalogger and the gas mixture composition is measured with a 5890 Series

II Hewlett-Packard gas chromatograph. Preliminary data collected for the cryocooler prototype can be found in Appendix 8.16.

7. Conclusions and Recommendations for Future Work

The heat transfer coefficient of the return stream in a GH heat exchanger is often neglected during the design of a JT cryocooler due to the much larger surface area that is present on this side related to the fins. However, there is no data or theory in the open literature that characterizes the heat transfer and pressure drop characteristics of two-phase multi-component mixtures on the shell side of these heat exchangers. The experimental work in this study aimed to gain insight into these thermal characteristics by developing a test facility capable of measuring the htc for this geometry at operating conditions consistent with a MGJT cryocooler. For the mixture examined, the two-phase htc was found to be between 12 to 19 W/m^2-K with uncertainties of approximately 12% for qualities in the range of 0.31 to 0.62. This data reveals that the shell side of a mixed gas recuperator is the dominant resistance even though it has a larger surface area and therefore the htc of the mixed gas on the shell-side of the GH heat exchanger is crucial for predicting the overall performance.

Additionally, a small number of measurements of the two-phase friction factor were captured for the shell side. The two-phase friction factor ranged from 20 to 35 with uncertainties of approximately 12% for qualities in the range of 0.52 to 0.61. Again, this suggests that predicting the pressure drop on the shell-side of the GH heat exchanger is vital for design.

While only a small amount of data was collected in this study, the data that was collected clearly demonstrates the need for and importance of developing accurate correlations for two-phase multi-component mixtures on the shell-side of the GH heat exchanger for operating conditions consistent with MGJT cryocoolers. Only with these developments can the MGJT cryocooler be designed for optimal performance.

Recommended future work includes a large test matrix of data collection for flammable, semi-flammable, and non-flammable multi-component mixtures with the test facility described and demonstrated here. Both two-phase and single-phase data need to be collected to determine the degree to which having a two-phase mixture on the shell-side provides any advantage. The geometrical parameters such as tube size, mean coil diameter, and fin height, thickness, and pitch of the GH heat exchanger prototype should be varied to gain a more in-depth understanding of how to optimize these parameters. Additionally, the clearance between the heat exchanger and inner diameter of the shell should be varied to determine if there is an optimal clearance for heat transfer and pressure drop. Finally, the operating conditions associated with the test matrix should be expanded in order to encompass relevant conditions for MGJT cryocoolers.

In order to enable a larger data collection campaign, the current test facility should be improved in several ways based on the experience obtained collecting the data presented here. Recommended updates to the test facility include better control of the inlet pressure and mass flow rate of the mixed gas stream to allow for consistent measurements. During operation, when the mixed gas decreases in quality, mass is drawn from the mixed gas compressor station into the inner volume of the vacuum chamber. In doing so, the mass flow rate and operating pressures of the mixed gas compressor station decrease and it becomes challenging to maintain these at their target values. A larger make-up tank is recommended to allow for additional mass to be added to the mixed gas station during operation which would allow measurements to be taken at lower qualities while maintaining the mass flow rate and inlet pressure of the mixed gas. The inlet pressure of the mixed gas can be better controlled with an in-line pressure regulator on the make-up tank that maintains a targeted downstream pressure for the mixed gas compressor station. Better control of the mass flow rate can be achieved with an electronic flow controller.

In addition to upgrades for the mixed gas stream, the helium flow controller should be replaced with one of a smaller volumetric flow range to decrease the uncertainty in the flow rate of the helium. Filters must be added to the helium stream to prevent contamination from compressor oil or small particulates inside the small diameter helically coiled tube. A shorter aftercooler is recommended to decrease the pressure-drop between and after the compressors and allow for increased operating pressure ratios and ranges. Lastly, an in-line pressure regulator should be added to GC line to maintain consistent sample flow rates and allow for more consistent measurements of the mixed gas composition.

With the large data collection campaign proposed here and enabled by the test facility developed in this work, correlations can be developed for two-phase multi-component mixtures on the shell-side of the GH heat exchanger. Then, and only then, the thermodynamic model for mixture optimization can be coupled with a heat exchanger model to predict the actual cooling capacity of a multi-component mixture by considering the effects of the mixture selection on the pressure drop in the high- and low-pressure streams and the effectiveness of the heat exchanger. The mixture optimization program will provide a robust study of the maximum achievable cooling capacity of all possible multi-component mixtures that can be made from a given list of fluids and operating parameters and the heat exchanger model will provide a more realistic assessment of their performance. This will allow for the selection of a mixture with the best real-world performance for a MGJT cryocooler.

8. Appendix

8.1. Outlier Detection in the Mixture Optimization Model

The mixture optimization model contains a two-stage outlier detection process in step 3 of the inner function. The first stage imposes a minimum and maximum restriction for enthalpy data to accomplish a robust outlier detection. The second stage implements the MATLAB function isoutlier with a moving window to target local outliers. Values of enthalpy greater than three scaled median absolute deviations (MAD) from the median value of enthalpy within that window are marked as outliers and removed from the data set. This method of outlier detection is more effective than using a standard deviation as the MAD is less affected by extremely high or low values of enthalpy. Using a moving window to target outliers reduces the possibility that the values of enthalpy near the limits of the temperature range are removed as outliers from the pressure stream data set. The effectiveness of the outlier detection was demonstrated by the low-pressure steam in Figure 4.3(b) to Figure 4.3(c).

8.2. Thermodynamic Consistency of Enthalpy in the Mixture Optimization Model

In step 4 of the inner function, the mixture optimization model removes enthalpy data if the value of enthalpy decreases with an increase in temperature and, in addition, removes the value of enthalpy and its corresponding temperature for the previous data point analyzed. While this method of checking for thermodynamic consistency removes two values of enthalpy instead of one, there is increased confidence that the enthalpy data that is removed is actually an outlier.

To illustrate, Figure 8.1(a) and Figure 8.1(b) display the raw data from REFPROP for the high-pressure stream of a mixture exhibiting "low" outliers (i.e., values below the true enthalpy) and for a mixture exhibiting "high" outliers (i.e., values above the true enthalpy), respectively. The mixture in Figure 8.1(a) is 20% R134a, 64% argon, and 16% isobutane on a molar basis (the same mixture as Figure 4.3) and the mixture in Figure 8.1(b) is theoretical. The values of enthalpy circled on the plots of Figure 8.1 are thermodynamically inconsistent as the value of enthalpy decreases with an increase in temperature.

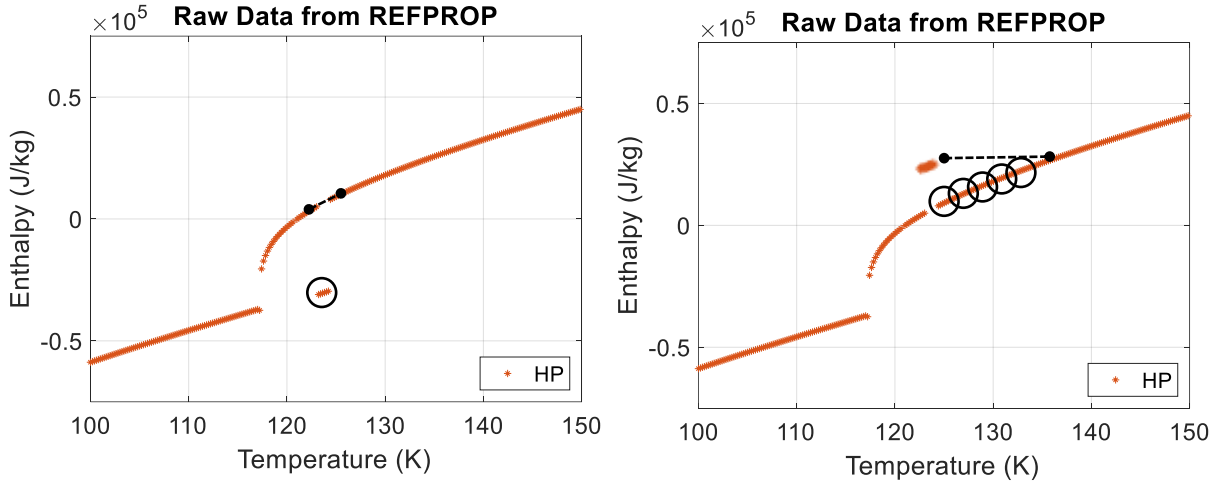

Figure 8.1. Thermodynamically inconsistent vales of enthalpy for "low" outliers (a) and "high" outliers (b).

If removing only values of enthalpy that decrease with increase in temperature from the temporary vector storing the pressure stream data, the model would remove these points and then

use the remaining values of enthalpy to interpolate information for this temperature range. While this method of checking for thermodynamically consistent values of enthalpy would work well for removing enthalpy data that appears as "low" outliers, it does not work well for removing values of enthalpy that appear as "high" outliers. For the "high" outliers shown in Figure 8.1(b), all the values of enthalpy circled and their corresponding temperatures would be removed from the temporary vector. The trend line for enthalpy that would be interpolated is shown as a dashed black line. While this ensures that the enthalpy data in the temporary vector is thermodynamically consistent, the values of enthalpy that would be removed by the model do not visually appear as outliers. In fact, the values of enthalpy proceeding these points appear to be the outliers and the model would calculate a more consistent Δh_T if these "high" outliers are removed. Therefore, it was found prudent to remove enthalpy data if the value of enthalpy decreases with an increase in temperature and, in addition, remove the value of enthalpy and its corresponding temperature for the previous data point analyzed.

The values of enthalpy circled in the plots of Figure 8.2 are removed from the pressure stream data with the current thermodynamic consistency check. The model then uses the remaining enthalpy data to interpolate enthalpy data for this temperature range. A comparison between the enthalpy trend line of these two varieties of thermodynamic consistency check can be seen by comparing the dashed black line in Figure 8.1 and Figure 8.2. For "low" outliers, no difference is seen between the thermodynamic consistency checks. For "high" outliers, it can be seen that the current thermodynamic consistency check will calculate a more consistent Δh_T.

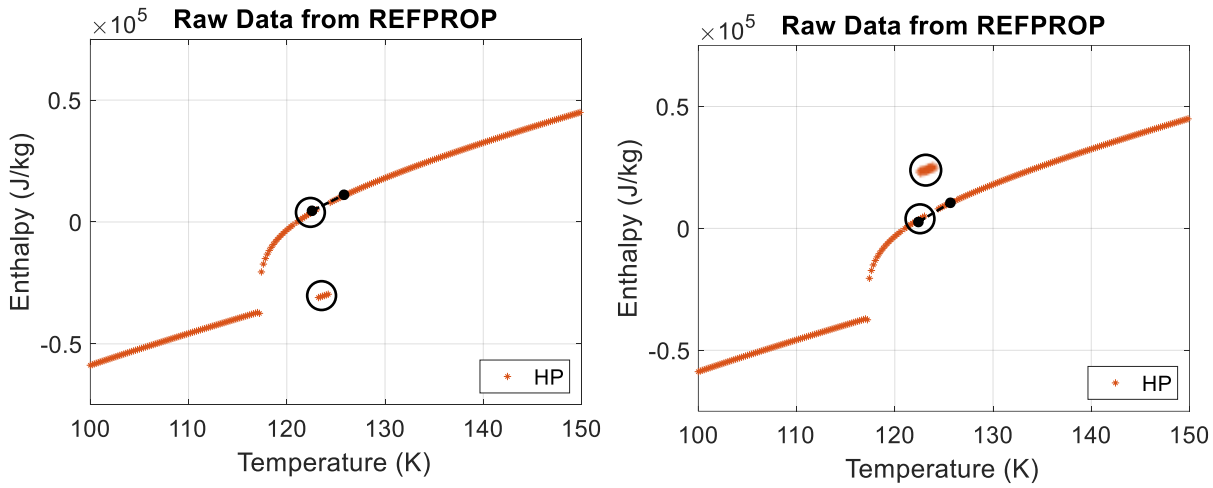

Figure 8.2. Visualization of thermodynamic consistent check.

8.3. Optimal Mixtures for 345 and 1034 kPa (50 and 150 psia)

Load Temp (K)	Gas Mixture (molar basis)	$\dot{Q}/\dot{m}$ (J/kg)
110	0.3 Butane + 0.56 Methane + 0.14 Nitrogen	11,151
120	0.3 Butane + 0.63 Methane + 0.07 Nitrogen	12,746
130	0.1 Argon + 0.27 Methane + 0.63 Propane	14,814
140	0.3 Butane + 0.14 Ethane + 0.56 Methane	34,922
150	0.3 Butane + 0.28 Ethane + 0.42 Methane	44,847
160	0.3 Butane + 0.35 Ethane + 0.35 Methane	49,521
170	0.3 Butane + 0.35 Ethane + 0.35 Methane	49,521
180	0.3 Butane + 0.42 Ethane + 0.28 Methane	53,499

Table 8.1. Optimal flammable gas mixtures for 345 and 1034 kPa (50 and 150 psi).

Load Temp (K)	Gas Mixture (molar basis)	$\dot{Q}/\dot{m}$ (J/kg)
110	0.3 R23 + 0.35 R134a + 0.35 Argon	5,745
120	0.3 R23 + 0.42 R134a + 0.28 Argon	6,182
130	0.6 R134a + 0.24 Krypton + 0.16 Argon	6,781
140	0.4 R23 + 0.36 R134a + 0.24 Argon	7,016
150	0.1 R14 + 0.63 R134a + 0.27 Krypton	7,172
160	0.7 R134a + 0.24 Krypton + 0.06 Argon	7,918
170	0.7 R134a + 0.3 Krypton	8,588
180	0.2 R14 + 0.08 R116 + 0.72 R134a	8,955

Table 8.2. Optimal non-flammable gas mixtures for 345 and 1034 kPa (50 and 150 psi).

8.4. Optimal Mixtures for 276 and 1103 kPa (40 and 160 psia)

Load Temp (K)	Gas Mixture (molar basis)	$\dot{Q}/\dot{m}$ (J/kg)
110	0.3 Butane + 0.56 Methane + 0.14 Nitrogen	13,811
120	0.3 Butane + 0.63 Methane + 0.07 Nitrogen	15,801
130	0.3 Butane + 0.07 Ethane + 0.63 Methane	30,259
140	0.3 Butane + 0.21 Ethane + 0.49 Methane	55,943
150	0.3 Butane + 0.28 Ethane + 0.42 Methane	61,035
160	0.3 Butane + 0.28 Ethane + 0.42 Methane	61,035
170	0.3 Butane + 0.35 Ethane + 0.35 Methane	65,646
180	0.3 Butane + 0.35 Ethane + 0.35 Methane	65,646

Table 8.4. Optimal flammable mixtures for 276 and 1103 kPa (40 and 160 psi).

Load Temp (K)	Gas Mixture (molar basis)	$\dot{Q}/\dot{m}$ (J/kg)
110	0.3 R23 + 0.35 R134a + 0.35 Argon	7,197
120	0.3 R23 + 0.42 R134a + 0.28 Argon	7,770
130	0.6 R134a + 0.24 Krypton + 0.16 Argon	8,146
140	0.4 R23 + 0.36 R134a + 0.24 Argon	8,425
150	0.1 R14 + 0.63 R134a + 0.27 Krypton	8,619
160	0.7 R134a + 0.24 Krypton + 0.06 Argon	9,797
170	0.7 R134a + 0.3 Krypton	11,542
180	0.7 R134a + 0.3 Krypton	12,728

Table 8.3. Optimal non-flammable mixtures for 276 and 1103 kPa (40 and 160 psi).

8.5. Optimal Mixtures for 517 and 1551 kPa (75 and 225 psia)

Load Temp (K)	Gas Mixture (molar basis)	$\dot{Q}/\dot{m}$ (J/kg)
110	0.3 Methane + 0.21 Nitrogen + 0.49 Propane	16,419
120	0.3 Methane + 0.21 Nitrogen + 0.49 Propane	16,553
130	0.4 Methane + 0.12 Nitrogen + 0.48 Propane	18,917
140	0.2 Butane + 0.72 Methane + 0.08 Propane	28,262
150	0.5 Methane + 0.45 Propane + 0.05 Pentane	35,142
160	0.2 Ethane + 0.32 Isobutane + 0.48 Methane	46,523
170	0.2 Ethane + 0.32 Isobutane + 0.48 Methane	46,523
180	0.3 Ethane + 0.35 Isobutane + 0.35 Methane	50,800

Table 8.6. Optimal flammable mixtures for 517 and 1551 kPa (75 and 225 psi).

Load Temp (K)	Gas Mixture (molar basis)	$\dot{Q}/\dot{m}$ (J/kg)
110	0.1 R116 + 0.36 R134a + 0.54 Argon	6,402
120	0.3 R23 + 0.28 R134a + 0.42 Argon	7,965
130	0.4 R23 + 0.24 R134a + 0.36 Argon	8,429
140	0.5 R134a + 0.35 Krypton + 0.15 Argon	9,477
150	0.5 R134a + 0.4 Krypton + 0.1 Argon	10,420
160	0.5 R134a + 0.5 Krypton	12,452
170	0.5 R134a + 0.05 R218 + 0.45 Krypton	14,348
180	0.3 R14 + 0.21 R23 + 0.49 R134a	18,337

Table 8.5. Optimal non-flammable mixtures for 517 and 1551 kPa (75 and 225 psi).

8.6. Sales Drawing of Finned-tubing for GH Prototype

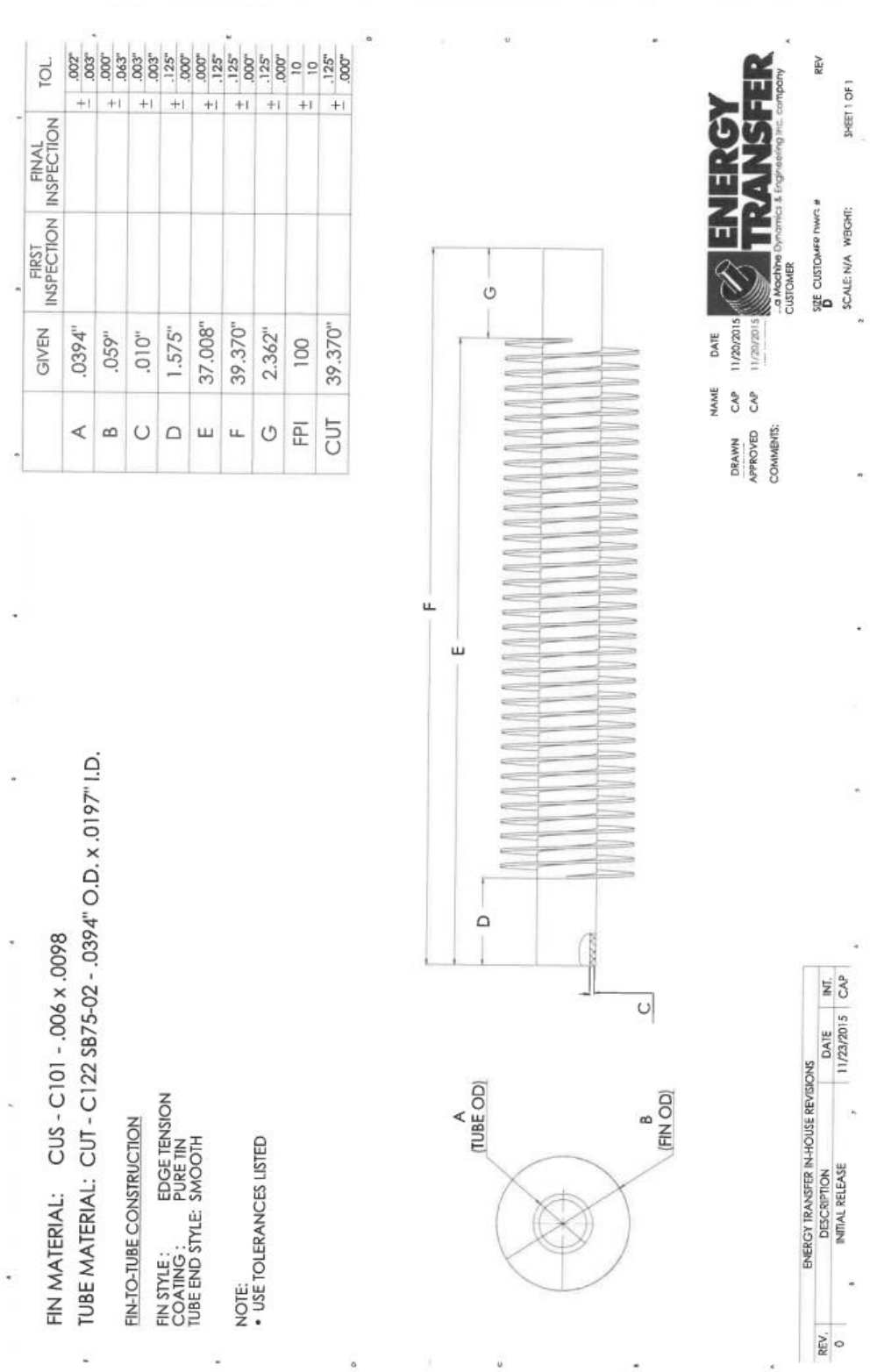

8.7. Further Details for the Mandrel Plugs

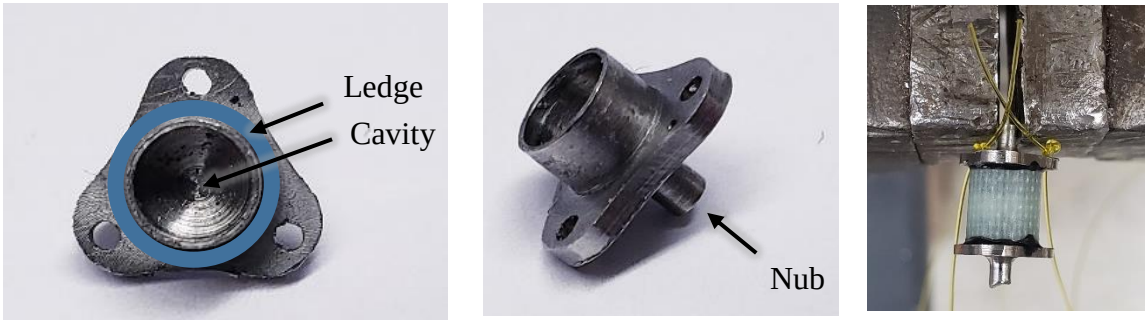

(a) (b) (c)

Figure 8.3. More images of the mandrel plug and set-up for heat exchanger winding.

Pictures of the mandrel plugs are shown in Figure 8.3. The mandrel plugs are carefully designed to block the flow of the low-pressure stream through the G10 mandrel and aid in the assembly of the heat exchanger. A few key features deserve further description to understand the design choices for the plug: the ledge of the propeller, the holes in the propeller, the cavity in the plug, and the nub of the plug

The propeller design is chosen for the plug to minimize the impedance of the low-pressure stream flow over the coiled finned-tube heat exchanger. While sizing the plug, it is important to leave a ledge on the propeller thick enough to hold the hollow G10 mandrel (i.e., it is important that the wings of the propeller did not cut in too close to the center of the plug). This ledge is scuffed up to promote adhesion with the epoxy and it is important to have enough surface area for the epoxy to adhere. Two of the holes in the propeller are used to hold and tie off the monofilament wire while winding the finned-tube heat exchanger. An unfinned portion of the finned-tube is positioned in the remaining hole to hold it in place to begin the winding. The cavity in the mandrel plug decreases the axial conduction along the plug. The cavity has a depth of 2.54 mm (0.1 inch), the diameter of the fins on the finned-tubing is 1.50 mm (0.059 inch) and the finned-tubing was only wound four times on the mandrel. If the plug is left as solid stainless-steel, this would

effectively reduce the length of the heat exchanger in half. Thus, it is important that a cavity is present. Finally, the nub on the back of the mandrel plug is used to hold the assembly in place in the vice during winding. This set-up is shown in Figure 8.3(c).

To machine the mandrel plugs from stainless steel stock, follow the following procedure:

1. A piece of round stainless-steel stock is placed in a collet and a collet block is used to secure it in the vice on the CNC mill.
2. An endmill is used to mill the outside circle that will touch the inside of the G10 mandrel. Then the same endmill is used to mill the propeller pattern.
3. To follow, center and drill the propeller holes.
4. Move to a lathe and use a turning tool to cut the propeller from the stock (let the propeller piece fall from the lathe).
5. Using another collet, clamp on the solid stainless-steel extrusion and turn down the nub needed for the mandrel plug.
6. If necessary (i.e. if PRT wires run through the mandrel plug), flatten out the material near the propeller using a flat turning tool. If necessary (i.e. a threaded rod will be used to attach and remove the heat exchanger from the rest of the experimental set-up), drill and thread the nub at this time and put the threaded rod into place.
7. Return to the mill, clamp on the nub, and mill the cavity in the plug. (Note that if a threaded rod is included in the design plan, it is necessary that it is in place at this time. Clamping on the nub will deform the nub and make it difficult to add or remove a threaded rod after this point.)
8. Finally, use the high-speed mill to drill the holes into the propeller and, if necessary, into the plug for the PRT wiring.

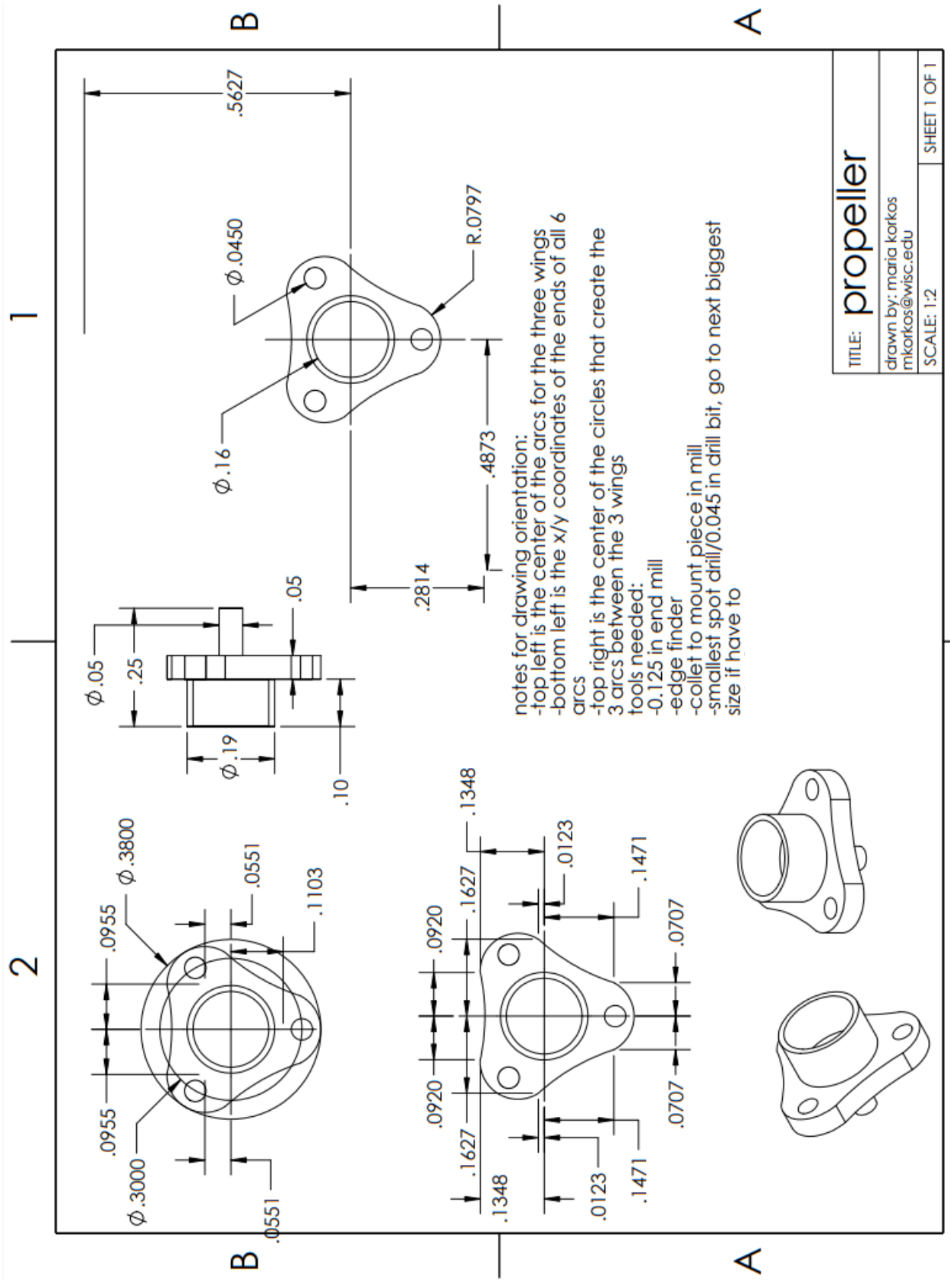
TITLE: propeller
drawn by: maria korkos
mkorkos@wisc.edu
SCALE: 1:2
SHEET 1 OF 1
notes for drawing orientation:
-top left is the center of the arcs for the three wings
-bottom left is the x/y coordinates of the ends of all 6 arcs
-top right is the center of the circles that create the 3 arcs between the 3 wings
tools needed:
-0.125 in end mill
-edge finder
-collet to mount piece in mill
-smallest spot drill/0.045 in drill bit, go to next biggest size if have to
.5627
Ø.0450
R.0797
Ø.16
.4873
.2814
Ø.05
.25
.05
Ø.19
.10
Ø.3800
.0955
.0551
.1103
Ø.3000
.0955
.0551
.1348
.0920
.1627
.0123
.1471
.0707
.0920
.1627
.1348
.0123
.1471
.0707

8.8. Further Details for the 33.8 mm (1.33 inch) CF Weld Necks

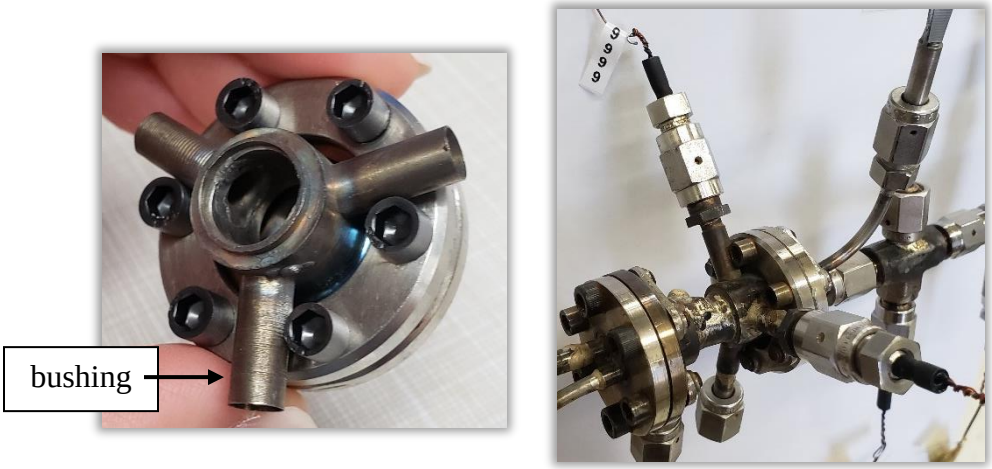

Figure 8.4. Weld necks adapted for temperature and pressure measurements.

Pictures of the 33.8 mm (1.33 inch) CF blank weld necks adapted to allow for temperature and pressure measurements are shown in Figure 8.4. The weld necks are carefully designed to maintain constant cross-sectional area throughout the test section. This means that the weld for the stainless-steel tube and weld necks is performed on the outside of the test section. Attention is also paid to the channels for the PRTs. To ensure that the channels remain wide enough for the PRT, the bushings are welded on the inside of the neck weld. The VCR socket welds cannot be directly welded to the weld neck as additional length is needed for the closure of the male and female nuts.

Given the size of these pieces and constraints for welding, it is challenging to make leak tight connections. If repeated, it is recommended that the weld necks and stainless-steel tube are brazed together instead of welded. The welding process deformed the inside of the test section causing a non-uniform inside diameter and the test section was made uniform by very carefully using a grinder attachment on a drill press to open up the inner diameter until the heat exchanger could fit inside. The connections between the bushings and the weld neck also suffered from leaks. This may have been from the initial weld or from using the grinder on the inside of the test section. This was remedied by brazing the leaking bushing on the outside to close up the leak.

To machine the adapted weld necks from the blank 33.8 mm (1.33 inch) CF weld necks, turn down the outside of the weld neck to the desired outer diameter and continue turning down material for a weld lip. Then turn the piece and drill the inner diameter. To follow, move to the mill and secure the weld neck with parallels. Drill a hole from the outside to the inside of the weld neck. Follow with a slightly larger drill bit that does not go all the way through the weld neck to create a ledge for the bushing. Repeat this two more times, turning the weld neck by 120^{o} each time.

8.9. LabVIEW Documentation for Compressor Inlet Heater

The LabVIEW program monitors the differential voltage for the temperature of the fluid entering the compressor, T_{in}, and the low pressure of the mixed gas, P_{LP}. It controls the voltage supplied to the heater to ensure the fluid has a quality of 1 when entering the compressor. User specified inputs into the LabVIEW program include ambient temperature T_{amb}, the mixture composition on a molar basis, the voltage range for the heater, and the Proportional-Integral-Derivative (PID) values (i.e. proportional gain, integral time, and derivative time). LabVIEW sets the voltage supplied to the compressor inlet heater by the process outlined in Figure 8.5.

Voltage values sent to the power supply are continuously updated in real time. PID values of proportional gain, integral time, and derivative time may need to be optimized during operation. The proportional response influences the speed of the control system response [90]. A higher proportional gain value increases the speed at which the control system responds. However, if this gain value is too large the voltage supplied to the heater will oscillate and T_{in} will never reach a steady-state value. The proportional gain is currently set to a value of 5.5.

The integral response affects the control system response time and steady-state error of the system (i.e. the difference between T_{in} and the set minimum allowable temperature of the inlet of the compressor T_{min}). A low integral time will reduce the steady-state error, but result in a longer settling time (i.e. a longer time to reach steady-state). It will reduce overshooting the desired set point temperature. However, some amount of overshoot is necessary for a fast system so that the control system can immediately respond to changes [90]. A high integral time constant will make

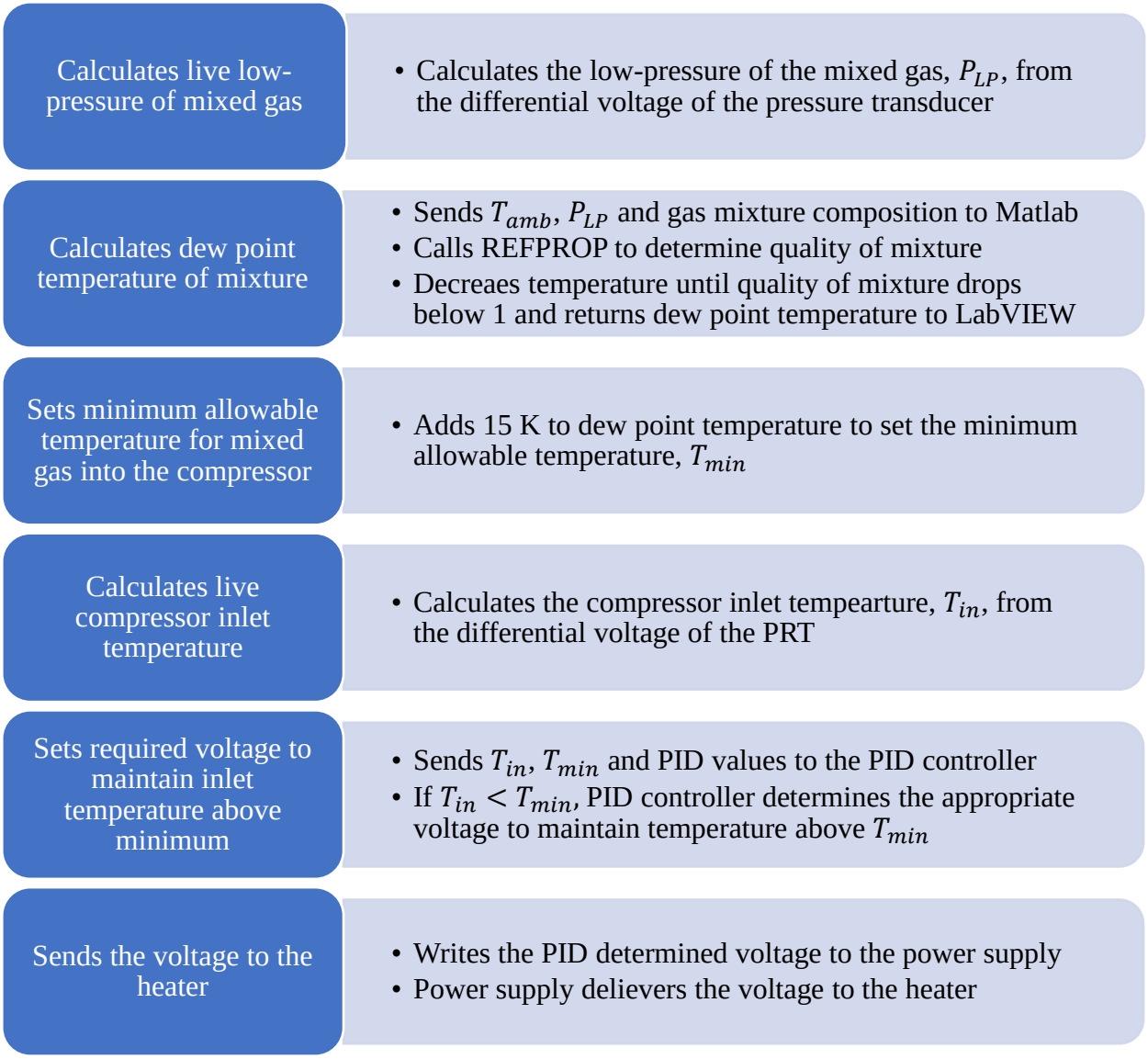

Figure 8.5. Outline of LabVIEW program for compressor inlet heater.

the system faster to respond but at the cost of possibly overshooting the desired temperature set point. The integral time is currently set to a value of 0.5.

Lastly, the derivative response is proportional to the rate of the change of T_{in}. Increasing the derivative time will cause the control system to respond more strongly to change in the steady-state error. This will increase the speed of the overall control system response. Generally, small values of the derivative time are used. The derivative response is highly sensitive to noise and if

the feedback signal is noisy, this can cause the system to become unstable at higher values [90]. The derivative time is currently set to a value of 1.

8.10. Construction of In-Stream PRTs

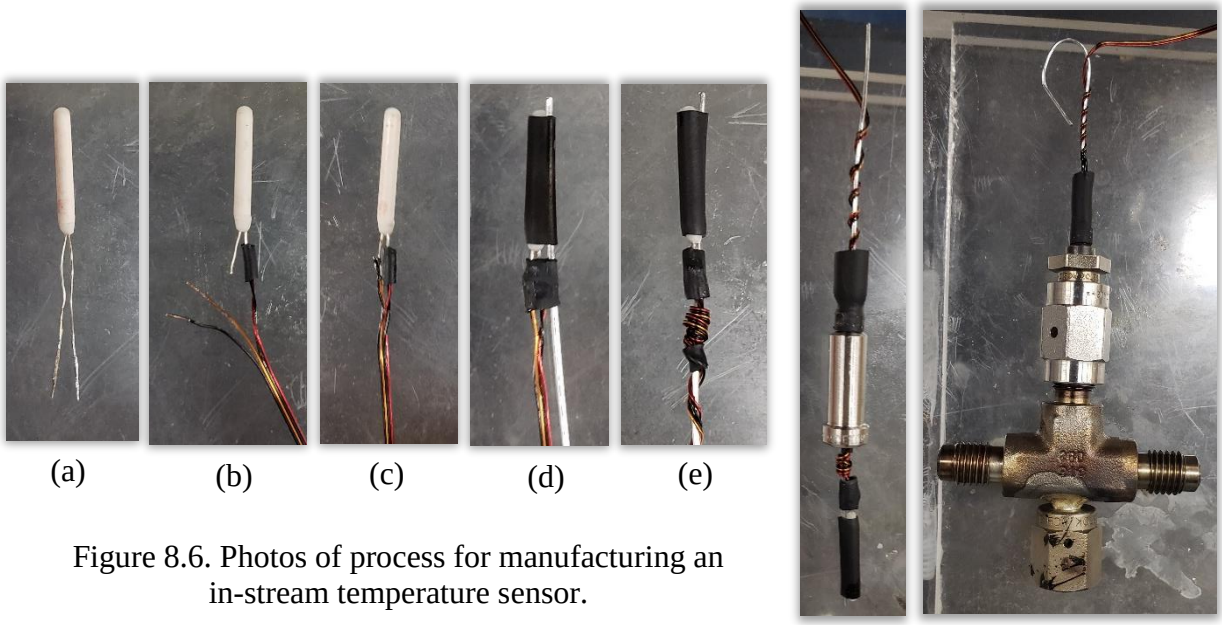

(a) (b) (c) (d) (e) (f) (g)

Figure 8.6. Photos of process for manufacturing an in-stream temperature sensor.

The temperatures of the fluid streams within the test section and the inlet of the compressor are monitored using Lake Shore Cryotronics PT-111 an PT-103 platinum resistance thermometers (PRTs). The PRTs are immersed in the fluid flow to provide a direct measurement of the temperature. The PRTs within the test section and at the inlet of the compressor are positioned inside 3.18 mm (1/8 inch) and 6.35 mm (1/4 inch) VCR connections, respectively. The small size of the 3.18 mm (1/8 inch) VCR connections make it challenging to construct the temperature sensors. One must assemble the temperature sensor such that it is short enough to fit inside the VCR union without contacting the VCR body and ensure a 3.18 mm (1/8 inch) VCR face seal gasket can slip over the assembly to be crushed upon closure. To fit the temperature sensor assembly inside the 3.18 mm (1/8 inch) VCR connection, drill open the channel with a #27 drill bit. Be careful not to nick the VCR ring.

The steps for constructing the in-stream temperature sensors are shown pictorially in Figure 8.6 and outlined as follows:

1. Punch center of 3.18 mm (1/8 inch) VCR face seal gasket with 3.18 mm (1/8 inch) punch to increase the inner diameter. The hole should be centered to increase the probability that the crush seal will be leak tight upon closure.
2. Shorten the leads of the PRT to shorten the required length for the temperature sensor assembly.
3. Attach two cryogenic wires to one of the leads and use shrink wrap to electrically isolate the connection as shown in Figure 8.6(b).
4. Attach two cryogenic wires to the remaining lead as shown in Figure 8.6(c). Do not place shrink wrap around these wires.
5. Use shrink wrap to attach the PRT leads to a support structure consisting of a small diameter wire or pipe as shown in Figure 8.6(d).
    - Take care that the shrink-wrapped leads are resting against the support structure (not the bare connection) to ensure electrical isolation.
    - Do not cover the entirety of the PRT leads. A small portion of the leads should be directly submerged in the fluid flow.
    - Lastly, a small portion of the support structure should stick out the top to protect the PRT.
6. Use shrink wrap to secure the PRT glass body to the support structure.
7. Carefully wrap the cryogenic wire around the support structure to create a heat sink in the fluid stream as shown in Figure 8.6(e). At this point it is important to check that the 3.18 mm (1/8 inch) VCR face seal gasket can be slipped over the top of the temperature sensor assembly.

8. Place a piece of shrink wrap at the end of the heat sink. This is the end of the temperature sensor assembly that is immersed in fluid flow. The shrink wrap will stop epoxy from running over the assembly as the epoxy sets in a later step.
9. Use sandpaper to rough the surface on the outside and inside of the VCR socket weld nub to increase the likelihood of a leak tight seal with the epoxy. The nub of the VCR socket weld is shown in Figure 8.7(a).
10. Run the wires through the VCR socket weld by wrapping them around the support structure as shown in Figure 8.6(f).
    - If the four cryogenic wires are attached in a bundle, use a razor blade to separate them. The four separate wires will fit in the socket weld opening, but a four-wire bundle will not fit without scraping the wires.
    - The cryogenic wires should be wrapped around the support structure past the VCR socket weld. The cryogenic wires tend to break at the connection to the epoxy. Wrapping the wires further up the support structure prevents tension of the wires directly at the epoxy.
    - A new 3.18 mm (1/8 inch) VCR socket weld from Swagelok will have a 1.89 mm (0.074 inch) opening. If drilling a blank socket weld or adapting a used socket weld, manufacture the opening to approximately 1.89 mm (0.074 inch), if possible. The larger the opening, the more difficult it is to create a leak tight seal for the temperature sensor assembly.
    - At this point it is important to check that the temperature sensor assembly will fit inside the VCR union and allow for closure.

11. Place heat shrink around the nub. Shrink the heat shrink around the nub and leave the rest of the heat shrink unaffected to leave a large opening for the epoxy.
12. Place the male nut on the assembly.
    - A male nut is always used in the 3.18 mm (1/8 inch) VCR temperature sensor assemblies. The 3.18 mm (1/8 inch) VCR face seal gaskets commonly get stuck in the female nuts. This can be problematic for opening and re-closing the temperature sensor assembly.
13. Use the tip of a needle to fill the heat shrink with epoxy. The epoxy should be of a consistency such that the epoxy slowly forms a droplet on the needle.
14. Let epoxy set for 24 hours and leak check.

The Lake Shore Cryotronics PT-103 PRT shown in Figure 8.6 was installed in a 3.18 mm (1/8 inch) VCR union cross as shown in Figure 8.6(g). The extra length available inside the union cross allowed for the use of a PT-103 PRT with glass body length of 11.49 mm (0.47 inch). When the in-stream temperature sensor is installed in a 3.18 mm (1/8 inch) VCR union tee as shown in Figure 8.7(b), the available length inside the VCR is reduced and the temperature sensor assembly must be shorter. A PT-111 PRT is required in the union tee as the glass body length is only 5.00 mm (0.197 inch). Additionally, PT-111 PRTs were required for the in-stream temperature measurement of the mixed gas as the shell inner diameter was only 10.03 mm (0.395 inch). An example temperature sensor assembly is shown in Figure 8.7(c).

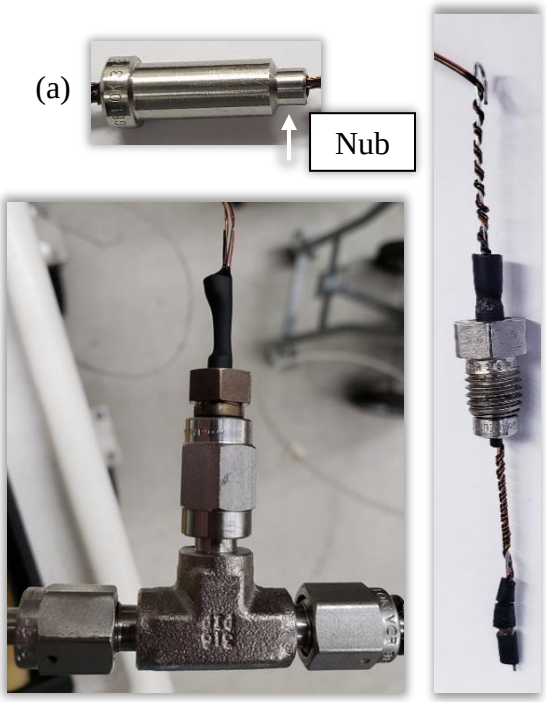

Figure 8.7. Photos of VCR socket weld nub (a), temperature sensor in union tee (b), and temperature sensor for measurement of mixed gas in the shell of the test section (c).

8.11. Testing of Operating Conditions for the Compressors

(a) (b) (c)

Figure 8.8. Photos of compressors and monitoring equipment – compressors (a), amp clamp (b), and outlet temperature sensor of the second compressor (c).

The mixed gas compressor station is equipped with two Danfoss SC18CLX.2 compressors in series as shown in Figure 8.8(a). The Danfoss SC18CLX.2 compressors are designed for working fluids of R404A, R452A and R507. The maximum winding temperature and discharge temperature is reported as 398 K and 403 K, respectively, and the rated load amps and cut in current are 9.6A and 63A, respectively [91].

A target objective of the experimental test facility is to collect data for a variety of gas mixtures, not only the gases for which the compressors are rated. As the thermophysical and transport properties of each gas mixture varies, so too does the compressor performance including the input power required to compress the gas, the outlet temperature of the gas and the maximum achievable pressure ratio of the compressors. As increased operating pressures and pressure ratios were found to be desirable for the experimental test facility, active monitoring of the compressor running current and outlet temperature became necessary to prevent failure. An amp clamp monitors the start-up and operating current of the compressors as shown in Figure 8.8(b). A Lake Shore PT-103 PRT mounted externally on a stainless-steel pipe of inner and outer diameter of 3.56 and 6.35 mm (0.14 and 0.25 inch), respectively, at the outlet of the second compressor

continuously monitors the outlet temperature as shown in Figure 8.8(c). An in-stream temperature sensor could not be mounted at this location as the maximum operating temperature of the Loctite Stycast 2850FT epoxy used in construction of an in-stream temperature sensor assembly is 378 K [92]. This is less than the maximum allowable discharge temperature of 403 K. Additionally, a fan blowing on the compressors provides direct cooling to the PRT as shown in Figure 8.9. Thus, the temperature sensor provides only an approximation of the temperature of the fluid exiting the compressor.

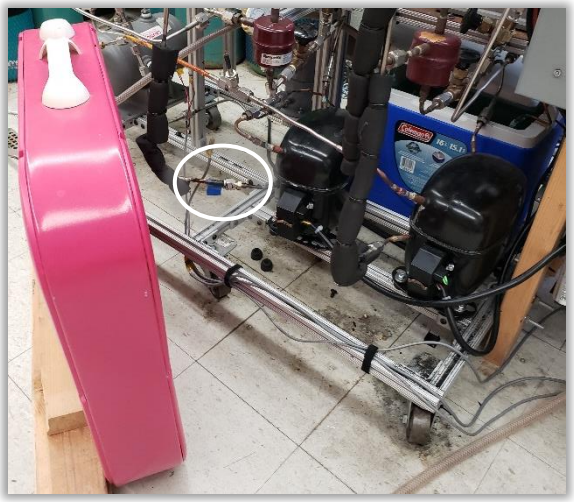

Figure 8.9. Photo of fan for compressors.

For testing the compressor operating conditions, the test section was removed from the experimental facility and replaced with a pipe connection. The second compressor was also removed to isolate the performance of one compressor and an external PRT was mounted on the first compressor. The mixed gas compressor station was charged with varying amounts of pure gases and gas mixtures to investigate the effects of working fluid and charge pressure on the compressor outlet temperature, flow rate and running current. The working fluids studied are listed

Working fluid (molar basis)	Plot Label
Pure R134a	R134a
Pure R23	R23
27% Argon, 10% R23, and 63% R32	RM1
20% R14, 72% R32, and 8% R125	RM2
20% Argon, 8% Butane, and 72% Ethane	HM1

Table 8.7. Working fluids used to test operating conditions of the compressors.

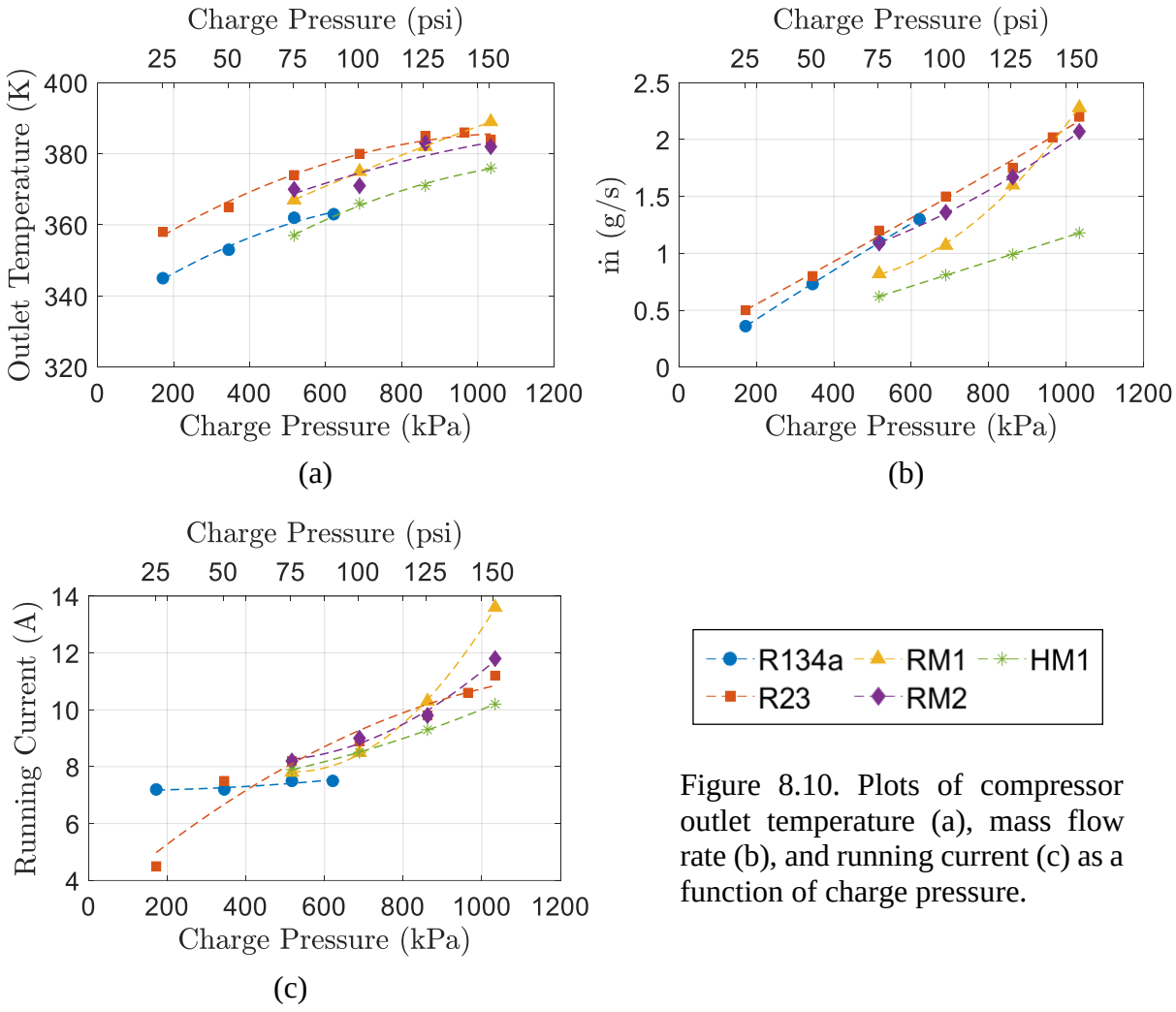

Figure 8.10. Plots of compressor outlet temperature (a), mass flow rate (b), and running current (c) as a function of charge pressure.

in . For the first set of trials, the test section by-pass and compressor return line were left open and conditions were recorded after 5 minutes of operation. The results are shown in Figure 8.10.

It is evident from Figure 8.10(a) that given the same charge pressure, R23 produces the highest compressor outlet temperatures compared to R134a and the other gas mixtures tested. It is also seen that even with the test section by-pass and compressor return line open, the outlet temperature of the compressor is approaching the maximum allowable outlet temperature as the charge pressure approaches 1034 kPa (150 psi) for R23 and the refrigerant mixtures. For the range of charge pressures tested, the compressor produced mass flow rates of approximately 0.4-2.3 g/s for both the pure refrigerants and refrigerant mixtures as shown in Figure 8.10(b). For the

hydrocarbon mixture, the mass flow rate was significantly reduced to approximately 0.6-1.2 g/s for charge pressures of 517-1034 kPa (75-150 psi). As shown in Figure 8.10(c), there was not significant variation in running current between the working fluids unless at the upper or lower limit of the charge pressures tested. However, it is important to note that above 862 kPa (125 psi) the running current for all the working fluids is higher than the reported rated load amps for this compressor.

Further testing ensued to investigate the effects of charge pressure and by-pass closure on compressor outlet temperature and running current. Given that R23 produced the highest compressor outlet temperatures for charge pressures of 172 – 862 kPa (25-125 psi), it was selected as the working fluid. The second compressor was re-installed, and the test facility was charged with varying amount of R23. The test-section by-pass ball valve and mass flow metering valve were incrementally closed as well as the ball valve on the compressor return line to achieve increased high pressures and pressure ratios from the compressors. Results are shown in Figure 8.11 and Figure 8.12.

As expected, as the by-pass valves are closed such that the pressure ratios and outlet pressures of the compressors are increased, the outlet temperatures of the compressors increase. Figure 8.11 illustrates the effects of charge pressure on the outlet pressure of the second compressor and the maximum outlet temperature of the first and second compressors. For a charge pressure of 517

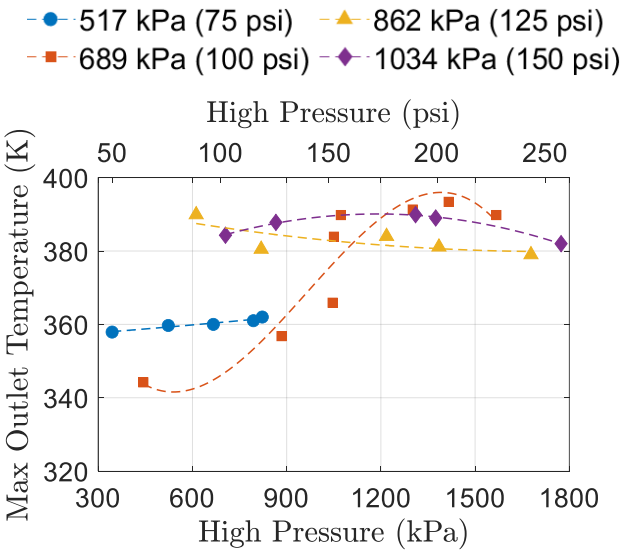

Figure 8.11. Plot of the high pressure versus maximum outlet temperature as function of charge pressure.

kPa (75 psi) the maximum outlet temperature plateaus at 360 K even at the highest achieved outlet pressure. For charge pressures of (125-100 psi), the maximum outlet temperature is approximately 385 K for all conditions tested. For a charge pressure of 689 kPa (100 psi), the maximum outlet temperature varied significantly with outlet pressure. The maximum outlet temperature approaches 385K at outlet pressures for the second compressor above 1034 kPa (150 psi). From these results, a maximum charge pressure of 689 kPa (100 psi) and maximum outlet pressure of 1034 kPa (150 psi) was determined appropriate for the test facility.

It should be noted that, in general, the first compressor had higher outlet temperatures until the ball valve on the compressor return line was closed (at the highest pressure ratios and outlet pressures). Additionally, the increased outlet temperatures at a charge pressure of 517 kPa (75 psi) compared to 689 kPa (100 psi) are speculated to be due to inadequate cool-down time between trials.

In addition to setting maximum operating conditions for the test facility, the individual compressor outlet temperatures as a function of pressure ratio and running current were investigated with the compressors operating in series to set the maximum operating conditions for each compressor. The results for the second compressor are shown in Figure 8.12. (Note that the high-pressure for each compressor was collected downstream after the aftercooler. Therefore, pressure drop in the aftercooler reduces the pressure ratio below 1 when data is collected for the by-pass valves fully open).

For all the charge pressures tested, pressure ratios greater than 2.5 result in compressor outlet temperatures approaching 385 K as shown in Figure 8.12(a). Thus, a maximum allowable pressure ratio of 2.5 was set for each compressor. From Figure 8.12(b), running currents above 10.5 Amps return significantly higher compressor outlet temperatures. However, these running

currents only produce outlet temperatures approaching 385 K for pressure ratios above 2.5. Nonetheless, it is still useful to use 10.5 Amps as a guide to the maximum allowable running amps for each compressor.

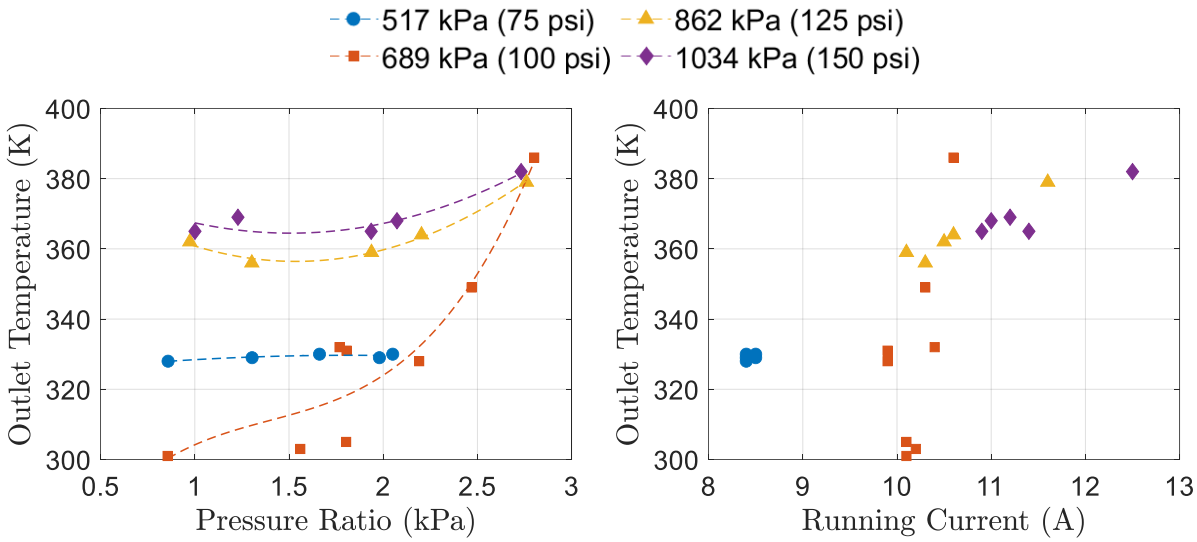

(a) (b)

Figure 8.12. Plots of the outlet temperature as a function of pressure ratio (a) and running current (b) for the second compressor.

8.12. Operating Conditions and Sample Data for the Gas Chromatograph

The equipment used in data collection and analysis of molar concentrations of gas mixtures consists of a HP 5890 Series II gas chromatograph (GC) equipped with a thermal conductivity detector (TCD) and packed column. A schematic of the external plumbing and theory of operation were presented in Section 5.3.4. A LabView program previously developed in-house was used for determining uncorrected peak areas, A_{uc}. The details of calculating response factors, RFs, corrected peak areas, A_c, and molar concentrations of each component of the gas mixture were outlined in the data reduction. Below are the GC operating conditions used during data collection, sample data for gas chromatograms, and details of the RF repeatability and sensitivity analysis.

Sample Data

Column	Alltech HayeSep D 100/120 20ft
Oven Temp	100 °C
Injector A Temp	100 °C
Detector A Temp	100 °C
Carrier Flow Rate	30 mL/min
Reference Flow Rate	50 mL/min
Sample Flow Rate	9-12 cc/min

Table 8.8. GC operating conditions for data collection.

Listed in Table 8.8 are the GC operating conditions used during data collection of the pure gases and gas mixtures. To calculate RFs, each pure gas was sampled multiple times under constant conditions and an average peak area, A_{avg}, was calculated for these trials. Listed in Table 8.9 is sample data obtained during this analysis. The retention time (RT), peak height (PH) and peak area (PA) are the average of three runs to determine the recorded values. The results have been qualitatively sketched in Figure 8.13 to show the relation of the pure fluids on a sample gas chromatogram. Note that the peak widths have been exaggerated on the sketch, but the peak base values are as observed and are important in determining if the peak areas of different pure

components will overlap during analysis. If this occurs, the GC operating conditions or column must be altered to separate the peaks.

Data	Argon	R23	R14	Nitrogen	Ethane	R32
RT	2.92 min	6.39 min	3.47 min	2.79 min	9.71 min	8.44 min
PH	Base = 125 Peak = 465	Base = 120 Peak = 425	Base = 120 Peak = 600	Base = 116 Peak = 460	Base = 128 Peak = 335	Base = 120 Peak = 345
PA	48.75	65.54	65.85	50.34	59.98	61.19
RF	0.02051	0.01526	0.01519	0.01987	0.01667	0.01634

Table 8.9. Sample data for gas chromatogram.

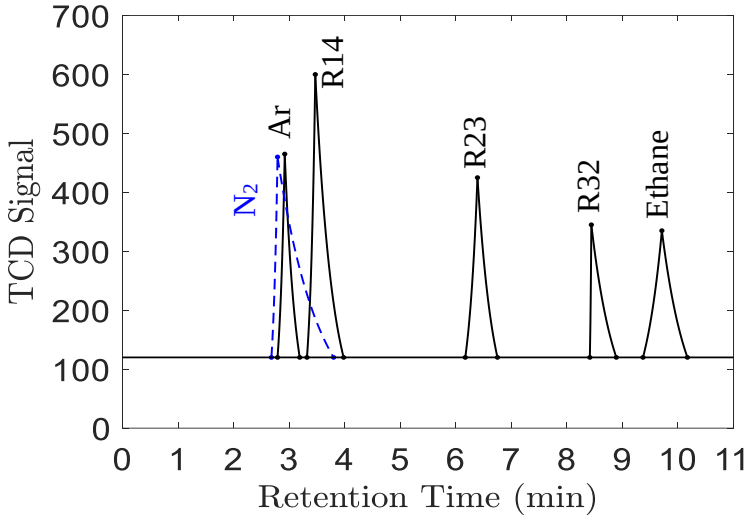

Figure 8.13. Qualitative sketch of gas chromatogram for pure gases investigated.

Repeatability Analysis

Two more trials with the same GC operating conditions, as shown in Table 8.8, were performed to investigate repeatability of the peak areas and determine uncertainty in the corresponding RFs. The data were collected 12 months and 15 months after the initial data set. The results are illustrated in Figure 8.14. The corresponding response factors and uncertainty are

reported in Table 8.10. The response factor is an average of the three measurements and the uncertainty is quantified by the standard deviation.

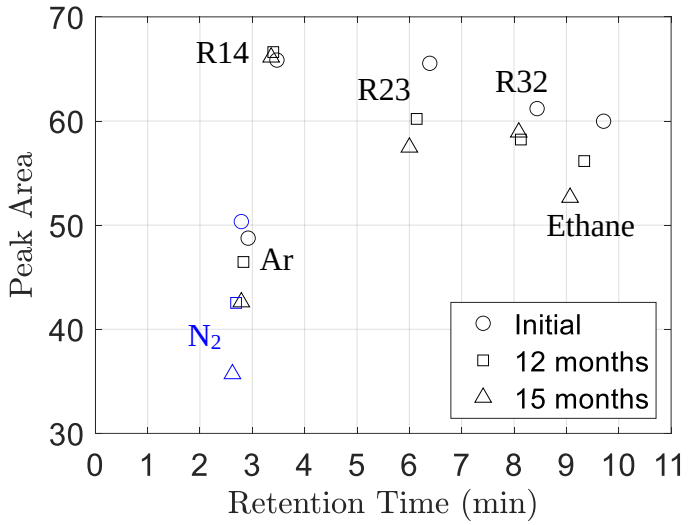

Figure 8.14. Repeatability of peak area and retention time for pure gases investigated.

Gas	Argon	R23	R14	Nitrogen	Ethane	R32
RF	0.02184 ±0.00123	0.01641 ±0.00087	0.01515 ±0.00003	0.02379 ±0.00333	0.01782 ±0.00095	0.01683 ±0.00036
%RU	5.62%	5.32%	0.19%	13.97%	5.31%	2.12%

Table 8.10. Response factors and uncertainties for repeatability analysis.

Sensitivity Analysis

A mixture of R14 and R32 was selected as the fluid for the heat transfer coefficient measurements. The operating pressures for the mixed gas were not sufficient for a flow rate of 9-12 cc/min to the GC. Therefore, response factors were collected for R14 and R32 to determine the sensitivity of the *RF* to the sample flow rate. All operating conditions remained the same as listed in Table 8.8 except that the sample flow rate was varied from 9-12 ccm to 4-7 ccm. The response factor for each flow rate was collected on the same day. The results are illustrated in Figure 8.15. The corresponding response factors and uncertainties for the sensitivity analysis are reported in Table 8.11.

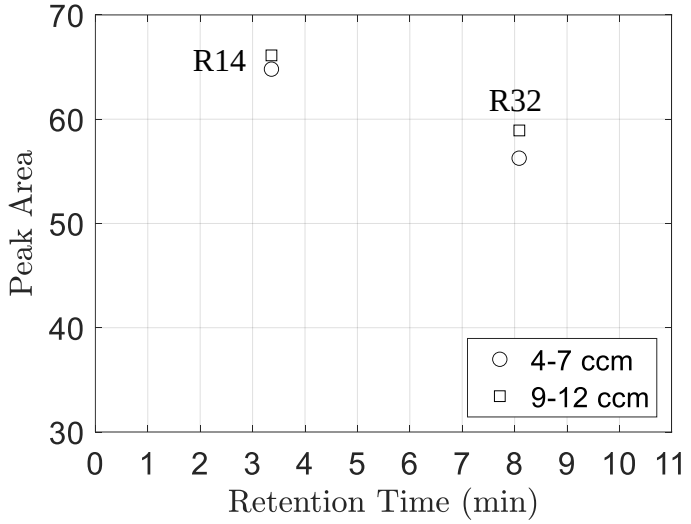

Figure 8.15. Sensitivty of peak area and retention time to sample flow rate for R14 and R32.

Gas	R14	R32
RF	0.01528 $\pm$0.00016	0.01738 $\pm$0.00041
%RU	1.01%	2.33%

Table 8.11. Response factors and uncertainties for sensitivity analysis.

Combined Uncertainty of RF for R14 and R32

There is more uncertainty in the response factor for R14 from the change in sample flow rate than from the repeatability analysis as shown in Table 8.10 and Table 8.11. For R32, the uncertainties from the repeatability and sensitivity analysis are about the same. For R14 and R32, the response factor for the sensitivity analysis is used in the data analysis and a combined uncertainty is calculated to account for repeatability. The combined uncertainty, U, is calculated as follows:

$$U = \sqrt{u_r^2 + u_s^2}$$

where u_r is the uncertainty from the repeatability analysis and u_s is the uncertainty from the sensitivity analysis. This gives response factors and uncertainties of R14 and R32 as listed in Table 8.12.

Gas	R14	R32
RF	0.01528 $\pm$0.00155	0.01738 $\pm$0.00056
%RU	1.01%	3.14%

Table 8.12. Response factors and uncertainties for R14 and R32.

8.13. Details of Gas Mixture Composition for Select Data Points

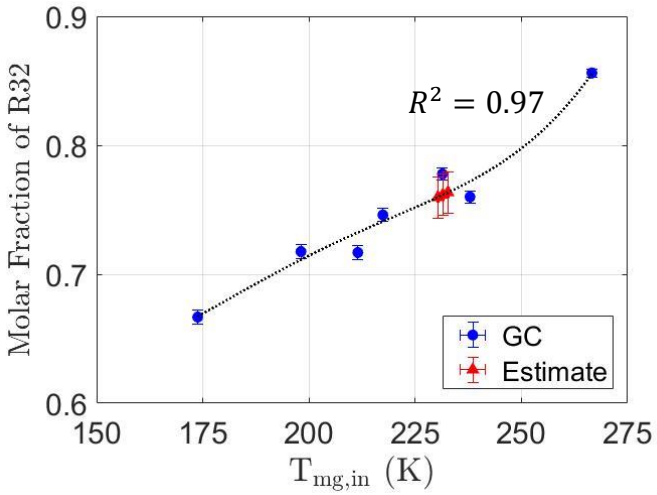

Figure 8.16. Molar fraction of R32 as a function of the inlet temperature of the mixed gas.

Figure 8.16 illustrates the molar fraction of R32 as a function of the inlet temperature of the mixed gas. The data points for which GC measurements were collected are shown as circles. As previously mentioned, the gas mixture experiences a change in quality from approximately 0.5 to 1 between 231 and 238 K for the operating pressures. Within this range, it was challenging to reach steady-state conditions due to variation in operating conditions. One factor contributing to varying operating conditions is data collection for the GC. At steady-state, the gas mixture is sampled from the compressor station three times to determine the gas mixture composition. This sampling requires removal of a small amount of mass from the mixed gas compressor station to the GC and thus causes variation in the both the mass flow rate and inlet pressure of the mixed gas to the test section.

To collect more data within the quality range of 0.5 to 1, three trials were performed in which GC measurements were not collected. To estimate the gas mixture composition of the circulating mixture, a 4th order polynomial was fit to the existing data as shown in Figure 8.16 by the dotted line. While this estimate does not consider variation in the molar concentration of R32

as a function of pressure, it still gives a reasonable approximation. The estimated values are shown in Figure 8.16 as triangles.

The uncertainty in the estimate of the molar fraction of R32 was quantified by the maximum error between the measured molar fraction of R32 and estimated value from the polynomial fit at the same inlet temperature. The maximum error was found to be approximately $\pm$1.6% molar fraction of R32.

8.14. Sales Drawing of Finned-tubing for Cryocooler Prototype

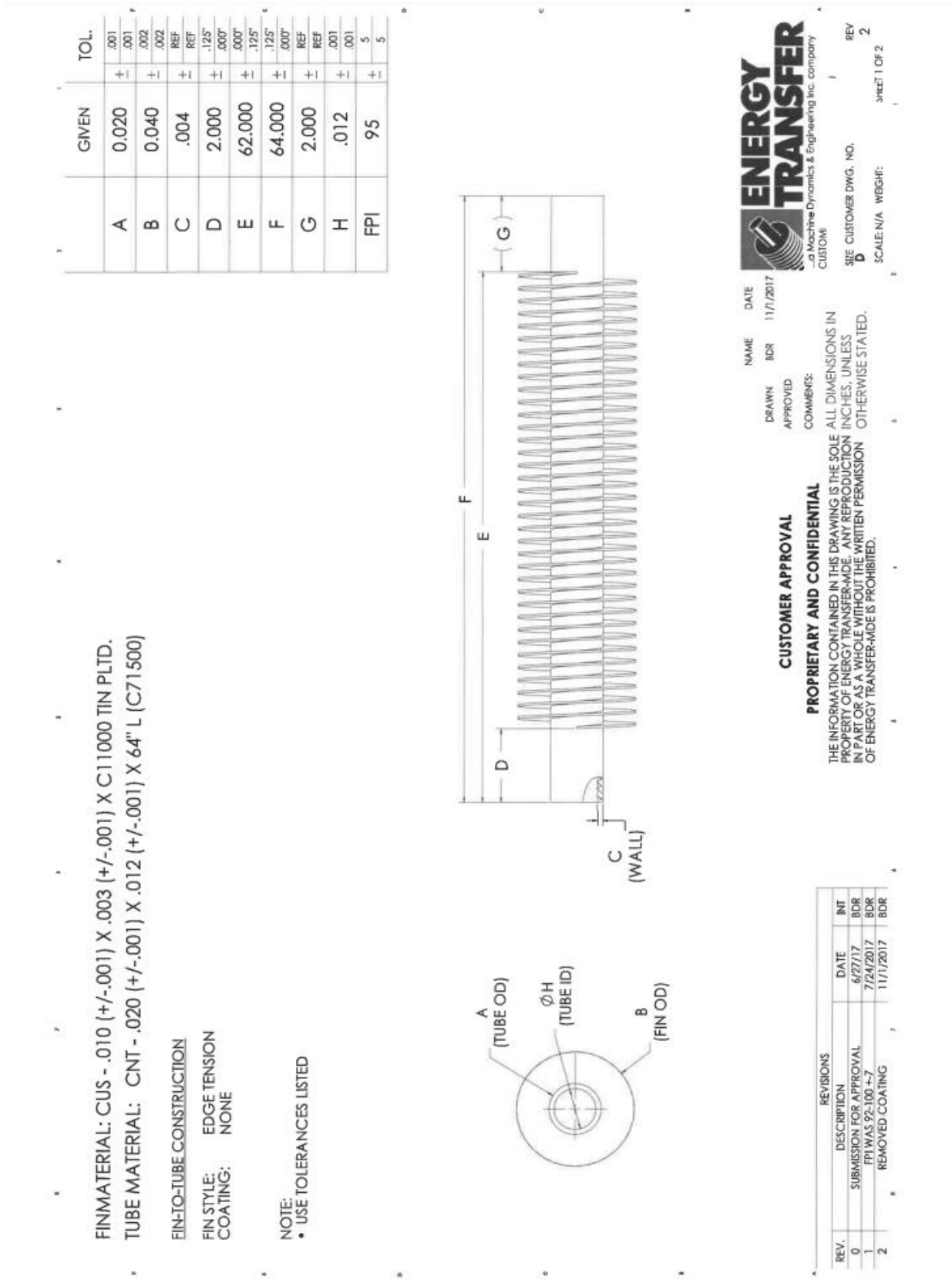

8.15. Manufacturing the JT Orifice

There are three ways in which the JT orifices can be manufactured – turning down previously made JT orifice structures to fit within the 3.18 mm (1/8 inch) VCR assembly, drilling the small diameter orifice directly into a 3.18 mm (1/8 inch) VCR blank, and machining a ledge on a 3.18 mm (1/8 inch) VCR blank to hold a ruby jewel orifice. The instructions for manufacturing the JT orifices in each of these manners are presented below.

Turning Down Pre-made JT Orifices

JT orifice structures previously made to fit within a 6.35 mm (1/4 inch) VCR assembly with ruby jewel orifices epoxied into a 6.35 mm (1/4 inch) VCR blank are available in the lab. These assemblies can be turned down by a lathe to fit within the 3.18 mm (1/8 inch) VCR assembly currently in use in the cryocooler. Care must be taken to not apply pressure to the epoxied ruby

Figure 8.18. Machined tools for turning down pre-made JT orifices.

Figure 8.18. Machining set-up to turn down pre-made JT orifices.

jewel such that the epoxy or orifice will not be damaged or altered in any way. A few ‘tools’ have been machined to allow for a friction hold on the 6.35 mm (1/4 inch) VCR blank such that material can be removed from the blank without applying pressure to the epoxied ruby jewel. These tools referred to as a dog bone, gasket holder, and plunger are shown in Figure 8.17. To turn down the blank VCR, install the dog bone in the lathe and add a live center to into the tailstock quill. Put the blank into the gasket holder and slide it onto the dog bone. Place the plunger on the live center and bring the live center to the blank until it is held in place. The tools are shown installed in the lathe in Figure 8.18. Run the lathe at 500 revolutions per minute (RPMs) and take off 0.13 to 0.25 mm (0.005 to 0.010 inch) of material per pass. If the live center stops rotating, the gasket may be damaged. If this happens, take smaller passes or replace the lathe tool.

Turning down the 6.35 mm (1/4 inch) VCR blanks to 3.18 mm (1/4 inch) blanks in this manner occasionally leaves a lip on the outer edge. Left this way, the blanks will get stuck in the 3.18 mm (1/8 inch) VCR female nuts. To remove the lip, use a new plunger with a smaller diameter of approximately 5 mm (0.2 inch), remove the gasket holder from the assembly, and switch the lathe cutting tool from a left-handed tool to a right-handed tool. The new plunger will be used to grip the 3.18 mm (1/4 inch) blank and the lip can be removed. An illustration of this set-up is shown in Figure 8.19.

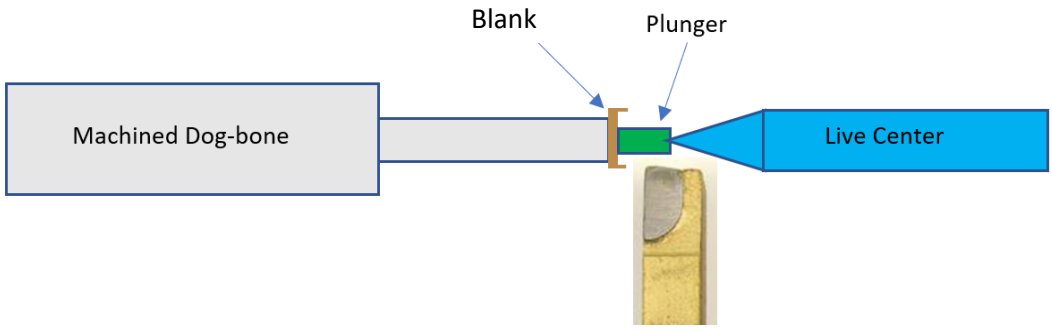

Figure 8.19. Machining set-up for removing lip from pre-made JT orifices.

Drilling JT Orifices

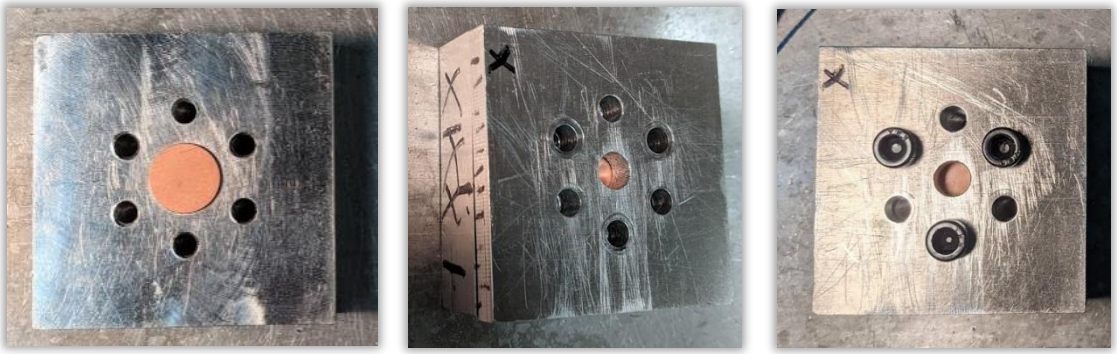

(a) (b) (c)

Figure 8.20. Holder for drilling small diameter JT orifices.

JT orifices with diameters as small as 0.17 mm (0.0067 inch) can be made by drilling holes in a copper 3.18 mm (1/8 inch) VCR blank with carbide drill bits. A holder for the 6.35 mm (1/4 inch) VCR blank has been machined for this purpose and is shown in Figure 8.20. To drill the orifice, install the copper blank into the holder with the marked sides lined up as shown in Figure 8.20(b). Finger tighten at least three bolts before using an allen key to turn them a quarter-turn more. Note that if the bolts are tightened too much, the holder will “bite” into the blank, making it more difficult to remove later.

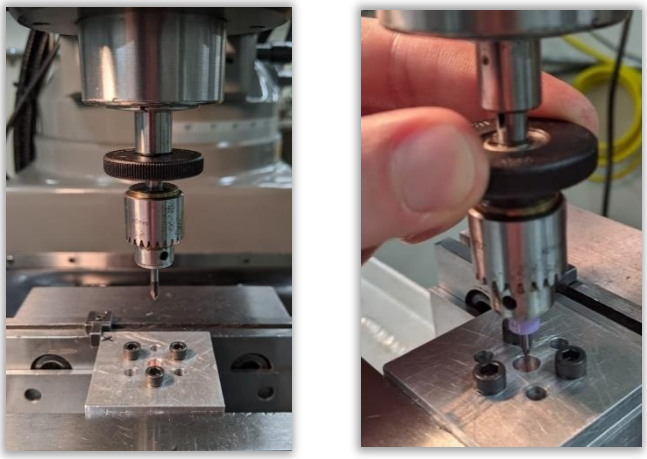

Figure 8.21. Micro-chuck for drilling JT orifices.

Use parallels in the vise to secure the holder and center with an edge finder. Install a micro-chuck and #00 center drill bit into the mill as shown in Figure X. Run the mill at 2800 RPM and lower the plunger to drill the centering hole. Replace the #00 center drill with the appropriately sized carbide drill bit for the JT orifice. Using the plunger on the micro-chuck, slowly drill through the blank. If the drill bit snaps, go slower, and ensure the center hole is deep enough in the future. Finally, use a punch and die set to reduce the outer diameter of the blank to the appropriate size.

Machining Ledges for Ruby Jewel Orifices

For JT orifices with diameters less than 0.17 mm (0.0067 inch), drilling through the copper VCR blanks has proved to be less successful. For these smaller sizes, ruby jewel orifices from Bird Precision are epoxied into the ledge of a VCR blank. The VCR blank is installed in the same holder as above, secured in the vice and centered. A 1.59 x 4.76 mm (1/16 x 3/16 inch) end mill at 2800 RPM is used to mill a 0.25 mm (0.010 inch) the ledge for the ruby jewel orifice. This is accomplished by positioning the end mill in contact with the VCR blank and moving the table in the z-direction by 0.25 mm (0.010 inch). A flow path through the VCR blank must be drilled after the ledge. Use the micro-chuck and the #00 center drill bit at 2800 RPM to drill the centering hole and then use the #68 drill bit at 2800 RPM to drill through the blank. The blank with ledge and flow bath is shown in Figure 8.22. Use a punch and die set to reduce the outer diameter of the blank to the appropriate size. Finally, epoxy the ruby jewel orifice into the blank using a needlepoint to carefully place epoxy on the ledge. Be careful not to epoxy the orifice closed.

Figure 8.22. Ledge and flow path through VCR blank for ruby jewel JT orifice.

8.16. Preliminary Experimental Results Collected for the Cryocooler

The prototype MGJT cryocooler has been operated while charged with a selection of flammable, semi-flammable and non-flammable mixtures composed of argon, ethane, krypton methane, nitrogen R14, R23, R32, R134a and R410a. The temperatures at the cold-end, on the dome and at the inlet and outlet were measured as well as the pressures at the inlet and outlet. Various sizes of the JT orifices were installed ranging from 0.0025” to 0.011” in diameter. Mass flow rates recorded ranged from 0.107 g/s to as low as 0.014 g/s.

Cool-down Time

Figure 8.23 shows an example cool-down curve for 20% R14, 16% R23 and 64% R134a on a molar basis with low and high pressures of 386 and 1138 kPa (56 and 165 psia), respectively. The JT orifice installed was 0.010 mm (0.004 inch) in diameter and the mass flow rate was 0.027 g/s. Within an hour, the cold-end temperature decreases over 85% of the temperature difference to the steady-state temperature of 214K. An additional thirty minutes later and the cold-end temperature is within 2% of steady-state.

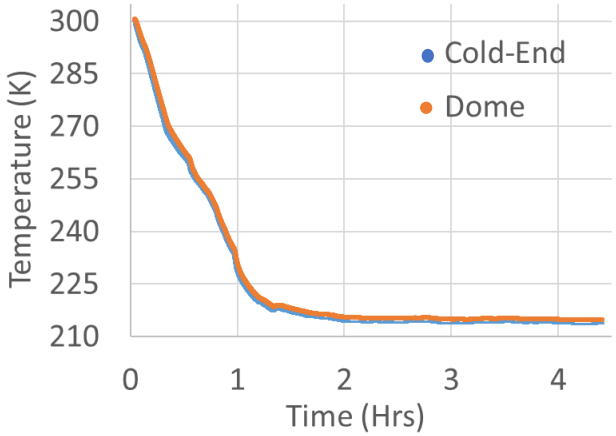

Figure 8.23. Cool-down curve for cryocooler.

Varying the JT Orifice

Values of the cold-end temperature were collected and compared for the mixture in Figure 8.23 while the JT orifice size was varied. The size of the JT orifice, mass flow rate and cold-end temperature for each run is indicated in Figure 8.24 and plotted upon the isothermal enthalpy difference for the mixture as a function of load temperature. The high- and low-pressure were 1151 kPa (167 psi) and 393 kPa (57 psi), respectively. As the size of the JT orifice is reduced from 0.279 to 0.076 mm (0.011 to 0.003 inch), the mass flow rate decreases from 0.107 g/s to 0.014 g/s. The cold-end temperature decreases with mass flow rate until an optimal mass flow rate is achieved, afterwards which the cold-end temperature begins to rise with a continued reduction of the mass flow rate. Shown by a black dashed line at approximately 204K on Figure 8.24 is the temperature limiting the cooling capacity of this mixture. It is observed that as the optimal mass flow rate is approached, so too is this limiting temperature.

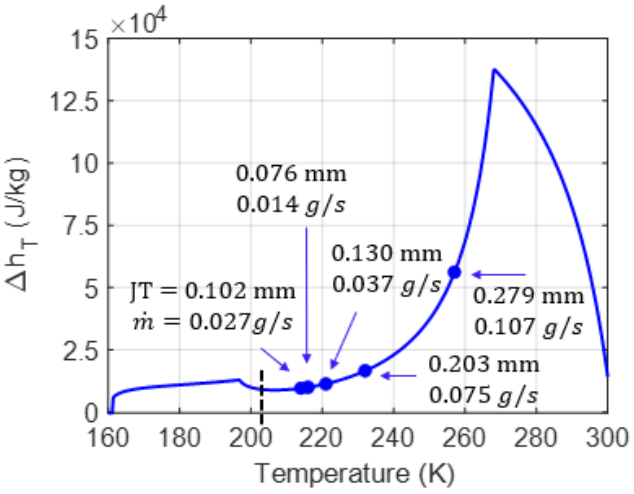

Figure 8.24. Visualization of experimental results for 20% R14, 16% R23 and 64% R134a while varying JT orifice size.

Parasitic Loss

The parasitic loss for the cryocooler can be estimated as the product of the mass flow rate and the minimum value of the Δh_T over the temperature range of the experimental run (where the parasitic loss includes both the heat load and the non-ideal behaviors of the heat exchanger). The parasitic loss and mass flow for the same experimental runs previously discussed are shown in Figure 8.25. If the heat exchanger was performing ideally, the parasitic loss would be equal to the

heat load, which increases with a decrease in cold-end temperature. However, this is not the trend observed in Figure 8.25 as the parasitic loss from non-ideal behaviors of the heat exchanger must be considered. The value of parasitic loss due to non-ideal behaviors of the heat exchanger will decrease with an increase in effectiveness. Decreasing the flow rate has the potential to increase the effectiveness of the heat exchanger and reduce the pressure drop in the high- and low-pressure streams (i.e. the heat exchanger behaviors more ideally). Therefore, as the mass flow rate decreases, the value of parasitic loss due to non-ideal behaviors of the heat exchanger decreases and the parasitic loss decreases to a value approaching the heat load.

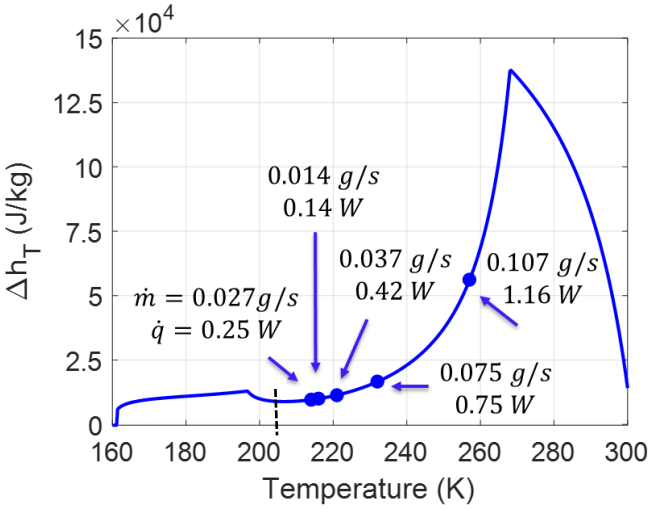

Figure 8.25. Parasitic loss for 20% R14, 16% R23 and 64% R134a while varying JT orifice size.

9. Works Cited

[1] W. A. Little, "Microminiature refrigeration," *Review of Scientific Instruments,* vol. 55, no. 5, pp. 661-680, 1984.

[2] B.-Z. Maytal and J. M. Pfotenhauer, Miniature Joule-Thomson Cryocooling: Principles and Practice, New York: Springer, 2013.

[3] J. R. Olson, E. Roth, M. Guzinski, A. Ruiz, C. L. Mangun, D. King, N. Hejmanowski and D. L. Carroll, "Joule-Thomson Microcryocooler Test Results," *Cryocoolers 20,* 2018.

[4] R. F. Barron, Cryogenic Systems, Oxford University Press, 1985.

[5] G. Nellis and S. Klein, Heat Transfer, New York: Cambridge University Press, 2009.

[6] R. Barraza, "Thermal-fluid behavior of mixed refrigerants for cryogenic applications [dissertation]," Madison: Univ. of Wisc. Madison, Available from: UW Madison Library System, 2015.

[7] H. Müller-Steinhagen and K. Heck, "A simple friction pressure drop correlation for two-phase flow in pipes," *Chem. Eng. Process. Process Intensif.,* vol. 20, pp. 297-308, 1986.

[8] D. Jähnig, "A Semi-Empirical Method for Modeling Reciprocating Compressors in Residential Refrigerators and Freezers [ms thesis]," Madison: Univ. of Wisc. Madison, Available from: UW Madison Library System, 1999.

[9] A. K. Gresin and N. D. Zacharov, "General principles of formation and optimization of multicomponent working fluids for cryogenic systems," *Proceedings fo the 15th International Congress on Refrigeration,* vol. 1, pp. 169-173, 1999.

[10] A. V. Mostitski, V. M. Khudzinski and V. V. Miklashevitz, "Working composition or use in refrigerators contains nitrogen, methane, propane, isobutane, and additional Freon-14 to increase efficiency of cooling cycle". SU Patent 1089099, 30 April 1984.

[11] K. Weckemann and L. R. Oellrich, "Results of the investigation of a mixed refrigerant cryocooler," *Proceedings of the International Congress of Refrigeration 2003,* 2003.

[12] E. C. Luo, Y. Zhou and M. Q. Mao, "Thermodynamic analysis and optimization of 80K closed-cycle Joule-Thomson with gas mixture," *Advances in Cryogenic Engineering,* vol. 43, pp. 1679-1683, 1988.

[13] H. Skye, "Modeling, Experimentation and Optimization for a Mixed Gas Joule-Thompson Cycle with Precooling for Cryosurgery [dissertation]," Madison: Univ. of Wisc. Madison, Available from: UW Madison Library System, 2011.

[14] K. L. Fredrickson, "Optimization of Cryosurgical Probes for Cancer Treatment [m.s. thesis]," Madison: Univ. of Wisc. Madison, Available from: UW Madison Library System, 2004.

[15] F. Keppler, G. F. Nellis and S. A. Klein, "Optimization of the Composition of a Gas Mixture in a Joule-Thomson Cycle," *HVAC&R Research,* vol. 10, no. 2, pp. 213-230, 2004.

[16] K. Passow, "Emprical Model Improvements for a Mixed Gas Joule-Thomson Cycle with Precooling for Cryosurgery [m.s. thesis]," Madison: Univ. of Wisc. Madison, Available from: UW Madison Library System, 2012.

[17] J. Pettit, "Numerical Modeling and Experimental Testing of a Mixed Gas Joule Thomson Cycle [m.s. thesis]," Madison: Univ. of Wisc. Madison, Available from: UW Madison Library System, 2006.

[18] K. C. Rule, "Emprical Modeling and System Optimization for a Precooled Joule-Thomson Cycle for Cryosurgery [m.s. thesis]," Madison: Univ. of Wisc. Madison, Available from: UW Madison Library System, 2014.

[19] N. Tzabar, "Joule-Thomson Cryocoolers Operating with Binary Mixtures".

[20] N. Tzabar and Z. Lapp, "Experimental Investigation on Mixed-Refrigerant for Closed-Cycle Joule-Thomson Cryocoolers," *AIP Conference Proceedings,* 2010.

[21] A. Hamersztein and N. Tzabar, "A hybrid analtyical method for evaluating thermodynamic properties of mixtures by the Peng-Robinson equation of state," *IOP Conf. Ser.: Mater. Sci. Eng,* vol. 502, 2019.

[22] V. T. Arkhipov, V. V. Yakuba, M. P. Lobko and O. V. Yevdokimova, "Multicomponent Gas Mixtures for J-T Cryocoolers," *Cryocoolers 10,* pp. 487-495, 1999.

[23] J. F. Hinze, S. A. Klein and G. F. Nellis, "Thermodynamic Optimization of Mixed Refrigerant Joule Thomson Cycle with Heat Transfer Considerations," *IOP Conf. Ser.: Mater. Sci. Eng. ,* 2015.

[24] J. Hinze, "Thermodynamic Optimization of Mixed Refrigerant Joule Thomson Cycle with Heat Transfer Considerations [m.s. thesis]," Madison: Univ. of Wisc. Madison, Available from: UW Madison Library System, 2015.

[25] A. Gresin and Y. Landa, "Design method for J-T micro cooler heat-exchanger applying multicomponent refrigerant," *Proceedings of the 19th International Congress of Refrigeration,* vol. IIIb, pp. 1102-1106, 1995.

[26] J. Geist and P. Lashmet, "Miniature Joule-Thomson Refrigeration Systems," *Advances in Cryogenic Engineering,* 1960.

[27] P. K. Gupta, P. K. Kush and A. Tiwari, "Experimental research on heat transfer coefficients for cryogenic cross-counter-flow coiled finned-tube heat exchangers," *International Journal of Refrigeration,* vol. 32, pp. 960-972, 2009.

[28] A. Croft and P. Tebby, "The design of finned-tube heat exchanger," *Cryogenics,* vol. 10, no. 3, pp. 239-240, 1970.

[29] J. Cosier and A. Croft, "A new form of finned-tube heat exchanger," *Cryogenics,* vol. 10, no. 3, pp. 239-240, 1970.

[30] P. Gupta, P. Kush and A. Tiwari, "Experimental studies on pressure drop characteristics of cryogenic cross-counter flow coiled finned tube heat exchangers," *Cryogenics,* vol. 50, pp. 254-265, 2010.

[31] F. Dittus and L. Boelter, Publication on Engineering Vol.2, vol. 2, Berkeley, CA: University of California Press, 1930.

[32] J. Howard, N. Hasan and P. Knudsen, "Thermal-Hydraulic Characterization of Shell-Side Flow in a Cryogenic Coiled Finned-Tube Heat Exchanger," *Journal of Heat Transfer,* vol. 143, 2021.

[33] A. Alimoradi, M. Olfati and M. Maghareh, "Numerical investigation of heat transfer intensification in shell and helically coiled finned tube heat exchangers and design optimizaiton," *Chemical Engineering & Processing: Process Intenstification,* vol. 121, pp. 125-143, 2017.

[34] M. Sepehr, S. Hashemi, M. Rahjoo, V. Farhangmehr and A. Alimoradi, "Prediction of heat transfer, pressure drop and entropy generation in shell and helically coiled finned tube heat exchangers," *Chemical Engineering Research and Design,* vol. 134, pp. 277-291, 2018.

[35] K. Timmerhaus and T. Flynn, Cryogenic Process Engineering, New York, USA: Plenum Press, 1989.

[36] S. Genić, B. Jaćimović, M. Jarić, N. Budimir and M. Dobrnjac, "Research on the sell-side thermal performances of heat exchangers with helical tube coils," *International Journal of Heat and Mass Transfer,* vol. 55, pp. 4295-4300, 2012.

[37] G. Jian, S. Wang, L. Sun, J. Wen and J. Tu, "Experimental study of the effects of key geometry parameters on shell-side vapor condensation of spiral-wound heat exchangers," *Applied Thermal Engineering,* vol. 166, 2020.

[38] N. Ghorbani, H. Taherian, M. Gorji and H. Mirgolbabaei, "Experimental study of mixed convection heat transfer in vertical helically coiled tube heat exchangers," *Experimental Thermal and Fluid Science,* vol. 34, pp. 900-905, 2010.

[39] B. Onal, S. Kirkar, D. Akgul, A. Celen, O. Acikgoz, A. Dalkilic, S. Kazi and S. Wongwises, "Heat transfer and pressure drop characteristics of two phase flow in helical coils," *Thermal Science and Engineering Process,* vol. 27, 2022.

[40] G. Nellis and S. Klein, Heat Transfer, New York, NY: Cambridge University Press, 2009.

[41] L. Cheng and D. Mewes, "Review of two-phase flow and flow boiling of mixtures in small and mini channels," *International Journal of Multiphase Flow,* vol. 32, pp. 183-207, 2006.

[42] G. Celata, M. Cumo and T. Setaro, "A review of pool and forced convective boiling of binary mixtures," *Experimental Thermal and Fluid Science,* vol. 9, no. 4, pp. 367-381, 1994.

[43] D. S. Jung, M. McLinden, R. Radermacher and D. Didion, "Horizontal flow boiling heat transfer experiments with a mixture of R22/R114," *Int. J. Heat Mass Transfer,* vol. 32, pp. 131-145, 1989.

[44] R. Radermacher, H. Ross and D. Didion, "Experimental determination of forced convective evaporative heat transfer coefficients for non-azeotropic refrigerant mixtures," in *ASME National Heat Transfer Conference,* 1983.

[45] H. Ross, R. Radermacher and M. Marzo, "Horizontal flow boiling of pure and mixed refrigerants," *Int. J. Heat Mass Transfer,* vol. 30, no. 5, pp. 979-992, 1987.

[46] G. Celata, M. Cumo and T. Setrao, "Forced convective boiling in binary mixtures," *Int. J. Heat Mass Transfer,* vol. 36, no. 13, pp. 3299-3309, 1993.

[47] K. Murata and K. Hashizume, "Forced convective boiling of non-azeotropic mixtures," *Trans. JSME,* vol. 54, pp. 2856-2863, 1988.

[48] D. Chen and Y. Shi, "Two-phase heat transfer and pressure drop of LNG during saturated flow boiling in a horizontal tube," *Cryogenics,* vol. 58, pp. 45-54, 2013.

[49] G. Nellis, C. Hughes and J. Pfotenhauer, "Heat transfer coefficient measurements for mixed gas working fluids at cryogenic temperatures," *Cryogenics,* vol. 45, pp. 546-556, 2005.

[50] R. Barraza, G. Nellis, S. Klein and D. Reindl, "Measured and predicted heat trasnfer coefficients for boiling zeotropic mixed refrigerants in horzontal tubes," *International Journal of Heat and Mass Transfer,* vol. 97, pp. 683-695, 2016.

[51] E. Granryd, "Heat transfer in flow evaporation of non azeotropic refrigerant mixtures - A theoretical approach," *Proc. 18th Int. congr. Refrig.,* pp. 1330-1334, 1991.

[52] W. A. Little, "Heat transfer efficiency of Kleemenko cycle heat exchangers," in *AIP Conf. Proc.*, AIP Publilshing, 2008, pp. 606-613.

[53] P. Ardhapurkar and A. A. M. Sridharan, "Flow boiling heat transfer coefficients at cryogenic temperatures for multi-component refrigerant mixtures of nitrogen-hydrocarbons," *Cryogenics,* vol. 59, pp. 84-92, 2014.

[54] D. Gomse and S. Grohmann, "Heat transfer and pressure drop in the main heat exchanger of a cryogenic mixed refrigerant cycle," in *IOP Conf. Ser.: Mater. Sci. Eng.*, 2019.

[55] P. Ardhapurkar, A. Sridharan and M. Atrey, "Performance evaluation of heat exchanger for mixed refrigerant J-T cryocooler," *Cryogenics,* vol. 63, pp. 49-56, 2014.

[56] C. A. and Z. R., "A dimensionless correlation for heat transfer in forced convection condensation," *Proceedings of the 6th int heat transfer conference,* vol. 3, pp. 309-313, 1974.

[57] P. Ardhapurkar, A. Sridharan and A. M.D, "Experimental investigation on temprature profile and pressure drop in two-phase heat exchanger for mixed refrigerant Joule-Thomson cryocooler," *Appl. therm. Eng.,* vol. 66, pp. 94-103, 2014.

[58] M. Boiarski, A. Khatri and V. Kovalenko, "Design Optimization of the Throttle-Cycle Cooler with Mixed Refrigerant," in *Cryocoolers 10*, New York, NY, Kluwer Acadmic/Plenum Publishers, 2002, pp. 457-465.

[59] M. Gong, J. Wu, E. Luo, Y. Qi, Q. Hu and Y. Zhou, "Study on the overall heat trasnfer coefficient for the tube-in-tube heat exchanger used in mixed-gases coolers," *AIP Conference Proceedings,* pp. 1483-1490, 2002.

[60] J. R. Olson, P. Champagne, E. Roth and T. Nast, "JT Micro Compressor Test Results," *Cryocoolers 19,* pp. 369-375, 2016.

[61] "MATLAB release R2019b, The MathWorks, Inc.,," Natick, Massachusetts, United States..

[62] E. W. Lemmon, I. H. Bell, M. L. Huber and M. O. McLinden, "NIST Reference Database 23: Reference Fluid Thermodynamic and Transport Properties - REFPROP, Version 10.0, National Institute of Standards and Technology, Standard Reference Data Program," Gaithersburg, 2018.

[63] S. Kandlikar, "Fundamental issues related to flow boiling in minichannels and microchannels," *Exp. therm. Fluid Sci.,* vol. 26, pp. 389-407, 2002.

[64] "PT-100 Series Platinum RTDs," [Online]. Available: https://www.lakeshore.com/docs/default-source/product-downloads/lstc_platinum_l.pdf?sfvrsn=9157869c_5. [Accessed 20 Oct. 2022].

[65] "Energy Transfer Durafin Tubes," [Online]. Available: https://durafintube.com/about-us/our-story/. [Accessed 2 Sept. 2022].

[66] "SECOP Technical Data for Compressor," [Online]. Available: https://www.secop.com/fileadmin/user_upload/SEPS/datasheets/sc18clx2_104l2198_r404a-r452a_115v_60hz_12-2020_ds.pdf. [Accessed 21 Oct. 2022].

[67] "Operating Instructions Proline Promass 83," [Online]. Available: https://portal.endress.com/wa001/dla/5000000/0476/000/09/BA00059DEN_1514.pdf. [Accessed 26 Sept. 2022].

[68] "Catch-All Filter-Driers," [Online]. Available: https://www.parker.com/literature/Sporlan/Sporlan%20pdf%20files/Sporlan%20pdf%20040/40-10.pdf. [Accessed 21 Oct. 2022].

[69] "Swagelok Filters," [Online]. Available: https://www.swagelok.com/downloads/webcatalogs/en/ms-01-92.pdf. [Accessed 21 Oct. 2022].

[70] "Manchester Tank Model 304978," [Online]. Available: https://www.mantank.com/pdf/Parts/304978/304978.pdf. [Accessed 21 Oct. 2022].

[71] "Users Guide to FMA 1700 & FMA 1800 Mass Flowmeter," [Online]. Available: https://assets.omega.com/manuals/M1680.pdf. [Accessed 26 Sept. 2022].

[72] "Swagelok Metering Valves," [Online]. Available: https://www.swagelok.com/downloads/webcatalogs/en/ms-01-142.pdf. [Accessed 21 Oct. 2022].

[73] "Temprite," [Online]. Available: https://temprite.com/products/coalescent-oil-separators/300-series/model-320/. [Accessed 21 Oct. 2022].

[74] "Item #532B-2M, Popoff Valves," Circle Valve Technologies Inc, [Online]. Available: https://catalog.circlevalve.com/item/relief-valves/500-series-relief-valves/cs-532b-2m. [Accessed 21 Oct. 2022].

[75] "PT-100 Series Platunium RTDs," [Online]. Available: https://www.lakeshore.com/docs/default-source/product-downloads/lstc_platinum_l.pdf?sfvrsn=9157869c_5. [Accessed 22 Oct. 2022].

[76] F. Schwartz, "Measurements of Mixed-Gas Heat Transfer Coefficients [masters thesis]," Madison: Univ. of Wisc. Madison, Available from: UW Madison Library System, 2015.

[77] "Cryogenic Wire Technical Specifications," [Online]. [Accessed 21 Oct. 2022].

[78] "Lake Shore Miscellaneous Accsesories," [Online]. Available: https://www.lakeshore.com/docs/default-source/product-downloads/catalog/lstc_miscaccess_l.pdf?sfvrsn=54cee8d8_1. [Accessed 28 Oct. 2022].

[79] "Series 943 Cold Cathod Vacuum Gauge System," [Online]. Available: https://www.idealvac.com/files/brochures/MKS_943_Brochure.pdf. [Accessed 28 Oct. 2022].

[80] "Setra Model 206 Industrial Pressure Transducer," [Online]. Available: https://www.setra.com/hubfs/Product_Data_Sheets/Setra_Model_206_Data_Sheet.pdf. [Accessed 28 Oct. 2022].

[81] "User's Guide for FMA 5400A/5500A Mass Flow Controllers," [Online]. Available: https://assets.omega.com/manuals/test-and-measurement-equipment/flow/mass-flow-meters/M5372.pdf. [Accessed 29 August 2022].

[82] A. Technologies, "Fundamentals of Gas Chromatography," May 2002. [Online]. Available: https://www.agilent.com/cs/library/usermanuals/public/G1176-90000_034327.pdf. [Accessed 9th Nov. 2022].

[83] S. Klein, "EES - Engineering Equation Solver. F-Chart Software. V11.422," 29 Sept. 2022. [Online]. Available: https://fchartsoftware.com.

[84] T. Bennett, "Laminar convection in circular tubes with developing flow," *Journal of Heat Transfer,* vol. 142, no. 11, 2020.

[85] G. (. Hewitt, Heat Exchanger Design Handbook, Part 2: Fluid Mechanics and Heat Transfer, New York: Begell House, 2008.

[86] R. Barron, Cryogenic Heat Transfer, Philadelphia: Taylor & Francis, 1999.

[87] "CR23X Micrologger Operator's Manual," [Online]. Available: https://s.campbellsci.com/documents/us/manuals/cr23x.pdf. [Accessed 31 Oct. 2022].

[88] P. K. Gupta, P. K. Kush and A. Tiwari, "Experimental studies on pressure drop characteristics of cryogenic cross-counter flow coiled finned tube heat exchangers," *Cryogenics,* vol. 50, pp. 257-265, 2010.

[89] R. F. Barron and G. Nellis, Cryogenic Heat Transfer, CRC Press, 2017.

[90] "The PID Controller & Theory Explained," National Instruments Corp., 22 Sept. 2022. [Online]. Available: https://www.ni.com/en-us/innovations/white-papers/06/pid-theory-explained.html. [Accessed 24 Oct. 2022].

[91] "SECOP Compressor Technical Data," [Online]. Available: https://www.secop.com/fileadmin/user_upload/SEPS/datasheets/sc18clx2_104l2198_r404a-r452a_115v_60hz_12-2020_ds.pdf. [Accessed 4 Nov. 2022].

[92] "Loctite Stycast 2850FT Technical Data Sheet," March 2015. [Online]. Available: https://tdsna.henkel.com/americas/na/adhesives/hnauttds.nsf/web/35541AEFDE6FDF8485257576004480E6/%5C$File/STYCAST%202850FT-EN.pdf. [Accessed 4 Nov. 2022].

[93] C. R. Wilke, "A viscosity equation for gas mixtures," *J. Chem. Phys.,* vol. 18, pp. 17-519, 1950.

[94] E. Lemmon, I. Bell, M. Huber and M. McLinden, "NIST Standard Reference Database 23: Reference Fluid Thermodynamic and Transport Properties - REFPROP, Version 10.0," National Institute of Standards and Technology, Gaithersburg, 2018.

[95] S. Kruthiventi, N. Rasu and H. Rao, "Performance of wire finned coiled tube heat exchanger in a small J-T refrigerator," *Materials Today: Proceedings,* vol. 46, pp. 9809-9813, 2021.

[96] S. Klein and G. Nellis, Thermodynamics, New York, NY: Cambridge University Press, 2012.

[97] D. S. Jung, M. McLinden, R. Radermacher and D. Didion, "Horizontal flwo boiling heat transfer experiments with a mixture of R22/R114," *Int. J. Heat Mass Transfer,* vol. 32, no. 1, pp. 131-145, 1989.

[98] C. Hughes, "Experimental Measurement of Heat Transfer Coefficints for Mixed Gas Working Fluids in Joule-Thompson Systems [masters thesis]," Madison: Univ. Of Wisc. Madison, Available from: UW Madison Library Systems, 2004.

[99] D. Gomse, T. Kochenburger and S. Grohmann, "Modeling of Two-Phase Heat Exchangers with Zeotropic Fluid Mixtures," *Journal of Heat Transfer,* vol. 140, 2018.

[100] V. Gnielinski, *Int. Chem. Eng.,* vol. 16, p. 359, 1976.

[101] R. Damle, P. Ardhapurkar and M. Atrey, "Numerical analysis of the two-phase heat transfer in the heat exchanger of a mixed refrigerant Joule-Thomson cryocooler," *Cryogenics,* vol. 72, pp. 103-110, 2015.

[102] A. Cicchitti, C. Lombardi, M. Silvestri, G. Solddaini and R. Zavalluilli, "Two-phase cooling experiments - Pressure drop, heat transfer and burnout measurement," *Energia Nucleare,* vol. 7, pp. 407-425.

[103] "USB-6008 Specifications," National Instruments, 3 May 2022. [Online]. Available: https://www.ni.com/docs/en-US/bundle/usb-6008-specs/page/specs.html. [Accessed 28 Oct 2022].